Università degli studi di Roma Tre

Dipartimento di Matematica e Fisica

Phylosophical Doctorat in Physics

The X-ray emission of AGN: investigating the surroundings of Black Holes

Ph. D. thesis in Physics

Supervisor:
Professor
Stefano Bianchi

Candidate:
Riccardo Middei

Ph. D. XXXI cycle 2015/2018

Contents

Incipit

Active galactic nuclei (AGN) are among the brightest sources enlightening the sky. These objects are observed in the local Universe as well as at high redshift (up to z$\sim$7), they are variable and shine in all the electromagnetic bands. The study of such peculiar sources has both opened up a series of new science topics and given rise to novel ways for estimating distances and enlarging the cosmic distance ladder.

AGN are among the most efficient engines in the Universe and, according to our current view, they are empowered by accretion of matter onto supermassive black holes. Thus, the optical-ultraviolet (UV) emission observed from these sources can be considered the result of this process. From an observational point of view, AGN are characterized by a complex and wide spectral energy distribution (SED) and by flux variations occurring over all frequencies. Such a broadband emission can be understood by the light of the composite nature of these systems and the interplay between these various components. AGN can be optically bright objects or not, they can display evidence of jet or be non-jetted, they may be strong X-ray emitters or their X-rays may contribute weakly to the bolometric luminosity.

This wide range of observational properties has given rise to a wide AGN taxonomy. Thanks to various facilities, our understanding of these sources has greatly improved, and, at present, AGN are described by the so-called unified model. The scenario presented by this model attempts to combine the various sub-classes of AGN as a function of the observer's line of sight, meaning that AGN are intrinsically the same phenomenon and all observational differences are due to the viewing angle between the observer's line of sight and the system axis.

As just briefly said, AGN can be X-ray bright objects, and this energetic emission cannot be ascribed to accretion. Presently, it is widely believed that X-rays emerge from the innermost region of AGN, in the proximity of black holes. Indeed, it has been shown that AGN X-ray emission is compatible with the result of an inverse-Compton process that involves seed optical-UV photons arising from the accretion disc and a hot thermal distribution of electrons which we commonly refer to as the corona. Then, the characterization of X-ray spectra is the best tool available to investigate the physical properties of the complex environment near the supermassive black holes (SMBH). The study and understanding of the nuclear X-rays emerging from AGN is the major topic of

this dissertation. In fact, although we are deepening our understanding of these sources, several questions concerning their physics are still open. In the following, we report a few key open issues:

- The high energy emission of AGN is the result of an inverse-Compton process and the emerging spectrum can be described as a power-law with a high-energy cut-off (at energies around a few hundred keV) that depends on the electron temperature (kT_e) and the optical depth (τ_e) of the corona. Can we derive models that, exploiting observational data, allow us to derive the physical properties of the Comptonising medium?

- The nature of the soft-excess is still unclear. This spectral component has been interpreted as an effect of relativistically blurred reflection or the result of a further Comptonisation mechanism by a colder optically thick gas (warm corona). Then, what is the origin of this spectral component?

- What is the origin of the reflected component? AGN spectra may display features of relativistically blurred reflection from the very inner part of the accretion disc. However, these features, likely produced within a few gravitational radii from the black hole, are not ubiquitous and in various cases the reflection component seems to originate only from distant material. In other sources, the reflection component is weak or even absent suggesting that, in some AGN, the standard accretion disc is truncated at some radius.

- Variability is a defining AGN property, and flux variations in the X-rays have been measured down to kilo seconds. Such a rapid variability has suggested that the region producing X-ray photons has to be compact and most likely located in the inner part of the accretion flow. However, long term flux variations are also observed in the X-rays. Then, is such a long term variability proper of the Comptonising corona (hot/warm), or is it, instead, an echo of flux variations due to the accretion process?

In the attempt to answer the above quoted questions, various approaches can be pursued, based on observations and simulations, focusing on the properties of nearby single AGN as well as working on statistically rich samples of sources.

Detailed spectral analyses are indeed our best tool for probing models and extracting physical parameters of interest, and such a kind of analysis has an enhanced outcome when multi-epoch and broadband data are studied. In fact, multiple observations allow for tracking the time-evolution of the source's spectral components, while a multiwavelength coverage allows for a comprehensive modelling of various emission components. In this work, the spectral properties of the Seyfert galaxies HE 0436-4717, NGC 7469 and NGC 4593 will be presented and discussed.

A further step in this dissertation is provided by the analysis of simulated spectra accounting for Comptonisation. In this context, we exploited the recently released code MoCA (MonteCarlo code for Comptonisation in Astrophysics) for studying Comptonisation spectra in AGN. In particular, the MoCA allowed us to study Comptonised spectra of a wide range of parameters describing both the seed optical spectrum (SMBH mass or accretion rate) as well as the coronal region (e.g. opacity and temperature). By analysing simulations, we built a physical self-consistent "theoretical" framework within which we could compare observations with expectations, thus allowing us to derive information on the emitting X-ray region.

Finally, we performed an ensemble study describing the averaged variability properties of a sample of AGN. In particular, this work aimed at scrutinising for the presence of a typical timescale for X-ray flux variations on the longest timescale ever investigated for the 0.2-2 keV band.

This thesis is made up of various Chapters arranged as follows:

- **Chapter 1:** an overview on Active Galactic Nuclei is given. We will focus on their observational behaviour, taxonomy and structure. Further, the unified model will be presented.

- **Chapter 2:** Two of the major processes occurring in AGN are discussed: accretion and Comptonisation. The first one fuels AGN while the latter accounts for the high energy emission emerging from these objects.

- **Chapter 3:** The complex X-ray spectrum of AGN is presented and discussed. We will focus on the various spectral components. Particular emphasis will be placed on the origin of the primary continuum and on the components arising from the reprocessing of the X-ray primary emission from the circumnuclear matter. Moreover, both flux and spectral variability will be presented and discussed.

- **Chapter 4:** We report on detailed spectral analyses of three AGN. In particular, we will discuss the high energy view of a nearby Seyfert galaxy serendipitously observed by NuSTAR. Then, the broadband optical-ultraviolet-to-X-ray spectral characterizations of NGC 7469 and NGC 4593 are presented.

- **Chapter 5:** To test Comptonisation in AGN, we present results based on the analysis of MonteCarlo simulations. Further, we present equations directly connecting phenomenological parameters with those describing the physics of the Comptonising medium.

- **Chapter 6:** The variability properties of a statistically rich sample of AGN is presented and discussed.

- **Chapter 7:** The bibliography is reported.

Chapter 1

Active Galactic Nuclei, what's in a name?

1.1 Introducion

Most of the electromagnetic radiation coming from galaxies is emitted in the optical-UV and infrared bands. This is the result of two main processes occurring in these sources: thermonuclear reactions of the stars and the reprocession of stellar radiation by matter in the form of dust and grains. These two processes account for the emission of about 90%[1] of galaxies which, at present, we refer to as quiescent. Weaker contributions to the bolometric luminosity are provided, for instance, by the X-rays, which can be produced by X-ray binary systems and supernova remnants. On the other hand, the remaining galaxies (∼10%) display additional peculiarities, such as high X-ray output and broad emission lines. Fath (1909) was the first astronomer who studied an AGN (NGC 1068) and he noted the presence of strong emission lines in its optical spectrum. Later, Slipher (1917) obtained a higher-quality, higher-resolution spectrum of the same source, and he commented that the emission lines were similar to those seen in planetary nebulae. Moreover, he observed that the lines were resolved, and commented that their widths were of hundreds of kilometers per second.About 30 years after the claim by Fath (1909), other sources were observed to share similar properties with NGC 1068, and Carl Seyfert defined a new class of objects characterized by high central brightness and lines with widths up to thousands kilometers per second (Seyfert 1943). A significant radio emission was then observed in NGC 1068 and just before the sixties Woltjer (1959) stated that all "Seyfert" galaxies share similar features: a high luminosity and a non-resolved bright nucleus. He also observed that the typical-lifetime of a Seyfert emission

[1]This percentage depends upon environment and redshift, as discussed by Brandt & Alexander (2015).

was greater than a hundred million years, and that the linear size of the central source must have been less than 100 pc. Adopting the Virial relation[2] and assuming that matter in the galaxy nucleus was gravitational bound, Woltjer found that a $10^8 - 10^{10} M_\odot$ mass was needed to bind the system. After World War II and the growth of technologies, radio astronomers had an increasing interest in surveying the sky and many sources observed in radio were coincident with star-like objects already detected in the optical band. The visible counterpart of the radio sources were galaxies or star-like objects (Matthews & Sandage 1963). Broad emission lines were observed in these sources at unknown wavelengths, and it was Maarten Schmidt who understood that the emission lines were those of the Balmer Hydrogen series and of the $MgII$ transitions explaining their anomalous wavelengths by the redshift of the source and the expansion of the Universe (Schmidt 1963). At that point it was clear that these galaxies/point-like objects were peculiar sources, and nowadays we call them Active Galactic Nuclei (AGN). AGN are therefore a sub-class of galaxies for which part of the below properties are observed:

- star-like objects or unresolved nucleus
- large optical-UV radiation flux;
- broadband emission and variability;
- narrow and broad lines in emission and/or absorption;

They are located in the very central part of their host galaxies and appear either as bright and unresolved nuclei embedded in nearby galaxies or as point-like sources. Most of the radiation coming from AGN is produced in the optical-UV band as the result of accretion and their broadband emission can be decomposed into about four main components: (i) a primary emission in the optical/UV band; (ii) an infrared continuum, which is due to thermal emission from dust heated by the primary UV radiation; (iii) the high-energy continuum, that can be ascribed to the reprocessing of the primary optical/UV emission by hot gas; (iv) the radio emission, due to synchrotron radiation, whose prominence can be strong (radio-loud AGN) or weak (radio-quiet AGN). Moreover, variability acts in all these spectral bands. Strong emission lines appear in the optical. In the following, I will introduce the various AGN phenomenologies, discuss their broadband emission and structure. Finally, the unified model is presented.

[2] $2\bar{T} + \bar{U} = 0$. The Virial theorem is a dynamical relation holding in systems at the equilibrium. This theorem relates the total mass of the system, the mean square of the velocities of the individual objects that constitute the system and its liner dimension R. Then in the context of active galaxies using $\bar{T} = \frac{M<v>^2}{2}$ and $\bar{U} = -GM^2/R$, the virial relation provides an estimate for the mass $M_{\rm SMBH}$ providing the binding gravitational potential.

1.2 AGN: Taxonomy

The set of galaxies fulfilling the above requirements is wide and varied, so AGN classification is complex and not always straightforward. Classifying AGN mainly means collecting their spectroscopical and observational properties (e.g. the presence of broad lines, see Fig. 1.1) and setting the different theoretical parameters accounting for them in order to define the various AGN classes. However, it is worth noticing that classification must be considered as a simplifying tool instead of a monolithic approach.

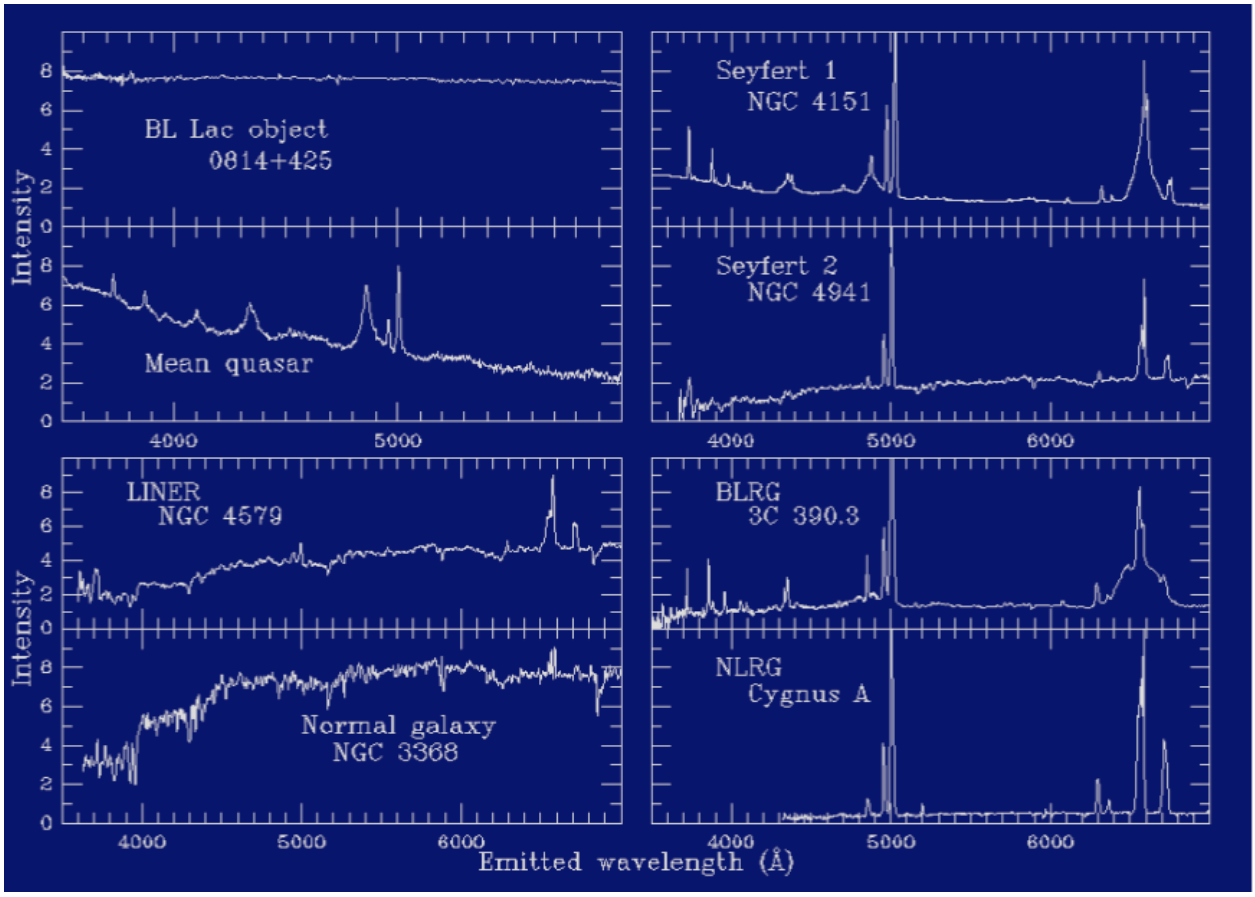

Figure 1.1. Various optical spectra of AGN belonging to different classes. Each active galaxy behaves peculiarly and in the bottom left panel the typical emission of a quiescent galaxy is reported, Peterson (1997).

- **Seyfert galaxies**: These galaxies, originally classified by Carl Seyfert (1943), are characterized by high optical outputs ($L \lesssim 10^{44} erg/s$), and they are bright in the X-ray band, $L_X \gtrsim 10^{42} erg/s$. An optical classification of Seyfert galaxies was

provided by Schmidt & Green (1983) who adopted a magnitude limit of $M_B > -23$. Optical radiation coming from the embedded AGN is comparable with the one of the host galaxy. These are radio-quiet objects and have high central surface brightness, although the host galaxy is still clearly detectable. Seyfert galaxies are often spirals characterized by massive galactic bulges. Since their original discovery, the classification has evolved such that they are also spectroscopically identifiable by the presence of high-ionisation emission lines. Seyfert galaxies can therefore be divided into two groups: Seyfert 1s and Seyfert 2s (Sy1s and Sy2s), as at first proposed by Khachikian & Weedman (1974).

  - Type-1 Seyfert galaxies display highly ionised, broad permitted lines, together with narrow forbidden lines. In accordance with our current understanding, narrow lines come from low-density gas, the Narrow-Line Region. These lines are characterized by a full width at half maximum (FWHM) of a few hundred km s^{-1}. Because the density in the NLR is low, transitions are not collisionally de-excited, and so the radiative transitions (and, hence, the forbidden lines) are observed. The broad lines have widths Doppler-broadened up to 10^4 km s^{-1} . The Broad Line Region (BLR) is located closer to the black hole, shown by the increased width of the lines; since only permitted lines are seen, the BLR is thought to be the denser of the two regions, with $n_e > 10^9$ cm^{-3}, compared to $\sim 10^3$-10^6 cm^{-3} for the NLR.
  - Type-2 Seyfert galaxies show only the narrow lines. They have an [O III]λ5007 to Hβ ratio of < 3 (Shuder & Osterbrock 1981); Seyfert 2s also tend to show weaker [Fe II] (or higher ionisation iron) emission lines than their Seyfert 1 counterparts.

- **Quasars**: These extragalactic objects are brighter than Seyferts ($10^{44} erg/s < L_{opt} < 10^{47} erg/s$) but they show a similar spectrum. These sources have been observed up to redshift ∼7.1 (e.g. Momjian et al. 2014; Page et al. 2014). The QSO spectrum is described using a power law ($F_\nu \propto \nu^\alpha$ where $\alpha = -0.46$, Vanden Berk et al. 2001).

- **Radio Galaxies**: These active nuclei are luminous in the radio wavelength. According to their spectroscopic properties these objects are classified as Broad Line Radio Galaxy (BLRG) and Narrow Line Radio Galaxy (NLRG) as for Seyfert galaxies. A further classification for radio emitting AGN is provided by the morphology of their emission, in terms of Fanaroff Riley I (FRI) or Fanaroff Riley II (FRII), (Fanaroff & Riley 1974). When most of the radio emission is observed from two extended lobes that are brighter towards the center we are dealing with a FRI AGN. On the other hand FRII display luminosity higher than FR I (i.e. $L_\nu > 10^{32} erg/s/Hz$) and they are observed as strong point-like radio sources with

two accompanying distant radio emitting lobes. The source is brighter at the border and its luminosity decreases towards the point-like component.

- **LINERS**: These sources are characterized by low ionisation lines and typically, display low luminosities. They are found in about half of the spiral galaxies and the diagnostic Baldwin-Phillips-Terlevich (BTP) (Baldwin et al. 1981) diagram is used to identify them. This diagnostic tool is based on the ratios of the emission lines $[OIII]/H\beta$ and $[NII]/H\alpha$ see Fig. 1.2.

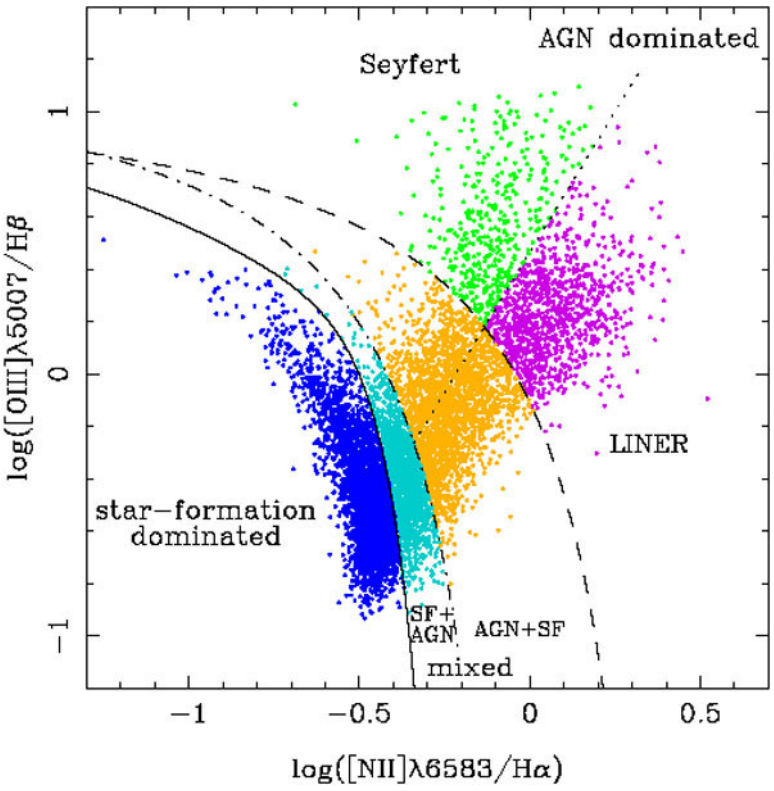

Figure 1.2. The Baldwin-Philips-Terlevich diagram, which classifies active galactic nuclei (AGN) and star-forming galaxies. (Bamford et al. 2008). This tool is also used for distinguishing between e.g. Seyfert galaxies, star burst galaxies.

- **Blazars**: Such kinds of sources are radio bright and their main emission component is a jet of relativistic particles emerging from the nuclear region of the galaxy. In particular, a Blazar occurs when our line of sight is approximately crossing the jet coming from the central supermassive black hole. The radiation emerging from these sources is affected by relativistic effects such as beaming. Blazars show a relativistic emission toward the observer and are classified as BL Lacertae objects (BL Lac) or Optical Violent Variable (OVV). Blazars are always radio loud sources

and the jet is their dominant component. The main feature of Blazar sources is a large and fast variability (up to 1 mag in a few days). The electro-magnetic emission also has some degree of polarization. A peculiar feature of BL Lac objects is that they display spectra free of strong emission lines.

- **Narrow Line Seyfert 1**: The spectra of these galaxies show the smallest Balmer lines (FWHM Hβ <2000 km/s) from the Broad Line Region (BLR) and the strongest FeII emission when compared with other AGN. Narrow line Seyfert are thought to have high accretion rates and, very probably, small black hole masses(Bian & Zhao 2003). Small central black hole masses, high accretion rate, strong soft X-ray emission and variability and smaller flux variations in the optical band have been commonly observed in NLS1. These peculiar sources are presently studied as one of the first steps in the AGN evolution, since the small mass of the BH and its Eddington-like accretion seem to be a clue to their young age (Komossa 2008). Finally, together with Blazars, these sources have been observed in the γ domain.

- **Broad absorption line quasars**: Broad absorption line quasars are a very peculiar AGN class. First, they are usually radio quiet and their optical-UV spectra contain broad (up to 10^4 km/s) absorption features. These sources have a relatively weak X-ray emission, i.e. with a low ratio between the X-ray emission and the UV radiation[3]. AGN belonging to this peculiar class are about one fifth of all the known radio quiet population.

In Fig. 1.3 a diagram with the different AGN sub-classes is shown.

1.3 AGN: Broadband emission

As discussed in the previous section, AGN are complex sources that radiate over the whole electromagnetic spectrum, see Fig. 1.4. The AGN widespread emission cannot be ascribed to a single process, rather it emerges from the interplay between various radiation mechanisms taking place in these sources. The AGN emission has both thermal and non-thermal origins, and, in the following, some information on the AGN multiwavelength emission is provided:

Radio: The study of AGN is strongly tangled with the analysis and growth of radio astronomy. AGN emission in this band is the result of a synchrotron mechanism. Radio

[3]This ratio is described through the α_{ox} parameter. The α_{ox} weights the ratio between X photons and UV photons throughout the relation $\alpha_{ox} = \frac{log[L_\nu(2KeV)/L_\nu(2500)]}{log[\nu(2KeV)/\nu(2500)]}$.

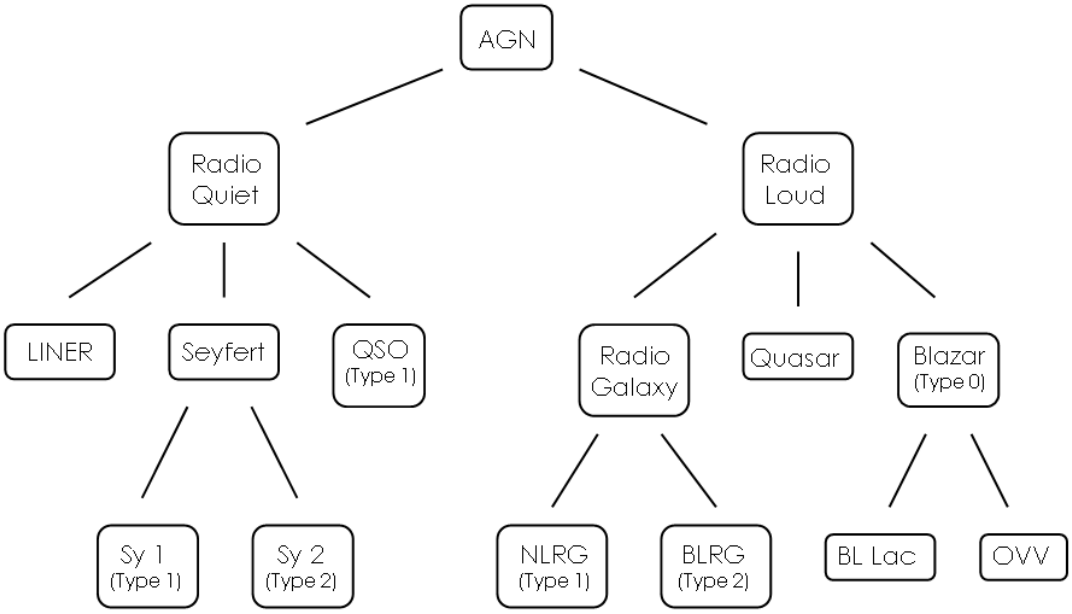

Figure 1.3. A summarizing scheme showing some of the various AGN "species" .AGN are subdivided into classes depending on observational aspects, such as their radio loudness or the presence of optical lines in their spectra.

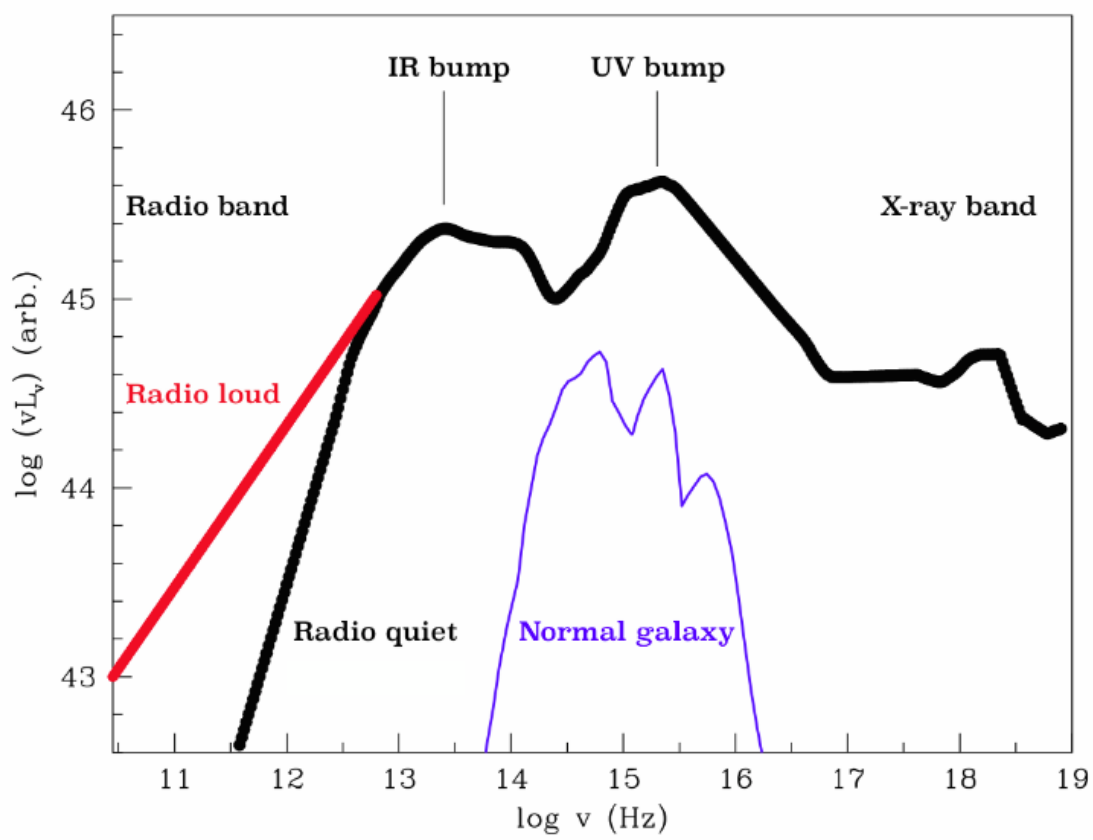

Figure 1.4. The broadband AGN emission (black-red lines) compared to the one expected form a quiescent galaxy (violet line). The solid black line across the graph describes the typical spectral energy distribution of a radio quiet AGN, and the red line is used to account for AGN that are bright in the radio band. Moreover, the main features of the broadband spectrum are reported.

photons weakly contribute to the bolometric source luminosity. In general, emission in this band is three orders of magnitude lower with respect to the optical-UV emission for radio loud AGN, while it is even smaller (three further orders of magnitude) with respect to radio quiet sources. The non-thermal emission in this band is commonly described using a flat power-law that steepens toward higher frequencies.

Infrared: It was believed that the infrared AGN emission was the tail of the power-law like radio spectrum. However, nowadays this emission is explained invoking a different and independent thermal process involving radiation and dust. In AGN, dust can be heated up to ∼2000 K. This is a limiting temperature for the reprocessing medium, in fact, at a higher temperature, grains and silicates sublimate. From a spectroscopical point of view, infrared spectra are characterized by a minimum at about 1 μm (strongly

correlated with the sublimation radius). The near-IR emission is weaker because at these wavelengths, for a ∼2000 K black body, the emission occurs in the Wien regime. Infrared emission also displays variability and it has been found to be correlated with the optical-UV band. Moreover, reverberation analysis shows that typical delays between infrared and optical-UV emission are of the order of hundreds of days (i.e. a light path of less than 10^{18} cm) suggesting that this thermal emission takes place at distances of the same order from the black hole (Barvainis 1992). Furthermore, it is worth noticing that at a distance of about $\sim 10^{18}$ cm corresponds to the sublimation radius of the dust grains.

Optical-UV: Most of the AGN luminosity is observed in the optical and in the UV band. As pointed out before, that emission is released converting potential energy into radiation through matter falling down onto the SMBH. This conversion occurs in the accreting disc. As a first order approximation, we can consider that the energy of a particle at distance r from the central BH is dissipated locally, and that the medium is optically thick. Then, the local emission can be approximated as a black body. Using the laws of thermal emission, it is found that the photons emerging from an AGN (e.g. $10^8 M_\odot$, Eddington accretion rate) display a peak in the UV domain. Experimentally, there is evidence of the so-called Big Blue Bump (BBB) that confirms this assumption. Temperatures are within the range of $10^4 - 10^6$ K. The BBB appears as a bump in the UV region (1000-4000) for AGN having masses of about $10^8 M_\odot$.
However, it is an oversimplified explanation that BBB derives only from black body emission. A peculiar behaviour of the optical-UV emission is that they both vary in phase in a non-periodical and irregular way.

X-rays: This energetic emission is likely produced near the central black hole and it is the result of Comptonisation of seed optical photons from thermal electrons (Haardt & Maraschi 1991a). Moreover, X-ray flux variations are observed down to kilo seconds timescales. This evidence suggests that the physical structure that is producing the flux variations can not be so extended ($R < c\Delta t$), and this suggests that Comptonisation has to occur in the compact region. More details are provided in the next chapters.

Gamma-ray: Active Galactic Nuclei can be copious extragalactic emitters of MeV-GeV-TeV γ-rays, and this phenomenon is thought to be linked with the presence of relativistic jets powered by a super-massive black hole in the center of the host galaxy. Both orbiting (*AGILE, FERMI-GLAST*) and ground-based telescopes (*MAGIC*) are involved in studying this high energy radiation.

1.4 AGN: Structure

AGN activity is always accompanied by broadband emission that cannot be attributed to the host galaxy, and it has to arise from the active nucleus. However, measurements of lags between photons of different wavelengths suggest the presence of various components

acting to produce AGN spectral energy distribution. AGN are, in fact, composite systems and the various components are related by the interplay between gravity and radiation pressure.

- **Supermassive black hole**: This is the engine of the whole structure since it provides the gravitational energy needed to bind the system. It lies in the innermost region of the active galaxy and it affects in different ways the orbiting material. Surrounding matter such as gas clouds orbiting in its vicinity are strongly affected by the compact source and this can be observed performing spectral analysis. A matter particle orbiting around the central BH undergoes the effects of the radiation pressure and potential well of the BH. The balance between these competitive forces is of primary importance when studying the physics of compact objects. Indeed, a system can exist until the Eddington limit holds, $L < L_{Edd}$ where $L_{Edd} \sim 1.26{\cdot}10^{46} \frac{M}{10^8 M_\odot} erg/s$. In other words, gravity exceeding the radiation pressure binds the system and avoids the AGN evaporation. Current models say that matter falling onto the BH explains the emitted power (see Chapter 2). The masses of the black holes span from $\sim 10^6 M_\odot$ up to $10^{10} M_\odot$ as discussed e.g. in Marconi et al. (2009).

- **Accretion disc**: Inflow of gas and matter accreted by the central engine. It accounts for the optical-UV emitted power. Many parameters are used to describe this system: magnetic field strength, accretion rate, viscosity and the presence (or absence) of jets (Blandford 1985). Energy is provided by an accretion mechanism. Matter falling onto the black hole loses angular momentum and potential energy. Potential energy is converted into radiation with high efficiency (e.g. $\eta \sim 10\%$ for a mass falling into a BH from a distance of a few R_S where $R_S = \frac{2GM}{c^2}$ is the Schwarzschild radius) as described by the equation $L = \eta \dot{M} c^2$. The released luminosity is directly proportional to the accretion rate and it is possible to define an Eddington accretion rate $\dot{M}_{Edd}$ that gives the maximum amount of mass accreted per unit time. If the Eddington ratio ($\dot{M}/\dot{M}_{Edd}$) is less than or about 1, the accretion disk has the standard structure studied by Shakura & Sunyaev (1973), optically thick and geometrically thin.

- **Broad Line Region**: This region has been invoked to explain the presence of broad emission lines (10.000 km/s $\leq$ FWHM) commonly observed in AGN. It is constituted by clouds rapidly orbiting around the central black hole and its mass has been estimated to be in the order of a few solar masses. The line broadening is due to the velocity dispersion of the clouds that intercept and reprocess part of the primary UV radiation coming from the inner part of the disc. Thermal broadening is not able to account for the width of these emission lines, indeed, temperature estimations of BLR retrieve a relatively low T of about 10^{4-5} K that

would explain the broadening of only some 10 km/s. BLR clouds occupy a small volume with respect to the total geometrical volume where they are contained. This characteristic is described using the so-called filling factor parameter ϵ_{BLR} which is found to be very small ($\sim 10^{-6} - 10^{-7}$). The electronic density in the clouds is about 10^{9-11} $\frac{electrons}{cm^3}$ and nowadays we think that this region is non spherical and stratified (e.g. Bon et al. 2006). The size of this region (R_{BLR}) varies from a few light-days up to hundreds light-days, and, as predicted by the photo-ionisation, $R_{BLR} \sim L^{0.5}$ (Bentz et al. 2006, 2009) is found. Bentz et al. (2006) corrected this relationship finding $R_{BLR} \sim L^{0.5}$ (also in Bentz et al. 2009). The supermassive black hole drives the dynamical properties of the clouds, and the analysis of their motion leads to important information about the SMBH. The clouds high velocities, in fact, are hints that the BLR is really close to the central engine (10^{16} cm). Then, analysing the delays between the emission line (expected from the BLR) and the illuminating continuum (arising from the accretion disc), allows us to measure the BLR size, and, further, to estimate the black hole mass using the reverberation mapping technique Peterson (1993).

- **Narrow Line Region**: The region emitting the narrow lines (NLR) is constituted by clouds and has a size of hundreds of pc, or is even comparable to the size of the host galaxy. The NLR size increases with the luminosity of the object following a relationship of $R_{NLR} \sim L^{\alpha}$ where $\alpha \sim 0.5$ up to the dimension of about 8 kpc (Hainline et al. 2013). Estimate of the NLR mass is in the order of $\sim 10^{6-7} M_{\odot}$. The volume occupied by these clouds is a small fraction of the whole volume in which they are embedded so that the NLR filling factor is $\epsilon_{NLR} \sim 10^{-2}$. The width of the emission lines produced in the NLR is hundreds of km/s. The broadening is due essentially to the bulk motion of the clouds. The emission lines produced here are found in both Type 1 and Type 2 AGN because the size of NLR greatly exceeds the one of the obscuring torus. Clouds constituting the NLR have low electronic density (10^{3-4} $\frac{electrons}{cm^3}$) so that both forbidden and permitted emission lines are produced.

- **Obscuring Torus**: The Obscuring Torus plays a fundamental role in the AGN classification. It is essentially made up of dust (graphite and silicates) capable of absorbing and reprocess the primary radiation produced by the central engine. It accounts for the IR emission. The torus has a size greater than the dust sublimation radius ($d \gtrsim 1$ pc).

- **Jets**: These structures largely exceeding the active nucleus size are commonly found in radio loud AGN, and, in the case of Blazars, they are the dominant emission component. As just said, these jets extend on parsec as well as kiloparsec scales (e.g Cygnus A). These structures are a collimated outflow of charged particles

that starts from the inner part of the active galaxy.

1.5 Unified Model

From an observational point of view, AGN can display several different behaviours and much effort was made in trying to represent the whole AGN phenomena using a single unified model. The unification model for active galactic nuclei invokes a paradigm for Seyfert 2 and Seyfert 1 galaxies (Antonucci 1993a) in which two different types of galaxies are believed to be intrinsically the same but differ, observationally, due to orientation effects only, see e.g. Fig. 1.5. Let us start considering the case of AGN for which we do not observe broad optical emission lines. Broad emission lines are due to the bulk motion of BLR, then type 2 AGN either have no BLR at all or it is somehow hidden from our sight. The first evidence of BLR for a Type 2 AGN is provided in the paper by Antonucci & Miller (1985). The authors, in fact, observed broad optical lines studying the polarized light of NGC 1068. This means that the BLR emission is obscured by an absorbing medium, and scattered toward our line of sight from material located at greater distances. The reflected spectrum is relatively weak, but still detectable thanks to an about ∼16%, while the direct light is essentially unpolarized. The study of the polarized spectrum of NGC 1068 suggested that the obscuring material has a toroidal shape (to prevent scattering in a large range of angles and polarization being washed out). Further, this structure must have the right dimension to obscure the BLR but not the NLR, then its size should be in the order of parsecs. This analysis leads to the important consequence that AGN observational differences are determined by different orientations relative to the obscuring torus (see Antonucci (1993b) for a previous review, and Bianchi et al. (2012) for a more recent one). In particular, type 2 AGN are observed approximately edge-on, appearing hidden by the torus, while type 1 AGN are seen approximately face-on or at low angles to the torus axis. This model can also be adopted to explain the different X-ray behaviour between type 1 and type 2 AGN. The major difference in their X-ray appearance is the strong drop of soft photons in type 2 objects, below 1-2 keV. Therefore, the presence of an obscuring torus still explains the soft X-ray depletion. More quantitatively, it is possible to classify AGN as a function of the absorbing column density (N_H) of the torus as:

- Compton Thin sources-those AGN presenting a typical N_H $<10^{24}$ cm^{-2} . They have a nuclear flux much higher than a Compton Thick object's source because the circumnuclear material is transparent to the radiation in the 2-10 keV band.

- Compton Thick sources being the AGN for which $N_H > 10^{24}$ cm^{-2}. In these sources, most of the radiation coming from the inner part of the galaxy is absorbed by the torus. In fact, the obscuring material causes photoelectric absorption of soft

X-rays and an energy cut-off function of the absorbers column density is expected to range between 1 and 10 keV.

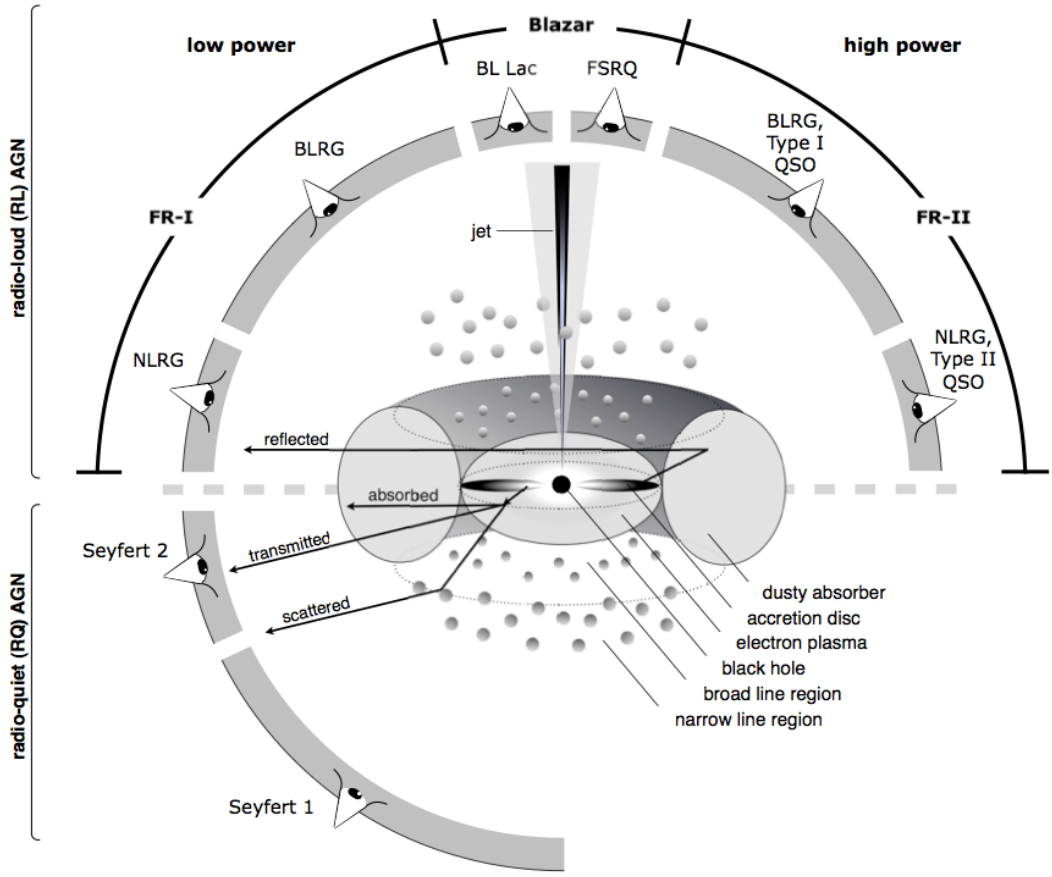

Figure 1.5. A sketch of the unified model. Details are shown and the regions constituting an AGN are all named. Moreover, the scheme displays how the AGN appear by changing the line of sight of the observer and how AGN are classified as a function of their luminosity (Beckmann & Shrader 2012).

Chapter 2

Main mechanisms

Both accretion of matter onto a compact object and Comptonisation are fundamental processes in AGN physics. The first one provides a viable paradigm to explain the huge amount of energy AGN emitt, while the latter is the only radiative process able to explain the AGN X-ray emission.

2.1 Accretion

Stellar reactions cannot explain the high luminosity of AGN, thus another physical mechanism is needed to account for the huge amount of energy they release. Accretion of matter onto a massive object can provide a very efficient way to convert matter energy into radiation. Moreover, accretion can occur in a very small region, thus it is a reliable explanation for how AGN are empowered. It is possible to consider the problem of accretion from the energetic point of view: the gravitational potential energy released by free-fall of a mass m onto an object with mass M and radius R is:

$$E_{tot} = \frac{1}{2}mv^2 = \frac{GMm}{R}. \tag{2.1}$$

Then the luminosity released assuming that the energy is converted into radiation is:

$$L = \frac{dE_{rad}}{dt} = \frac{dU}{dt} = \frac{GM}{R}\frac{dm}{dt} = \frac{GM\dot{m}}{R} \tag{2.2}$$

being $\dot{m}$ the rate of matter accreted. The higher the accretion rate, the higher the luminosity output of the system will be. However, this output also depends on the compactness of the source of the gravitational potential. Therefore, introducing the gravitational radius $R_g = \frac{GM}{c^2}$ we can rewrite the previous equation as:

$$L = \frac{R_g}{R}\dot{m}c^2 \simeq \eta\dot{m}c^2 \ . \tag{2.3}$$

In this equation η represents the efficiency of the conversion of the mass energy into radiation. As already said, this efficiency depends on the nominal compactness of the accreting object, i.e. by the ratio of its mass M and linear dimension R. High efficiency can be reached by very compact accreting objects (e.g. collapsed stars). Concerning black holes, the definition of a linear dimension is not trivial, thus, commonly, what is used is the last stable orbit radius.

According to general relativity, the last stable orbit depends only on the BH spin in terms of R_g while the linear physical scale of R_g is a function of the source mass. Concerning the efficiency of the energy conversion, η can be as large as 6% in case of non-rotating black holes or it may reach values of 30% for supermassive black holes spinning maximally. The high conversion rate typical of matter accretion can straightforwardly account for the high luminosity of AGN (10^{45}<L<10^{46} erg/s) if $\dot{m}$ ∼0.1-1 $M_\odot$/year. However, a limit for the accretion power holds. In fact, to maintain the system at equilibrium the radiation pressure provided by the AGN emission has to be counterbalanced by the gravitational energy. Then it can be demonstrated that this limit holds when L_{output}<$L_{Eddington}$ being:

$$L_{\rm Eddington} \simeq 1.3 \times 10^{45} \left(\frac{M}{10^7 M_\odot}\right) erg/s. \tag{2.4}$$

.

2.1.1 Disc model

First, in all the following dissertations we have to remember that the mass contained in the disc is small (negligible) with respect to the compact object, thus its self-gravity can be ignored. When considering accretion onto massive objects we have to discuss a way through which the infalling matter loses its angular momentum. In fact, the presence of angular momentum prevents the matter from free falling, then there must be an effective mechanism for transporting the angular momentum outward. From a classical point of view, this problem is solved invoking viscosity forces and dissipative processes between disc annuli, originated by the differential disc rotation, that converts part of the energy of the bulk orbital motion into heat. Then this heat is radiated away and lost. On the other hand in the case of an optically thick medium, it is possible to derive directly the radiation spectrum of the accretion disc considering that the annulus of matter emits as a black body:

$$L \simeq 2\pi R^2 \sigma_{SB} T^4 \ . \tag{2.5}$$

In this equation R is the radius of the annulus, T is its temperature and σ_{SB} is the Stefan-Boltzmann constant. Then in the case in which most of the radiation is produced

in the innermost part of the system, i. e. in the limit of L$\sim L_{Eddington}$ and R$\sim$R$_g$, we obtain a temperature of

$$T \simeq 5 \times 10^5 \left(\frac{M}{10^8 M_\odot} \right)^{-1/4} K \ . \tag{2.6}$$

In agreement with this equation, the energy spectrum of the black body will move towards lower energies as its mass increases, then the more massive is the central black hole, the cooler the accretion disc will be. Further, we can translate the above equation in terms of energy using the Boltzmann constant:

$$k_B T \simeq 40 \left(\frac{M}{10^8_\odot} \right)^{-1/4} eV \ . \tag{2.7}$$

Substituting typical mass values for supermassive BH (10^6-10^{10} M$_\odot$) we find the emission peak to be into the optical-UV band. Then, the lower the system mass is, the higher the energy where the black body peaks , will be. Noticeably, this simple treatment qualitatively explains the UV bump observed in the AGN spectral energy distribution, while for smaller objects (e.g. stellar black holes) the peak is shifted into the X-ray domain.

2.1.2 Shakura-Sunyaev disc

The simplest model of accretion was developed in the fifties by Bondi (1952) and it was based on a spherical accretion approximation. However, accretion flows in astrophysics always have some angular momentum that breaks spherical symmetry, thus the correct geometry we have to consider is the cylindrical one. Then we can imagine a roughly two dimensional inflow of material that is vertically confined to its orbital plane. Moreover, it is assumed that the radial dimension of the disc largely exceeds its vertical one, thus we consider it to be geometrically thin.

To describe how such a disc behaves we have to consider the mass-energy and momentum conservation laws and require vertical hydrostatic equilibrium. The properties of a geometrically thin accretion disc are discussed in detail in the fundamental paper by Shakura & Sunyaev (1973). Then, general relativistic effects were included by Novikov & Thorne (1973).

The model by Shakura & Sunyaev (1973) requires extra assumptions: the disc has to be in steady state and matter orbiting around the black hole is in Keplerian motion. Therefore, assuming that the disc viscosity is mainly due to turbulence, we introduce v to be the kinematic viscosity described (according to the so-called α prescription) as:

$$v = \alpha c_s H \ , \tag{2.8}$$

with c_s the sound speed, α ranging between 0 and 1 and H that sets the half thickness of the disc. These additional assumptions and the above definition for the viscosity ensure that this model has a set of algebraic and linear equations for different radial ranges. Then we can define the correlation length of the turbulence as λ and the turbulence velocity as v_t with $v \sim v_t \times \lambda$. If $c_s > v_t$ the $\lambda \lesssim H$ the above equation is recovered.
Then, in the Shakura-Sunyaev framework, we can find the energy flux radiated from a disc surface unit, i.e. a ring at a radius r, per unit time:

$$F(r) = \frac{3GM\dot{m}}{8\pi r^3}\left[1 - \left(\frac{R}{r}\right)^{1/2}\right] , \tag{2.9}$$

where the accretion rate $\dot{m}$ is constant because of the mass conservation. This means that the energy radiated by the disc does not depend on the disc viscosity v, and then if we consider that vertical transport is radiative, we are left with:

$$F(r) = \frac{4\sigma_{SB}T_c^4(r)}{3\tau(r)} \tag{2.10}$$

where τ is the optical depth along the z direction and T_c(r) the disc temperature as a function of r. A particular solution for this equation can easily be derived by assuming that the disc is optically thick in the vertical direction. In different words, we set $\tau \gg 1$ and we neglect the dependence on r. Then, it can be derived that each disc element radiates as a black body characterized by its peculiar T(r):

$$F(r) = \sigma_{SB}T^4(r) , \tag{2.11}$$

that, with Eq. 2.9 leads to:

$$T(r) = \left\{\frac{3GM\dot{m}}{8\pi r^3\sigma_{SB}}\left[1 - \left(\frac{R}{r}\right)^{1/2}\right]\right\} \tag{2.12}$$

Further, considering now the "outer" part of the disc (i.e. $r \gg R$), we have:

$$T(r) \sim 3.7 \times 10^5 \left(\frac{M}{10^8 M_\odot}\right)^{-1/2}\left(\frac{\dot{m}}{1M_\odot/yr}\right)^{1/4}\left(\frac{r}{R_g}\right)^{-3/4} K. \tag{2.13}$$

Interestingly, characteristic temperature of the disc here obtained is in rough agreement with the one of Eq. 2.6 that has been derived for a generic accretion. Moreover, Eq. 2.13 does not differ much from a more accurate solution of the Shakura-Sunyaev equations, at least when large radii are considered. (Frank et al. 2002). In particular, $T(r) \propto r^{-3/4}$ is valid and can be used to find the disc spectrum. Let's assume now that each element of the disc can be considered as a small black body. Then, using the black body

assumption, the spectrum emitted by an element of the disc is given by Planck's law, thus spectral radiance is:

$$B_\nu[T(r)] = \frac{2h\nu^3}{c^2} \frac{1}{e^{\frac{h\nu}{k_B T(r)}} - 1} \ , \tag{2.14}$$

and from this equation, integrating over the disc radius, we can compute the emitted luminosity for a specific frequency:

$$L_\nu = \int_{r_{in}}^{r_{out}} B_\nu[T(r)] 2\pi r dr = \frac{4\pi h\nu^3}{c^2} \int_{r_{in}}^{r_{out}} \frac{r}{e^{\frac{h\nu}{k_B T(r)}} - 1} dr \ , \tag{2.15}$$

with r_{in} and r_{out} the inner radius and the outer one respectively. The Rayleight-Jeans regime (i.e. $h\nu \ll k_B T$) approximates the Planck function, thus $L_n u \propto \nu^2$. On the other hand, when $h\nu \gg k_B T$ holds, then Wien regime takes place and the emerging spectrum will behave as a decaying exponential function ($L_\nu \propto e^{-h\nu/k_B T}$). Finally when far from these extreme regimes, the characteristic $L_\nu \propto \nu^3$ is expected (e.g. Frank et al. 2002).

A schematic view of the spectrum is given in Fig. 2.1. In the case of active galaxies, the accretion disc cannot account for the high X-ray output we observe, but can provide soft-photons to be Comptonised by thermal electrons.

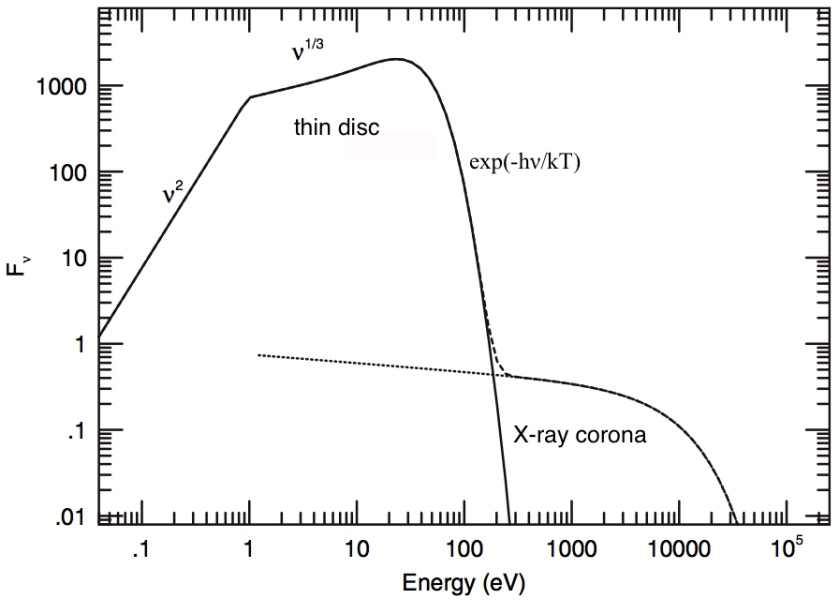

Figure 2.1. Schematic view of the spectrum emitted by a thin accretion disc (adapted from Netzer 2006). The disc spectrum peaks in the UV/soft X-ray band, while the X-ray emission is explained by a different emitting source, the so-called corona

2.1.3 Altenative disc models

The disc as treated by Shakura & Sunyaev (1973) represents a standard model for accretion disc around compact objects in astrophysical contexts. However, several different models have been proposed for explaining accretion in astrophysics. A typical Shakura & Sunyaev (1973) disc has to be geometrically thin, though many other alternative models relax this requirement. The physical meaning can be straightforwardly derived. Imagine, in fact, a highly accreting disc whose temperature and radiation pressure are high enough to thicken the disc. In this case the vertical dimension of such an "inflated" disc is not negligible if compared with its radial one. In such cases, we have to consider the vertical structure of the accretion disc.

We start by computing the hydrostatic equilibrium equation of a matter element belonging to the disc. Focusing on the z-axis (orthogonal to the disc plane), for a matter element that moves at an angle θ out of the disc plane holds:

$$\frac{dP}{dz} = -\rho \frac{GM \sin\theta}{R^2} \ . \tag{2.16}$$

In this equation, P represents the sum of the radiation and the gas pressure while ρ is used to describe the local density as $\rho = \rho(R, z)$. In the case in which P dominates, we have P=ρc_s^2 with c_s the isothermal sound speed. Then if the disc is thin we have $\sin\theta \sim z/R$ so we can rewrite the above equation as:

$$\frac{d\rho}{dz} = -\rho z \frac{GM}{c_s^2 R^3} \ , \tag{2.17}$$

and the corresponding solution is:

$$\rho(R, z) = \rho(R,0) e^{-\frac{z^2}{H^2}} \ . \tag{2.18}$$

In the above formula $H = c_s\sqrt{R^3/GM} = c_s/\Omega_K$ and Ω_K is the Keplerian angular velocity. If we now consider the thin disc, we then have that $R >> H$ so that $c_s << v_K$ meaning that the local Keplerian velocity has to largely exceed the sound speed. However, c_s increases as a function of the temperature that depends on the accretion rate. Therefore, when we are dealing with highly accreting sources, the thin disc regime cannot be reached. Besides the standard Shakura-Sunyaev disc, other models have been proposed. Slim and thick disc (e.g. Abramowicz et al. 1988; Paczynski 1980; Paczyński & Wiita 1980) are invoked for states of high accretion rates. These discs radiate inefficiently since the time needed by the photon to reach the disc surface and escape from it is much larger with respect to the typical accretion time. This means that photons are trapped in the accretion flow and fall into the black hole. On the other hand, the radiatively-inefficient accretion flows (RIAF; e.g. Narayan & Yi 1994) model is adopted with very low accreting sources. This model is based on the following concept: in a very low accretion

state, the disc can be very diluted and the Coulombian interactions are not sufficient to maintain thermal coupling between ions (mostly protons) and electrons anymore. In other words, the particles in the disc will undergo a temperature segregation. Then, the more massive protons will carry most of the gravitational energy, while the radiative energy losses will be due to electrons. Moreover, as just stated, in very diluted discs, particles are decoupled. Then, via advection, protons go toward the central black hole. This means that most of the gravitational power is dissipated by the advection of protons rather than radiated away from the colder electrons. According to this reasoning, RIAF are extremely hot discs, but radiatively inefficient. All the above cited disc models beyond the Shakura-Sunyaev are called advection dominated accretion flows. ADAF thick or slim discs are optically thick and cold and are adopted for modelling high-luminosity, high-accretion rate objects (e.g. Mineshige et al. 2000), while ADAF/RIAF are hot and optically thin and can be used to describe low-luminosity sources with low accretion rate (Yuan & Narayan 2014). Furthermore, RIAFs are invoked to interpret the emission from low-luminosity AGN and this mechanism could explain the different spectral variability with respect to standard AGN.

2.2 Comptonisation

In 1923 Arthur Holly Compton discovered the Compton effect. This process is an inelastic scattering between a photon and a charged particle (always an electron for our purposes), and, thanks to the discovery of this process, A.H. Compton won the Nobel Prize in 1927.

The Compton scattering (see Fig 2.2) extends at relativistic regime (i.e. when the incoming photon energy ϵ is compatible with the electron rest energy E) the classical Thomson scattering. In the Thomson limit, before and after the interaction with the target particle, the energy of the test photon is the same (Eq. 2.19) and the angular distribution of the scattered photons depends on the $cos^2\theta$ (Eq. 2.20), when θ accounts for the angle between the direction of the incident photon and the direction of the scattered one. Noticeably, in both Eq. 2.20 and 2.21, the (differential) cross-section of the Thomson scattering does not depend on the energy of the incoming photon. Finally, r_0 is the classical electron radius defined as $r_0 = e^2/m_e c^2$ corresponding to $2.8{\times}10^{-13}$ cm.

$$\epsilon_i = \epsilon_f \tag{2.19}$$

$$\frac{d\sigma_{Th}}{d\Omega} = \frac{1}{2}\, r_0^2(1 + cos^2\theta) \tag{2.20}$$

$$\sigma_{Th} = \frac{8\pi}{3}\, r_0^2\ . \tag{2.21}$$

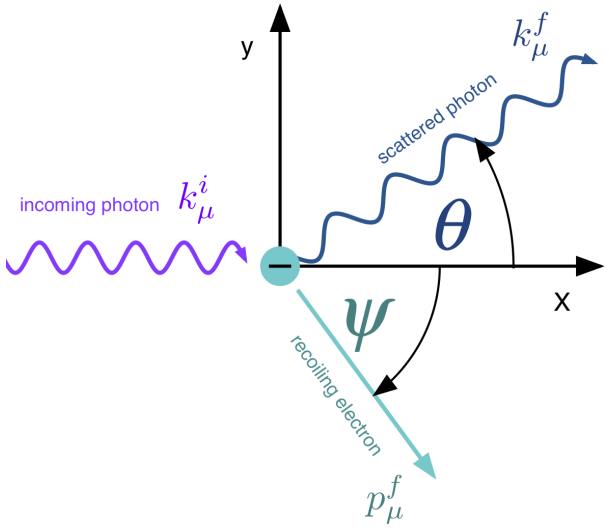

Figure 2.2. A graphic representation of Compton scattering. In particular, a photon with initial 4- momentum k^i_μ collides with a static electron. After the collision, the photon will have a 4-momentum k^f_μ and the electron will recoil with a 4-momentum p^f_μ-

On the other hand, in the relativistic regime (i.e. $\epsilon \sim$E) Comptonisation takes place, and, the scattering is no longer elastic. As in the Thompson case, the number of photons is conserved, but, in this case, the incident spectrum can be dramatically affected by the Compton scattering.

Invoking the energy-momentum conservation it is possible to compute the energy of the photon after the scattering by the electron:

$$\epsilon_f = \frac{\epsilon_i}{1 + \frac{\epsilon_i}{m_e c^2}(1 - cos\theta)} \ . \tag{2.22}$$

This equation can be straightforwardly written in terms of wavelengths:

$$\lambda_f - \lambda_i = \lambda_C(1 - cos\theta) \ . \tag{2.23}$$

In this last formula a characteristic wavelength appears, the so-called Compton wavelength (λ_C) that corresponds to $\frac{h}{m_e c^2} \simeq$0.024 Å. This typical wavelength can be used to define a regime in which the energy loss of the photon due to the electron recoil is negligible, i.e. when $\lambda_{ph} \gg \lambda_C$.
A further effect in the Compton regime is the change of the differential cross-section as was given by the Klein-Nishima formula (1928):

$$\frac{\sigma_{K.N.}}{d\Omega} = \frac{r_0^2 \ \epsilon_f^2}{2 \ \epsilon_i^2} \left(\frac{\epsilon_i}{\epsilon_f} + \frac{\epsilon_f}{\epsilon_i} sin^2\theta \right) \ , \tag{2.24}$$

which, in the case of elastic recoil, reduces to the Thomson one. Contrary to the classical Thomson cross-section, the Klein-Nishina formula depends on the energy of the incoming photon, and decreases as ϵ_i increases as shown by Fig. 2.3. Defining $x \equiv h\nu/mc^2$, the cross-section $\sigma_{K.N.}$ becomes:

$$\sigma_{K.N.} = \sigma_{Th.}\frac{3}{4}\left\{\frac{1+x}{x^3}\left[\frac{2x(1+x)}{1+2x} - ln(1+2x)\right] + \frac{1}{2x}ln(1+2x) - \frac{1+3x}{(1+2x)^2}\right\} . \quad (2.25)$$

Then it is possible to define two regimes for which Eq. 2.25 is accordingly modified: for $x << \frac{h\nu}{mc^2}$ we are left with:

$$\sigma_{K.N.} \sim \sigma_{Th.}\left(1 - 2x + \frac{26x^2}{5} + ...\right) , \quad (2.26)$$

while, in the opposite case of an extremely relativistic regime $x >> \frac{h\nu}{mc^2}$ we obtain:

$$\sigma_{K.N.} = \frac{3}{8}\sigma_{Th.}x^{-1}\left(ln(2x) + \frac{1}{2}\right) . \quad (2.27)$$

All these computations are valid in the framework of a static electron that, after inter-

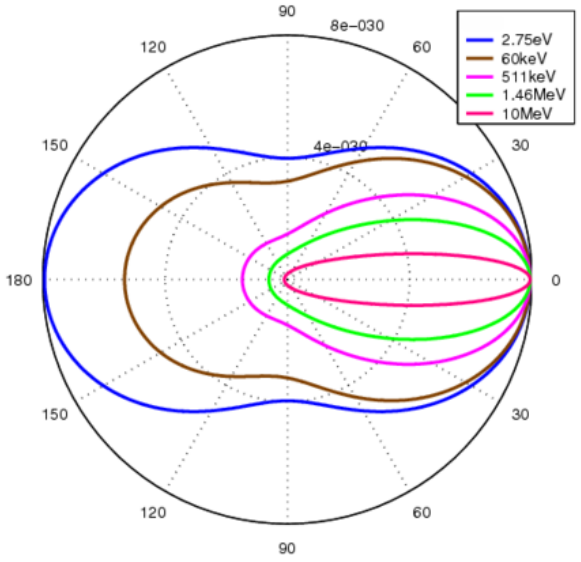

Figure 2.3. The Klein-Nishima cross-section as a function of the incoming photon energy. As the energy of the photons increases, the probability of a backscatter decreases.

action with the scattering photon, always gains energy.

On the other hand, if we allow for moving particles, Comptonisation can have different outcomes, and, in particular, the electron can transfer its energy to the photon. Under these circumstances we are formally talking about an Inverse-Compton process. So if the electron is moving in the observer's reference frame, the photon up-scattering on it can gain energy instead of transferring its own momentum to the electron. Assume now that we are in the electron rest-frame. In this frame, the relativistic corrections accounted in for the Klein-Nishima equation are negligible, and if the electron kinetic energy E is larger with respect to the incoming photon energy ϵ, the electron loses its energy that is transferred to the photon. Imagine calling our laboratory/observer frame K and that K$'$ is the reference frame of the electron. To calculate the energy of the interactions we have to perform a Lorentz transformation twice: first we have to go from our lab frame into the electron one and then back to our rest frame. If in K the relativistic electron has kinetic energy β and the incoming photon with energy (ϵ_i) has a direction which forms an angle θ_i with β, then in the primed reference frame we are left with:

$$\epsilon_i' = \epsilon_i \gamma (1 - \beta cos\theta) \ . \tag{2.28}$$

The amount of energy gained by the photon in the electron reference frame K$'$ is given by Eq. 2.28, then in the case in which ϵ_i in K$'$ is negligible if compared with the electron rest-energy, we can rewrite the equation as follows:

$$\epsilon_f' \simeq \epsilon_i' \left[1 - \frac{\epsilon_i'}{m_e c^2} (1 - cos\theta) \right] \simeq \ \epsilon_i'. \tag{2.29}$$

and performing a Lorentz transformation back to our original reference frame we obtain:

$$\epsilon_f = \epsilon_f' \gamma (1 - \beta cos\theta') \ . \tag{2.30}$$

This means that the photon in the process of being scattered is boosted by a factor γ^2. In fact, the approximate ratios of the energies of the photon before scattering in K, in K$'$ and then after the scattering in the observer reference frame K are:

$$1 : \gamma : \gamma^2 \ .$$

All of this holds in the case in which the incoming electron energy in the rest frame of the electron (i.e. $\gamma\epsilon_i$) is lower with respect to the rest-energy of the electron itself ($m_e c^2$ =511 keV). In fact, as already stated, when the photon energy is compatible with $m_e c^2$, then the relativistic effects become relevant, and in agreement with Eq. 2.24 the cross-section of the Compton interaction decreases. This means that, for instance, a 50 keV energy photon can be boosted up to very high energies, even though the energy conservation principle limits this energy gain to $\gamma m_e c^2$.

An extensive discussion about the high energy emission process is provided in Rybicki & Lightman (1979), and, in the following, we discuss Comptonisation further in more physical frameworks. We start extending the above reasoning for the case of an isotropic incoming photon field. Then we have to consider an initial photon density (U_{ph}) for the isotropic distribution of photons. Then, it can be demonstrated that the total emitted power averaged over the angles is:

$$P_{I.C.} = \frac{4}{3} c\sigma_{Th.}\gamma^2\beta^2 U_{ph} \ . \tag{2.31}$$

Noticeably, this is the same expression as the synchrotron power, except for the presence of U_{ph} instead of the magnetic energy density U_B . Then, also the synchrotron process can be understood as if a given energy flux cU_B were scattered by the electron (but in accordance with the Thompson cross-section). Therefore we find:

$$\frac{P_{I.C.}}{P_{Sync.}} = \frac{U_{ph}}{U_B} \tag{2.32}$$

meaning that losses by the Inverse Compton and Synchrotron are in the same ratio as the photon energy density and magnetic energy density.

The power emitted by a distribution of electrons can be computed integrating Eq. 2.31 over their energy distribution. Considering then the power emitted by a thermal distribution of non-relativistic electrons ($\gamma \sim 1$, $\beta \sim 3k_BT/m_ec^2$) characterized by a number density $n = dN_e/dV$ is:

$$\frac{dP_{tot}}{dV} = \frac{4k_BT}{m_ec^2} c\sigma_{Th.} U_{ph} \frac{dN_e}{dV}. \tag{2.33}$$

Therefore, the power dP_{tot} is the result of the scattering of the incident power $c\sigma_{Th.}U_{ph}$ off the dN_e electrons. For each single scattering event $4k_BT/m_ec^2$ is the fractional energy gained by the photons. However, when computing the real amount of energy gained by the electron we have to consider the losses due to the recoil, thus:

$$\frac{\Delta E}{E} = \frac{4k_BT - E}{m_ec^2} \ . \tag{2.34}$$

This equation demonstrates that the photons may gain energy only if the electrons are hot enough to satisfy $4k_BT > E$. If Inverse Compton takes place, then we estimate the cooling time associated with this process as the ratio between the energy density of the photons U_{ph} and the emitted power P_{tot}:

$$t_C = \frac{3m_ec}{8\sigma_{Th.}U_{ph}} \sim \frac{1.6 \times 10^7 s \ erg \ cm^{-3}}{U_{ph}}. \tag{2.35}$$

To compute the Inverse-Compton power spectrum we have to proceed as for estimating the photon energy after a Compton process. This means that we can start with a

monochromatic distribution of photons and subsequently perform transformations, from the observer frame to the one of the electron distribution, and then, after the scattering, back to the observer reference frame. For instance, the spectrum of a photon ensemble scattering off a distribution of electrons with a certain temperature dispersion can be computed integrating over the corresponding particle distributions. Noticeably, Comptonisation has a further similarity with synchrotron emission. In fact, if we consider a beam of photons with a defined energy that Compton scatters on a power law-like distribution of non thermal and relativistic photons with index p, then the resulting spectrum will be a power law with index $\alpha = p-1/2$, exactly the same as expected for synchrotron (Rybicki & Lightman 1979). Up to now, in our reasoning we have considered only 1-shot photon-electron interactions, i.e. single scattering processes. However, a scenario in which multiple scatters are allowed is more consistent with a physical case. To deal with multiple scatterings it is convenient to introduce the so called Compton parameter y. This parameter measures the average energy gain of an ensemble of photons scattering on a plasma and allowing for multiple interactions. Following Rybicki & Lightman (1979), y can be defined as follows:

$$y = \frac{\Delta E}{E} \times max(\tau^2, \tau) \ , \tag{2.36}$$

with $max(\tau^2, \tau) \ \equiv (\tau^2 + \tau)$. In accordance with this equation, the Compton parameter is defined as the average fractional energy change per scattering $\Delta E/\mathrm{E}$, multiplied by the mean number of scatterings. Since multiple scatters are considered we have to take into account the opacity of the plasma. This is considered in y, in fact if the plasma has optical depth τ then the number of scatters will be of order $(\tau^2 + \tau)$. In the case of a very opaque medium the number of the scatters becomes proportional to $\sim \tau^2$. We can then define two different regimes for Eq. 2.36. If the plasma is made of thermal non-relativistic electrons, then the energy gain of the photons $\Delta E/E$ is provided by Eq. 2.34. In the case of E«4 k_BT i.e. when Inverse Compton occurs, the energy gain $\Delta E/E \sim 4k_B\mathrm{T}/\mathrm{m}_e\mathrm{c}^2$ and y is defined as:

$$y_{nr}^{th} = \frac{4k_BT}{m_ec^2} \times max(\tau^2, \tau) \ . \tag{2.37}$$

Then, adopting y, the final energy of the emerging photons will be on average:

$$\epsilon_f = \epsilon_i e^y. \tag{2.38}$$

This last equation further demonstrates that once ϵ_f=4k_BT, the process saturates and photons cannot be Comptonised.
Let us now consider if electrons are in a relativistic regime i.e. γ»1. Then we can recover $\Delta E/E$=$(4/3)\gamma^2$.

Being on average $<\gamma^2>=<(\mathrm{E}/\mathrm{m}_e c^2)^2>\sim 12(\mathrm{k}_B\mathrm{T}/\mathrm{m}_e\mathrm{c}^2)^2$ we obtain:

$$y_{re}^{th} = \left(\frac{4k_BT}{m_ec^2}\right)^2 \times max(\tau^2, \tau) \ . \tag{2.39}$$

We can further specialise our reasoning on Comptonisation considering the scattering of low optical depth material and an opaque medium.
High τ: we have to compute the kinetic equation describing the evolution of a photon density $\mathrm{n}(\omega)$ in the scattering phase space, i.e. we have to find the solution of the Boltzmann equation for Comptonisation. If we assume an isotropic and homogeneous radiation field, then we can write the kinetic equation as:

$$\frac{1}{c}\frac{\partial n}{\partial t} = n_e\sigma_{Th.}(+e - n) \ . \tag{2.40}$$

The terms n and e account for the extinction and the scattered emission ($\mathrm{e}=\mathrm{e}(\omega,\mathrm{t})$) respectively. It was Kompaneets who, in 1957, defined the scattering term considering non-relativistic electrons ($\mathrm{k}_B\mathrm{T}\ll\mathrm{m}_e\mathrm{c}^2$) and that the photon energy satisfies $\mathrm{h}\nu\ll\mathrm{m}_e\mathrm{c}^2$. In the case of emitting sources in an astrophysical context we have to consider two further contributions to the equation, a source and diffusion term, both inversely proportional to the mean number of scatterings. Then we are left with the modified Kompaneets' equation (Liedahl 1999):

$$\frac{\partial n}{\partial t_c} = \frac{k_BT}{m_ec^2}\frac{1}{x^2}\frac{\partial}{\partial x}\left[x^4\left(\frac{\partial n}{\partial x} + n + n^2\right)\right] + Q(x) - \frac{n}{max(\tau^2, \tau)} \ . \tag{2.41}$$

The term $t_c=\mathrm{t}(\mathrm{n}_2,\sigma_{Th.},c)$ here accounts for time measured in units of the mean time between the various scatterings, while we used $\mathrm{Q}(\mathrm{x})$ to describe incoming photons number density produced per unit Compton time. An analytical solution of the modified Kompaneets' equation can be found considering the source term emitting only low energy photons ($\mathrm{Q}(\mathrm{x})=0$) and considering $\mathrm{n}\ll 1$. Further performing the temporal derivative, we are left with the steady state solution:

$$\frac{y}{4}\frac{\partial}{\partial x}\left[x^4\left(\frac{\partial n}{\partial x} + n\right)\right] - nx^2 = 0 \ , \tag{2.42}$$

where y is y_{nr}^{th} of Eq. 2.37. The Wien law can be an approximated solution of this equation for $x >> 1$, $n(x) \propto e^{-x}$ and the corresponding intensity has a high energy cut-off above $\mathrm{k}_B\mathrm{T}$ being $I_\nu \propto \nu^3 e^{-x}$. On the other hand, when $x << 1$, n becomes negligible and we get a power-law like solution $n \propto x^m$ with:

$$m = -\frac{2}{3} \pm \sqrt{\frac{4}{y} + \frac{9}{4}} \ . \tag{2.43}$$

The emerging spectrum also has power law behaviour: $I_\nu \propto \nu^{3+m}$ and, in other words, $I_\nu \propto \nu^{-\alpha}$ where:

$$\alpha = -\frac{3}{2} \mp \sqrt{\frac{4}{y} + \frac{9}{4}} \, . \tag{2.44}$$

For $y < 1$ the positive root is considered and the resulting power spectrum has $\alpha > 1$ up to the high energy cut-off. On the other hand, the negative root is appropriate when y largely exceeds 1 ($y >> 1$). This is the circumstance of a saturated Comptonisation, and accordingly with $m = 0$ and $\alpha = -3$, where we have the low-energy tail of the Wien spectrum.

Low τ: We consider the amount of energy gained after each scatter to be $A'=\Delta E/E$. Then if $\tau < 1$ we have $y=A\tau$, so that after the first scattering, a fraction τ of the photons undergoes an energy increase by a factor A. If we then consider k subsequent scatters, we find that the energy of the τ^k Comptonised photons increases by a factor A^k. However, this holds until the average photon energy is compatible with the electron temperature and further scatterings cannot increase the photon energy. The emerging power spectrum can be seen as the sum of the various scattering orders (see Fig 2.4), and it has a power law shape: $F_\nu \propto \nu^{-\alpha}$ with:

$$\alpha = -\frac{\ln \tau}{\ln A} = -\frac{\ln \tau}{\ln y - \ln \tau}. \tag{2.45}$$

In case of $A >> 1$ and $\tau << 1$ Comptonisation is extremely efficient and in a few scatterings photons undergo a high energy gain. Moreover, the spectrum has a bumpy shape rather than power law-like.

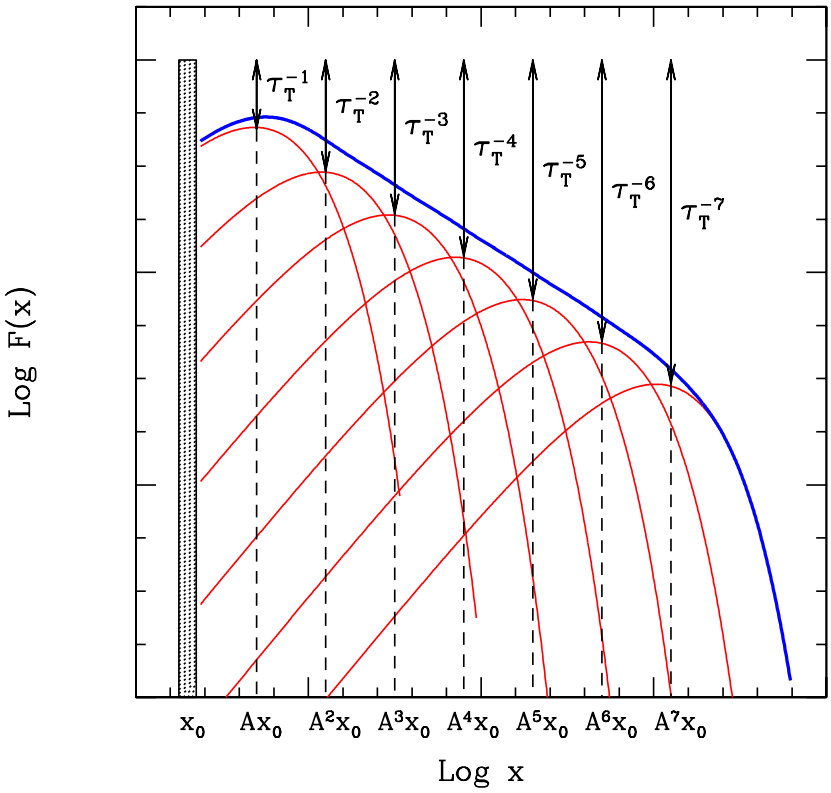

Figure 2.4. Comptonisation spectrum for small optical depth (as a function of $x \equiv h\nu/mc^2$). From the superposition of all the scattering orders a power law stems out (adapted from Ghisellini 2013).

Chapter 3

The X-ray view: Spectral components

Active galaxies are strong X-ray emitters, and this energetic emission is a defining characteristic shared by all AGN classes. Typically, for an unobscured AGN, X-ray radiation extends well above 100 keV, while a strong drop in the soft X-rays is observed in obscured sources. The X-ray domain can be set in different energy bins:

- soft X-rays ($0.1 < E < 2$ keV)
- hard X-rays (E>2 keV)

X-ray photons emitted by AGN cover about three magnitudes in energy, being measured from the low energy cut-off due to Galactic absorption ($\sim$ 0.1 keV) up to several hundreds of keV. As a first order approximation, X-ray emission in AGN can be described by a simple phenomenological model such as a power law:

$$F_\nu \propto \nu^{-\alpha} \ , \tag{3.1}$$

where $\alpha \sim 1$. However, in X-ray astronomy the photon index Γ is commonly used rather than α, then the photon flux per unit of energy can be defined as follows:

$$F_E \propto E^{-\Gamma} \ , \tag{3.2}$$

where $\Gamma = 1 + \alpha$.

In more detail, additional complexities characterize the X-ray emission of AGN. These second order components are the results of interactions between the primary emission and circumnuclear matter. A strong iron Kα fluorescence line and a photon excess at energies as high as $\sim$ 30 keV are commonly observed in AGN. These features exceeding the underlying continuum are both interpreted as effects of the reprocessing of the primary radiation in matter close to the black hole. Further, a smooth rise above the extrapolated high energy power law below 1-2 keV is commonly observed and the origin of the component is still under debate. Finally, absorbing material intercepting the observer's line of sight can further explain count drops with respect to the power law primary emission.

3.1 Primary continuum

As just stated, the underlying continuum of AGN can be modelled by a simple power law. From an observational point of view, AGN spectra of nearby Seyfert galaxies and Quasars display a photon index ranging between 1.5 and 2.2; while flatter values correspond to radio loud objects.
Moreover, various high energy cut-offs for the continuum emission have been measured in the past (e.g. Nicastro et al. 2000; Perola et al. 2002; De Rosa et al. 2002; Molina et al. 2009, 2013; Malizia et al. 2014), and, nowadays by *NuSTAR* (e.g. Fabian et al. 2015, 2017; Tortosa et al. 2018).

Comptonisation of photons scattering off a distribution of thermal electrons can explain the observed power law spectrum with a high-energy cut-off. The Inverse Compton mechanism is thought to occur in a very compact region called the corona. Comptonisation has to be favoured with respect to other mechanisms such as Bremsstrahlung is because of its higher efficiency for high luminosities and compact objects. This is also shown in (Fabian et al. 2015) who compared the cooling time of the two processes.

On the other hand, for radio sources, especially when radio lobes are observed, Synchrotron emission has to be considered. In fact, the AGN flatter spectral shape can be produced by a synchrotron self-Compton emission, in which radio-synchrotron photons Compton scatter off the jet's electrons (e.g. Ghisellini et al. 1985; Reeves & Turner 2000). X-ray spectroscopy can therefore give information on the physics of the Comptonising medium since the interplay between the coronal temperature (kT_e) and its optical depth (τ_e) is found to drive the AGN power-law spectral shape, while the high-energy turnover is mainly a function of the coronal temperature (Rybicki & Lightman 1979).

Our knowledge of the coronal region is still lacking and much effort was made to understand better this medium. A key point in understanding the hot electron corona is its geometry. Different models accounting for alternative geometries have been proposed: the corona could be a slab sandwiching the accretion disc, or a sphere, or consist of blobs of matter (patchy corona). However, in accordance with observations, it is widely accepted that the corona has to be a compact optically thin and geometrically thick medium. Finally, since the coronal electrons heat the soft photons up to the X-rays, there must be a process that counterbalances the cooling of the corona. Dissipation of magnetic flux through reconnection has been proposed as the mechanism that maintains the coronal electron at a high enough temperature to allow for Comptonisation.

As already stated, it is widely accepted that the origin of X-rays is a compact region overlying the central black hole in which seed optical photons undergo Comptonisation. This emitting component is required to explain the observational properties commonly shared by AGN. Let us now focus on this component for which, in Fig.3.1 some possible representations are shown.

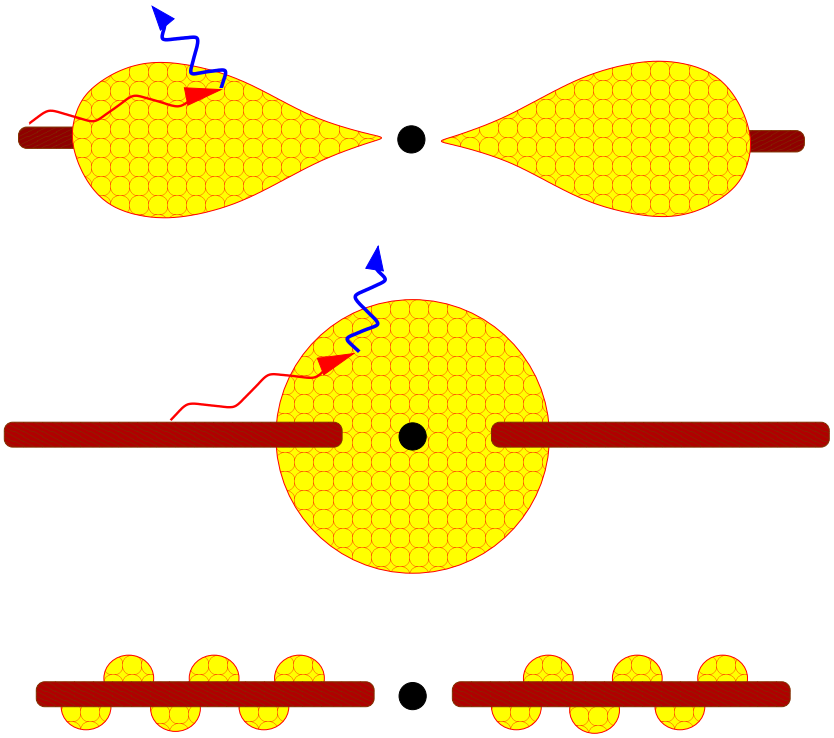

Figure 3.1. Various geometries have been proposed for the hot corona. In this sketch, Reynolds & Nowak (2003) reports some of them.

3.1.1 Thermal Comptonisation

In their seminal paper, Sunyaev & Titarchuk (1980) solved the steady-state Kompaneets' equation for a plasma illuminated by a source of colder photons. In their computations the authors assumed different geometrical configurations for the Comptonising plasma. Then five years later, in Sunyaev & Titarchuk (1985) they further extend their computations to include the angular dependence and the polarization of the emerging spectrum and finally relativistic effects are considered in Titarchuk (1994). The solution of the equation relates the incoming photons, the process of thermal Comptonisation and the amount of photons escaping from the plasma cloud. The treatment of the diffusion in the plasma leads to the distribution of the photons over the escape time (P(t)). $I_0(\nu,t=0)$ is the input spectrum and the outcoming Comptonised spectrum $I(\nu,t)$ is obtained solving Kompaneets' equation. Then we compute the stationary spectrum of the escaping radiation:

$$F(\nu) = \int_0^\infty I(\nu,t)P(t)dt \ , \tag{3.3}$$

with P(t) depending on the geometry and the matter opacity τ, and the temperature effects on the Comptonisation process. This means that the Comptonised spectrum depends on the plasma optical depth and temperature. In principle this means that an ad libitum high number of combinations between the coronal temperature and optical depth can provide an equally high number of spectral indices. However, from observations, we know that both Quasars and Seyfert galaxies display a limited range of photon indices ($1.5<\Gamma<2.2$), and this could suggest that the X-ray AGN spectrum is determined by some universal mechanism, for instance an interplay between the accretion disc and the corona (Haardt & Maraschi 1991a).

3.1.2 The two-phase model

This model, first proposed by Haardt & Maraschi (1991a, 1993), is a fundamental tool for understanding the AGN X-ray emission. Essentially, if we neglect the obscuring torus and the line regions, AGN are left with the hot corona (optically thin geometrically thick), and a geometrically thin and optically thick accretion disc emitting in the optical-UV band.

The two-phase model couples these two phases: the cold phase (i.e. the disc) provides the low temperature photons for Comptonisation in the hot phase (i.e. the corona), and part of the hard, Comptonised emission from the corona contributes to the heating of the cold phase. The basic model accounts for a plane parallel geometry where the two phases are homogeneous and isothermal layers, while further updates have been proposed for the case of a non-uniform and patchy corona (e.g. Haardt et al. 1994). Let us now focus on this model from a quantitative point of view. We define P_G as the total

gravitational power and f its fraction that is dissipated in order to heat the corona. The "heating" power is then re-emitted as the result of Comptonisation, thus we can define a Compton luminosity $L_h eating = f P_G$, while what remains of the gravitational power (1-f) is dissipated in the accretion disc. Then introducing the amplification factor A due to Comptonisation, we can derive the total luminosity provided by the corona as $L_s \times A$, with L_s the seed luminosity. Concerning the amplification factor A, it can be evaluated by energetics of the disc/corona system and geometrical considerations (see Petrucci et al. 2013a). Comptonisation conserves the number of photons, thus there must be a relationship between the luminosity of the seed photons entering and cooling a corona and the observed Comptonised luminosity. Then, by conservation, the number of observed photons n_{obs} has to be the same as the sum of $n_{s,0}$ and $n_{C,up}$ where these quantities account for the number of seed photons crossing the corona without being scattered and the number of photons which are Comptonised and up-scattered, respectively. Then, if the total number of soft photons is n_s and the opacity of the corona is τ we can formulate:

$$n_{s,0} = n_s e^{-\tau} \tag{3.4}$$

$$n_{C,up} = \frac{1}{2} n_s (1 - e^{-\tau}) \ . \tag{3.5}$$

The factor 1/2 is used for isotropic media where half of the power is emitted upward , while the remaining half downward. Continuing our reasoning we have:

$$n_{obs} = n_{s,0} + n_{C,up} = \frac{1}{2} n_s (1 - e^{-\tau}) \ , \tag{3.6}$$

so we compute n_s as:

$$n_s = \frac{2 n_{obs}}{1 + e^{-\tau}} \ . \tag{3.7}$$

At this point we can consider different cases in accordance with the values of τ: if $\tau \ll 1$ then $n_s \sim n_{obs}$ and only a small percentage of photons are Comptonised; if $\tau \gg 1$ then $n_s \sim 2 n_{obs}$. Consider now the total power emitted by the corona L_{tot} as the sum of the seed luminosity L_s and the heating power L_h, i.e.:

$$L_{tot} = L_s + L_h \ . \tag{3.8}$$

The two components constituting the total coronal luminosity can be viewed as the sum of the upward and downward luminosities. The sum of the Comptonised and up-scattered (down-scattered) photons and the seed photons going upward (downward) without being scattered is $L_{s,up}$ ($L_{s,do}$), therefore:

$$L_h = L_{h,up} + L_{h,do} = 2 L_{h,up} \tag{3.9}$$

$$L_a = L_{s,up} + L_{s,do} = \left[L_s e^{-\tau} + \frac{1}{2} L_s (1 - e^{-\tau}) \right] + \frac{1}{2} L_s (1 - e^{-\tau}) \ . \tag{3.10}$$

The first equation comes from the assumption of isotropy of the Comptonisation mechanism. Now, the observed luminosity is obtained summing up the upward (downward) luminosities e.g.:

$$L_{obs} = L_{s,u} + L_{h,u} \ . \tag{3.11}$$

Adopting the above formulae we can rewrite the luminosity L_h in accordance with:

$$L_h = 2L_{obs} - L_s(1 - e^{-\tau}) \ , \tag{3.12}$$

that using Eq. 3.6 becomes:

$$L_{tot} = 2L_{obs} - L_s e^{-\tau} \ . \tag{3.13}$$

Again we can have two regimes: for $\tau \ll 1$, $L_{tot} \simeq 2L_{obs}$-L_s, while when $\tau \gg 1$ then $L_{tot} \simeq 2L_{obs}$. At this point, we are ready to write down the amplification factor as:

$$A = \frac{L_{tot}}{L_s} = \frac{L_h + L_s}{L_s} \ . \tag{3.14}$$

The radiative equilibrium of the seed source (i.e. the disc) allows us to derive a further expression for L_s. To do this, let us introduce the intrinsic disc emission $L_{s,intr}$:

$$L_s = L_{s,intr} + L_{s,do} + L_{h,do} = L_{s,intr} + \frac{1}{2}L_s(1 - e^{-\tau}) + \frac{1}{2}L_h \ . \tag{3.15}$$

Dividing this last equation by L_s we get:

$$1 = \frac{L_{s,intr}}{L_s} + \frac{1}{2} - \frac{e^{-\tau}}{2} + \frac{L_h}{2Ls} \ , \tag{3.16}$$

that can be re-written as:

$$\frac{L_h}{L_s} = 1 + e^{-\tau} - 2\frac{L_{s,intr}}{L_s}. \tag{3.17}$$

Finally we can derive a further expression of the amplification factor:

$$A = 1 + \frac{L_h}{L_s} = 2 + e^{-\tau} - 2\frac{L_{s,intr}}{L_s}. \tag{3.18}$$

In the case of a passive disc (i.e. $L_{s,intr}$=0) all the gravitational power is dissipated in the Comptonising medium, thus f=1. In other words, there is not any radiation from the disc that, instead, reprocesses and re-emits the Comptonised photons emerging from the corona. Typically, an optically thin corona above a passive disc is characterized by A=3, while A=2 for an optically thick corona.

We can go further in our reasoning by introducing η as the fraction of the Comptonised power emitted by the corona. This parameter can be seen as an estimator of the anisotropy of the Compton scatter (η=1/2 means a fully isotropic scenario). Let us

consider a further parameter, a accounting for disc albedo. Then the radiative balance between the disc and the optically thin corona leads to the following equation for A (Haardt & Maraschi 1991b):

$$A = 1 + \frac{f}{1 - f[1 - (1 - a)\eta]} \ , \tag{3.19}$$

where $(1-a)$ accounts for the fraction of Comptonised radiation that is absorbed by the disc. In the limiting case of a=0 and f=1, and assuming an isotropic emission, we find A=3.

From observations we know that AGN has typical power-law like spectral shapes:

$$I(E) = I(E_0) \left(\frac{E}{E_0} \right)^{-\alpha} . \tag{3.20}$$

If we assume that the seed luminosity is black body-like (with the corresponding peak at $\sim 3k_B$T), we can derive an approximated expression for L_s=I(E_0)E_0, while the heating Comptonised luminosity is:

$$L_h = \int_{E_{min}}^{E_{max}} I(E) dE \ . \tag{3.21}$$

The integral is performed from E_{min} ~E_1 that is the energy of the photons after just one scatter to $E_{max} \sim 3k_B$T with T is the coronal temperature. Then, assuming that A_1 is the average gain in a single scattering process (E_1=E_0A_1), we find an equation describing the heating/cooling ratio depending now on the spectral shape (Haardt & Maraschi 1991b):

$$A - 1 \simeq \frac{1}{1 - \alpha} \left[\frac{3k_B T}{E_0} - (A_1)^{1-\alpha} \right] \ . \tag{3.22}$$

As already seen, the spectral index α is a function of both the corona opacity and temperature, and, in particular, $\alpha = -ln\tau / lnA_1$ for τ<1.
An iterative solution of Eq. 3.20 was found by Haardt & Maraschi (1991b). According to this solution, for f=1, α always varies between 1.1 and 1.4 (corresponding to Γ between 2.1 and 2.4) for a large range of coronal temperatures and optical depths. This means that the heating/cooling ratio is kept constant by adjusting the values of the corona opacity and temperature and this leads to a constant amplification factor A that only depends on the assumed geometry. An important work which confirmed this behaviour via simulations is provided by Beloborodov (1999). The author used the Comptonisation code by Coppi (1992) and found empirical relationships between the photon index Γ and the Compton parameter and the amplification factor:

$$\Gamma \sim \frac{9}{4} y^{-2/9} \tag{3.23}$$

$$\Gamma \sim \frac{7}{3} A^{-0.1} \ . \tag{3.24}$$

These relationships yield similar results to the theoretical prescriptions by Eq. 2.44 . The two-phase model was further developed for different geometries of the corona. In particular, a patchy corona was considered according to the formation of magnetic loops storing the energy that, at that point, is not dissipated via reconnection. In this model, the blob-like hot component provides only a fraction of the accretion power, and the disc is no longer passive and can supply most of the optical-UV luminosity. In this new scenario the patchy corona does not illuminate uniformly the disc that reprocesses the radiation only locally, in hot-spots.

According to this model, and particularly when the X-ray and UV luminosities are similar (e.g. Haardt et al. 1994, 1997), a correlation between the hard X-ray Comptonised emission and the seed reprocessed photons is expected. Therefore, variability in this band can be explained thanks to the stochastic variations in the hot spots number or via different accretion rate states.

3.1.3 Pairs production

For compact and luminous objects such as AGN, the electron-positron pair production due to photon-photon interaction may be significant. AGN cores are the perfect laboratories for this process, since they are compact, so interactions involving significant energy exchanges between photons and particles are common in the source. The role of pair production in AGN coronae can be studied via the so-called compactness parameter (e.g. Guilbert et al. 1983):

$$l = \frac{L}{R} \frac{\sigma_{Th.}}{m_e c^2} \ , \tag{3.25}$$

where R is the radius of the source assumed to be spherical, and L represents the source luminosity. In accordance with this and introducing n_γ as the photon density and $\sigma_{\gamma\gamma}$ to be the photon-photon cross-section, we estimate the optical depth for pair production to be $\tau_{\gamma\gamma} \sim n_\gamma \sigma_{\gamma\gamma} R$. Then we can rewrite $n_\gamma \sim U_{rad}/E_\gamma \sim L/(4\pi R^2 c \ m_e c^2)$. The photon-photon cross-section $\sigma_{\gamma\gamma}$ is a function of the energy of the incoming photon and has a maximum $\sigma_{\gamma\gamma}^{max} \sim 0.2\sigma_{Th.}$ (e.g. Ghisellini 2013). After a few computations we are left with:

$$t_{\gamma\gamma} \sim \frac{l}{20\pi} \ . \tag{3.26}$$

Therefore, according to the compactness parameter we can have a regime $l \leq 60$ in which pair production can be negligible, and a second case where $t_{\gamma\gamma}$ exceeds unity ($l \gtrsim 60$) and a significant fraction of the photons produce pairs. Let us now focus on thermal Comptonisation in a hot corona. It is now possible to define the corona compactness l_h and its corresponding heating power l_h. In a similar way, we define the compactness and

the luminosity of the source emitting soft photons as l_s and L_s. As shown by Ghisellini & Haardt (1994), the ratio between l_h and l_s is fully determined by spectral characteristics of the source such as its spectral index. Thus we can further reason on both l_s and l_h

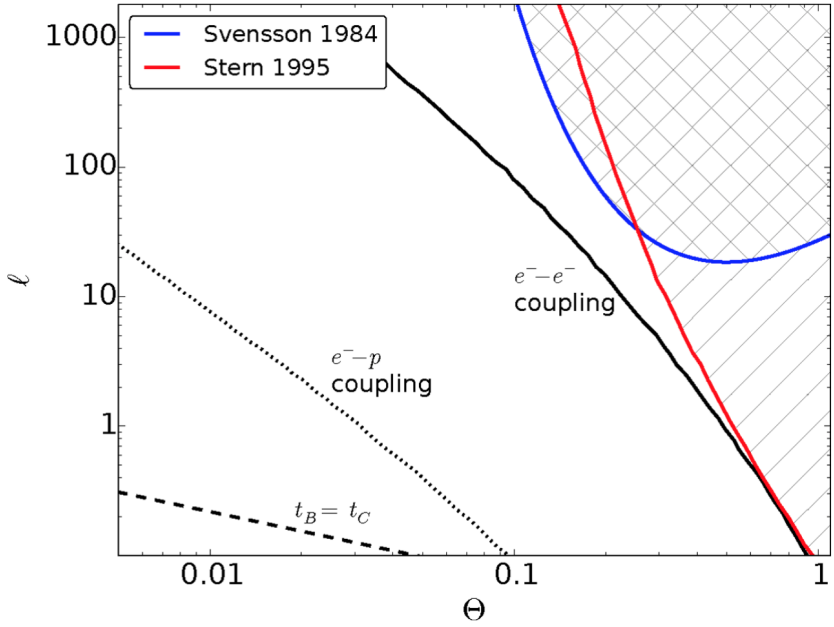

Figure 3.2. The compacteness-temperature diagram, (Fabian et al. 2015). The so-called pair runaway lines identifying the regions in which the pair production becomes a runaway process are shown.The position of these lines depends on the shape of the source and on the radiation mechanism. In red the computed pair balance curve for a slab corona while in blue the pair balance for an isolated cloud.

considering the pair balance. In case of small compactness we expect the heating power to increase and this yields an increase the temperature up to the limits of $\sim 2m_ec^2$ ($\sim 1MeV$). At that limit, in fact, the production of electron-positron pairs becomes more effective, and, subsequently, the number of particles grows. However, now a larger number of particles has to share the same amount of energy, thus the temperature starts decreasing and the compactness l_h increases. This means that the increased luminosity does not lead to an increase in the plasma temperature, but it increases the number of particles. Then when the pair equilibrium is reached (i.e. same number of created and destroyed particles) and for a given compactness (temperature) there is a maximum in the temperature (compactness) that can be reached in order to satisfy the pair equilibrium. Therefore, there is a direct relationship between l_s, l_h and the spectral properties of the source.

Let us now focus on the case in which a pair-dominated plasma undergoes an increase in the soft luminosity (L_s). Then, assuming the heating is constant, the result will be

an increase in the plasma temperature rather than a cooling. This can be understood following this reasoning: for an increase in the "cold" luminosity we expect the plasma to become cooler. In a cooler plasma, pair production is less efficient, thus we are left with a smaller number of particles sharing the same amount of energy. Once the pair equilibrium is reached, the plasma will have a higher temperature (e.g. Ghisellini & Haardt 1994; Ghisellini 2013). When $l_h \ll 60$ the production of electrons and positrons can be neglected, but l_h has been found higher than this threshold in different sources (Done & Fabian 1989a,b; Fabian et al. 2015).

Further effort in understanding the coronal plasma in AGN has been made e.g. (e.g. Fabian et al. 2015, 2017; Tortosa et al. 2018) and measurements of the compactness and the temperature of AGN coronae have been found to follow the relation locus imposed by the pair equilibrium see Fig. 3.3, suggesting that electron-positron production may have a role in shaping the spectral properties of AGN.

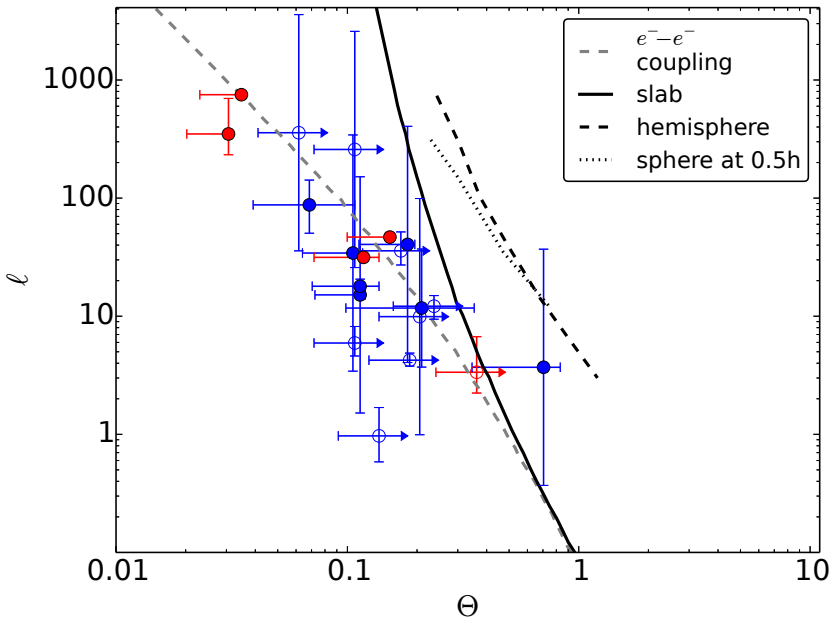

Figure 3.3. The distribution for NuSTAR observed AGN and BHB (blue and red points, respectively) in the $\Theta - l$ plane. The pair lines are from Stern et al. (1995), and the e-e coupling line discussed by Ghisellini et al. (1993) is also included. The slab line has been extrapolated slightly to higher l. Adapted from Fabian et al. (2015).

3.2 Soft-excess

This spectral component was first observed in the Active galaxy *Mrk* 841 by Arnaud et al. (1985), and, at present, it is commonly observed in AGN spectra (e.g. Walter &

Fink 1993; Page et al. 2004; Gierliński & Done 2004; Bianchi et al. 2009).

The soft excess is a featureless extra emission with respect to the extrapolated primary power law, and, in general, it starts becoming relevant below 1-2 keV. The origin of this component is still unclear and it has been object of many speculations (e.g. Done et al. 2012). From a spectroscopical point of view, different models accounting for blurred ionised reflection, ionised absorption or partial covering and thermal Comptonisation have been proposed for reproducing the soft excess, all of them with acceptable results in terms of statistics (e.g. Walter & Fink 1993; Page et al. 2004; Gierliński & Done 2004; Ponti et al. 2006b; Crummy et al. 2006; Bianchi et al. 2009; Jin et al. 2012; Done et al. 2012a).

Historically, a black body with a temperature between 0.1-0.2 keV was adopted to fit this component. However, this is unrelated to the black hole mass or the X-ray luminosity (Gierliński & Done 2004; Bianchi et al. 2009) and too high for a standard Shakura-Sunyaev disc emission. Ross & Fabian (1993) explained the soft excess as the reprocessing of the primary continuum off an ionised disc, as recombination continuum and line emission following photoionisation. Then in the framework of relativistic reflection, the smooth and featureless profile of the soft excess can be due to the blending of several relativistically blurred soft X-ray emission lines (Crummy et al. 2006; Cerruti et al. 2011; Walton et al. 2013a).

On the other hand, as for the primary emission, Comptonisation off a warm optically thick medium is also found to reproduce the soft excess component (Petrucci et al. 2013a; Boissay et al. 2014; Matt et al. 2014). This additional Comptonisation component leads to the so-called two-corona model in which besides the optically thin and geometrically thick hot electron corona, there is an extended medium optically thick and geometrically thin (likely an upper layer of the disc (e.g. Janiuk et al. 2001a; Różańska et al. 2015), or the disc itself (Done et al. 2012a) in which seed optical disc photons are Comptonised. Furthermore, this model accounts for the correlation between the optical-UV luminosity and the soft X-rays (Walter & Fink 1993).

The two-corona model was first tested in the Seyfert 1 Mrk 509, using data from a long multiwavelength campaign (Kaastra et al. 2011a) In that case, Mehdipour et al. (2011a) found a correlation between the optical/UV and soft (< 0.5 keV) X-ray flux, but no correlation between the optical/UV and hard (> 3 keV) X-ray flux. The spectral analysis suggested that the Mrk 509 spectrum (Fig. 3.4) was dominated by two Comptonisation processes: the hot component was consistent with being produced by an optically thin ($\tau_e \sim 0.5$) and hot component, while the second one was produced by a corona with a temperature of ~ 1 keV and an optical depth τ_e of ~ 15.

Moreover, Petrucci et al. (2013b) estimated the amplification ratio A for this warm plasma to be close to the theoretical prediction for a slab corona lying above a passive disc ($A = 2$, see previous Sect. 3.1). Moreover, the temperature of the soft seed photons was found to be different for the warm and hot corona, indicating that the two components

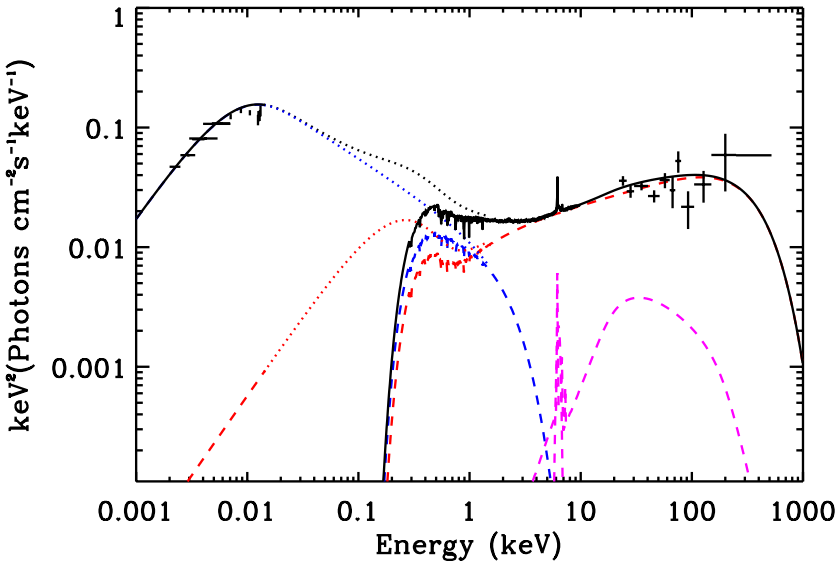

Figure 3.4. Best-fit model of the UV/X-ray spectrum of Mrk 509 (Petrucci et al. 2013b). The data (from HST, FUSE, XMM-Newton, INTEGRAL) are the black crosses. The solid black line is the best-fit model including absorption. The dashed lines are the different spectral components: the hot corona emission (in red), the warm corona emission (in blue), the reflection component (in magenta). The dotted lines are the corresponding component, but absorption-free.

are at two different radial distances. A tentative sketch of this two-corona model is shown in Fig.3.5.

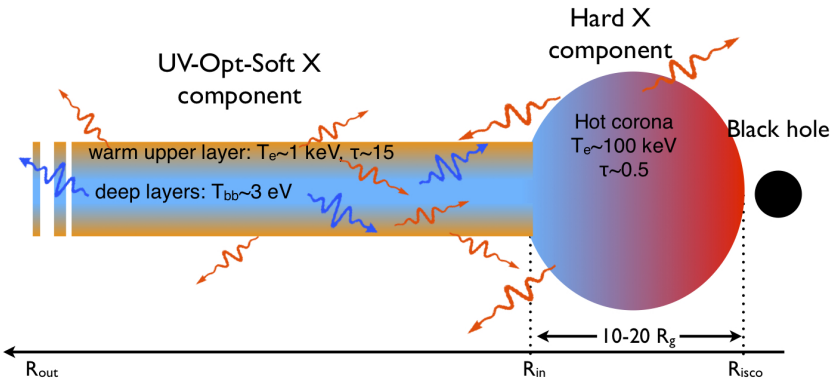

Figure 3.5. The geometry of the accretion flow in Mrk 509 as discussed in Petrucci et al. (2013b). The hot, optically thin corona produces the hard X-ray emission, and is located in the inner part of the accretion flow. The warm, optically thick corona produces the optical/UV up to soft X-ray emission, and it extends over a large part of the accretion disc.

Following what was found for Mrk 509, the presence of a warm Comptonisation component has been investigated in various other sources.

Petrucci et al. (2018) further tested the Comptonisation origin of the soft-excess of a large sample of Seyfert 1 galaxies extracted from the CAIXA catalogue (e.g. Bianchi et al. 2009). In particular, fitting simultaneous optical-UV and X-ray data, they found that a warm-corona producing the soft X-ray excess was a viable explanation for the considered sample of AGN. For all the sources, the authors also studied the temperature and photon index for the warm corona and compared these values with those studied by Fabian et al. (2015) and corresponding to the hot corona, see Fig. 3.6

3.3 Reprocessed emission: The Fe Kα line and the Compton reflection

Additional complexities are very often observed in AGN X-ray spectra. In particular, the primary coronal emission can be reflected via a Compton process by surrounding materials such as clouds. As a function of the column density of the reflectors, we will refer to Compton thin or thick sources. In the former case, the reflecting matter has a column density smaller than $N_H \sim 1.5 \times 10^{24}$ cm^{-2}, while when this density exceeds this threshold, we are in the Compton-thick regime and the resulting reflected spectrum will be largely affected by this reprocessing as shown by Fig. 3.7.

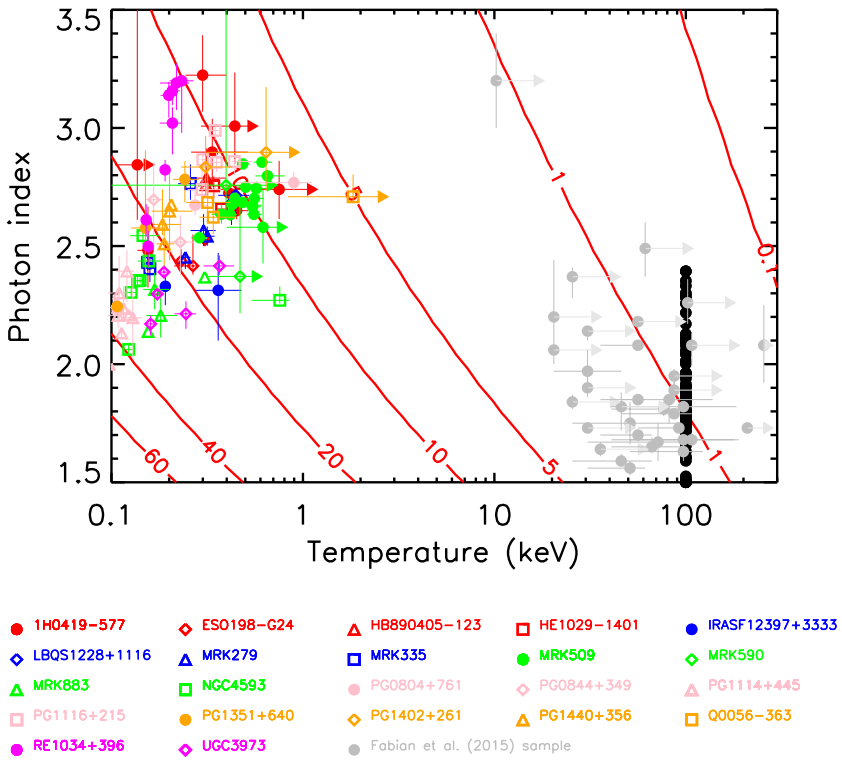

Figure 3.6. For the object studied by Petrucci et al. (2018), the best fit temperature and photon index of the warm corona. Different coloured symbols are used for each object. Moreover, the best fit photon indices of the hot corona (black circles on the right). The temperature of the hot corona being fixed to 100 keV in the fits, they are all aligned vertically. The grey filled circles correspond to the best fit parameters of the hot corona by Fabian et al. (2015). It worth noticing that warm corona values cluster at a low temperature and high optical depth, while for the hot corona higher temperature values are found and τ_e is compatible with being close to unity.

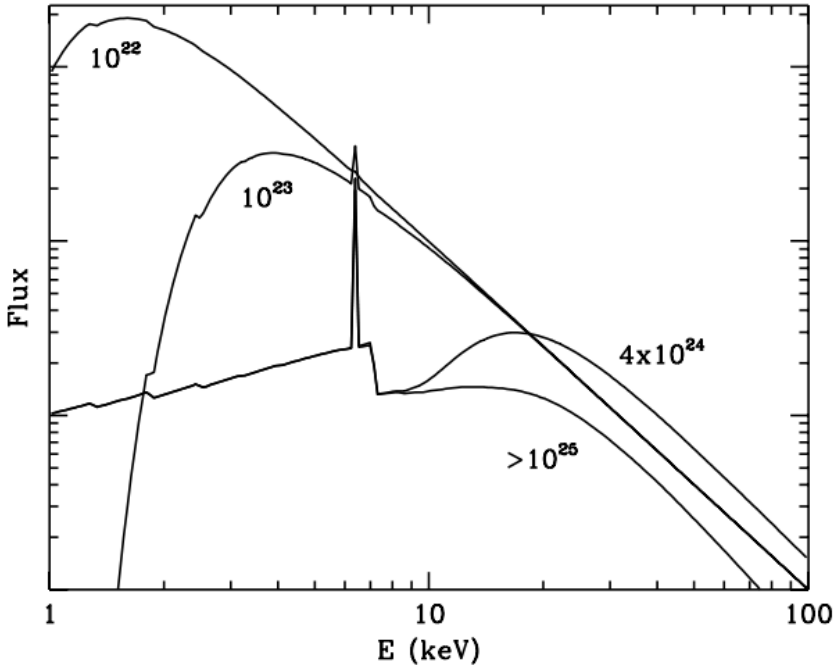

Figure 3.7. X-ray spectrum of an obscured Seyfert galaxy as a function of the column densities of the absorber (cm^{-2}). A geometrically thick torus with an opening angle of 30 degrees is assumed (Matt et al. 2003).

- Once a coronal X-ray photon interacts with the circumnuclear material (e.g. it can belong to the accretion disc or the obscuring torus), it can underlie a further Compton scatter or be absorbed via a photoelectrical process. The latter case occurs if the energy of the incoming photon is larger with respect to that of a specific atomic-transition. The largest cross-section for a photoionisation process is the one of the K-shell i.e. n=1. After the K-shell photoionisation, the resulting ion can de-excite via fluorescence or in accordance with the Auger effect. In the former channel the energy is radiated as a Kα photon if the excited electron drops from the L-shell (n=2) to the K-shell. On the other hand, if de-excitation occurs via the Auger effect, then the same amount of energy is transferred to another L-shell electron that is then ejected. Interestingly, the probability associated to the de-excitation channel of the fluorescence is an increasing function of the atomic number. Then de-excitation preferentially occurs via fluorescence rather than Auger effect for high atomic number elements such as iron.

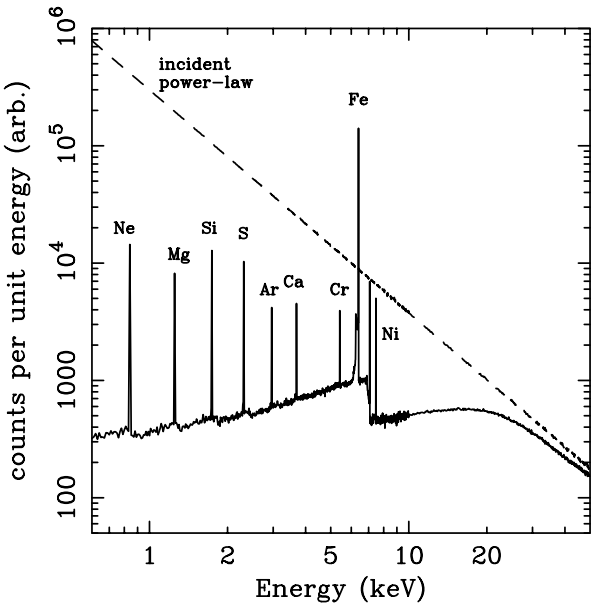

Figure 3.8. X-ray reflection from an illuminated slab. Dashed line shows the incident continuum and solid line shows the reflected spectrum (integrated over all angles). M onte Carlo simulation from Reynolds, 1996

Iron is the most abundant of the heavier elements in the Universe (Lodders 2003), thus the strongest fluorescence emission line is the Fe Kα at 6.4 keV (e.g. Matt et al. 1997; Fabian et al. 2000). The study of the Fe Kα profile is a powerful tool for investigating the innermost regions of AGN. Several effects such as the Doppler shift (Special Relativity) and the gravitational redshift (General Relativity) can

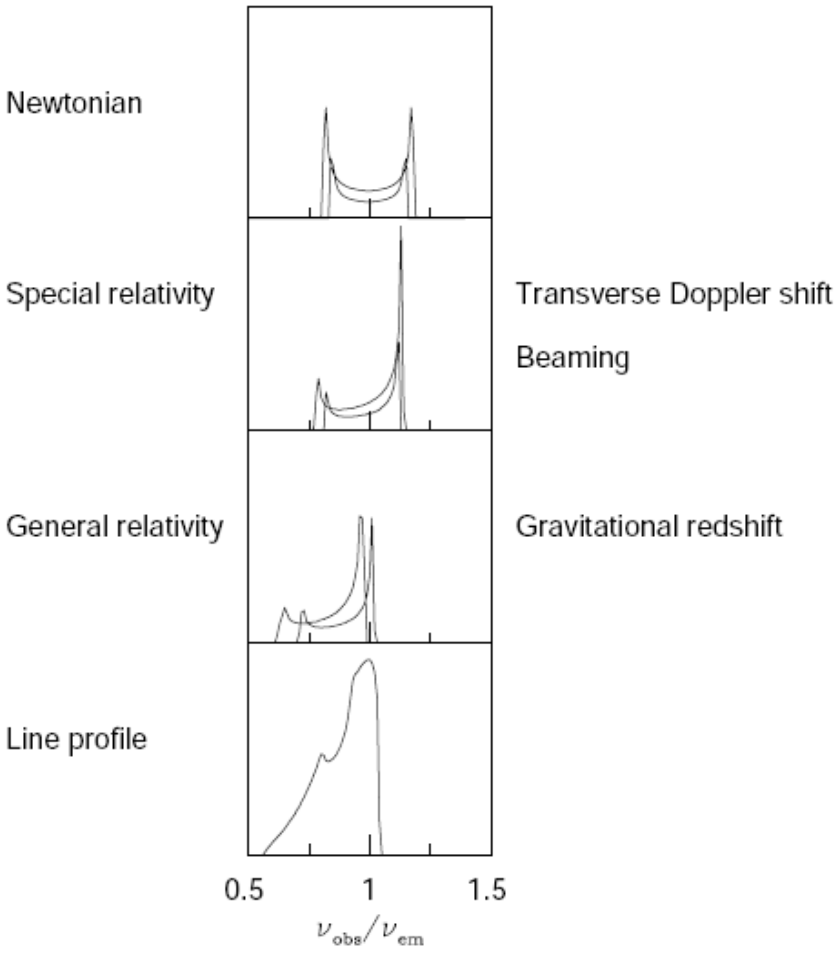

Figure 3.9. The different individual effects contributing to the characteristic double-horned relativistic line (Fabian et al. 2000).

in fact modify the intrinsic narrow profile of the Fe Kα, see Fig. 3.9. In fact, in the case in which fluorescence occurs near the black hole (e.g. a few gravitational radii apart), the line profile appears broader and skewed toward lower energies (e.g. Fabian et al. 1989). The supermassive black hole spin is also found to dramatically

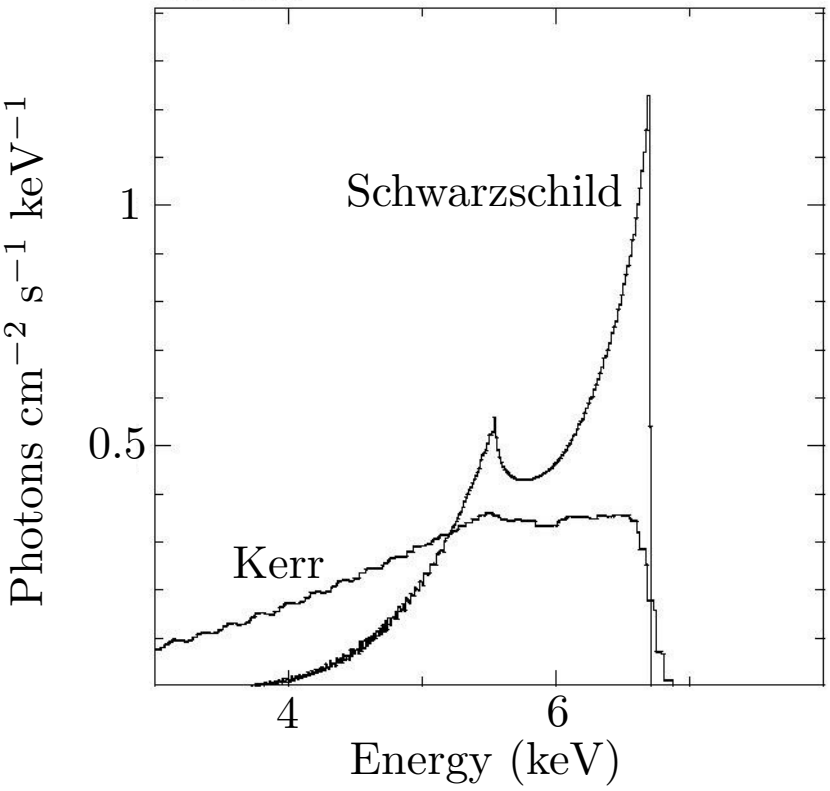

Figure 3.10. Various relativistic Fe Kα line profiles from an accretion disc around a Schwarzschild black hole and a maximally rotating (Kerr) black hole (Fabian et al. 2000).

affect the iron line profile, in fact, at higher spin values correspond closer inner stable orbits (the disc inner radius can extend down to 1.23 R_g for a maximally rotating BH (Laor 1991), see Fig. 3.10. Finally, assuming that the shape of the Fe Kα is affected by General Relativity, the analysis of the line profile can be used as a tool for constraining the black hole spin and the disc inner radius.
The first observational evidence of line broadening has been provided in Tanaka et al. (1995) who analysed *ASCA* data of the Seyfert galaxy MCG-6-30-15. Nowadays, broad emission lines are observed in AGN spectra from various sources (Nandra et al. 2007). For completeness, broad emission lines have been explained in terms of absorption rather than general relativistic effects (Miller et al. 2008). However, in one of the first papers including *NuSTAR* data, Risaliti et al. (2013) studying the X-ray spectrum of the low mass AGN NGC 1365, found the source

X-rays arising from a region within 2.5 gravitational radii of the rapidly spinning black hole, and ruled out the absorption-dominated models not including relativistic disc reflection, see Fig. 3.11.

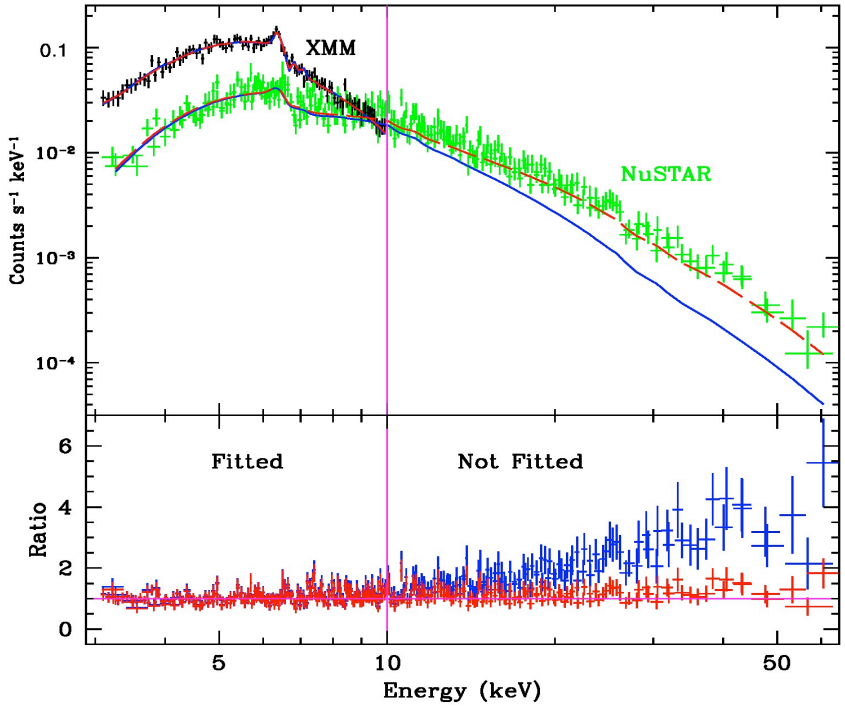

Figure 3.11. A relativistic reflection (red) and a multiple absorber (blue) models are compared for XMM-Newton and NuSTAR data of NGC 1365. Below 10 keV both models fit the data, but above this energy they strongly deviate from each other. In particular, the double partial covering model fails in reproducing the data simultaneously in the XMM-Newton and NuSTAR bands. From Risaliti et al. (2013).

- Compton reflection as well can further affect the primary Comptonised X-rays. Reprocessing of the primary emission can be due to the accretion disc, clouds orbiting around the central black hole or the obscuring torus. In fact, if we consider a primary power-law illuminating spectrum scattering on slab-like Compton-thick matter, we are left with a bump of the primary emission at about 30 keV, with a corresponding cut-off at $\sim$ keV due to photoelectric absorption (e.g. Magdziarz & Zdziarski 1995). A fundamental parameter used in spectroscopical analyses is the reflection fraction R. This parameter measures the amount of reflection, and in particular it is the ratio between the reflected and the primary flux. Compton reprocessing is largely affected by the physical conditions of the reflecting materials. Reflection off neutral (cold) matter (e.g. George & Fabian 1991; Matt et al. 1991; Magdziarz & Zdziarski 1995; Nandra et al. 1997a; Murphy & Yaqoob 2009) largely

differs from reprocessing by ionised materials (e.g. Ross & Fabian 1993; Matt et al. 1993; Zycki et al. 1994; Zycki & Czerny 1994; Matt et al. 1996; Ross & Fabian 2005; García & Kallman 2010; García et al. 2014a, 2015). From an observational point of view, the reflected spectrum is affected by the geometry and the location of the primary source and by the inclination angle of the reflectors.
The shape of the reflected spectrum is also dependent on the chemical composition and the ionisation degree of the scattering materials. The ionisation parameter can be defined as:

$$\xi = \frac{4\pi F_X}{n} \ . \tag{3.27}$$

where n is the number density of the reflector, F_X is the illuminating X-ray flux. Typical values of cold reflecting matter (i.e. low ionised or neutral) correspond to $\xi \leq 100$ erg/s. Then material can be further ionised up to $\xi \geq 10^4$ erg/s. In the low ionisation regime a significant fluorescence Fe Kα is expected, while other recombination lines from Fe XXV (6.67 keV) and Fe XXVI (6.966 keV) occur for higher ionisation degrees. Finally, when ξ exceeds the limiting values no signatures from atomic physics are expected, see Fig. 3.12

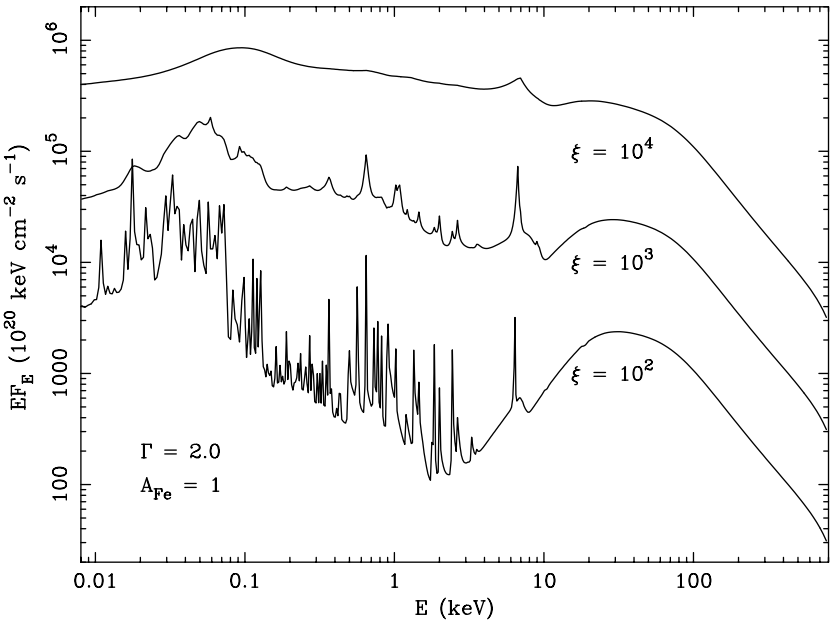

Figure 3.12. Reflected spectra for three values of the ionisation parameter ξ, in units of erg s^{-1} cm (Ross & Fabian 2005). Besides the Fe Kα fluorescence line, the lower-ionisation spectrum shows a forest of soft X-ray emission lines due to emission of different highly ionised ions.

3.4 Absorption

AGN are composite systems and their spectral behaviour may be affected by absorbing material crossing the line of sight to the observer. Absorption can be due to neutral or ionised matter.

Neutral absorption: the main effect of absorption by cold material is a suppression of the soft X-rays. In type 2 AGN, the flux suppression is remarkable and it may be explained as the result of the photoelectric effect due to the obscuring torus. Variations of the column density of the absorbers of type 2 Seyferts have been observed with characteristic timescales of months and years (Risaliti et al. 2002). Absorption variability has been found to occur on even shorter timescales (days/hours) for a number of sources, namely NGC 4388 (Elvis et al. 2004), NGC 4151 (Puccetti et al. 2007), NGC 1365 (Risaliti et al. 2009), NGC 7582, (Bianchi et al. 2008), and they may even switch from Compton-thick to Compton-thin (Matt et al. 2003), or completely to an unobscured state (NGC 1365 Walton et al. 2014) Then, the complex behaviour of the absorption variability supports the idea of a clumpy structure rather than a simple toroidal shape of the torus (e.g. Elitzur & Shlosman 2006; Nenkova et al. 2008).

Evidence of rapid absorption variability has been obtained also for Type 1 AGN (e.g. Mrk 766, Risaliti et al. (2011); ESO 323-G77,Miniutti et al. (2014)). Absorption events in type 1 objects may be associated to eclipse events likely being the result of BLR clouds intercepting our line of sight (e.g Markowitz et al. 2014; Torricelli-Ciamponi et al. 2014). Because of eclipses, type 1 objects have switched to obscured state (Coffey et al. 2014; Kaastra et al. 2014, for H0557-385 and NGC 5548 respectively).

Ionized absorption: The UV and X-ray emission of about 50% of type 1 AGN shows absorption effects (e.g Crenshaw et al. 2003) due to ionised absorbers. We commonly refer to these absorbing materials as "warm absorbers". It is worth noticing that often warm absorbers display peculiar velocities, generally blueshifted, with respect to the systemic velocity of the AGN. These velocities suggest that warm absorbers are outflows of matter (v_{out}=10^2-10^3 km/s). Kaastra et al. (2000) showed that they can be modelled as shell of outflowing matter at photoionisation equilibrium, while Costantini (2010) discusses the fact that outflows are generally found to be multiphase, i.e. they span a large ranges of values for the ionisation and velocity parameters. From a spectroscopic point of view, analysing the variability of the absorption lines can be used to estimate the distance between the warm absorbers and the central source (e.g. Crenshaw et al. 2003).

Different and more extreme outflows presented in AGN are called ultra-fast outflows (UFOs, e.g. Tombesi et al. 2010a,b). These phenomena are commonly observed through highly blue-shifted Fe XXV and Fe XXVI absorption lines in the Fe Kα band (e.g. Chartas et al. 2002; Cappi et al. 2009; Tombesi et al. 2010a,b; Giustini et al. 2011; Gofford et al. 2013; Tombesi et al. 2015; Vignali et al. 2015).

A major property of UFOs is their high degree of ionisation ξ being $3<\log\frac{\xi}{erg\ cm\ s^{-1}}<6$ erg cm s^{-1}, while the column density of the absorbing material ranges between 10^{22}-10^{24} cm^{-2}. The blueshift of the Fe XXV and Fe XXVI is then used to infer the velocity of the outflow and such velocities were found to be v$\sim$0.03c-0.3c, with c the speed of light (e.g. Tombesi et al. 2011; Gofford et al. 2013).
Noticeably, evidence of ultra fast outflows has also been obtained in the soft X-ray band (e.g. Pounds 2014; Longinotti et al. 2015; Gupta et al. 2015; Reeves et al. 2016a). In this band, the O VII and O VIII lines have been found highly blue-shifted, suggesting in turn a much lower ionisation state with respect to UFOs. In this framework, the work by Tombesi et al. (2013) provides an important contribution the overall picture of outflows: This study compares the properties of the UFOs in the Fe Kα band and WA in the soft X-ray band in a sample of 35 Seyfert galaxies. In particular, Tombesi et al. (2013) found a correlation between the ionisation state, column density and velocity with the distance from the black hole: a UFO is therefore closer to the SMBH than the WA and the two phenomena occupy a different and never overlapping region in this diagram. Then, UFO and warm absorbers can be intended as different states of the same large scale outflow structure:meaning that the UFO are likely launched at high velocities from the innermost regions of AGN while WA lie at distances compatible with the torus or the external edge of the accretion disc.

3.5 X-ray variability

Variability is hallmark of AGN activity (e.g. Giallongo et al. 1991; Mushotzky et al. 1993; Vanden Berk et al. 2004; Barvainis et al. 2005; MacLeod et al. 2010; Kozłowski 2017; Vagnetti et al. 2016), and it interests both spectral properties as well as flux. There is still great uncertainty about the origin of variability, although it is believed that disc instabilities are likely to generate the observed flux variations in the optical/UV band. Simulations of accretion disc instabilities (e.g Chen & Taam 1995; Vanden Berk et al. 2004; Kelly et al. 2009; Zu et al. 2013; Kozłowski 2017) support this scenario, although other explanations, such as thermal fluctuations, have been proposed (Kelly et al. 2009). With the exception of candidate binary sources (e.g., Graham et al., 2015a,b), for which a periodic variability is found, the typical AGN variability is stochastic (Kelly et al. 2009; Andrae et al. 2013; Zu et al. 2013) and depends on the length of the monitoring time (e.g. Middei et al. 2016a).

3.5.1 Flux variability

Variability in AGN is observed in all the electromagnetic bands and affects both continuum and emission lines. Matthews & Sandage (1963) pointed out that optical

flux variations were a defining characteristic of AGN, and, variability itself was used to rule out alternatives to supermassive black holes as their central engine (e.g. Elliot & Shapiro 1974a). In the optical band, variability was observed in quasars which varied their luminosity of $\sim 0.3 - 0.5$ mag within some months and in blazars for which more dramatic variations (up to ~ 1 mag) were measured on a few days' timescales. However, it is in the X-rays that faster flux variations are observed. AGN variability appears to be aperiodic and of variable amplitude. Nowadays, variability is a powerful tool for probing the innermost regions of AGN. Let us now focus on X-ray flux variations: in X-rays variability is observed down to hour timescales meaning that the emitting source has to be very compact. The variation timescale (i.e. Δt_{var}) in the source reference frame allows us to constrain the size of emitting region $R \lesssim c\Delta t_{var}$ where c is the light speed:

$$R \lesssim ct \simeq \frac{t}{50\ s}\left(\frac{M}{10^7 M_\odot}\right) r_g\ . \tag{3.28}$$

When the source size is larger than the one estimated through variability it means that the different components of the emitting sources are not causally connected so that they would vary with different phases. Furthermore, in this context, the equation $R \lesssim c\Delta t_{var}$ leads to important considerations: using variability indeed, it is possible to find where the primary radiation originates. When the same source shows different variabilities on different time scales and, when variations also occur at the same frequency, the most rapid variations are those indicative of the source size. The slower variations account for physical effects as slow changes in the source structure (e.g. in size as well as in temperature).
Multiwavelength variability analysis are also important in understanding AGN. Moreover, broadband variability analysis can lead to important results, especially if similar patterns are found at different frequencies. When the same variability pattern is observed, than variations at different wavelengths are in phase, suggesting that the radiation comes from the same source region and it is produced via similar processes. Noticeably, variations in a specific band may lag with respect to variability in a different band. The delay between these variations can be explained as the time that the light needs to cross the space that separates the two emitting regions. In that occurrence, cross-correlating the variability patterns that occur in different wave-bands, it is possible to model and define the geometry of that cosmic source.

A common tool for investigating AGN variability is the power spectral density (PSD) defined as the product of the Fourier transform of the light curve and its complex conjugate. Let us call $C(t)$ the light curve of a source. For $C(t)$ it is possible to find its Fourier transform:

$$\hat{C}(f) = \int_{-\infty}^{\infty} C(t) e^{-2i\pi f t} dt\ . \tag{3.29}$$

The power spectrum P(f) of the light curve is given by the product of the light curve Fourier transform and its complex conjugate, (e.g. Peterson 1997):

$$P(f) = \hat{C}(f)^{*}\hat{C}(f) \ . \tag{3.30}$$

In other words, the amount of variability $P(f)$ is estimated as a function of the Fourier frequency f. In accordance with this estimator, AGN variability can be modelled as a power-law $P(f) \propto f^{\alpha}$ (Green et al. 1993; Lawrence & Papadakis 1993), where α is found between 1 and 2 on hour-month timescales (Vaughan et al. 2003a). This behaviour ($\alpha > 1$) is also called red-noise. When a red-noise like shape is found, the power variability is correlated with the Fourier frequency, while, on the contrary, a flat (white-noise) like shape of the power spectrum indicated no time correlation. The power spectral density needs well sampled light curves (also on year timescales) to be computed and thanks to observatories such as *RXTE* it has been calculated for a sample of nearby Seyfert galaxies (e.g. McHardy et al. 2004). Typically, the PSD of AGN is characterized by a slope $\alpha \simeq 2$ at high frequencies (short timescales in the time domain) and a flatter shape at low frequencies (long timescales) ($\alpha \simeq 1$). The slope change, also called frequency break, is usually found on day-month temporal scales (e.g. Edelson & Nandra 1999; Markowitz et al. 2003a; Markowitz & Edelson 2004; McHardy et al. 2004; Sobolewska & Papadakis 2009), and, interestingly, high frequencies breaks are also observed in stellar-mass Galactic X-ray binaries. Noticeably, the frequency break has been found to be directly correlated with the black hole mass and the source accretion rate: the break timescale increases proportionally with the black hole mass and decreases for highly accreting sources (e.g. Papadakis 2004a; O'Neill et al. 2005; McHardy et al. 2006):

$$log(1/f_{break}(days)) = 2.1 \log\left(\frac{M_{BH}}{10^{6} M_{\odot}}\right) - 0.98 \log\left(\frac{L_{bol}}{10^{44}}\right) - 2.32 \ . \tag{3.31}$$

This correlation supports the scale invariance of accreting black holes and suggests that black holes hosted in active galaxies are just scaled-up versions of the Galactic black holes. In principle, a low frequency break is also expected, but experimental evidence is strongly limited by the requirement of long and richly sampled light curves. However, some evidence for this additional break is found in a couple of sources, namely *Ark 564* (Pounds et al. 2001a; Papadakis et al. 2002; McHardy et al. 2007a) and NGC 3783 (Markowitz et al. 2003a). The physics behind the PSD high frequency break observed in AGN is still unclear and Ishibashi & Courvoisier (2012) discuss its relation with the inverse Compton cooling time. The Compton cooling time t_C is, in fact, inversely

proportional to the radiation density U_{ph} (see Eq. 2.35) that considering the emitting source to be at distance R is:

$$U_{ph} = \frac{L_s}{4\pi R^2 c} \ , \tag{3.32}$$

with L_s the soft luminosity that can be set as defined by Eq. 2.3 . Then rewriting R in units of gravitational radii we are left with:

$$t_C \propto \frac{M^2}{\dot{m}} \ , \tag{3.33}$$

and this relationship is in agreement with the empirical correlation (anticorrelation) between the PSD break and the black hole mass (accretion rate).

Variability can be estimated even if light curves are not well sampled, and a very popularly used method to estimate the amount of variability characterising an AGN is the so-called normalized excess variance (NXS). NXS provides a straightforward way to evaluate the source variability and it was first used in the ultraviolet domain (Edelson et al. 1990). Later Nandra et al. (1997a) utilized this variability estimator in the X-ray band, and, thereafter, it was used by several authors in this domain (e.g. Turner et al. 1999; Vaughan et al. 2003a; Ponti et al. 2012).

This parameter measures the degree at which the observed variance of the light curve exceeds the squared uncertainties associated to the flux and can be defined in accordance with the following equation:

$$\sigma^2_{NXS} = \frac{S^2 - \sigma^2_{noise}}{\langle f \rangle^2} \ . \tag{3.34}$$

The equation above is made up of the following components: the unweighted arithmetic mean flux for all the N observations,

$$\langle f \rangle = \frac{1}{N} \sum_{i=1}^{N} f_i \ , \tag{3.35}$$

the variance of the flux as observed,

$$S^2 = \frac{1}{N} \sum_{i=1}^{N} (f_i)^2 - \langle f \rangle^2 \ , \tag{3.36}$$

and the mean square uncertainties of the fluxes,

$$\sigma^2_{noise} = \frac{1}{N}\sum_{i=1}^{N}\sigma_i^2 \ . \tag{3.37}$$

It is worth noticing that the PSD and σ^2_{NXS} are strongly related since:

$$S = \int_0^\infty PSD(f)df \ , \tag{3.38}$$

where S is just the variance of the light curve. Even if the NXS is a simple method to estimate variability, it suffers from several effects such as sampling Allevato et al. (2013), light curves length (e.g. Lawrence & Papadakis 1993; Papadakis et al. 2008; Vagnetti et al. 2011a, 2016), then various caveats have to be considered when using this tool. However, when the various caveats are considered the normalised excess variance can be used to estimate black hole masses (e.g. La Franca et al. 2014; Pan et al. 2015; Ponti et al. 2012)

Finally, X-ray variability is also measured on timescales as long as years and decades (Vagnetti et al. 2011a, 2016; Gallo et al. 2018) and this is interesting if we consider that X-ray photons are produced in a very compact region. On such long timescales PSD cannot be computed since none of the available light curves is sampled enough, thus an alternative method can be used, the structure function (SF). This method has been adopted in various electromagnetic bands, in the optical-UV (e.g. Trevese et al. 1994; Kawaguchi et al. 1998; de Vries et al. 2003; Bauer et al. 2009) as well as in the radio domain (Hughes et al. 1992). SF works in the time domain and for ensemble characterization, it can be also used when the source light curves have only some data points (i.e. at least 2). It provides the measurement of the mean deviation between two observations separated by a time lag τ and it is defined as:

$$SF(\tau) = \sqrt{\langle[\log f_X(t+\tau) - \log f_X(t)]^2\rangle - \sigma_n^2} \ . \tag{3.39}$$

Structure function studies have been used to analyse large samples of sources.

The NXS and SF are related by:

$$\sigma^{2\ *}_{NXS} = \sigma^2_{NXS}\left(\frac{\Delta t^*}{\Delta t_{rest}}\right)^{2\beta} = \sigma^2_{NXS}\left(\frac{\Delta t^*}{\Delta t_{obs}}\right)^{2\beta}(1+z)^{2\beta} \ , \tag{3.40}$$

where β is obtained from ensemble studies (Middei et al. 2016b; Vagnetti et al. 2016).

In addition, time lags between different X-ray energy bands have been observed in local Seyferts. In particular X-rays above $\sim$ 2 keV lag with respect to soft X- rays (below 1-2 keV) (Papadakis et al. 2001; Vaughan et al. 2003a). These so-called hard lags are commonly larger on longer time-scales, and at higher energies. On the other hand,

also soft lags have been detected in a number of sources, meaning that the soft X-ray variations lag behind the hard X-ray variations. The first case of a soft-lag was claimed for the NLS1 1H 0707-495 (Fabian et al. 2009). The authors interpreted this variation as the result of relativistic reflection varying in agreement with the continuum changes after the light-crossing time from the source to the reflecting region. A correlation between soft-lags and the black hole mass has been observed, and typical delays are in the order of $\sim 100s$, (e.g. De Marco et al. 2013; Kara et al. 2016).

3.5.2 Spectral variability

The origin of flux variability in AGN is still evading our understanding, and a valuable tool for studying the relationship between accretion disc and variability properties is the study of the spectral variability, i.e. the changes of the spectral shape of the continuum.

Different studies in the optical-UV band have been published on this topic (Giveon et al. 1999; Trèvese & Vagnetti 2002; Vagnetti et al. 2003), finding that a hardening of the spectra corresponds to brighter AGN phases. This behaviour is called "harder when brighter".

On the other hand, spectral variability is commonly observed also in the X-rays where a correlation holds between the PSD frequency break and the spectral photon index after normalising for the black hole mass (Papadakis et al. 2008). Several authors studied this AGN property focusing on single sources (Magdziarz et al. 1998; McHardy 2001; Zdziarski et al. 2003), monitorings (Ursini et al. 2016; Middei et al. 2018), and on a large AGN sample (Serafinelli et al. 2017), such as MEXSAS (Vagnetti et al. 2016). In the X-rays, a typical trend of the spectral variability is "steeper when brighter", and it is observed in local Seyfert Galaxies and in Quasars (Sobolewska & Papadakis 2009; Soldi et al. 2014). In other words, to larger values of Γ correspond higher flux states. Different possible origins for this behaviour have been proposed, and in the following, a few of them are summarized:

- The simplest interpretation states that the observed variability of the source photon index is due to an intrinsic variations in the underlying continuum emission (e.g. Haardt et al. 1997; Coppi 1999).

- the complex interplays and variability of the various components giving rise to the AGN spectrum can produce the observed spectral variability. For instance, the spectrum may be composed of a power law continuum, variable in amplitude only, and of a reflection component, which is constant (e.g. McHardy et al. 1999; Shih et al. 2002; Taylor et al. 2003; Ponti et al. 2006a; Miniutti et al. 2007). It is not excluded that a variable power-law slope, combined with a constant reflection, is also present.

- Due to the Comptonisation origin of X-rays, when the soft input photon luminosity increases (e.g. because of an increase in the accretion rate), the cooling of the corona will be more efficient. Therefore, the lower coronal temperature would, in turn, produce a softer spectrum.

- It may be possible that the constant behaviour of the primary continuum is modified by complex absorption events and by variations in the absorbers (e.g. column density, ionisation state, covering factor) Turner & Miller (2009).

In order to quantify the spectral variability of a source, Trèvese & Vagnetti (2002) introduced a spectral variability estimator β, defined as follows:

$$\beta = \frac{\alpha(t + \Delta t) - \alpha(t)}{logF_B(t + \Delta t) - logF_B(t)} = \frac{\Delta\alpha}{\Delta logF_B} \ . \tag{3.41}$$

In these equations $\alpha(t)$ describes the spectral variability at time t and F_B(t) stands for the flux in a certain band. The β estimator has been extensively used by Serafinelli et al. (2017) for describing the bulk spectral variability properties of a large sample of AGN. In particular, the authors confirmed the general trend softer when brighter behaviour also for the high luminosities and redshift sources in their sample. Moreover, no dependences on redshift, X-ray luminosity, black hole mass or Eddington ratio were found for the spectral variability.

Chapter 4

Broadband spectral analyses

In this Chapter, detailed spectral analyses based on both proprietary and archival data will be presented and discussed. The spectral modelling of multi-epoch data sets is a valuable tool for probing the emission properties of supermassive black holes and their circumnuclear material. Indeed, this approach provides a solid way to answer to the questions reported in the Incipit of this dissertation. Detailed broadband spectral analysis, with the study of the source variability properties allows one to consistently model all the source spectral components (e.g. Nandra et al. 1998) and the success of these kinds of studies is demonstrated by the increasing number of outstanding outcomes and related papers based on various multiwavelength campaigns of nearby Seyfert galaxies, such as Mrk 509 (e.g. Kaastra et al. 2011a, and related series of papers), NGC 5548 (Mehdipour et al. 2015a, and related works), NGC 4593(Ursini et al. 2016, and part of this thesis), NGC 7469(e.g. Behar et al. 2017, and connected papers and part of this dissertation), and NGC 3783 (Mehdipour et al. 2017).

In this framework, we test phenomenological and physical models on multiple observations of a nearby Seyfert galaxy HE 0436-4717. This source has been serendipitously observed by NuSTAR three times ($\sim$2 days apart) between December 2014 and January 2015, and a further time at the end of 2015. Then, by performing detailed spectral analyses we are able to describe well the high energy properties of this AGN obtaining information on its emission mechanisms and to study the time-dependent evolution of the various spectral components. However, the lack off a simultaneous soft X-ray band coverage prevents us from determining a favoured scenario out of those tested on the data.

Then, we performed spectral analyses on broadband multi-epoch observations obtained in the context of multiwavelength monitorings. In particular, we will present and discuss detailed spectral characterisations of two nearby and bright AGN, namely NGC 7469 and NGC 4593. Both these AGN have been selected as being the best candidates (see next Sections 4.2 and 4.3) for studying a number of physical processes occurring

in AGN. Moreover, the simultaneous XMM-Newton-NuSTAR coverage will allow us to describe well all the spectral components while, thanks to the different time intervals between the observations we will track the variability properties of the various components.

4.1 Overview: HE 0436-4717 and the monitoring

We discuss the spectral analysis on four serendipitous *NuSTAR* observations of HE 0436-4717 extracted from the *NuSTAR* Serendipitous Survey (Lansbury et al. 2017). The AGN HE 0436-4717 lies in the field of view of the pulsar PSR J0437-4715, which was the target of the observations (Guillot et al. 2016), and it is 4 arcmin apart. HE 0436-4717 is one of the few AGN that have been pointed by *NuSTAR* in multiple epochs, and is the second brightest among those serendipitously observed. This source is a type 1 Seyfert galaxy (Véron-Cetty & Véron 2006) lying at redshift z=0.053 (Wisotzki et al. 2000), and hosting a supermassive black hole with mass $M_{\rm BH} = 5.9 \times 10^7\ M_{\odot}$, (Grupe et al. 2010). The spectral coverage of this active galactic nucleus is very peculiar since it is one of the eight AGN that have been detected in the extreme ultraviolet (EUV) band (Barstow & Holberg 2003). Moreover, a long monitoring of $\sim$ 20 days by the *Extreme UltraViolet Explorer* (EUVE) revealed a possible periodic variability (P=0.9 days) in the extreme ultraviolet (EUV) (Halpern & Marshall 1996; Halpern et al. 2003; Leighly 2005). In the X-rays, based on *ASCA* and *ROSAT* observations, Wang et al. (1998) showed that it was possible to reproduce the HE 0436-4717 spectrum with a power law with Γ $\sim$2.15 and a black body with temperature 29$\pm$2 eV accounting for the soft X-ray emission. A narrow Fe Kα emission line was also detected in the two *ASCA* observations with equivalent widths of 430$\pm$220 and 210$\pm$110 eV respectively. Moreover, the authors found no spectral variability, while the source continuum increased in flux remarkably ($\sim$50%) among the pointings (four months apart) the 2-10 keV flux being in the range 2.9-4.4 $\times 10^{-12}$ erg/cm^2/s. Bonson et al. (2015) analysed more recent *XMM-Newton* and *Swift* data, testing three models: partial covering absorption, blurred reflection, and soft Comptonisation. All these scenarios were consistent with the data on a purely statistical basis. On the other hand, the authors argued that if the source variability and the UV emission are taken into account, the blurred reflection model provides the best self-consistent view of the data. According to this model, Bonson et al. (2015) found that the emission of HE 0436-4717 is due to a primary continuum that dominates over the emission from a distant neutral reflector and a blurred ionised disc reflection. Moreover, the authors modelled the Fe Kα using the sum of a very broad emission line (σ=$3.6^{+3.9}_{-1.1}$ keV, EW=2.5 keV) occurring at $R_{\rm in}$<1.8 $r_{\rm g}$ and a narrow component (σ=1 eV, EW=46 eV) arising from distant and neutral material.

4.1.1 Observations and data reduction

This analysis is based on *NuSTAR* (Harrison et al. 2013) data, and in particular on four serendipitous observations of HE 0436-4717, reported in the *NuSTAR* Serendipitous Survey (Lansbury et al. 2017). The first three observations are separated by approximately day, while the time that elapsed between the third and fourth observations is

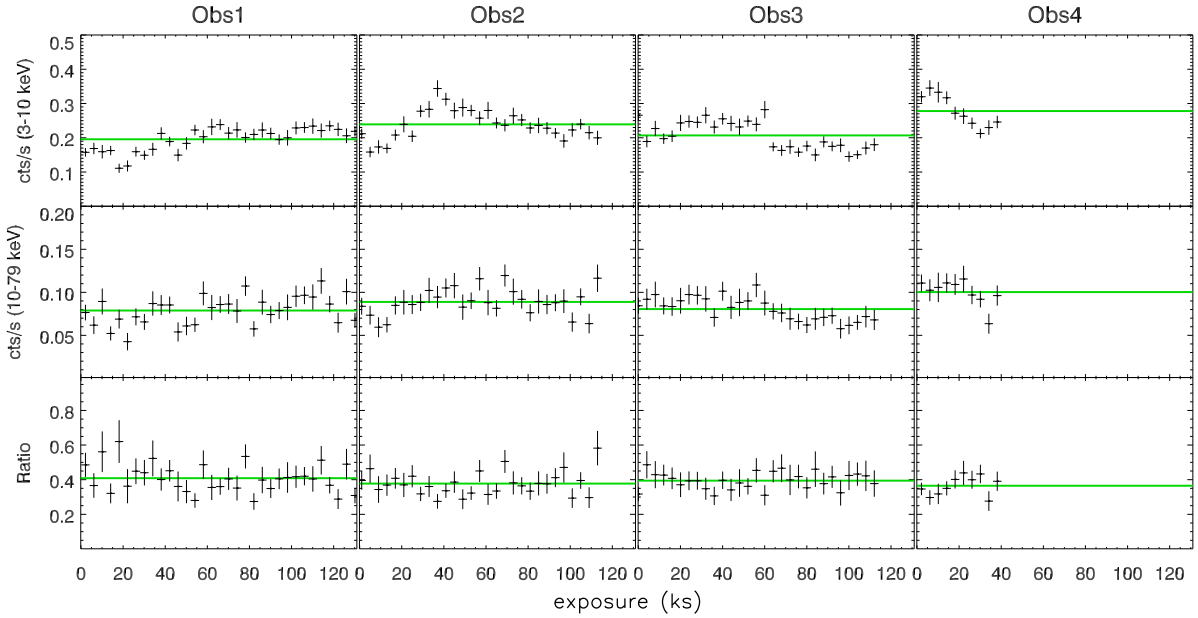

Figure 4.1. The co-added *FPMA* and *FPMB* light curves are shown in the top and middle panels, in the 3-10 keV and 10-79 keV energy bands, respectively. For the various pointings, the ratios between the 10-79 keV light curves and those computed in the 3-10 keV band are shown. The adopted time binning is 4 ks for all the observations. Solid green lines account for the average count rates within each pointing. The exposures in the graph are twice as long as those reported in Table 4.1 because half of the *NuSTAR* time is cut due to Earth occultations.

about one year (see Table 4.1). Therefore, long- and short-term flux variability and/or variation in the physical and phenomenological parameters of HE 0436-4717 can be investigated.

NuSTAR data were reduced using the pipeline (*nupipeline*) in the *NuSTAR* Data Analysis Software (nustardas release: nustardas_14Apr16_v1.6.0, part of the *heasoft* distribution[1]), adopting the calibration database (20171204). Both Focal Plane Modules A and B (*FPMA/B*) on board *NuSTAR* were analysed. We obtained the light curves and the spectra for both modules using the standard tool *nuproducts*. To extract the source counts, we used a circular region with a radius of 30 arcseconds while, using a circle of the same radius, we extracted the background from a blank area close to the source.

We have binned the *NuSTAR* spectra in order to have a signal-to-noise (S/N) ratio greater than three in each spectral channel and not to over-sample the instrumental

[1]NuSTARDAS software guide, Perri et al. (2013), https://heasarc.gsfc.nasa.gov/docs/nustar/analysis/nustar_swguide.pdf.

Table 4.1. The observation ID, the start date and the net exposure time in kiloseconds are reported for the *NuSTAR* serendipitous observations here presented analysed. The rates account for the average of modules *FPMA* and *FPMB*.

Obs.	Obs. ID	Net rates (10^{-2}) cts/s	Net exp. ks	Start-date
1	30001061002	4.0	74	2014-12-29
2	30001061004	4.9	64	2014-12-31
3	30001061006	4.2	63	2015-01-02
4	60160197002	6.9	20	2015-12-09

resolution by a factor larger than 2.5. The obtained spectra of module A and B are in agreement with each other, their cross-normalisation being within $\leq$3% in all the performed fits. The spectra were analysed taking advantage of the standard software *Xspec* 12.9.1p (Arnaud 1996).

In the forthcoming, all errors in text and tables are quoted at 90% confidence level, unless otherwise stated, and plots are in the source reference frame.

4.1.2 Temporal analysis

X-ray flux variations are a hallmark of AGN activity and they are commonly observed on timescales from years and decades (e.g. Vagnetti et al. 2011b, 2016; Zheng et al. 2017) down to hours, (e.g. Ponti et al. 2012). Adopting the *nuproducts* standard routine, we computed light curves in the 3-10 and 10-79 keV bands for HE 0436-4717 (see Fig. 4.13). Intra-observation variability is found in the 3-10 keV light curves already at kiloseconds timescales (up to a factor of approximately 2 in observation 2), while, smaller flux variations appear in the 10-79 keV band (consistent with variability found extracting light curves in the 10-24 keV band). The ratios of the light curves in the 10-79 keV band and those in the 3-10 keV band are found to be compatible with being constant. Between the different pointings, the mean counts for each of the four observations (solid line in Fig. 4.13) is found to be modestly variable. The most relevant increase of the counts ($\sim$40%) is observed in observation four, while in the first three observations the mean of the counts has a variation of the order of 15%. Therefore, since no strong spectral variability is found even where modest flux variations are observed, we use the average spectra of each observation to improve the spectral fitting statistics.

The normalised excess variance σ^2_{nxs} (e.g. Nandra et al. 1997a; Turner et al. 1999; Vaughan et al. 2003b; Ponti et al. 2012) provides a quantitative estimate of the AGN X-ray variability. This estimator can be defined as $\sigma^2_{nxs} = (S^2 - \sigma^2_{noise})/\langle f \rangle^2$, where

f is the unweighted arithmetic mean flux for all the N observations, S represents the variance of the flux as observed, while the mean square uncertainties of the fluxes are accounted for by σ^2_{noise}.
Following this formula and computing the associated error to σ^2_{nxs} using Eq. A.1 by Ponti et al. (2012), we computed the σ^2_{nxs} in the 3-10 keV for all the observations in 10 ks time bins, obtaining an upper limit of $\sigma^2_{nxs}<0.05$. Short-term variability has been found to be tightly correlated with the BH mass by many authors (e.g. Nandra et al. 1997b; Vaughan et al. 2003b; McHardy et al. 2006; Ponti et al. 2012); therefore, adopting the relation in Ponti et al. (2012) for the σ^2_{nxs} and M_{BH}, we estimated a lower limit for the BH mass $M_{BH} > 3{\times}10^6$ $M_{\odot}$, in agreement with the single-epoch measurement by Grupe et al. (2010).

4.1.3 Data analysis:Phenomenological modelling

As a first step, we try to reproduce the continuum emission of HE 0436-4717 with a power law absorbed by the Galactic hydrogen column ($N_H{=}1{\times}10^{20}$ cm^{-2}, Kalberla et al. 2005). In the fit, the photon index and the normalisation are free to vary between the various pointings. To account for the intercalibration of modules A and B, we use a constant set to unity for *FPMA* and free to vary for *FPMB*. The two modules are found to be in good agreement ($\leq$3%). This simple model leads to a good fit ($\chi^2 = 460$ for 452 d.o.f) but some residuals around 6.4 keV and at energies greater than $\sim$30 keV are still present, suggesting the existence of reprocessed components (see Fig. 4.2). Therefore, we added a Gaussian component to account for the residuals between 6-7 keV (see Fig 4.2), obtaining the following model: *const×phabs×(po+zgauss)*. The power law shapes the primary continuum, while the *zgauss* accounts for the presence of neutral or ionised emission lines. The photon index and the normalisation between the different observations are untied and free to vary. For the Gaussian component, we let free to vary and untied among the pointings its energy, intrinsic width (σ), and normalisation. The energy of the Gaussian component is not well constrained since it is 6.50$\pm$0.15 keV. Therefore in the subsequent modelling we fix it at 6.4 keV, as for the neutral Fe kα. In a similar fashion, the line width is found consistent with being zero in all the observations with a corresponding upper limit of 400 eV. Thus, in the forthcoming, we set its value to zero. This procedure yielded a best-fit χ^2=432 for 448 degree of freedom (d.o.f) and the corresponding best-fit values for the parameters are reported in Table 4.2. When we fit all the observations together, letting free to vary only the line normalisation, a $\Delta\chi^2$=23 for 4 d.o.f. less is found. The presence of this component is then supported by the *F-test*[2] according to which its significance is $>$ 99.9 per cent. The emission line is

[2]To reliably assess the Fe Kα significance via the *F-test*, we allowed its normalisation to be negative and positive, as discussed by Protassov et al. (2002).

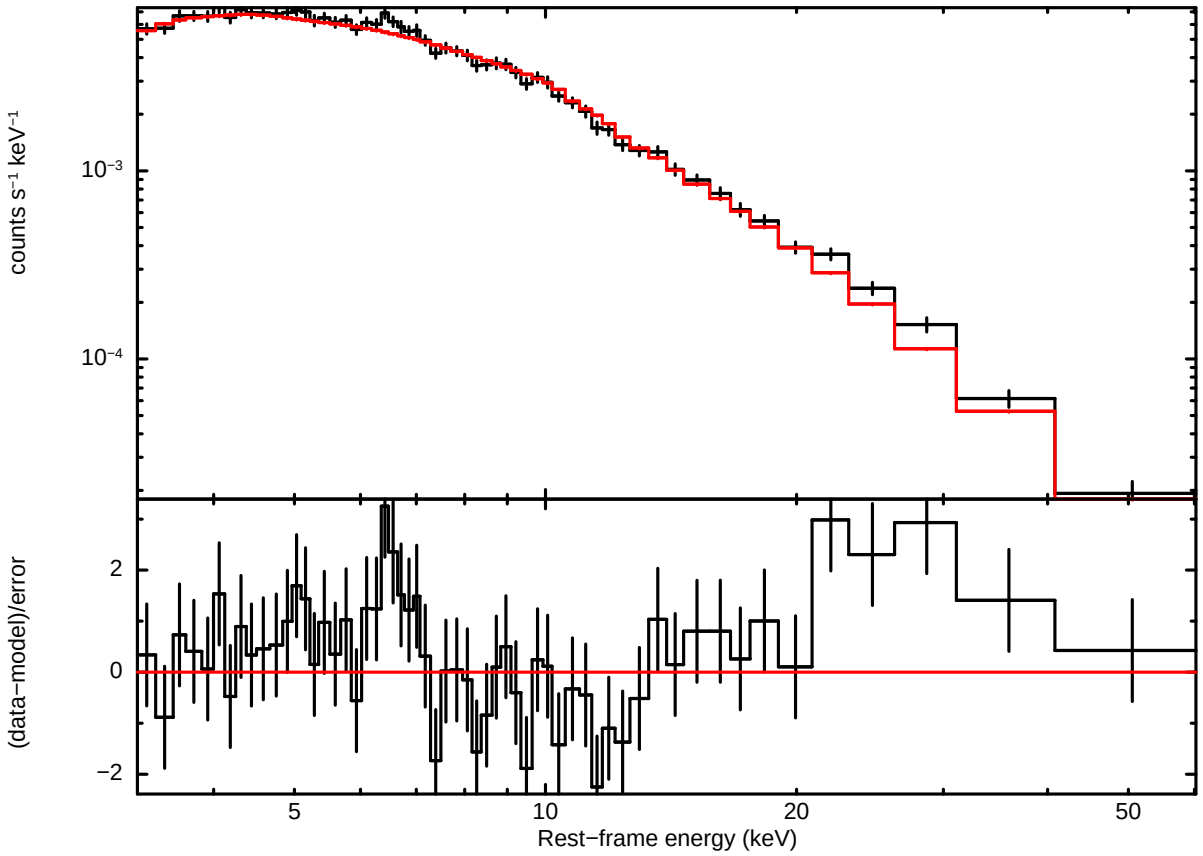

Figure 4.2. The comparison of the data (black) and power law model (red) is reported. An excess of photons is observed between 6.4 and 7 keV suggesting the presence of emission features ascribable to neutral and/or possibly ionised iron. Also a bump of unmodelled photons is found above $\sim$ 10 keV. For plotting purposes the *FPMA* and *FPMB* spectra of all the epochs and their residuals in terms of errors with respect to the model are displayed grouped (*setplot group* in *Xspec*).

formally detected in three out of four observations, but its flux is consistent with being constant between all the pointings. The average Fe kα flux is 5.5$\pm$3.8 $\times 10^{-6}$ ph cm^{-2} s^{-1}, with a corresponding equivalent width of 100$\pm$10 eV. We also tested for the presence of a broad component of the line in our spectra. However, this additional broad feature is not required in terms of statistics, with a negligible $\Delta\chi^2$ improvement, and its normalisation is consistent with being zero in all the observations.

The primary photon index is found to be constant among the different pointings, while weak variability is observed in the primary continuum normalisation. The unmodelled photons above 10 keV in Fig. 4.2 indicate that part of the emission of HE 0436-4717 is due to reflection of the primary continuum, thus we replace in our best-fit model the power law with *pexrav* (Magdziarz & Zdziarski 1995). In this new model

(*const*×*phabs*×*(pexrav+zgauss)*), *pexrav* reproduces the power-law-like primary continuum with its associated reflected component, while the Gaussian line accounts for the Fe Kα. In the fitting procedure the iron abundance is frozen to solar value for all the observations, while the photon index, the normalisation and the reflection fraction are free to vary between the pointings. We also let the high energy cut-off free to vary and untied among the observations. The adoption of this model yields a best-fit of χ^2=404 for 440 d.o.f., for which we report the best-fit values in Table 4.2, second panel.

Allowing for a reflection hump, we find that the photon index is compatible with being constant, and its best-fit values appear steeper than those previously obtained using a simple power law. Within the errors, the reflection fraction is constant between the pointings, and the *pexrav* normalisation exhibits modest variations. For the high energy cut-off, only lower limits are found. We further test the reflected Compton component using the following model: *const*×*phabs*×*(cutoffpl+pexrav)*. The cut-off power law (*cutoffpl*) models the primary continuum, while *pexrav* shapes the reflected component only. The photon index and high energy cut-off are tied between the components and free to vary. Both the primary and reflected component normalisations are free to vary and untied. This model yields a best fit of χ^2=406 for 447 d.o.f, and the best-fit parameters are equivalent within the errors with those in the second panel of Table 4.2. We therefore fit the *NuSTAR* data tying the normalisation of the reflected component between the observations. The obtained fit (χ^2=410 for 450 d.o.f.) is statistically equivalent to the previous one, thus a constant normalisation of the reflected component is found, $N_{refl}=1.5\pm0.5\times10^{-3}$ ph/keV/cm^2/s with a corresponding constant flux $F_{20-40keV}=2.6\times10^{-12}$ erg/cm^2/s.

4.1.4 Data analysis: Physical modelling

The narrow and constant Fe Kα suggests that the origin of the reprocessed emission of HE 0436-4717 is far from the central BH. However, the geometrical configuration of the reflecting material is unknown. We then tested few models to account for different geometries. At first we tried to reproduce the data set adopting *pexmon* (Nandra et al. 2007). *Pexmon* combines *pexrav* with self-consistently generated Fe and Ni emission lines. To fit the data with *pexmon* we adopt the same procedure used for testing *pexrav*, thus we let free to vary and untied between the observations the photon index, the high energy cut-off, the reflection fraction, and the normalisation. Moreover, we fit the iron abundance A_{Fe} tying it between the pointings. The obtained best fit (χ^2= 407 for 444 d.o.f.) is statistically equivalent to the one in which *pexrav* was adopted, and the best-fit values of the parameters are compatible with each other (see Table 4.2, third panel). Adopting this model that self-consistently accounts for the fluorescence emission lines, we estimate the iron abundance to be $A_{Fe}=1.1^{+1.3}_{-0.3}$.

As an additional test, we have fitted our data set adopting *MYTORUS* (Yaqoob

2012). Through this model we further test the origin of the HE 0436-4717 reprocessed emission. In fact, *MYTORUS* accounts for a narrow Fe Kα and its accompanying reflection component by a Compton-thick toroidal material. We assumed a power-law-like illuminating continuum. Both the Γ and normalisation of the primary emission are free to vary and untied between the pointings. At first, we used the *MYTORUS* tables, accounting for the emission lines and scattering being untied and free to vary. However, the two table normalisations were consistent with each other. Thus we kept them tied together accordingly with the coupled reprocessor solution (Yaqoob 2012). Then, for each observation, we tied the underlying continuum Γ with the one characterising the reflected emission. Finally, we performed the fit, tying the normalisations of the primary continuum and reprocessed component and adding a further constant to account for their mutual weights. This procedure leads to a best fit characterized by χ^2=404 for 444 d.o.f, and in the fourth panel of Table 4.2 we report the corresponding best-fit values. We notice that the constant accounting for the relative normalisations of the primary emission and reflected one ($N_{myTorus}/N_{po}$) has fairly high values. These may suggest a larger covering factor with respect to the default one in *MYTORUS*. However, the interpretation of this constant is not trivial since it embodies different degenerate information about the chemical abundances and the covering factor itself (see Yaqoob 2012). Moreover, from the fit, only lower limits are obtained for the column density of the reflectors (1.6-2.4 $\times 10^{24}$ cm^{-2}).

Finally we tested *Xillver* (García & Kallman 2010; García et al. 2013), a model that reproduces the primary continuum and reflection off an accretion disc. *Xillver* assumes a cut-off power law for the primary emission, and it is commonly used to model reflection from distant material (e.g. Parker et al. 2017). We performed the fit letting free to vary the photon index, the reflection fraction, the normalisation, and the high energy cut-off for each observation. The iron abundance was free to vary but tied between the observations. At first we also fitted the ionisation parameter ξ, but since no improvements were found during the fitting procedure, we fixed its value to the lowest allowed by the model (logξ =0), close to neutral matter. The obtained best-fit parameters can be found in the fifth panel of Table 4.2, while the best-fit model for all the observations is shown in Fig. 4.3.

As found when adopting pexmon, the photon index is compatible with being constant, and, similarly, the iron abundance is found to be $A_{Fe}=1.2^{+1.4}_{-0.4}$. Besides a marginally variable underlying continuum, most of the components have a constant behaviour, thus we try to fit the data tying the photon index and the high energy cut-off between the various pointings. The reflection fraction and normalisation of the primary continuum are untied and free to vary between the observations. Following this procedure we obtained a best fit statistically equivalent with the one just discussed (χ^2=406 for 449 d.o.f. versus χ^2=404 for 443 d.o.f). The best-fit value for the photon index is $\Gamma=2.01\pm0.08$, while the obtained lower limit for the high energy cut-off is E_{cut} >280 keV. We therefore

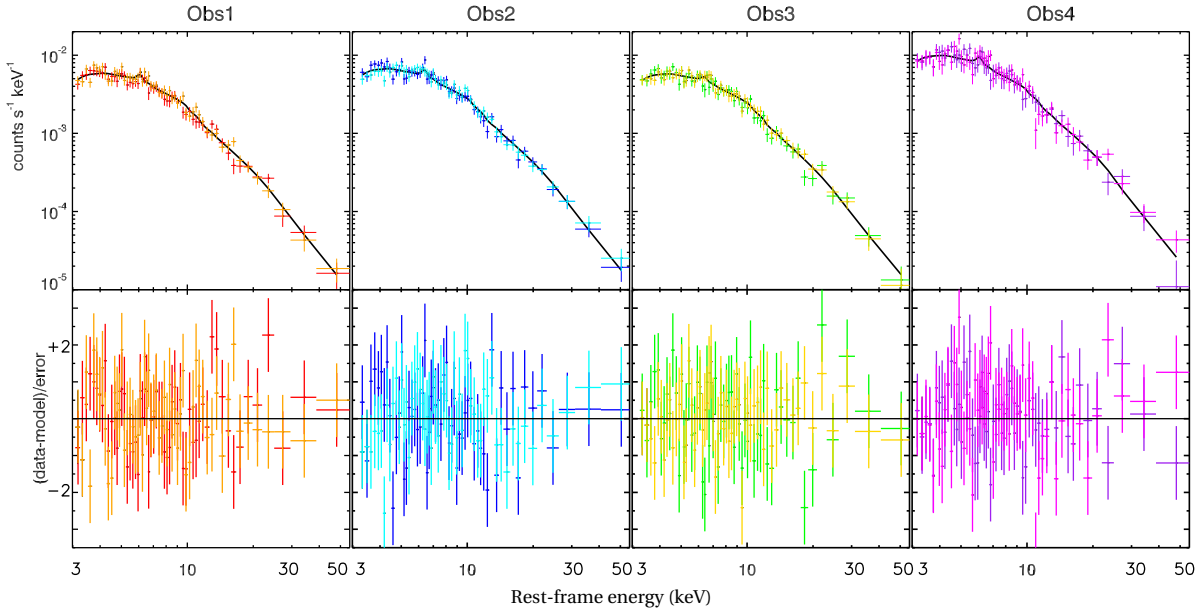

Figure 4.3. Best-fit model *const*×*phabs*×*xillver* to the *NuSTAR* data is displayed for each observation. In the x-axis the energy is reported in keV and different colours are used to represent the *NuSTAR* module A and B spectra.

tried to better constrain the reflection fraction R, letting its value free to vary but tied between the observations. This procedure does not change the quality of the fit, but allows us to estimate the averaged value of the reflection fraction to be R=$0.7^{+0.2}_{-0.3}$. We then compute the contour plots for the parameters that are shown in Fig. 4.17.

Comptonisation is widely accepted to be the origin of the X-ray emission in AGN, therefore, substituting *xillver* with *xillvercp* (García & Kallman 2010; García et al. 2013), we tried to investigate the physical properties of the HE0436-4717 hot corona. This model differs from *xillver* because the primary continuum is shaped by thermal Comptonisation through the *nthcomp* model (Zdziarski et al. 1996). We perform the fit, tying the parameters between the observations, and we let free to vary only the temperature of the hot electrons. In terms of statistics, this fit (χ^2= for 405 d.o.f. 443) is compatible with the previous one in which *xillver* was adopted. For the sake of simplicity, in the panel referring to *xillver* in Table 4.2 we only report the obtained values for the hot electron temperature kT_e, as the other parameters are compatible with those already obtained using *xillver* within error bars. Furthermore, assuming a spherical geometry and using the *nthcomp* internal routine for the Thomson optical depth τ_e, we obtained upper limits for the coronal optical depth of He 0437-4717. These upper limits are reported in the fifth panel of Table 4.2. Moreover, we fit again the data tying the kT_e between the observations (χ^2= for 408 d.o.f. 452). This procedure leads to a lower limit for the corona temperature: kT_e>65 KeV. Again, under the assumption of a spherical Comptonising

medium, we computed a corresponding optical depth $\tau_e < 1.3$. Even though the analysed *NuSTAR* data did not require any relativistic component, this feature seems to be needed by the *XMM-Newton* data. Thus we have tested for the presence of a broader and relativistic component adding *relxill* to our best-fit model. Since the parameters are not well constrained, we set *relxill* according to the values reported by Bonson et al. (2015): Γ=2.14, R_{in}=1.8 r_g, A_{Fe}=0.36, inclination θ=43°. However, adding *relxill* yields a fit of χ^2=406 for 445 d.o.f., thus, on a statistical basis, these *NuSTAR* data do not require a relativistic component.

4.1.5 Discussion

The *NuSTAR* high sensitivity above 10 keV makes it suitable for investigating the physical conditions of AGN coronae. However, the lack of sufficient statistics limits comparative studies concerning the AGN coronal region. In fact, at present, the largest sample of these sources analysed taking advantage of *NuSTAR* data counts a few AGN only (<20) (e.g. Fabian et al. 2017; Tortosa et al. 2018). In this framework, the analysis of these multi-epoch *NuSTAR* observations adds information about the coronal parameter of this particular Seyfert galaxy, enlarging at the same time the number of AGN analysed thanks to *NuSTAR*.

The 3-79 keV HE 0436-4717 *NuSTAR* spectra are found to be consistent with being the superposition of two spectral components, a persistent and weakly variable primary emission and a narrow iron Kα with its associated distant reflection continuum. The primary continuum can be described by a power law with photon index Γ=2.01±0.08 and a lower limit E_c>280 keV for the cut-off energy. Moreover, a neutral Fe Kα emission line is present in three out of observations and it is found to be narrow. The reflected component is found to be compatible with being constant in flux, and the high energy emission of HE 0436-4717 is in agreement with a scenario in which this reprocessed emission arises from neutral material far from the central engine. Therefore, we have tested a few models that account for different geometrical scenarios. Disc reflection provides a good fit to the data, and, similarly, reprocessed emission by toroidal matter with $N_H \gtrsim 2\times10^{24}$ cm^{-2} is statistically supported.

The *NuSTAR* data analysed in this work do not require a broad line, consistent with Wang et al. (1998) who found the line to be narrow and likely due to distant reflection. However, *XMM-Newton* data requires a broad component (Bonson et al. 2015). This discrepancy can be ascribed to the poorer spectral resolution of *NuSTAR* with respect to *XMM-Newton*, since part of the broad component flux might be absorbed by the narrower feature. Moreover, we are further limited in testing a complete blurred reflection scenario because any soft excess would occur outside the *NuSTAR* operating band.

Adopting different models, the source iron abundance is found within the errors compatible with being solar ($A_{\rm Fe}$=$1.2^{+1.4}_{-0.4}$). HE 0436-4717 shows modest flux variations within each observation while the average of the counts exhibits a more constant behaviour between the *NuSTAR* pointings. The largest flux variations are measured on timescales shorter than a day. Past flux measurements in the 2-10 keV band performed using *ASCA* and *XMM-Newton* data (Wang et al. 1998; Bonson et al. 2015, respectively) are compatible (3.3-4.6$\times10^{-12}$ erg/cm^2/s) with the flux observed during the *NuSTAR* pointings. We estimated the 2-10 keV luminosity to be $L_{2-10\ \rm keV}$=3$\pm$0.5$\times10^{43}$ erg/s. Adopting the proper bolometric correction from Marconi et al. (2004), we found the bolometric luminosity of HE 0436-4717 to be $L_{\rm bol}$=7$\times10^{44}$ erg/s. Considering a $M_{\rm BH}$=5.9$\times10^7 M_\odot$ (Grupe et al. 2010), HE 0436-4717 has an Eddington ratio of $L/L_{\rm Edd} \sim 0.09$.

This spectral analysis reveals that HE 0436-4717 did not experience any spectral variation, and this is compatible with what was found in previous works. In fact, Wang et al. (1998) measured a photon index of Γ=2.15$\pm$0.04, while Bonson et al. (2015) obtained Γ=2.12$\pm$0.02. Our *NuSTAR* measurements are compatible with previous estimates, thus no evidence for long-term spectral variability is found.

The adoption of realistic models including Comptonisation allowed us to study the coronal physics of different AGN (e.g. Petrucci et al. 2013b; Ursini et al. 2018), thus we included in our analysis *nthcomp* to investigate the coronal properties of HE 0436-4717. Accounting for Comptonisation and tying the electrons temperature between the various pointings, a lower limit for the coronal temperature is found: kT_e >65 keV. From this value, we derived an upper limit for the electron optical depth of τ_e <1.3 . Our values for the τ_e and kT_e are in agreement with what is expected for an optically thin and hot medium responsible for the AGN hard X-ray emission. Tortosa et al. (2018) present results on the hot corona parameters of 19 AGN measured with NuSTAR and, in particular, the authors discuss various relations between phenomenological parameters and physical ones. The HE 0436-4717 τ_e and kT_e values are in perfect agreement with the strong anti-correlation they found for the optical depth and the coronal temperature of the 19 Seyfert galaxies.

Moreover, the estimated temperature kT_e can be used to investigate how HE 0436-4717 behaves on the compactness-temperature diagram (Fabian et al. 2015, 2017, and references therein). These two parameters are defined as: Θ_e=kT_e/m_ec^2 and l=$\frac{L}{R}\times\sigma_T/m_ec^3$. The first equation accounts for the coronal electron temperature normalised by the rest-frame energy of the electrons, while the second one is used to define the dimensionless compactness parameter (Fabian et al. 2015). In this latter formula, L is the luminosity and R is the radius of coronal (assumed to be spherical). For HE 0436-4717, $\Theta_e > 0.13$ is obtained. Following Fabian et al. (2015), we computed the luminosity extrapolating its value to the 0.1-200 keV band, L=1.4$\times10^{44}$. Since R is not measured, we assume a value of 10 r_g. We then compute the compactness of HE 0436-4717 to be l=230 $(R_{10})^{-1}$, where R_{10} is just the ratio between the radius and 10 r_g. In the $\Theta_e - l$ diagram by Fabian

et al. (2015), HE 0436-4717 lies, as does the bulk of the sample analysed by the authors, below the forbidden runaway pair production line. This supports the theory that AGN coronae are hot and radiatively compact. The flux of the reflected component is found to be constant between the observations, and a corresponding averaged reflection fraction R=$0.7^{+0.2}_{-0.3}$ is obtained. This latter value is compatible with the bulk of the measurements commonly found for Seyfert galaxies (e.g. Perola et al. 2002; Ricci et al. 2017).

4.1.6 Summary

This work focuses on the spectral properties of the Seyfert galaxy HE 0436-4717, and it is based on the analysis of four serendipitous *NuSTAR* observations performed from December 2014 to December 2015. The main results of this analysis are:

- Modest flux variability is observed within the various *NuSTAR* observations on timescales of a few kilo seconds. The average count rate of each epoch in the 3-10 and 10-79 keV bands is only weakly variable. Moreover, we have quantified the source variability, computing the normalised excess variance for this source. We obtained an upper limit for this estimator, $\sigma_{\rm NXS}$ <0.05 . We then converted this value into a lower limit for the BH mass obtaining $M_{\rm BH}$ >$3\times10^6 M_\odot$, in agreement with the single epoch measure by Grupe et al. (2010).

- A power-law-like spectrum with a corresponding Γ=2.01±0.08 is found to phenomenologically describe the high energy emission of HE 0436-4717. Between the different observations, the photon index is consistent with being constant, and a lower limit $E_{\rm cut-off}$ >280 keV is obtained. We tested a few Comptonisation models, obtaining a lower limit of kT_e >65 keV for the hot corona temperature. This temperature allowed us to estimate the optical depth for the HE 0436-4717 hot corona τ_e <1.3 .

- A narrow and constant Fe Kα emission line is observed, while a broader component is not required by these data. Both the line and the associated Compton reflection component are in agreement with a scenario in which they arise from Compton-thick matter located far away from the central BH.

- To provide an exhaustive answer on the origin of the soft-excess and to further prove/disprove the rather extreme parameters in the model adopted by (Bonson et al. 2015), a simultaneous XMM-Newton-NuSTAR observation is required.

Table 4.2. Best-fit values of the parameters for all the models tested in this 3-79 keV band analysis. For each model we have accounted for the *FPMA/B* intercalibration constant and the Galactic hydrogen column.

Model: *POWER LAW*	Obs	Γ	N_{po} (10^{-3}) ph/keV/cm^2/s	$N_{Fe\ K\alpha}$ (10^{-6}) ph/cm^2/s	EW eV	$Flux_{3-10}$ (10^{-12}) erg/cm^2/s
χ^2= 432 for 448 d.o.f.	1	1.84 ± 0.05	1.1 ± 0.1	3.1 ± 2.5	70^{+80}_{-60}	$2.9^{+1.1}_{-1.0}$
	2	1.84 ± 0.04	1.3 ± 0.1	6.2 ± 3.0	130^{+70}_{-90}	$3.0^{+0.9}_{-1.4}$
	3	1.84 ± 0.05	1.1 ± 0.1	<4.1	<130	$2.5^{+1.0}_{-1.5}$
	4	1.87 ± 0.07	1.6 ± 0.2	7.2 ± 5.1	110^{+120}_{-110}	$3.9^{+1.0}_{-1.7}$

Model: *PEXRAV*	Obs	Γ	E_c keV	R_{frac}	N_{pexrav} (10^{-3}) ph/keV/cm^2/s	$N_{Fe\ K\alpha}$ (10^{-6}) ph/cm^2/s
χ^2= 404 for 440 d.o.f.	1	$2.07^{+0.06}_{-0.03}$	>100	$1.3^{+0.7}_{-0.7}$	$1.5^{+0.1}_{-0.1}$	2.2 ± 2.0
	2	$1.97^{+0.08}_{-0.03}$	>140	$0.6^{+0.5}_{-0.4}$	$1.6^{+0.2}_{-0.1}$	4.7 ± 2.4
	3	$2.08^{+0.07}_{-0.03}$	>130	$1.5^{+0.7}_{-0.8}$	$1.5^{+0.3}_{-0.2}$	<2.61
	4	$2.02^{+0.08}_{-0.12}$	>60	<1.2	$1.9^{+0.3}_{-0.1}$	7.2 ± 4.4

Model: *PEXMON*	Obs	Γ	E_c keV	R_{frac}	N_{pexmon} (10^{-3}) ph/keV/cm^2/s
χ^2=407 for 444 d.o.f.	1	$2.02^{+0.09}_{-0.09}$	>150	$0.7^{+0.4}_{-0.3}$	$1.4^{+0.2}_{-0.2}$
A_{Fe}=$1.1^{+1.3}_{-0.3}$	2	$2.02^{+0.08}_{-0.12}$	>105	$0.7^{+0.4}_{-0.3}$	$1.7^{+0.3}_{-0.2}$
	3	$1.97^{+0.08}_{-0.10}$	>130	$0.4^{+0.4}_{-0.3}$	$1.4^{+0.2}_{-0.2}$
	4	$2.08^{+0.13}_{-0.12}$	>95	$0.8^{+0.7}_{-0.5}$	$2.1^{+0.4}_{-0.4}$

Model: *MYTORUS*	Obs.	Γ	N_{po} (10^{-3}) ph/keV/cm^2/s	$N_{myTorus}/N_{po}$	N_H (10^{24}) cm^{-2}
χ^2= 404 for 444 d.o.f.	1	$2.05^{+0.10}_{-0.09}$	$1.5^{+0.2}_{-0.2}$	$1.8^{+0.7}_{-0.6}$	>1.6
	2	$1.96^{+0.06}_{-0.07}$	$1.6^{+0.2}_{-0.1}$	$1.6^{+0.6}_{-0.5}$	>2.4
	3	$1.99^{+0.9}_{-0.9}$	$1.4^{+0.6}_{-0.4}$	$1.2^{+0.6}_{-0.5}$	>1.8
	4	$2.08^{+0.12}_{-0.12}$	$2.1^{+0.6}_{-0.4}$	$2.3^{+1.1}_{-0.9}$	>2.6

Model: *XILLVER*	Obs.	Γ	E_c keV	R_{frac}	N_{xi} (10^{-5}) ph/keV/cm^2/s	kT_e keV	τ_e
χ^2= 404 for 443 d.o.f.	1	$1.98^{+0.13}_{-0.09}$	>140	$0.6^{+0.5}_{-0.3}$	$2.3^{+0.2}_{-0.4}$	>30	<2.4
A_{Fe}=$1.2^{+1.4}_{-0.4}$	2	$2.00^{+0.12}_{-0.09}$	>115	$0.7^{+0.4}_{-0.3}$	$2.9^{+0.2}_{-0.7}$	>30	<2.4
	3	$1.94^{+0.16}_{-0.14}$	>110	$0.4^{+0.4}_{-0.2}$	$2.5^{+0.2}_{-0.4}$	>20	<3.3
	4	$2.07^{+0.16}_{-0.16}$	>120	$0.8^{+0.8}_{-0.5}$	$3.0^{+0.4}_{-0.7}$	>30	<2.2

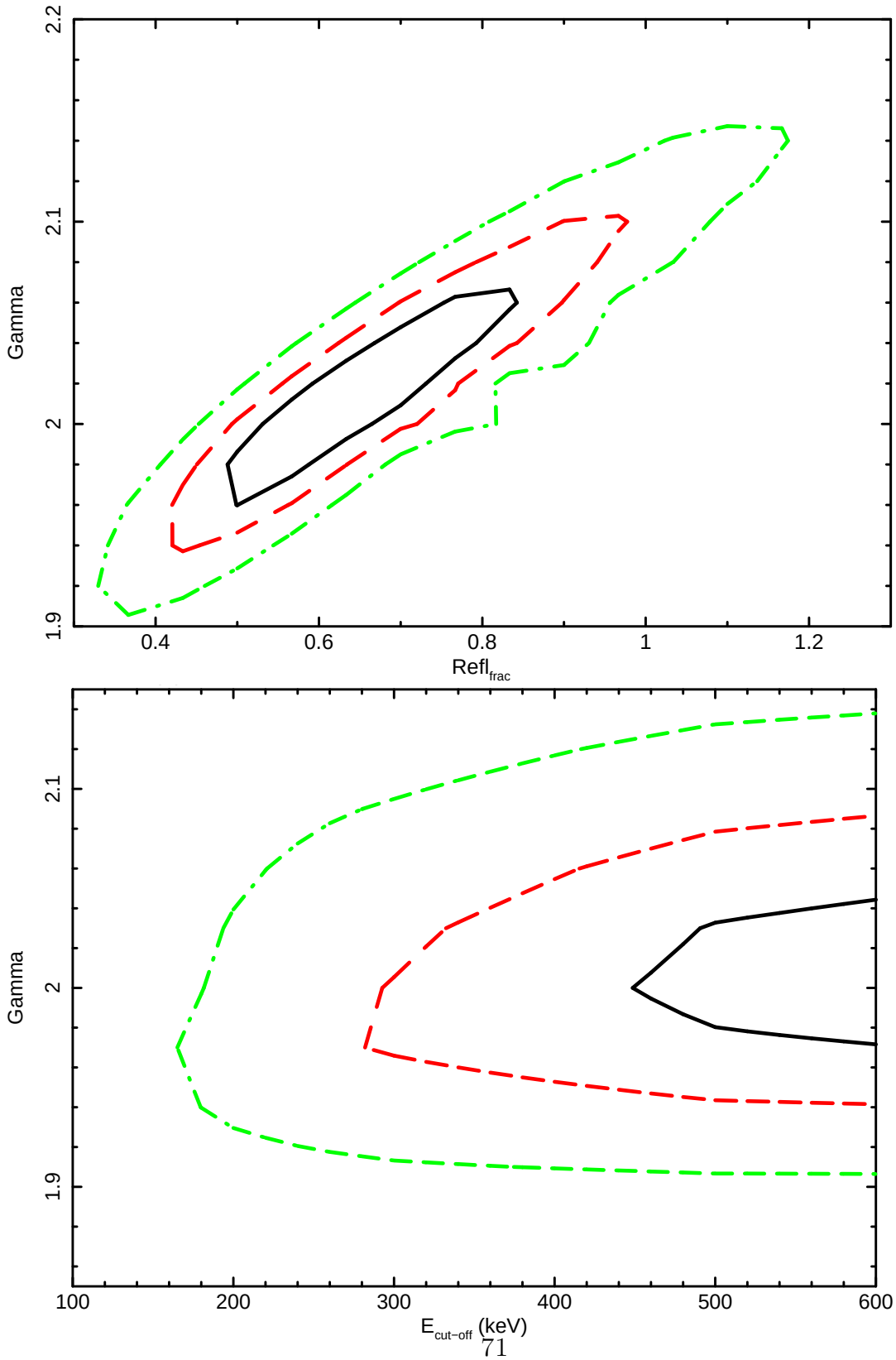

Figure 4.4. The 68%, 90% and 99% contours in black, red, green respectively computed adopting *const*×*phabs*×*xillver*. Top panel: The photon index and the reflection fraction are shown. Bottom panel: Contours for the photon index and the high energy cut-off.

4.2 NGC 7469: overview and the monitoring

The luminous source NGC 7496 has been selected for a multiwavelength campaign who involved different space based observatories, namely XMM-Newton, NuSTAR, the Hubble Space Telescope and Swift. The program, as proposed and accepted, was aimed to characterize in detail the matter outflow emerging from the innermost regions of NGC 7469. NGC 7469 is the best target to perform such investigations for the following reasons:

- it is a luminous AGN (L_{bol} $\sim 10^{45}$ erg/s) and it is one of the brightest active nucleus in the X-ray domain ($F_{0.3-10\ keV} = 4 - 5 \times 10^{-11}$ erg/s/cm^2).
- The source is characterized by a remarkable soft-excess.
- The emission of this source is characterized by prominent flux variability already on timescales as short as few kiloseconds.
- Luminosity variations of up to a factor of 2 are expected based on the Rossi X-ray Timing Explorer monitoring, so that the resulting spectral changes can be easily measured by XMM-Newton.
- At the time of the proposal, the source was only poorly observed in the X-rays.

Besides the main goal of the project the broadband multi-epoch campaign provides an excellent data set for testing and studying the emission properties of the source circumnuclear material around the central BH. Indeed, such deep X-ray and UV observations can be used for testing the Comptonisation origin of the high energy emission of this sources. On one side, the *NuSTAR* data allow to constrain the reflection component and the high energy cut-off, and this latter, in turn, gives direct access to the Comptonising plasma temperature. On the other one, *XMM-Newton* observations provide a great look on all aspects of Fe-K lines (narrow,relativistic). Moreover, thanks to the Optical Monitor (OM, Mason et al. 2001a) carried by *XMM-Newton* it is possible to constrain the broadband emission of NGC 7469 from the optical-UV domain paying particular attention on the origin of the NGC 7469 soft-excess), up to the higher energy accessible to *NuSTAR*.

The spectral analysis presented here is based on *XMM-Newton* (Jansen et al. 2001) and *NuSTAR* (Harrison et al. 2013) observations (see Table 4.3) of NGC 7469 belonging to the multiwavelength campaign first described by Behar et al. (2017). The two satellites observed the source simultaneously between June 12 and December 28, 2015. The seven observations are spaced by different time intervals, allowing us to study flux and spectral variations on different timescales, see Tab. 4.3. Using reverberation mapping, Peterson et al. (2014) found that NGC 7469 hosts a BH with a mass of $1.1 \pm 0.1 \times 10^7$ $M_\odot$ and an Eddington ratio of the order of

Table 4.3. For the 7 observations analysed in this work we report for each satellite the observation ID, start date, and net exposure time (ks).

Obs. satellites	Obs. ID	Start date	Net exp. (ks)
XMM-Newton	0760350201	2015-06-12	63
NuSTAR	60101001002	2015-06-12	21
XMM-Newton	0760350301	2015-11-24	59
NuSTAR	60101001004	2015-11-24	20
XMM-Newton	0760350401	2015-12-15	59
NuSTAR	60101001006	2015-12-15	22
XMM-Newton	0760350501	2015-12-23	62
NuSTAR	60101001008	2015-12-22	23
XMM-Newton	0760350601	2015-12-24	65
NuSTAR	60101001010	2015-12-25	21
XMM-Newton	0760350701	2015-12-26	67
NuSTAR	60101001012	2015-12-27	21
XMM-Newton	0760350801	2015-12-28	70
NuSTAR	60101001014	2015-12-28	23

0.3. In X-ray wavelengths, this Seyfert galaxy was first observed by the *Uhuru* satellite (Forman et al. 1978) in the seventies, and it was subsequently studied by many other observatories that found this source to have a complex X-ray emission. Since the *EXOSAT* observation, we know that its X-ray spectrum displays an excess in the soft band (Barr 1986). Other authors (Turner et al. 1991; Brandt et al. 1993; Guainazzi et al. 1994; Nandra et al. 1998, 2000; De Rosa et al. 2002) analysed this source using data obtained by *Einstein*, *ROSAT*, *ASCA*, *RXTE* and *BeppoSax*. NGC 7469 was also studied more recently: Petrucci et al. (2004) investigated the UV/X-ray variability, Scott et al. (2005) analysed its simultaneous X-ray, far-ultraviolet, and near-ultraviolet spectra using *Chandra*, *FUSE* and *STIS*, while Patrick et al. (2011) studied this source taking advantage of *Suzaku* observations. Previous *XMM-Newton* data were analysed in Blustin et al. (2003) and De Marco et al. (2009), while some results from the 2015 observational campaign have been presented in Behar et al. (2017) and Peretz et al. (2017).

4.2.1 Data extraction

XMM-Newton data were obtained using the EPIC cameras (Strüder et al. 2001a; Turner et al. 2001a) in the Small Window operating mode and they were processed

taking advantage of the *XMM-Newton* Science Analysis System[3] (*SAS*, Version 15.0.0). Because of its larger effective area with respect to the two MOS cameras, we only report the results for the PN instrument. We extract spectra from circular regions of 50 arcsec radius for the background, and 40 arcsec radius for the source. These regions are selected by an iterative process that maximizes the signal-to-noise ratio (S/N) (Piconcelli et al. 2004). All the spectra were rebinned in order to have at least 30 counts for each bin and not to oversample the spectral resolution by a factor greater than 3. *NuSTAR* data were reduced taking advantage of the standard pipeline (*nupipeline*) in the *NuSTAR* Data Analysis Software (nustardas release: nustardas_14Apr16_v1.6.0, part of the *heasoft* distribution[4]), adopting the latest calibration database. The *NuSTAR* observatory carries in its focal plane two modules A and B corresponding to the hard X-ray detectors FPMA and FPMB. Spectra and light curves were extracted for both modules using the standard tool *nuproducts*. A circular region with radius of ∼70 arcsec is used to extract the source counts while the background is obtained from a blank area with the same radius, close to the source. Similar to the *XMM-Newton* spectra, we binned *NuSTAR* spectra to have a S/N ratio greater than 5 in each spectral channel, and to avoid oversampling the instrumental resolution by a factor greater than 2.5. The spectra of the two modules are in good agreement with each other, the cross-normalization constant for FPMB with respect to FPMA in all the fits being unity within 1 per cent. An example of the regions adopted for extracting the source and background from *XMM-Newton* and *NuSTAR* observations are showed in Fig. 4.5.

4.2.2 Temporal analysis

We started investigating the NGC 7469 temporal properties computing the light curves for all the observations. We used the standard command *epiclccorr* for the *XMM-Newton* data to compute corrected for the background light curves in the 0.5-2 keV and 2-10 keV bands, while, we used the *nuproducts* pipeline to compute the *NuSTAR* light curves in the 10-80 keV band. The *XMM-Newton* and *NuSTAR* light curves of all the observations of our campaign are shown in Fig 4.6. The source shows a remarkable intra-observation flux variability (e.g. up to ∼60% in the sixth observation for the *XMM-Newton* in the 0.5-2 and 2-10 keV bands) and has significant flux variations on timescales of a few ks. On longer timescales, flux

[3] "Users Guide to the XMM-Newton Science Analysis System", Issue 13.0, 2017 (ESA: XMM-Newton SOC).

[4] NuSTARDAS software guide, Perri et al. (2013), https://heasarc.gsfc.nasa.gov/docs/nustar/analysis/nustar_swguide.pdf

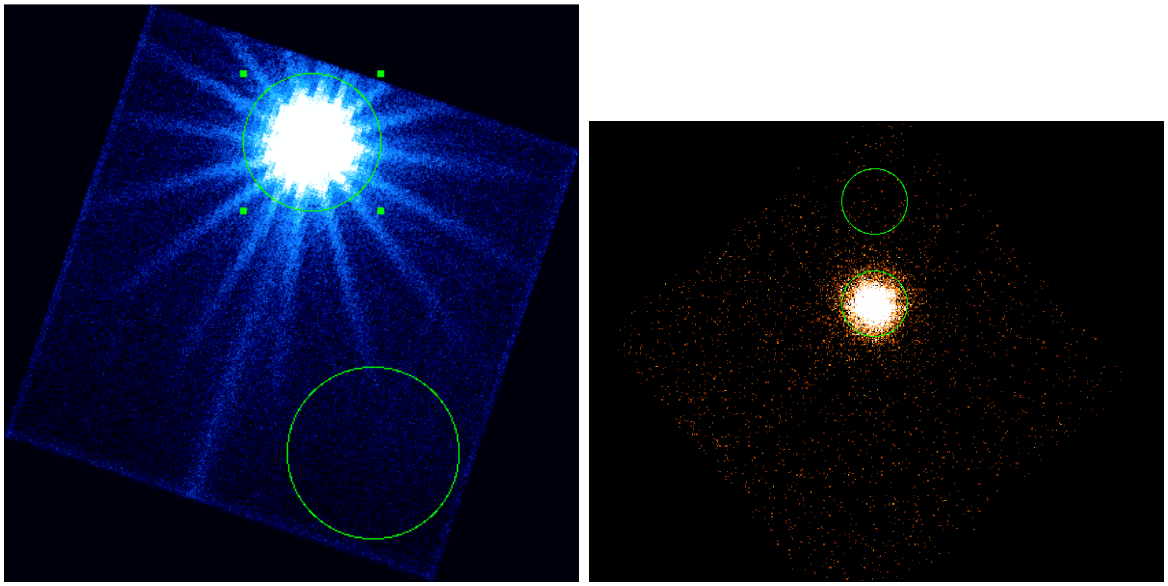

Figure 4.5. NGC 7469 as observed by XMM-Newton (left) and NuSTAR (right). Green circles delimit the extraction regions for the source and the background.

variability appears to be less significant. The mean counts for each of the seven observations is observed to be, on average, weakly variable (∼15%, ∼9%, and few per cent in the 0.5-2, 2-10, and 10-80 keV bands, respectively).

A convenient analysis tool for variability characterization is the so-called normalized excess variance (NXS). The NXS is defined as $\sigma^2_{rms} = \frac{1}{N\mu^2}\sum_{i=1}^{N}(X_i-\mu)^2-\sigma_i^2$, where μ is the unweighted count rate mean within the segment of the light curve, N is the number of the good time bins in that segment, and X_i represents the count rate with σ_i^2 as associated uncertainty. We computed the σ^2_{rms} in the 2-10 keV band for all the observations of our campaign in the 20 ks time bin (see Ponti et al. (2012) for more details), finding an average value σ^2_{rms}=0.0021±0.0005. A tight correlation between the X-ray variability of the source and its BH mass has been found by several authors (e.g. Nandra et al. 1997b; Vaughan et al. 2003b; McHardy et al. 2006; Ponti et al. 2012). In particular, adopting the relation among σ^2_{rms} and M_{BH} in Ponti et al. (2012), we are able to estimate the BH mass $M_{BH} = 1.1 \pm 0.1 \times 10^7$ $M_\odot$ for NGC 7469, in very good agreement with the reverberation mapping estimate by Peterson et al. (2014). The soft X-ray appears to be the most variable band, but hardness ratios do not display a large variation (however significant from a statistical point of view) both within and among the observations (∼8%), see Fig. 1.
Therefore, we decided to use the average spectra of each observation in the following spectral analysis.

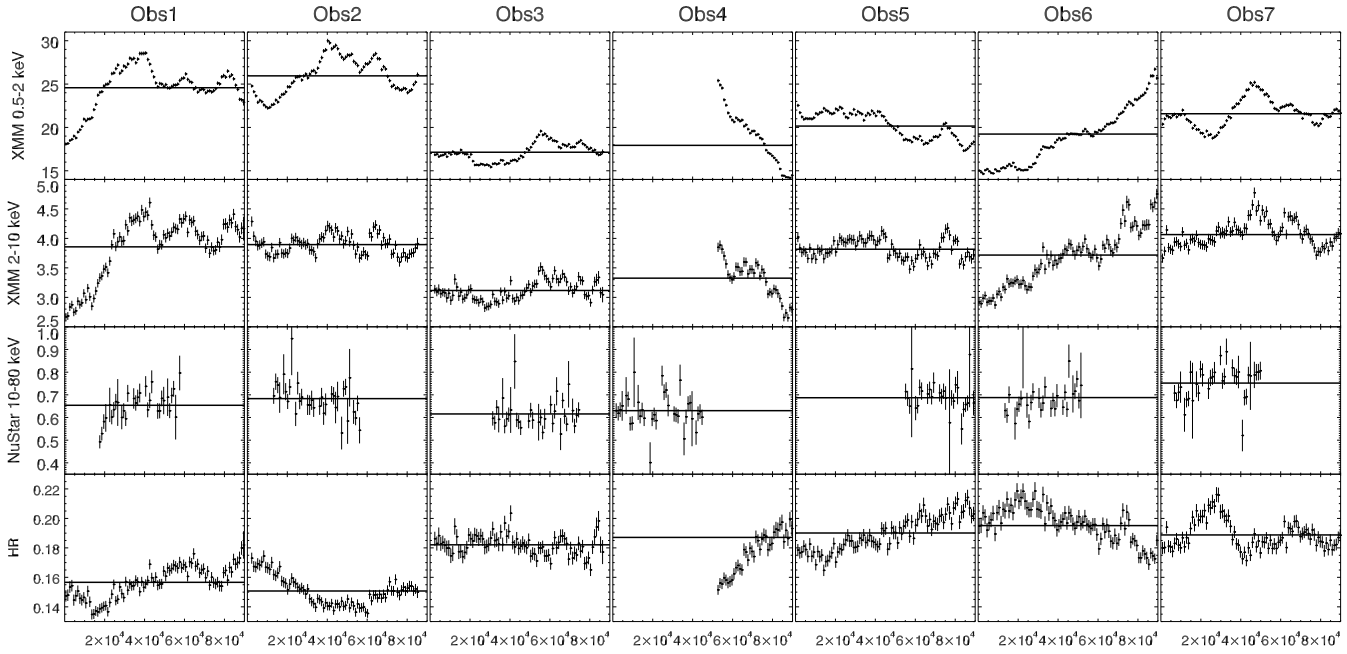

Figure 4.6. Light curves corresponding to the 7 simultaneous observations performed by *XMM-Newton* and *NuSTAR* for NGC 7469, in 3 different energy bands: 0.5-2 keV (first row), 2.0-10 keV (second row), and 10-80 keV (third row). Panels in the fourth row show the ratio between the soft 0.5-2 keV and hard 2.0-10 keV light curves. The axis units are sec and counts for the x-axis and y-axis, respectively. The solid line overlapping all the light curves in each sub-panel represents the average of the counts for the specific light curve.

4.2.3 *XMM-Newton*: Iron line energy band

We start our spectral analysis adopting a simple power law model for all our *XMM-Newton* data. This crude fit leaves strong residuals in the soft X-rays. This soft excess extends up to 4 keV and is shown in the top left panel in Fig. 4.10; this value is obtained by fitting the data above 4 keV and then plotting the best-fit model with the whole spectrum, i.e. extending the model into the soft X-ray band. Therefore, as a first step for our analysis, we decided to characterize the limited energy band 4-10 keV. The residuals in this energy band are dominated by strong emission features, readily identified with the Kα lines from neutral and H-like iron, and the possible presence of weaker contributions from neutral Nickel, Fe Kβ, and ionised iron (see Fig. 4.8).

We therefore adopted the following model to fit the 4-10 keV spectra:
zashift×*(pexrav+zgauss+zgauss)*.
The *pexrav* code (Magdziarz & Zdziarski 1995) is adopted to model the primary

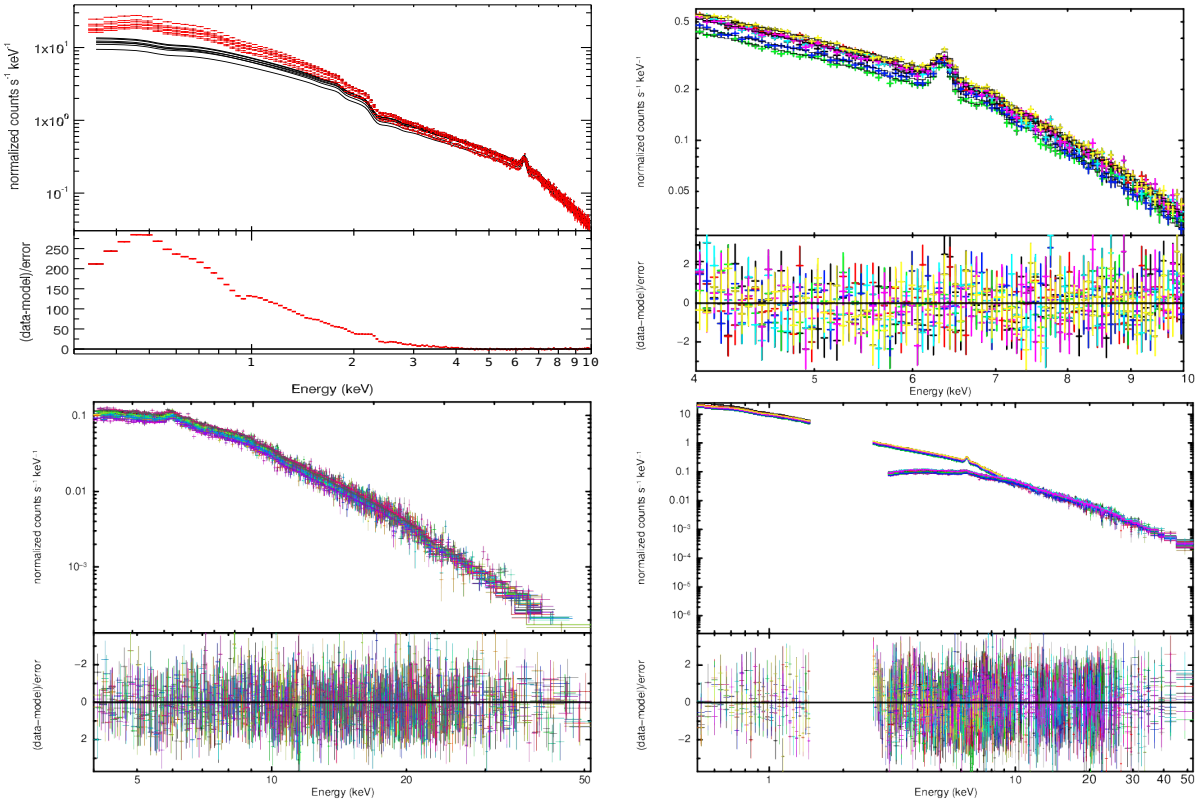

Figure 4.7. Top left panel: Seven *XMM-Newton* spectra shown in red; the best–fit model to the data above 4 keV shown in black. Bottom panel: The residuals of the 7 spectra that are grouped using in *Xspec* the command "setplot group". A secondary component clearly extends up to 4 keV. Top right plot: The best fit to the 7 *XMM-Newton* data and corresponding residuals shown with the basic model (i.e. *zashift×(pexrav+zgauss+zgauss)*), to which we added other Gaussian lines when weaker emission lines were found in the observation. Bottom left plot: Best fit for all *NuSTAR* spectra above 4 keV is shown; top sub-panel shows the best fit obtained adopting the model that employs *xillver*, while the bottom sub-panel refers to the corresponding residuals. In the last panel, the best fit (χ^2=3041 for 2765 d.o.f.) for the NGC 7469 *XMM-Newton* and *NuSTAR* spectra.

emission and any reflected component likely associated with the fluorescent emission line from neutral iron model by the first Gaussian line, while the second Gaussian line accounts for the Fe xxvi Lyα at 6.966 keV. The *zashift* component is used to correct the well-known *XMM-Newton* calibration issue affecting the EPIC pn (a detailed discussion on this topic can be found in Cappi et al. 2016). Within this discussion, a *zashift* correction of about -8×10^{-3} (corresponding to ~ 50 eV at 6.4 keV), will always be applied for all the *XMM-Newton* spectra. To model the data, we let free to vary among the observations the normalizations of both

the Fe Kα and the Fe xxvi Lyα lines, the reflection parameter and the photon index in *pexrav*, and its normalization. The iron abundance is also free to vary but tied among the different observations. This simple model leads us to a very good best fit in the 4-10 keV band ($\chi^2 = 586$ for 567 *d.o.f.*); see top right side panel Fig. 4.2.2.

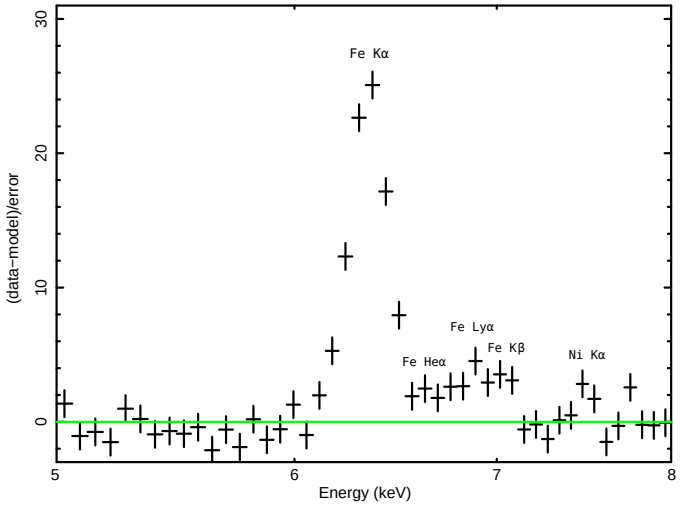

Figure 4.8. Residuals (in the observer frame) to a simple power law fit to the *XMM-Newton* spectra in the energy range 5-8 keV. Emission lines are clearly present. The residuals of the 7 spectra are grouped for plotting purposes.

The Fe Kα and Fe xxvi Lyα lines are both statistically significant ($>$ 99.9 per cent according to the F-test), and have a constant flux (3σ level) during the 7 observations of our campaign with average values of 3×10^{-5} and 4×10^{-6} ph cm^{-2} s^{-1}, respectively, corresponding to equivalent widths of $\sim$ 90 and $\sim$ 20 eV (see Fig.4.9 for the Fe Kα line); however De Marco et al. (2009) analysing previous *XMM-Newton* data found possible hints of variability in the Fe xxvi Lyα component. We found both the Fe Kα and Fe xxvi Lyα lines are narrow and their intrinsic line width is consistent with zero in all the observations. In particular, the line profiles do not show any evidence for the relativistic effects (see Fig. 4.8) expected to occur in the innermost regions of the accretion disc.

The residuals in Fig. 4.8 suggest the presence of the Fe xxv Heα, Fe Kβ, and the Ni Kα emission lines expected at 6.64-6.7, 7.06 and 7.47 keV, respectively, so we tried to fit these lines adding three further Gaussian lines to our best-fit model. However, the inclusion of these lines does not improve the χ^2 of the fit significantly. In fact, these three lines are very weak: the Fe Kβ flux is only an upper limit in all the spectra, the nickel line is a detection only in two observations with an average flux of $\sim 4.6 \times 10^{-6}$ ph cm^{-2} s^{-1}, and Fe xxv Heα is detected just in three observations

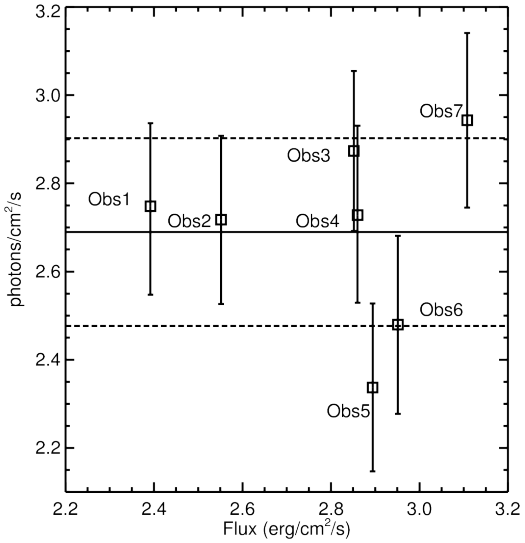

Figure 4.9. Fe Kα line flux vs. 2-10 continuum flux for the 7 *XMM-Newton* observations. The average line flux is shown together with the standard deviation (dashed lines).

with an average flux $\sim 4.0 \times 10^{-6}$ ph cm^{-2}. Indeed, none of these lines is more significant than 98 per cent, according to the F-test. The best-fit normalizations, or their upper limits, are reported in Table 4.4 for all the emission lines discussed in this section.

4.2.4 *NuSTAR*: The 4-80 keV spectra

Our preliminary analysis on the 4-10 keV *XMM-Newton* data shows a non-variable and narrow neutral iron line, likely produced by Compton-thick gas far from the central SMBH. For the *NuSTAR* data we adopted the self-consistent model *xillver* (García & Kallman 2010; García et al. 2013) to fit both the neutral iron line and the associated reflection continuum; we use *xillver* with its ionisation parameter fixed to zero. A Gaussian emission line is included to model the observed emission line at 6.966 keV and a second Gaussian line is used for the Fe xxv Heα lines. Strong soft-excess features also appear in *NuSTAR* spectra; thus, similar to what we already performed for *XMM-Newton*, we preliminary cut *NuSTAR* spectra below 4 keV. The reflection fraction, the high energy cut-off, normalizations, and the inter-calibration constant are free to vary, while the iron abundance is free to vary but tied among the observations. Following this approach, we obtained the best fit to the data ($\chi^2 = 1762$ for 1665 d.o.f.), and this best fit is plotted the bottom

Table 4.4. Best-fit normalizations for the emission lines observed in the *XMM-Newton* observations. The normalizations are in units of 10^{-6} ph cm^{-2}.

Obs	Fe Kα	Fe xxvi Lyα	Fe xxv Heα	Fe Kβ	Ni Kα
1	$28.7^{+1.8}_{-1.8}$	$4.3^{+1.6}_{-1.7}$	<3.12	<5.2	<3.3
2	$24.7^{+2.0}_{-2.0}$	$3.5^{+2.0}_{-2.0}$	<1.7	<6.3	$4.3^{+2.8}_{-3.0}$
3	$27.4^{+2.0}_{-1.9}$	$6.1^{+2.0}_{-1.7}$	<3.1	<6.9	<4.21
4	$27.1^{+1.9}_{-1.9}$	$2.6^{+1.9}_{-1.9}$	$4.2^{+2.8}_{-2.5}$	<4.4	$4.9^{+3.0}_{-3.0}$
5	$23.3^{+1.9}_{-1.9}$	$2.4^{+2.0}_{-2.0}$	$4.1^{+3.0}_{-2.7}$	<6.0	<4.9
6	$27.2^{+2.0}_{-1.9}$	$4.4^{+2.0}_{-2.0}$	<4.2	<6.9	<4.0
7	$29.4^{+2.0}_{-1.9}$	$4.7^{+2.0}_{-2.0}$	$3.9^{+2.8}_{-2.8}$	<5.5	<6.4

left panel of Fig. 4.2.2. The values of the best-fit parameters are reported in Table 4.5.

This best-fit model requires a super-solar iron abundance $A_{\rm Fe} = 2.8 \pm 0.6$. The photon index is consistent with being constant between the observations and has average value of 1.78±0.02 (see Fig. 4.10, top left panel, showing contour plots). A high energy cut-off is well constrained only in two observations, with values around 150 keV, and there are some indications of variability up to higher values in other observations (see same panel in Fig. 4.10). However, fitting the *NuSTAR* spectra tying the high energy cut-off among the seven observations yields a value of 170^{+60}_{-40} keV with a χ^2=1775 for 1671 d.o.f. very similar to the previous one in which the high energy cut-off was untied. Some hints of variability are also found for the reflection fraction in the range 0.3-0.6 (see Fig. 4.10, top right-hand plot, showing contour plots). The flux of the reflection component is consistent with being constant when the primary continuum varies, which is in agreement with an origin from distant matter; we obtained larger reflection components for lower flux states.

Although the iron Kα line does not present any broadening of its profile, we tested for the presence of a relativistic reflection component. Therefore, we added a further reflection component to the best-fit model, accounting for the relativistic effects arising in matter in the innermost regions of the accretion disc. We used *relxill* (e.g. García et al. 2014b; Dauser et al. 2016). The photon index and the high

Table 4.5. Values from the best-fit model for all the *NuSTAR* spectra analysed in the 4-78 keV band using the best-fit model *xillver+zgauss+zgauss* ($\chi^2 = 1762$ for 1665 d.o.f.). The 10-78 keV flux is in units of 10^{-11} erg/cm^2/s, and the iron abundance was let free to vary but tied among the observations.

Obs	Γ	$E_{cut}(keV)$	R	$\mathrm{Norm_{xi}}(10^{-4})$	$\mathrm{A^{\dagger}_{Fe}}$	$\mathrm{Flux_{10-78}}$
1	$1.82^{+0.06}_{-0.06}$	110^{+85}_{-35}	$0.50^{+0.14}_{-0.10}$	$1.56^{+0.10}_{-0.08}$	2.8±0.6	$7.4^{+0.4}_{-0.3}$
2	$1.77^{+0.06}_{-0.06}$	190^{+650}_{-90}	$0.32^{+0.11}_{-0.10}$	$1.84^{+0.07}_{-0.30}$	2.8±0.6	$8.2^{+0.7}_{-0.4}$
3	$1.73^{+0.07}_{-0.07}$	85^{+60}_{-20}	$0.62^{+0.16}_{-0.13}$	$1.23^{+0.09}_{-0.07}$	2.8±0.6	$6.6^{+0.4}_{-0.3}$
4	$1.83^{+0.03}_{-0.05}$	> 230	$0.33^{+0.08}_{-0.09}$	$2.14^{+0.02}_{-0.29}$	2.8±0.6	$7.6^{+0.6}_{-0.6}$
5	$1.78^{+0.05}_{-0.06}$	> 120	$0.34^{+0.10}_{-0.10}$	$1.89^{+0.30}_{-0.20}$	2.8±0.6	$8.1^{+0.6}_{-0.3}$
6	$1.75^{+0.06}_{-0.06}$	> 110	$0.37^{+0.11}_{-0.10}$	$1.75^{+0.30}_{-0.19}$	2.8±0.6	$7.8^{+0.8}_{-0.6}$
7	$1.78^{+0.05}_{-0.05}$	195^{+420}_{-80}	$0.35^{+0.10}_{-0.09}$	$1.98^{+0.30}_{-0.16}$	2.8±0.6	$8.9^{+0.6}_{-0.4}$

energy cut-off are tied between *relxill* and *xillver*, while the *relxill* ionisation parameter ξ and its normalization are free to vary in all the observations. No significant improvement in terms of $\chi^2/d.o.f.$ is found: $\Delta\chi^2 = 30$ for 18 d.o.f. less, corresponding to 80 per cent confidence level according to F-test. No relativistic reflection is required by the *NuSTAR* data: indeed, in all but three of the observations, the normalization of *relxill* is consistent with zero.

According to the standard scenario, hard X-rays are produced by Comptonisation, thus as a further investigation, we decided to model the *NuSTAR* spectra using a self-consistent Comptonisation model. In our model we substitute *xillver* with *xillvercp* (García et al. 2014b; Dauser et al. 2016). This different code accounts for the primary emission produced by *nthcomp* (Zdziarski et al. 1996) and a non-relativistic reflection. The parameters of this new model are treated as in the previous fit and the hot corona electron temperature is free to vary. The best fit obtained ($\chi^2 = 1768$ for 1658 d.o.f.) adopting *xillvercp* shows larger values for the photon index with respect to the previous best-fit model with *xillver* (on average 0.08). On the other hand, the parameters of the reflection component are in agreement with the values previously quoted. The best-fit values for the parameters of this fit are shown in Table 4.6 .

In the bottom left panel of Fig. 4.10, the contour plots for the photon index and

Table 4.6. Values and errors for the best-fit parameters of all the *NuSTAR* spectra analysed in the 4-78 keV band adopting *xillvercp*. Optical depth estimates are obtained following Beloborodov (1999). The iron abundance is free to vary but tied among the observations.

Obs	$\Gamma_{\rm hard}$	$kT_{\rm hc}(keV)$	R	$\tau_{\rm hc}$	$\rm Norm_{xicp}$ (10^{-4})	$\rm A^{\dagger}_{Fe}$
1	$1.89^{+0.02}_{-0.02}$	20^{+15}_{-4}	$0.45^{+0.10}_{-0.10}$	$3.0^{+0.1}_{-0.1}$	$1.39^{+0.18}_{-0.11}$	2.4±0.4
2	$1.83^{+0.02}_{-0.01}$	> 21	$0.27^{+0.10}_{-0.09}$	> 3.1	$1.75^{+0.11}_{-0.30}$	2.4±0.4
3	$1.85^{+0.02}_{-0.02}$	22^{+16}_{-5}	$0.52^{+0.11}_{-0.11}$	$2.9^{+0.1}_{-0.1}$	$1.25^{+0.11}_{-0.09}$	2.4±0.4
4	$1.85^{+0.01}_{-0.02}$	> 20	$0.30^{+0.10}_{-0.11}$	> 3.3	$2.17^{+0.05}_{-0.30}$	2.4±0.4
5	$1.82^{+0.01}_{-0.02}$	> 20	$0.30^{+0.09}_{-0.09}$	> 3.2	$1.95^{+0.20}_{-0.19}$	2.4±0.4
6	$1.81^{+0.01}_{-0.02}$	> 26	$0.29^{+0.10}_{-0.09}$	> 2.8	$1.98^{+0.30}_{-0.18}$	2.4±0.4
7	$1.83^{+0.01}_{-0.01}$	37^{+140}_{-15}	$0.30^{+0.10}_{-0.10}$	$2.2^{+4.0}_{-0.1}$	$1.94^{+0.20}_{-0.17}$	2.4±0.4

hot electron temperature are reported. Weak variations in the photon index are observed, while the electron temperature has a more constant behaviour. To test the variability of the hot electron temperature, similar to what we already performed for the high energy cut-off, we fit the *NuSTAR* spectra tying the electron temperature among the observations of this campaign. This yielded a measure of kT=45^{+15}_{-12} keV corresponding to a best fit ($\chi^2 = 1773$ for 1664 d.o.f.) very similar to the previous value.

4.2.5 *XMM-Newton*+*NuSTAR*: broadband spectrum

As shown, (see also Fig.4.2.2, top left hand panel) the data below 4 keV are characterized by a strong soft-excess. In order to properly model the continuum emission associated with this excess, we first characterize any discrete emitting and absorbing feature expected in the 0.5-4 keV band. On one side, these are features that can be directly attributed to the detector systematic calibration uncertainties, i.e. issues on its quantum efficiency at the Si K-edge (1.84 keV), and on the mirrors effective area at the Au M-edge ($\sim$ 2.4 keV). To avoid these issues, we ignored the spectral bins in the energy range 1.7-2.6 keV (see e.g. Kaastra et al. 2011b; Di Gesu et al. 2015; Ursini et al. 2015; Cappi et al. 2016). We then included all the

emission and absorption features (e.g due to the warm absorbers) derived from the analysis of the *XMM-Newton RGS* spectra of our campaign by Behar et al. (2017). Since none of these components displayed significant variability during our campaign (Behar et al. 2017; Peretz et al. 2017), we kep all their parameters fixed in our following fits to the values found from the *RGS* data (see Behar et al. 2017, for a detailed description of all the components). Some line-like features still remained in the *pn* spectra, and even if very weak, they result significant in terms of χ^2, as a consequence of the high number of counts in the soft band. Two narrow Gaussian lines untied and free to vary among the observations at ∼0.75 keV and ∼1 keV are enough to correct these residual narrow features (see also e.g. Kaastra et al. 2011b; Di Gesu et al. 2015; Ursini et al. 2015; Cappi et al. 2016).

At first, we model the soft X-ray emission with a phenomenological continuum model, such as a power law or a black body. However, in both cases we do not get an acceptable fit, obtaining χ^2=3542 for 2793 d.o.f. and χ^2=7430 for 2793 d.o.f. respectively. We then tried to reproduce the soft excess via two self-consistent models: blurred relativistic reflection arising from the innermost regions of the accretion disc, and Comptonisation from a warm corona.

There are a number of reasons (e.g. high BH spin and high ionisation parameters) that could lead to a weak broad iron line, but still a prominent relativistic reflection continuum, particularly in the soft X-rays. Indeed, Walton et al. (2013b), analysing *Suzaku* data, found a good fit modelling the NGC 7469 soft excess using a relativistic reflection model. Thus, even if our previous analysis failed to find significant signatures from relativistic effects in the hard X-ray band (and, notably, in the iron line profile), we tested for a relativistic origin for the soft excess in this source.

To perform this test, we again added *relxill* to the model, similar to what previously had been carried out in the *NuSTAR* data alone, leaving the ionisation parameter, coronal emissivity, BH spin, and the normalization free to vary among the observations, while the photon index and high energy cut-off are linked to those in *xillver*. We get parameters (ξ=2.4±0.2, i=45°, emissivity=4.8±0.3, a>0.996) consistent with those found by Walton et al. (2013b), but our fit is not statistically acceptable (χ^2=6036 for 2788 d.o.f.). This discrepancy is likely due to the much higher S/N of our data (especially in the soft X-rays) with respect to that used by Walton et al. (2013b).

We finally tried *nthcomp* (Zdziarski et al. 1996; Życki et al. 1999), accounting for a Comptonised continuum from a warm corona, as discussed by Petrucci et al. (2013b), Różańska et al. (2015), and Petrucci et al. (2018). For this model we untie and let free to vary the electron temperature and seed photons temperatures among the observations. For each observation, all the parameters among *XMM-Newton*

and *NuSTAR* are tied during the fit, however we need to allow for different values of photon index between *XMM-Newton* and *NuSTAR* in every observation. *XMM-Newton* slopes are harder than the *NuSTAR* derived slopes and this discrepancy, likely due to residual inter-calibration issues, is, on average, of the order of $\Delta\Gamma \sim 0.17$ (see e.g. Cappi et al. 2016, and Appendix A for more details). We report values of the photon index derived from *NuSTAR* data.

Following this procedure, we obtained a very good fit to the whole dataset, with χ^2=3041 for 2765 d.o.f. (see Fig. 4.2.2, bottom right side plot). The parameters of the hard X-ray components are fully compatible with those obtained from the fit of the data above 4 keV. We report the best fit values for the parameters describing the soft excess in Table 4.7. Most of the observed variability can be attributed to the *nthcomp* normalization that varies among all the observations. On the other hand, the electron temperature is found consistent with being constant, while for the photon index marginal variations are observed; see bottom right plot of Fig. 4.10. The measured warm corona temperature (kT_{wc}) is found to be, on average, 0.67 ± 0.03 KeV.

The obtained electron temperature can be used to estimate the optical depth τ for the warm corona. Following Beloborodov (1999), and using his equation 13 and the average values for the kT_{wc} and Γ reported in Tab. 5, we estimate the NGC 7469 warm corona $\tau_{\rm wc}$ to be 9.2 ± 0.2 .

4.2.6 Discussion

The broadband X-ray spectrum of NGC 7469 shows the presence of two main components, the primary power-law at high energies and a strong soft excess which starts dominating below $\sim$ 4 keV. This is commonly found in Seyfert galaxies (e.g. Piconcelli et al. 2005; Bianchi et al. 2009; Scott et al. 2012).

The high energy X-ray spectrum can be phenomenologically characterized by a cut-off power law with average spectral index $\Gamma = 1.78 \pm 0.02$ and high energy cut-off E_{cut}=170^{+60}_{-40} keV. These parameters are consistent with being constant among all the observations, with only some marginal evidence of variability of the cut-off energy. The latter value is compatible within the errors with measures based on *Suzaku* data ($E_{cut} = 119^{+65}_{-31}$ keV, Patrick et al. 2011) and *BeppoSAX* ($E_{cut} \sim 150$ keV; De Rosa et al. 2002). On the other hand, the rapid Γ variability reported by Nandra et al. (2000) could be due to the contamination from the soft excess, which could not be properly modelled in *RXTE* data. Indeed, it is clear from our monitoring that the soft X-ray energy part of the spectrum varies more than the high energy part, generating variations of the hardness ratio, which could mimic a photon index variability if the two spectral components are not properly modelled

Table 4.7. Best-fit parameters for the soft excess, where $kT_{\rm wc}$ is the electron temperature of the warm corona. The obtained seed photons temperature is ∼3 eV with no signature of any variability among the observations. The best-fit parameters for the hard X-ray model components are consistent, within the errors, with those obtained in the 4-78 keV band, and are not reported here for the sake of simplicity.

Obs	$\Gamma_{\rm soft}$	$kT_{\rm wc}(keV)$	$\tau_{\rm wc}$	Norm$_{nthcomp}$ (10^{-3})
1	$2.73^{+0.02}_{-0.02}$	$0.63^{+0.04}_{-0.03}$	$8.8^{+0.5}_{-0.5}$	$5.77^{+0.01}_{-0.01}$
2	$2.66^{+0.02}_{-0.02}$	$0.71^{+0.04}_{-0.03}$	$8.7^{+0.7}_{-0.6}$	$5.42^{+0.01}_{-0.01}$
3	$2.62^{+0.02}_{-0.02}$	$0.65^{+0.04}_{-0.03}$	$9.4^{+0.8}_{-0.6}$	$4.24^{+0.01}_{-0.01}$
4	$2.65^{+0.02}_{-0.02}$	$0.68^{+0.03}_{-0.03}$	$9.0^{+0.5}_{-0.4}$	$4.10^{+0.01}_{-0.01}$
5	$2.58^{+0.02}_{-0.02}$	$0.68^{+0.03}_{-0.05}$	$9.6^{+0.3}_{-0.7}$	$5.11^{+0.01}_{-0.01}$
6	$2.61^{+0.02}_{-0.02}$	$0.65^{+0.04}_{-0.03}$	$9.5^{+0.6}_{-0.6}$	$4.56^{+0.01}_{-0.01}$
7	$2.62^{+0.02}_{-0.02}$	$0.69^{+0.03}_{-0.03}$	$9.2^{+0.6}_{-0.6}$	$5.15^{+0.01}_{-0.01}$

separately (see e.g. Fig.4.6 and Fig. 4.2.2, top left panel.). However, the rapid Γ variability reported by Nandra et al. (2000) could also be due to a different state of NGC 7469 at the epoch of the *IUE/RXTE* campaign. In fact, a comparison between our data and those studied by the authors reveals that the source was in a more variable state compared to 2015.

The cut-off power law that reproduces the high energy spectrum of NGC 7469 can be naturally ascribed to Comptonisation of the accretion disc photons onto a corona of hot electrons. Adopting a self-consistent Comptonisation model, we recovered an average electron temperature of $kT_{\rm hc} = 45^{+15}_{-12}$ keV and, under the assumption of a spherical geometry, an optical depth $\tau_{hc} = 2.6 \pm 0.9$. These values are within ranges generally found in other Seyfert galaxies (e.g. Petrucci et al. 2013b, 2018; Tortosa et al. 2018) and are consistent with being constant among the observations of our monitoring campaign, which is in agreement with what found with phenomenological models. Interestingly, the coronal parameters measured in NGC 7469 lie along the $kT_e - \tau$ anti-correlation found by Tortosa et al. (2018) in a sample of Seyfert galaxies observed by *NuSTAR*. As discussed in their paper, this anti-correlation is suggestive of variations in the heating-cooling ratio of the corona, as a result of different disc-corona geometries and/or intrinsic disc emission. The

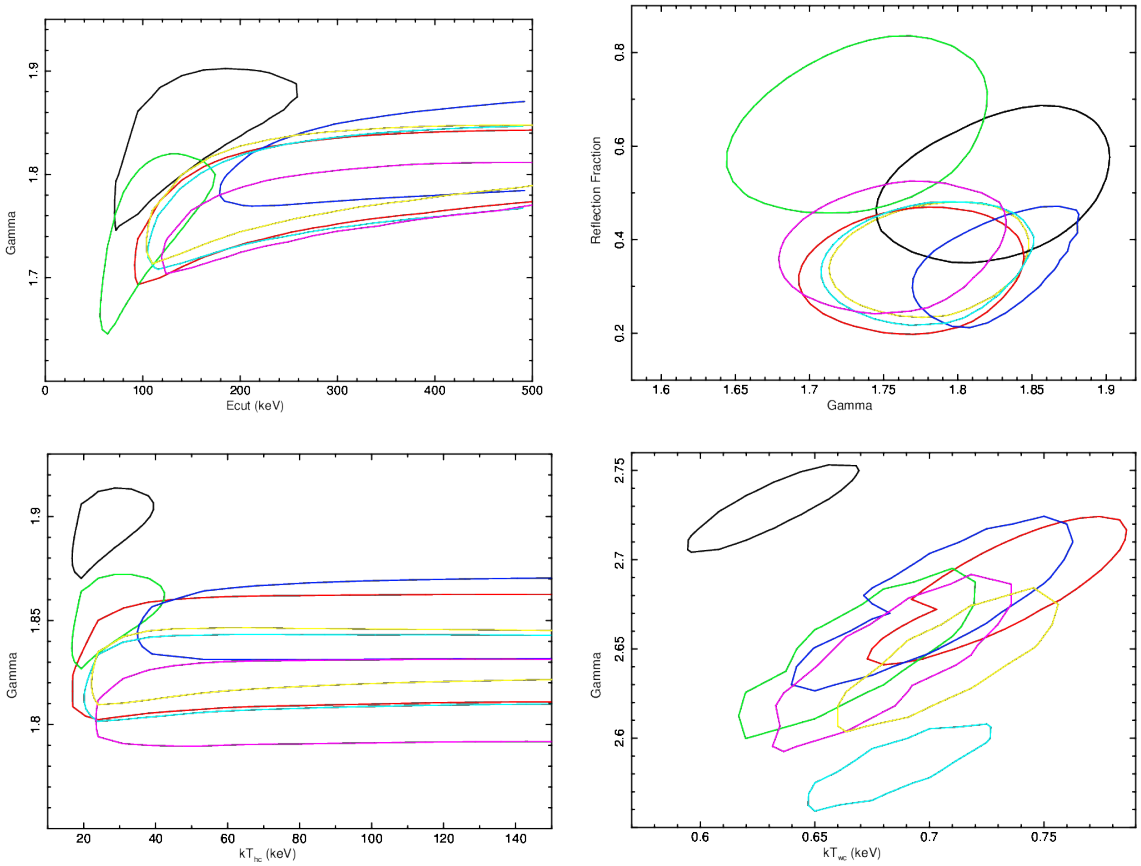

Figure 4.10. Contours for the high energy cut-off and photon index for all the *NuSTAR* observations in the top left panel. These contours account for the data analysed with *xillver* and above 4 keV. The best-fit parameters are shown in Table 4.5. The top right plot shows the best-fit values for the reflection fraction as a function of the photon index for the various observations. The contours are computed on the *NuSTAR* data above 4 keV adopting the model with *xillver*. The bottom left figure shows contour plots for the photon index and hot electron temperature computed on the *NuSTAR* data above 4 keV with *xillvercp*. The last plot shows the contour plots for the warm corona parameters for all the observations of our campaign.

soft excess cannot be satisfactorily modelled by simple phenomenological models, such as a steep power law of a black body, as often found in large samples of objects and/or low S/N spectra (Bianchi et al. 2009; Matt et al. 2014; Ursini et al. 2015). Moreover, a self-consistent model in terms of blurred relativistic reflection is also statistically unacceptable for reproducing this soft excess.

An additional Comptonised spectral component provides a good representation of the soft excess in this source. Assuming the same seed photons as for the hot

corona (i.e. those arising from the accretion disc), the temperature of the electron cloud responsible for the Comptonisation of the spectrum is on average $kT_{wc} = 0.67 \pm 0.03$ keV and the optical depth $\tau_{wc} = 9.2 \pm 0.2$, again with marginal evidence for variability among the observations of our campaign. These values are well in agreement with those found in a sample of Seyfert galaxies, within the framework of the so-called two-corona model (e.g. Petrucci et al. 2013b; Mehdipour et al. 2015b; Różańska et al. 2015; Petrucci et al. 2018). According to this model, the soft X-ray emission is produced by Comptonisation of the disc photons by a warm optically thick and extended medium (the warm corona), which is different from the compact, optically thin, and hot medium (the hot corona) that is responsible for the high energy emission. The ranges of the coronal values found for the warm corona in Seyfert galaxies (including NGC 7469) are consistent with the warm corona covering a large percentage of a quasi-passive accretion disc, whose intrinsic emission is negligible because most of the accretion power is released in the warm corona itself (Petrucci et al. 2018).

It is important to note that this two-corona scenario for NGC 7469 is also consistent with the observed optical-UV emission of this object by *HST* and *Swift* UVOT, as quantitatively shown by Mehdipour et al. (2018).
Along with the main continuum components discussed in the previous section, all the *XMM-Newton* and *NuSTAR* spectra of our campaign on NGC 7469 are characterized by the presence of a prominent emission line that was readily identified as a neutral Fe Kα fluorescent line. We find that this line is unresolved, has no evidence of any broadening and a flux compatible with being constant among all the observations, and with the past *XMM-Newton* observation in 2000 (Blustin et al. 2003). As expected if originating in Compton-thick matter, the iron line is associated with a reflection component whose flux is also consistent with being constant among the observations of our campaign. Consequently, its reflection fraction with respect to the primary continuum is slightly variable (R being in the range $0.3 - 0.6$), and higher values are measured when the primary flux is lower. Self-consistent reflection models agree with a scenario in which both the iron line and reflection component arise from Compton-thick matter far from the accretion disc, as commonly found in the X-ray spectra of Seyfert galaxies (e.g. Bianchi et al. 2009; Cappi et al. 2016; Tortosa et al. 2017).

As already noted, we find no evidence for relativistic effects in the iron line profile of NGC 7469. However, it has to be compared with the rich literature for this source. Guainazzi et al. (1994) found the Fe Kα line to be narrow in a 40 ks *ASCA* spectrum. In particular, the authors estimated the line-emitting region to be at several tens of Schwarzschild radii from the central engine of the galaxy. This result was confirmed by Nandra et al. (1997b) with the same dataset. Subsequently, Blustin et al. (2003) working on *XMM-Newton* data observed the Fe Kα line to

be narrow, and they modelled it with a single narrow Gaussian line. On the other hand, the analysis of *Bepposax* data by De Rosa et al. (2002), pointed to a relativistically broadened component of the line, together with an unresolved core. The presence of a relativistic component was confirmed, albeit marginally, by *Suzaku* (Patrick et al. 2011; Mantovani et al. 2016).

Although we cannot exclude the presence of a broad component of the iron line in past observations, we may speculate that the narrow core we observe in *XMM-Newton* data may be contaminated by other emission lines in spectra with lower spectral resolution and/or S/N ratio. Indeed, other emission features are clearly present in the *XMM-Newton* spectra, as shown in Fig. 4.8: a strong Fe xxvi Lyα emission line, which was significantly detected in all the observations of our campaign, and weaker emission lines such as Fe xxv Heα, neutral Fe Kβ and Ni Kα, which were not always significant. While the latter two emission lines are expected to accompany the neutral Fe Kα emission, and therefore share the same origin, the other lines must arise in a much more ionised plasma. Such lines are often observed both in Seyfert 1s and in Seyfert 2s and are likely produced in a Compton-thin, photoionised material illuminated by the nuclear continuum (e.g. Bianchi & Matt 2002; Bianchi et al. 2005; Costantini et al. 2010).

4.2.7 Conclusions

We report the spectral analysis of seven simultaneous *NuSTAR* and *XMM-Newton* observations of the Seyfert galaxy NGC 7469 performed from June 2015 to December 2015 in the context of a multiwavelength campaign. In the following we summarise the results of our analysis:

- NGC 7469 displayed a significant flux variability during this observational campaign with intra-observation variability at a timescales of few ks. We quantified this variability using the normalized excess variance estimator (e.g Ponti et al. 2012) σ^2_{rms}=0.0021±0.0005; this also allowed us to estimate the BH mass to be $M_{BH} = 1.1 \pm 0.1 \times 10^7\ M_{\odot}$, which is in agreement with the measure based on reverberation mapping (Peterson et al. 2014).
- The high energy spectrum can be phenomenologically characterized by a cut-off power law with average spectral index $\Gamma = 1.78 \pm 0.02$ and high energy cut-off E_{cut}=170^{+60}_{-40} keV. These parameters are consistent with being constant among all the observations, with only some marginal evidence of variability of the cutoff energy. Using a realistic Comptonisation model, the derived coronal parameters are $kT_{\rm hc} = 45^{+15}_{-12}$ keV and $\tau_{\rm hc} = 2.6 \pm 0.9$ for a spherical geometry.

- A strong soft excess is observed in all the observations, extending up to 4 keV. The best description for this component is through another Comptonised spectrum that is produced by a warm corona with $kT_{\rm wc} = 0.67 \pm 0.03$ keV and $\tau_{\rm wc} = 9.2 \pm 0.2$, again with only marginal evidence for variability among the observations of our campaign. Indeed, most of the observed variability of the soft X-ray data may be simply ascribed to variations of the normalization of this component. The overall scenario is consistent with the so-called two-corona model (e.g. Petrucci et al. 2013b; Różańska et al. 2015; Petrucci et al. 2018), where most of the accretion power is released in a warm optically thick and extended medium instead of the accretion disc.
- A neutral Fe Kα emission line is present in all the observations. The line is found to be narrow, with no indications for relativistic broadening, and consistent with being constant. An accompanying Compton reflection component is also found to be constant among the observations, which is in agreement with a scenario in which both components arise from Compton-thick matter located far away from the central BH. Weak neutral Fe Kβ and Ni Kα emission lines, which were only detected in some observations, have the same origin.
- A Fe xxvi Lyα emission line is significantly detected in all the observations of this campaign, and is likely to arise in a photoionised material illuminated by the central continuum, together with a weaker Fe xxv Heα emission line.

4.2.8 Γ discrepancy between *XMM-Newton* and *NuSTAR*

We reported in our analysis that our simultaneous *XMM-Newton* and *NuSTAR* data yielded photon indexes differing on average of ~ 0.17. In this appendix, we report our investigations concerning a plausible origin for this issue.

- *Different energy band*: The energetic range of *NuSTAR* is different with respect to that of *XMM-Newton*, thus we performed a simple analysis on the same observational band for both the satellites. For the whole sample of observations, we try to fit the spectra with a simple power law model in the common energy band 4-10 keV. The measurements for the photon indexes we obtained were still discrepant of the same amount.
- *Pile-up*: Our *XMM-Newton* spectra could, at least marginally, suffer from pile-up. According to the XMM-Newton hand guide[5], pile-up can affect pn

[5] *https://xmm-tools.cosmos.esa.int/external/xmm_user_support/documentation/uhb/epicmode.html*

observations performed in Small Window mode, when a total count rate of ~ 25 c/s is exceeded. Therefore, at least the first and second *XMM-Newton* observations could suffer from pile-up problems. We thus tried to extract the spectra from source annular regions, using different values for the annulus inner radius (from 50 up to 200 pixels). However, our tests show that any choice of the inner annular radius improves the $\Delta\Gamma$ discrepancy between the *XMM-Newton* and *NuSTAR* spectra.

– *Intrinsic variability*: *XMM-Newton* observations are longer with respect to those performed by *NuSTAR*, thus the difference in the two Γ could be due to the not truly simultaneity of the observations. To verify this hypothesis we extracted *XMM-Newton* spectra exactly in the same temporal range of those obtained using *NuSTAR*[6]. As in the previous cases, analysing these truly simultaneous spectra does not affect the $\Delta\Gamma$ discrepancy.

We therefore conclude that the most likely origin for the spectral index discrepancy has to be found in residual inter-calibration issues between *XMM-Newton* and *NuSTAR*, whose significativity may vary from observation to observation, and whose impact on the analysis is larger for high S/N data. We estimate that our results are not qualitatively affected by this issue, but a systematic uncertainty in the reported best-fit parameters should be taken into account.

[6]For the fourth observation the two satellites do not observe NGC 7469 simultaneously so that we cannot perform this test on it.

4.3 NGC 4593:

The multiwavelength campaign on NGC 4593 provides a further excellent data-set for testing the two-corona model. The source was observed simultaneously by *XMM-Newton* and *NuSTAR*, thus data extend from the optical-UV band up to the hard X-rays. A phenomenological spectral analysis of the campaign is reported in Ursini et al. (2016), hereafter P1. In P1 the source was found to be variable, both in flux and spectral shape, and the characteristic softer-when-brighter behaviour was observed. During the observational campaign, a strongly variable high energy cut-off was measured ($E_{cut-off}$ from 90^{+40}_{-20} keV to >700 keV), and the spectral index varied on timescales down to two days between 1.6 and 1.8. A prominent Fe Kα line was measured, best explained as the superposition of a narrow constant component and a broader component likely arising, respectively, from distant cold material and from cirmunuclear matter at about $\simeq$40 R_{grav} (R_{grav}=2GM/c^2). In agreement with past studies on this source, a warm absorber consistent with a two-phase ionised outflow was needed to reproduce the data set. From the analysis of *RGS* data, an additional photoionised component in emission was required to fit the data. Furthermore, NGC 4593 showed a remarkable and variable soft-excess during the monitoring, see Fig. 4.11. In this work, exploiting the high S/N data of the NGC 4593 observational campaign, we test Comptonisation, and, in particular, the two-corona model on this source. The standard cosmology ΛCDM with H_0=70 km/s/Mpc, Ω_m=0.27, Ω_λ=0.73, is adopted.

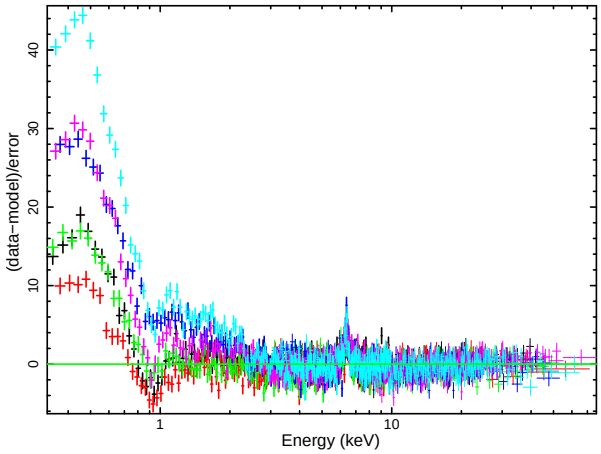

Figure 4.11. Residuals of the *XMM-Newton* and *NuSTAR* data to a power model fitted in the 4-10 keV energy range and extrapolated down to 0.3 keV. A prominent and variable soft-excess is clearly present below 2-3 keV. Black, red, green, blue, magenta and cyan colours refer to obs. 1a, obs. 1b, obs. 2, obs. 3, obs. 4 and obs. 5, respectively.

4.4 Data

Table 4.8. For each satellite the observation ID, the start date and the net exposure time are reported.

Obs. satellite	Obs. ID	Start date yyyy-mm-dd	Net exp. ks
XMM-Newton	0740920201	2014-12-29	16
NuSTAR	60001149002		22
XMM-Newton	0740920301	2014-12-31	17
NuSTAR	60001149004		22
XMM-Newton	0740920401	2015-01-02	17
NuSTAR	60001149006		21
XMM-Newton	0740920501	2015-01-04	15
NuSTAR	60001149008		23
XMM-Newton	0740920601	2015-01-06	21
NuSTAR	60001149010		21

The data set analysed here belongs to the joint *XMM-Newton* and *NuSTAR* monitoring program on NGC 4593, and consists of 5× ∼20 ks simultaneous observations. The monitoring covers the time period between December 29 2014 and January 06 2015, with consecutive pointings being about two days apart, (see Table 4.8).

XMM-Newton data of NGC 4593 were obtained with the EPIC cameras (Strüder et al. 2001b; Turner et al. 2001a) in *Small Window* mode with the medium filter applied. Because of its larger effective area with respect to the two MOS cameras, we only used the results for the PN instrument. Data are processed using the *XMM-Newton* Science Analysis System (*SAS*, Version 16.1.0). The choice of source extraction radius and the screening for high background time intervals are performed by an iterative process that maximizes the S/N, as in Piconcelli et al. (2004). The source radii span between 20 and 40 arcsec. The background is then extracted in a blank region close to the source using a region with a radius of 50 arcsec. We then rebbined all the spectra to have at least 30 counts for each bin, and without oversampling the instrumental energy resolution by a factor larger than 3. Moreover, for the present analysis we take advantage of data provided by the Optical Monitor, (*OM*, Mason et al. 2001a), on-board *XMM-Newton*. This instrument observed NGC 4593 with the filters U (3440 Å), UVW1 (2910 Å) , UVW2 (2120 Å) for all the pointings of the campaign. Data provided by the *OM* are extracted using the on-the-fly data processing and analysis tool *RISA*, the Remote Interface SAS Analysis. To convert the spectral points into convenient format to be analysed with *Xspec* (Arnaud 1996), we used the standard task *om2pha*.The light curves for the *OM* various filters are reported in Fig 4.12.

NuSTAR data were reduced taking advantage of the standard pipeline (*nupipeline*) in the *NuSTAR* Data Analysis Software (nustardas release: nustardas_14Apr16_v1.6.0, part of the *heasoft* distribution). The adopted calibration database is 20171204. High scientific products were then obtained using the standard *nuproducts* routine for both the hard X-ray detectors *FPMA/B* carried on the *NuSTAR* focal plane. A circular region with a radius of 75 arcsec is used to extract the source spectra, while the background is extracted from a blank area with the same radius, close to the source. We have then binned the *NuSTAR* spectra in order to have a S/N greater than 5 in each spectral channel, and to not oversample the resolution by a factor greater than 2.5.

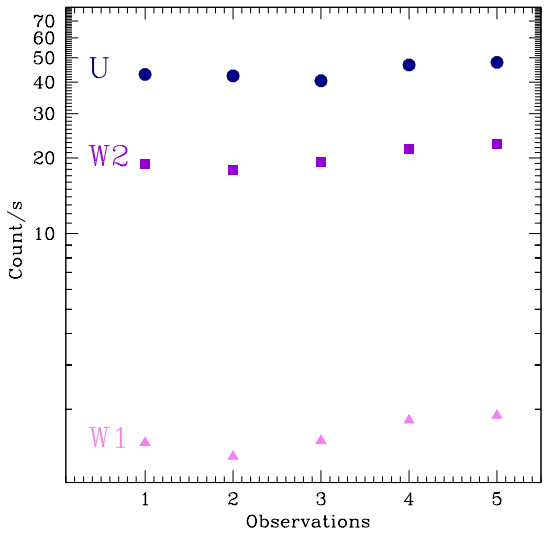

Figure 4.12. The *OM* rates for the available filters are shown.

Light curves and hardness ratios are discussed and shown in P1 to which we refer the reader. In all the observations of the campaign both spectral and flux variability can be observed. In particular, in the first pointing variability is very significant (see Fig. 4.13), thus we split observation one in two segments of 10 ks each. Then similarly to P1, we are left with six spectra for testing the two-corona model.

Finally, we notice that in other multiwavelength campaigns different photon index estimates were obtained from *XMM-Newton* and *NuSTAR* data in AGN and X-ray binaries (e.g. Cappi et al. 2016; Middei et al. 2018; Ponti et al. 2018). This issue, likely due to residual-intercalibration, leads to a variable $\Delta\Gamma_{XMM\text{-}NuSTAR}$, and, usually, Γ_{NuSTAR} is steeper with respect to $\Gamma_{XMM\text{-}Newton}$. The present data set is marginally affected by this intercalibration problem since only in observation two we find a discrepancy among the photon index estimates: $\Delta\Gamma_{XMM\text{-}NuSTAR}$=0.07. For the sake of simplicity, in Table 4.9 we quoted the photon index derived by *NuSTAR*. Furthermore, we notice that allowing for different values of photon index does not modify the quality of the fit for the present

data set.

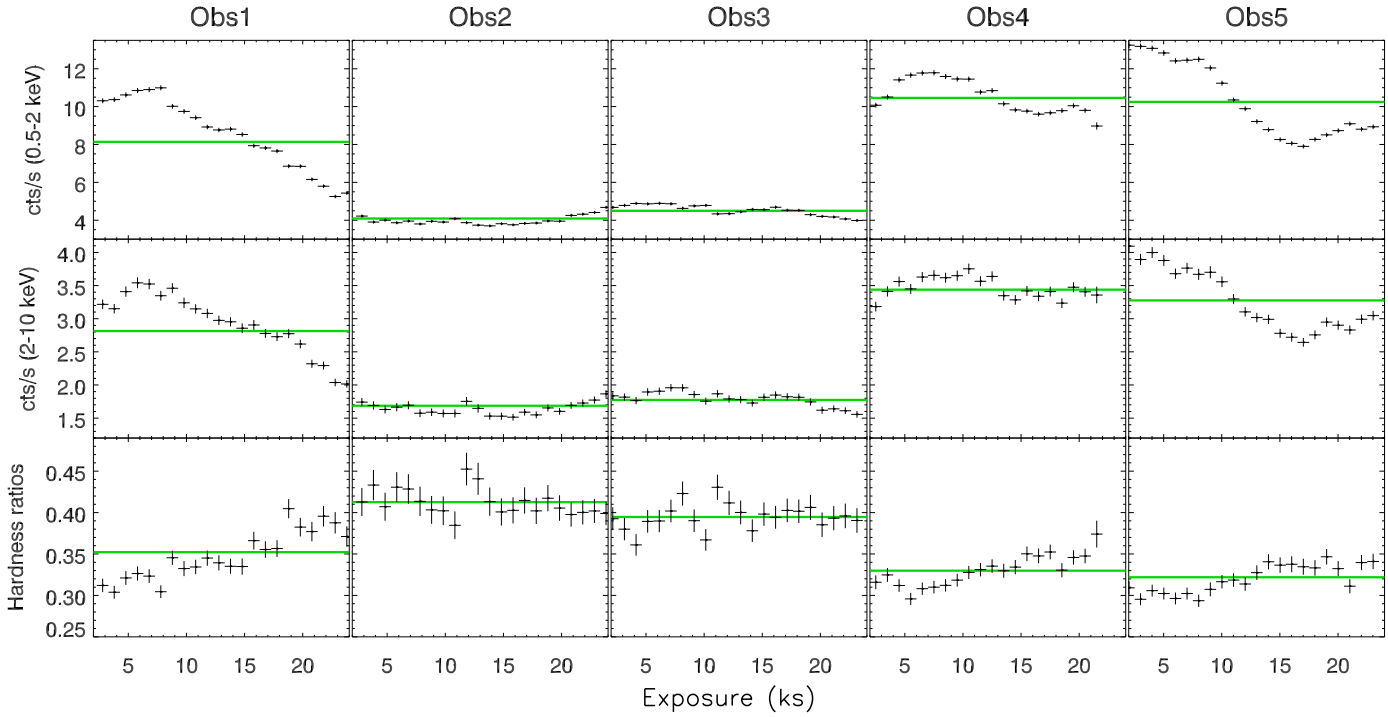

Figure 4.13. The *XMM-Newton* light curves in the 0.5-2 keV and 2-10 keV energy bands are shown in the top and middle panels respectively. Bottom panels display the ratios between the hard light curves and those computed in the soft band. The adopted time binning is 1 ks for all the observations, and the solid green lines account for the average count rates within each pointing.

4.5 Spectral Analysis

We performed the spectral analysis using *Xspec*. In the forthcoming fits a free cross-calibration constant is used to take into account residual calibration problems between *XMM-Newon* and *NuSTAR* data. The *NuSTAR* modules are in good agreement with each other ($\sim$2%), and the detectors of both satellites agree within $\lesssim$10%. In this analysis we take into account the absorption due to the Galactic hydrogen column through the *Xspec* model *phabs* for which the Galactic column density is set to N_H=1.89$\times10^{20}$ cm^{-2} (Kalberla et al. 2005). During the fitting procedure, the Galactic N_H is kept fixed.

Optical-UV: This spectral investigation extends from the optical-UV domain up to hard X-rays, thus we have to consider the Broad Line Region (BLR) contribution. In fact, the BLR is responsible for the so-called small blue bump (SBB) at about 3000 Å.

We account for this component using an additive table in *Xspec*. A detailed description of this table for the case of NGC 5548 is provided by Mehdipour et al. (2015b). While performing the fit we let free to vary (but tied among the pointings) the normalization of this table. From the fit, a flux of $(1.2\pm0.1)\times10^{-11}$ erg s^{-1} cm^{-2} was found for this component. Finally, we include the effect of the Galactic extinction using the *redden* model in *Xspec*. The reddening is kept fixed while fitting the data to the value E(B-V)=0.021 (Schlafly & Finkbeiner 2011).

Soft X-rays: The *nthcomp* model (Zdziarski et al. 1996; Życki et al. 1999) is used to reproduce the soft-excess. This model provides a thermally Comptonized continuum and the high energy roll-over is parametrized by the electron temperature. In the fitting procedure the normalization, the photon index, and the warm electron temperature kT_{wc} are free to vary between the observations. In *nthcomp*, we assumed the seed photons to arise from a disc-like blackbody. As a first step, the seed photon temperature (kT_{bb}) was fitted for each observation. However, since the kT_{bb} were consistent with being constant, we fit the kT_{bb} temperature tying its value among the various pointings. In P1 two ionized warm absorbers and a photoionised emission component were confirmed to contribute to the NGC4593 soft X-ray emission, thus, in the present modelling, we account for these spectral components adopting tables in *Xspec* (*mtable(WA1)*, *mtable(WA2)* and *atable(REFL)*). These tables are computed thanks to the spectral synthesis code *CLOUDY* (v13.03 Ferland et al. 2013). The best-fit values for these components are shown in P1 (its Sect. 3.1, Tab. 3). Here, we adopt the same best-fit values published in P1 keeping them frozen during the fit. Moreover, it is well known that in the soft band some spectral features cannot be directly attributed to the targeted source. For instance, spectral features close to the Si K-edge (E=1.84 keV) and the Au M-edge (E$\sim$ 2.4 keV) may be an artefact of the detector systematic calibration uncertainties. To avoid these issues, we ignored the spectral bins in the energy range 1.8-2.4 keV (see e.g. Kaastra et al. 2011b; Di Gesu et al. 2015; Ursini et al. 2015; Cappi et al. 2016; Middei et al. 2018). However, after this procedure, a line-like feature still remains in the *pn* spectra, and even if very weak (EW=8 eV), it is significant in terms of χ^2, as a consequence of the high number of counts in the soft band. A single narrow Gaussian line untied and free to vary among the observations at $\sim$0.6 keV is enough to correct this residual narrow feature (see also e.g. Kaastra et al. 2011b; Di Gesu et al. 2015; Ursini et al. 2015; Cappi et al. 2016).

Hard X-rays: The primary continuum in the 2-79 keV band is then described by a second *nthcomp* where the seed photons are assumed to arise from a disc-blackbody whose temperature is fixed to the *nthcomp* model of the Soft X-rays. On the other hand in P1, the hard X-ray emission of NGC 4593 displays additional complexities. In fact, a prominent Fe Kα is found to be the superposition of a relativistically broadened and narrow components, thus we add to the primary Comptonisation continuum the reflection models *relxillcp* and *xillvercp* (García et al. 2014b; Dauser et al. 2016). These

models self-consistently incorporate fluorescence emission lines and the corresponding accompanying Compton reflection hump. Then, *xillvercp* supplies the narrow line component, while *rellxillcp* accounts for the relativistic effects and the broad line component. We assumed the same iron abundance A_{Fe} for *xillvercp* and *relxillcp*, and, in the fitting procedure, we let this parameter free to vary but tied between the various pointings. We tied the photon index and the electron temperature of the hot corona kT_{hc} between *nthcomp* and *relxillcp*, while the normalizations are free to vary and untied between models and observations. In P1 the narrow line component coming from cold material is found to be constant among the various observations thus for *xillvercp* the photon index and normalizations are free to vary but tied between the observations. Moreover, since the source is spectrally variable, there is no reason to assume that the radiation incident on the distant reflector is the same as that from the primary component. We therefore allow for different photon index between *xillvercp* and *relxillcp*. In P1 the inner radius is found consistent with being constant among the pointings, similar to the ionization parameter ξ, which best-fit values are found to be $R_{in} \simeq 40\ r_g$ and $\log \xi \simeq 3$ [$\log$(erg cm s^{-1})]. While fitting, we let free to vary but tied between the observations both R_{in} and $\log \xi$. We show the Comptonising and the reflection components in Fig. 4.14. The primary kT_{bb} is tied

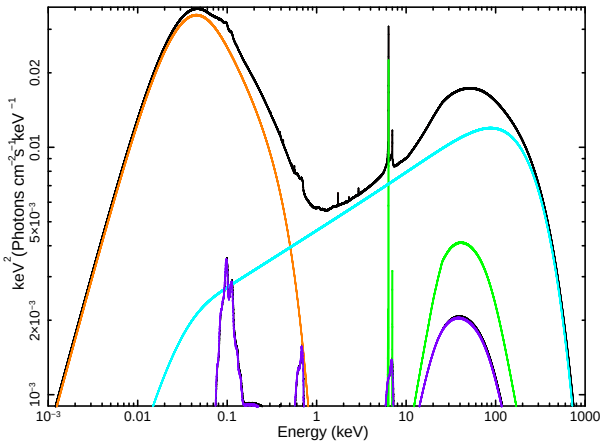

Figure 4.14. The Comptonising and reflection components are displayed. In orange and cyan the warm and hot corona contribution while components in green and purple account for distant and relativistic reflection, respectively. For the sake of simplicity we do not report the different absorbing components. Example of the Comptonising and reflection components from the best fits of Obs 1b.

to the same parameter of the *nthcomp* component used for reproducing the soft-excess. Then, we end up with the following model:

$$redden\times\ phabs\times\ const\times\ mtable(WA1)\times\ mtable(WA2)\times[gauss+\ atable(small\_BB)+\ nthcomp_{wc}+ +atable(REFL)+xillvercp+\ \ nthcomp_{hc}+\ \ relxillcp]\ .$$

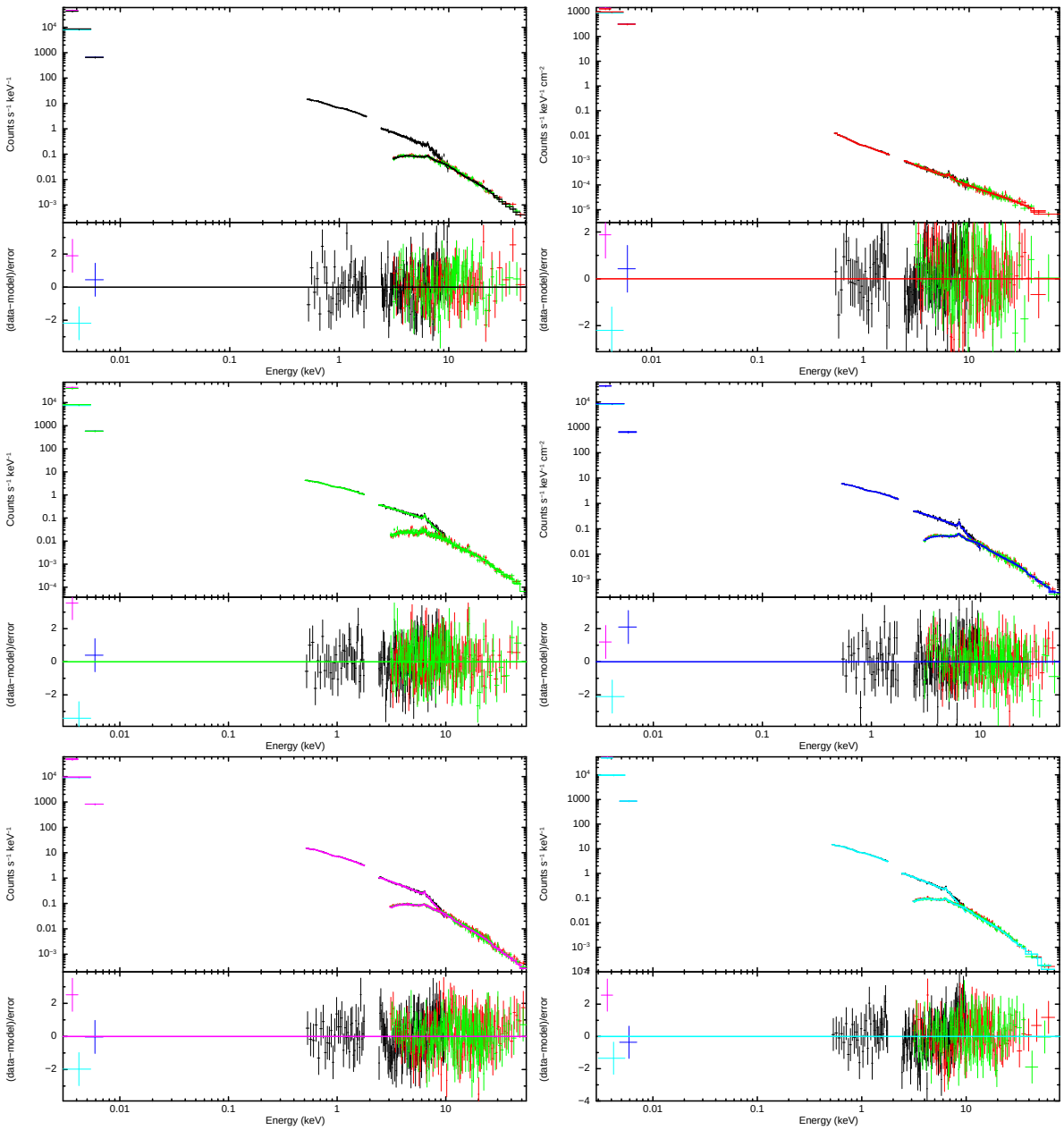

Figure 4.15. The broadband best-fit corresponding to χ^2=2357 for 2189 d.o.f. is showed for all the observations in the top part of the graphs while the residuals with respect to the errors are displayed in the bottom sub-panels.

The adoption of this model results in a best-fit of χ^2=2357 for 2189 d.o.f., see Fig. 4.15. The values of the best-fit parameters are reported in Table 4.9. A super Solar iron

abundance $A_{Fe}=2.8^{+0.2}_{-0.3}$ is required by the fit, and this value is in agreement with the abundance quoted in P1 ($A_{Fe}=2.6^{+0.2}_{-0.4}$). The disc temperature is found to be constant among the pointings with a corresponding best-fit value of $kT_{bb}=12\pm1$ eV. As in P1, the hard component displays variability since Γ_{hc} ranges between 1.71 and 1.85, and a similar behaviour is found for the *nthcomp* modelling the soft-excess ($\Delta\Gamma_{wc}$ ∼0.3), see Fig 4.16 and Fig. 4.17. The electron temperature kT_{hc} remains unconstrained in most of the observations, apart from observation 2, where the fit returns $kT_{hc} = 17^{+20}_{-4}$ keV. However, from Fig. 4.17, hints of variability for the physical properties of the hot corona remain. On the other hand, the warm corona temperature is consistent with being constant: $kT_{wc} = 0.12 \pm 0.01$ keV. We then use the best-fit values of the hot corona and

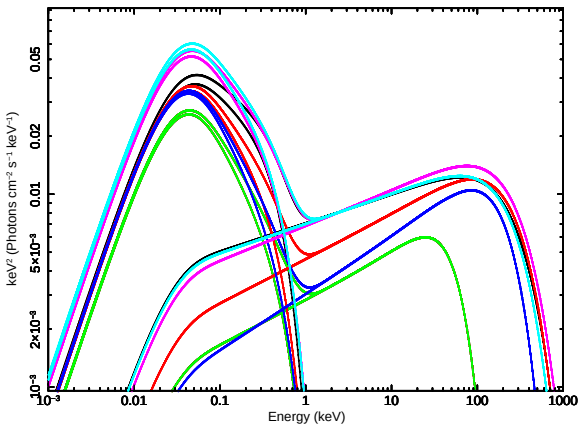

Figure 4.16. The warm and hot Comptonising components for the various observations.

warm corona temperature to calculate the corresponding optical depths of the electron distributions. To do this, we take advantage of the *nthcomp* internal routine used to compute the Thomson optical depth. This procedure assumes a spherical plasma geometry. For both the Comptonising components the best-fit values for the optical depths are reported in Table 4.9 . The optical depth of the hot component can be constrained only for observation 2, $\tau_{hc}=2.1^{+0.4}_{-0.9}$, and, for the remaining observations, upper limits are found to be in the range $0.9\leq\tau_{hc}\leq3.2$ The optical depth of the warm component is found to vary. The τ_{wc} ranges between ∼35 and ∼50.

Finally, we searched for correlations between the best-fit parameters quoted in Table 4.9 The Pearson cross-correlation coefficients (P_{cc}) and the corresponding null probability P(r>) are shown in Table 4.10. Strong anticorrelations are found between the coronal temperature and the optical depth for both the hot and warm components. A noticeable anticorrelation occur also between Γ_{hc} (Γ_{wc}) and τ_{hc} (τ_{wc}), and, interestingly, the photon index of these two components are significantly anticorrelated. In fact, as shown in Fig. 4.19, lower Γ_{hc} values correspond to steeper Γ_{wc}. The Pearson cross-correlation coefficient is P_{cc}=-0.82 with a corresponding null probability of 0.03. We have further

tested this latter correlation checking for dependencies or degeneracies due to the model. Contours in Fig. 4.19 show that the correlation is not due to model parameter degeneracy. Moreover, we checked for the presence of additional degeneracies between the parameters, in particular focusing on the hard Comptonising component and the reflection one. However, the computed contours are flat, thus no degeneracy is present between the parameters of interest, see Fig. 4.18.

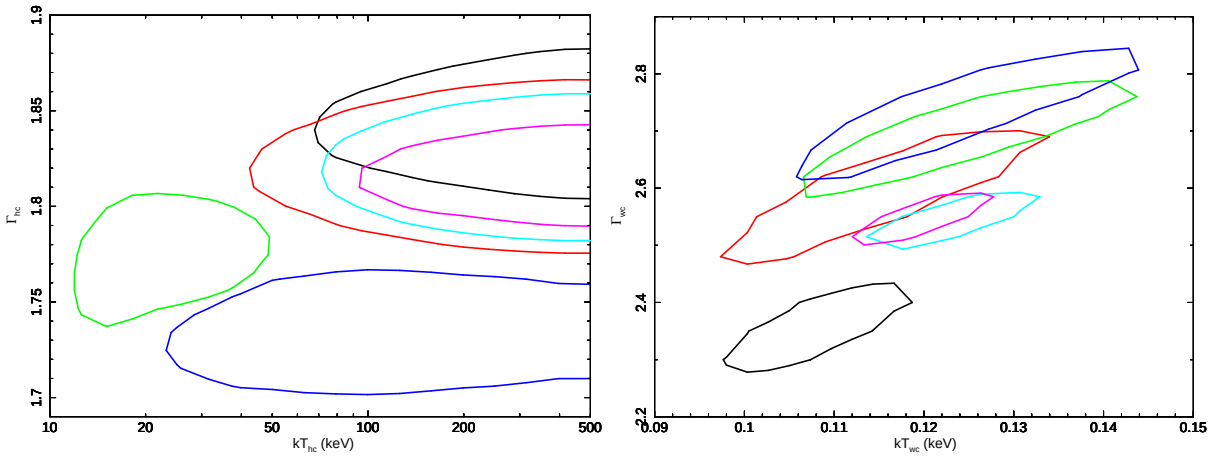

Figure 4.17. Confidence regions at 90% confidence level for the photon index and hot corona temperature (top panel), and for the warm corona.

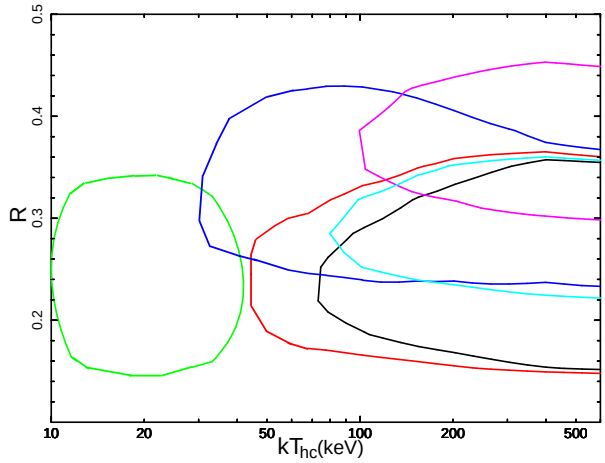

Figure 4.18. Contours at 90% confidence level for the reflection fraction and the hot corona temperature (top panel). Contours are flat, thus no degeneracy is present between the parameters.

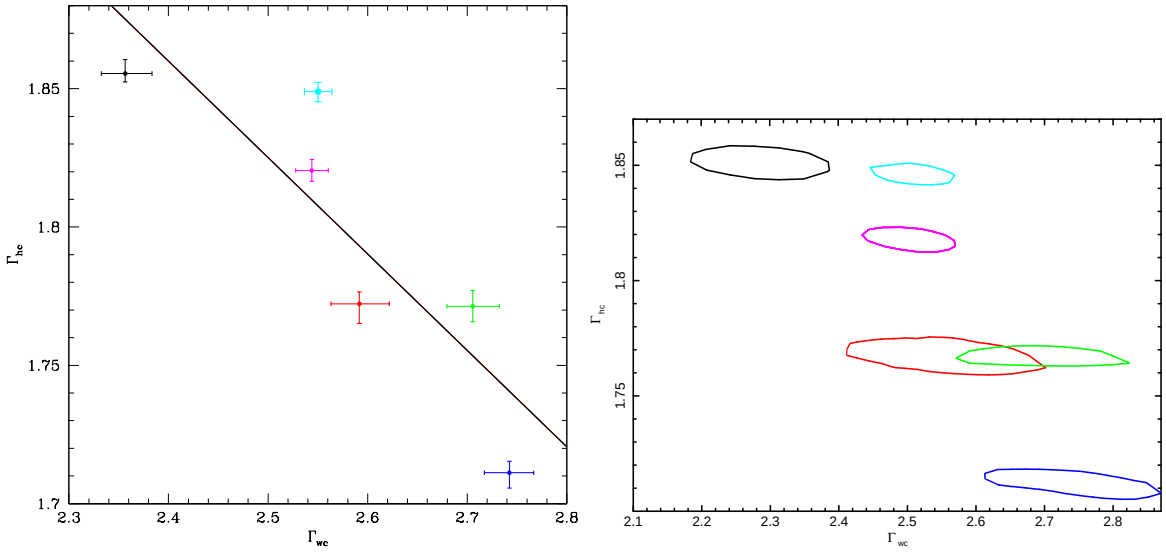

Figure 4.19. *Left panel*: The photon index for the hot corona and warm corona are reported. The solid line represent the fit to the points and the associated Pearson coefficient and null probability are also shown. *Right panel*: Contours at 90% confidence level of both $\Gamma_{\rm hc}$ and $\Gamma_{\rm wc}$ for each observation. Flat contours indicate that the two interesting quantities are measure independently, therefore the correlation is not due to the presence of degeneracy.

Table 4.9. Best-fit values for the parameters corresponding to the best-fit model (χ^2=2357 for 2189 d.o.f.). This fit is also characterized by a seed photons temperature of kT_{bb}=12±1 eV and an Iron abundance $A_{Fe}=2.8^{+0.2}_{-0.3}$. Both these parameters were free to vary but tied between the different pointings. The luminosities and observed fluxes for the 0.3-2 keV and 2-10 keV bands are also showed.

Obs	Γ_{hc}	kT_{hc} (keV)	τ_{hc}	$N_{hc}(10^{-4})$ ph/keV/cm^2/s	N_{rel} (10^{-5}) ph/keV/cm^2/s	Γ_{wc}	kT_{wc} keV	τ_{wc}	N_{wc} (10^{-4}) ph/keV/cm^2/s	$L_{0.3-2}(10^{42})$ erg/s	$L_{2-10}(10^{42})$ erg/s	$F_{0.3-2}$ (10^{-10}) ergs/cm^2/s	F_{2-10} (10^{-11}) ergs/cm^2/s
1a	$1.85^{+0.01}_{-0.01}$	>60	<1.7	$7.1^{+0.2}_{-0.2}$	$3.6^{+0.6}_{-1.0}$	$2.35^{+0.04}_{-0.04}$	$0.11^{+0.01}_{-0.01}$	47^{+3}_{-3}	$4.9^{+1.6}_{-0.6}$	3.68±0.02	4.61±0.02	$2.05^{+0.40}_{-0.01}$	$2.56^{+0.05}_{-1.0}$
1b	$1.77^{+0.01}_{-0.01}$	>80	<1.5	$4.6^{+0.9}_{-0.9}$	$2.9^{+0.8}_{-0.3}$	$2.59^{+0.03}_{-0.08}$	$0.11^{+0.01}_{-0.01}$	42^{+2}_{-2}	$3.0^{+1.2}_{-1.1}$	2.34±0.02	3.47±0.03	$1.29^{+0.30}_{-0.01}$	$1.92^{+0.12}_{-0.90}$
2	$1.77^{+0.01}_{-0.01}$	17^{+20}_{-4}	$2.1^{+0.4}_{-0.9}$	$2.8^{+0.8}_{-1.0}$	$1.3^{+0.3}_{-0.3}$	$2.74^{+0.05}_{-0.05}$	$0.14^{+0.01}_{-0.01}$	35^{+3}_{-2}	$2.7^{+0.7}_{-0.4}$	1.49±0.02	2.45±0.03	$0.82^{+0.01}_{-0.01}$	$1.37^{+0.02}_{-0.02}$
3	$1.71^{+0.01}_{-0.01}$	>30	<3.2	$3.0^{+1.0}_{-0.5}$	$2.9^{+0.6}_{-0.9}$	$2.74^{+0.05}_{-0.04}$	$0.12^{+0.01}_{-0.01}$	38^{+3}_{-2}	$2.7^{+0.7}_{-0.6}$	1.66±0.02	2.62±0.03	$0.92^{+0.3}_{-0.11}$	$1.46^{+0.02}_{-0.08}$
4	$1.82^{+0.01}_{-0.01}$	>150	<0.9	$6.9^{+0.2}_{-0.2}$	$5.7^{+0.7}_{-0.8}$	$2.54^{+0.03}_{-0.01}$	$0.12^{+0.01}_{-0.01}$	41^{+2}_{-2}	$7.6^{+0.1}_{-0.1}$	3.86±0.02	4.91±0.02	$2.14^{+0.80}_{-0.01}$	$2.73^{+0.04}_{-0.06}$
5	$1.85^{+0.01}_{-0.01}$	>140	<0.9	$7.0^{+1.2}_{-1.2}$	$4.2^{+0.6}_{-0.8}$	$2.55^{+0.03}_{-0.02}$	$0.12^{+0.01}_{-0.01}$	41^{+2}_{-2}	$7.3^{+0.5}_{-0.6}$	3.82 ±0.02	4.67±0.02	$2.12^{+0.50}_{-0.01}$	$2.60^{+0.03}_{-0.10}$

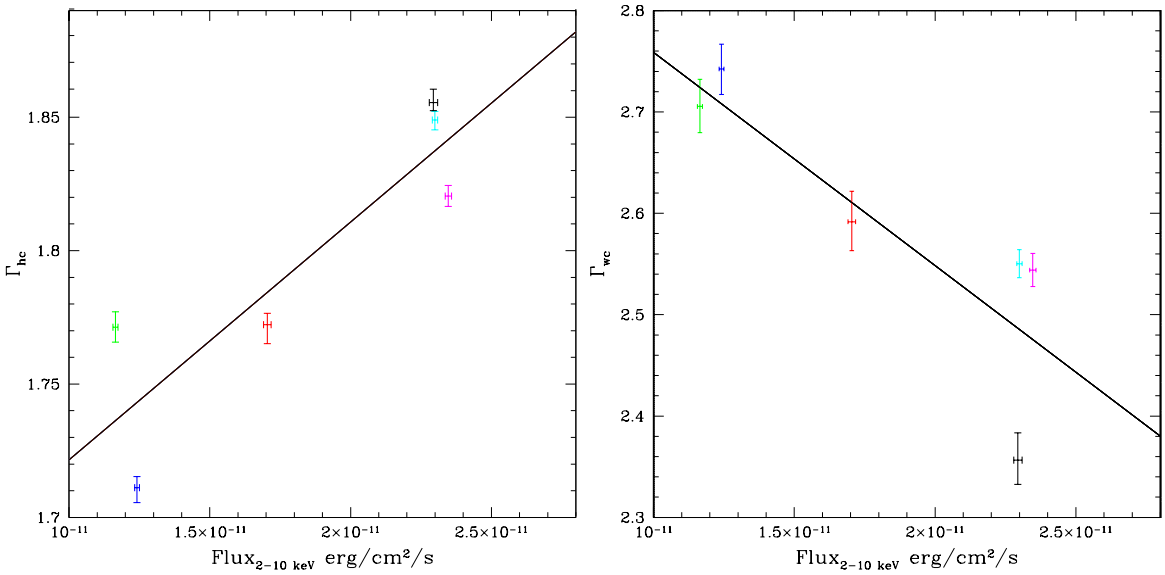

Figure 4.20. The photon index of the hot and warm corona are shown as a function of the 2-10 keV hot component flux. The photon index for both the components are found correlated with the 2-10 keV flux with corresponding Pearson coefficients P_{cc}=0.88 (P(>r)=0.03) and P_{cc}=-084 (P(>r)=0.03) for the Γ_{hc} and Γ_{wc}, respectively.

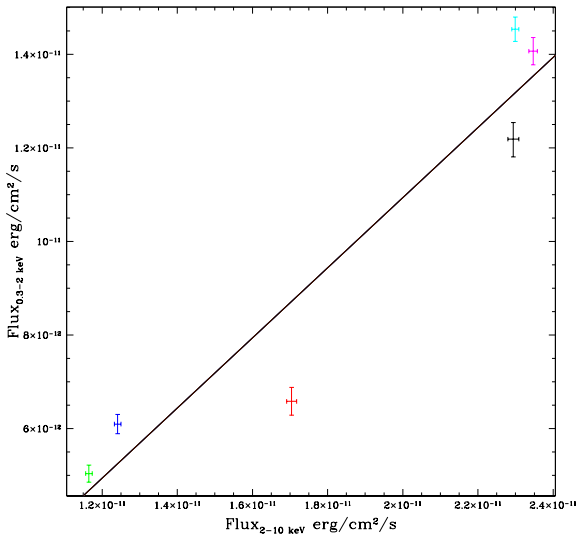

Figure 4.21. The primary X-ray flux (2-10 keV) of the hot *nthcomp* component versus the flux (0.3-2 keV) of the warm *nthcomp* component, as measured in the different observations. The linear fit to the data is displayed by the solid black line (P_{cc}=0.95 and P(>r)=0.02). Fluxes are in units of 10^{-11} erg/cm^2/s.

Table 4.10. The Pearson cross-correlation coefficients and their corresponding null hypothesis probabilities are reported for all the best-fit values of the parameters quoted in Table 4.9. The X is used when the two parameters of interest are not significantly correlated ($P_{cc}<\pm0.70$).

P_{cc} P(r>)	Γ_{hc}	kT_{hc}	τ_{hc}	N_{hc}	N_{rel}	Γ_{wc}	kT_{wc}	τ_{wc}	N_{wc}	$L_{0.3-2}$	L_{2-10}	$F_{0.3-2}$	F_{2-10}
Γ_{hc}	-	X	-0.82	0.9	X	-0.82	X	X	0.77	0.89	0.87	0.89	0.87
			0.04	0.03		0.04			0.05	0.03	0.03	0.03	0.03
kT_{hc}	X	-	-0.85	0.80	0.88	X	X	X	0.91	0.84	0.85	0.83	0.85
			0.04	0.05	0.03				0.02	0.04	0.04	0.04	0.04
τ_{hc}	-0.82	-0.85	-	-0.80	X	X	X	X	-0.79	-0.79	-0.81	-0.79	-0.81
	0.04	0.04		0.05					0.05	0.05	0.05	0.05	0.05
N_{hc}	0.9	0.80	-0.80	-	0.81	-0.87	X	0.77	0.87	0.99	0.99	0.99	0.99
	0.03	0.05	0.05		0.05	0.03		0.06	0.03	0.01	0.01	0.01	0.01
N_{rel}	X	0.88	X	0.81	-	X	X	X	0.88	0.85	0.87	0.85	0.87
		0.03		0.05					0.03	0.04	0.03	0.04	0.03
Γ_{wc}	-0.82	X	X	-0.87	X	-	X	-0.95	X	-0.82	-0.83	-0.83	-0.83
	0.04			0.03				0.02		0.04	0.04	0.04	0.04
kT_{wc}	X	X	X	X	X	X	-	-0.86	X	X	X	X	X
								0.04					
τ_{wc}	X	X	X	0.77	X	-0.95	-0.86	-	X	X	X	X	X
				0.06		0.02	0.04						
N_{wc}	0.77	0.91	-0.79	0.87	0.88	X	X	X	-	0.91	0.90	0.91	0.91
	0.05	0.02	0.05	0.03	0.03					0.02	0.03	0.02	0.03
$L_{0.3-2}$	0.89	0.84	-0.79	0.99	0.85	-0.82	X	X	0.91	-	0.99	0.90	0.95
	0.03	0.04	0.05	0.01	0.04	0.04			0.02		0.02	0.02	0.02
L_{2-10}	0.87	0.85	-0.81	0.99	0.87	-0.83	X	X	0.90	0.99	-	0.89	0.96
	0.03	0.04	0.05	0.01	0.03	0.04			0.03	0.02		0.03	0.02
$F_{0.3-2}$	0.89	0.83	-0.79	0.99	0.85	-0.83	X	X	0.91	0.90	0.89	-	0.99
	0.03	0.04	0.05	0.01	0.04	0.04			0.02	0.02	0.03		0.01
F_{2-10}	0.87	0.85	-0.81	0.99	0.87	-0.83	X	X	0.91	0.95	0.96	0.99	-
	0.03	0.04	0.05	0.01	0.03	0.04			0.03	0.02	0.02	0.01	

4.6 Discussion

We have performed a multiwavelength spectral investigation on the high S/N data of five simultaneous *XMM-Newton* and *NuSTAR* observations of NGC 4593. As commonly observed in Seyfert galaxies (e.g. Piconcelli et al. 2005; Bianchi et al. 2009; Scott et al.

2012), the broadband emission of NGC 4593 displays the presence of two main components, a primary power law and a soft-excess that becomes prominent below $\sim$ 1 keV (see P1).

Both components show strong variability (see Fig. 1 of P1). Flux variations are typical of AGN activity, and in the X-rays, they are observed down to timescales of hours. On such short timescales, variability can be used to probe the innermost regions of AGN. Several authors showed that this variability is correlated with the BH mass (e.g. Nandra et al. 1997b; Czerny et al. 2001; Vaughan et al. 2003b; Nikolajuk et al. 2004; McHardy et al. 2006). We then follow Ponti et al. (2012) to compute the normalised excess variance and its associated error for NGC 4593 obtaining $\sigma^2_{\rm rms}$=0.003$\pm$0.002 in the 2-10 keV band. Adopting the relation between $\sigma^2_{\rm rms}$ and $M_{\rm BH}$, we estimate the NGC 4593 BH mass to be $M_{\rm BH}$=(5.8$\pm$2.1)$\times10^6$ $M_\odot$. Our estimate is marginally compatible with the reverberation mapping value provided by Denney et al. (2006): $M_{\rm BH}$=(9.8$\pm$2.1)$\times10^6$ $M_\odot$.

Moreover, in the present study we show that the optical-UV/X-rays emission of NGC 4593 can be explained in terms of two Comptonising components, a warm optically thick corona, and a hot optically thin medium. The soft-component photon index shows significant variations between the different observations (2.35$\lesssim \Gamma_{\rm wc} \lesssim$2.74, see Fig. 4.16), while the corresponding electron temperature displays a more constant behaviour (on average $kT_{\rm wc}$=0.12$\pm$0.01 keV). Therefore, the observed variability has to depend on $\tau_{\rm wc}$, which we estimate to vary in the range 35$<\tau_{\rm wc}<$47. On the other hand, also the hot component displays remarkable spectral variations (see Fig. 4.16), with variability found for both the hot electron temperature and $\tau_{\rm hc}$.
For the hot corona, $kT_{\rm hc}$ and $\tau_{\rm hc}$ seem to be anticorrelated and their trend is in agreement with that reported by Tortosa et al. (2018). However, our result is not very significant since it is only based on lower (upper) limits for $kT_{\rm hc}$ ($\tau_{\rm hc}$).

4.6.1 Warm and hot corona regions in NGC 4593

From the best fit model we can compute the total flux emitted by the warm and hot corona ($F_{\rm tot-soft(hard)}$), as well as the seed soft photon flux entering them and cooling them ($F_{\rm soft(hard)}$), see Table 4.11. With the estimate of the coronal best-fit optical depth we can deduce the so-called Compton amplification factor A (see Petrucci et al. 2018, for details). This factor accounts for the ratio between the total power emitted by the warm corona and the seed soft luminosity from the accretion disc, and it can be used to estimate the geometrical properties of the Comptonising medium. In particular, following the steps described by Petrucci et al. (2018) we find that the amplification factor for the warm corona $A_{\rm wc}$ ranges between 1.6 and 2. An amplification $A_{\rm wc} \simeq$2 is theoretically expected for an optically thick and slab corona corona fully covering a passive disc (e.g. Petrucci et al. 2013b), thus this is in agreement with a scenario in which the soft-excess

Table 4.11. We report in this table the best-fit fluxes entering (F_{soft} and F_{hard}) and emitted ($F_{tot-soft}$ and $F_{tot-hard}$) by the soft and hard corona. Moreover, the flux due to relativistic reflection is also reported. All fluxes $F_{tot-soft}$, $F_{tot-hard}$, F_{soft}, F_{hard} and $F_{rel-refl}$ are in units of 10^{-11} erg/cm^2/s, and are computed in the 0.001-1000 keV energy interval.

	Obs. 1a	Obs. 1b	Obs 2.	Obs. 3	Obs. 4	Obs. 5
F_{soft}	9.2	8.9	6.9	8.9	13.4	14.6
F_{hard}	1.0	0.5	0.3	0.3	0.9	1.0
$F_{rel-refl}$	1.8	1.3	0.8	1.3	2.7	2.1
$F_{tot-soft}$	17.8	15.2	11.3	14.3	23.6	25.6
$F_{tot-hard}$	26.0	20.6	9.0	15.1	27.2	25.5

Table 4.12. The Pearson cross-correlation coefficients and their associated null probabilities are displayed for the warm and hot corona components flux. The subscript *tot* indicates the total flux emerging from the specified component, otherwise fluxes refer to the seed photons flux entering in that highlighted component. The photon index for the warm and the hot corona are also reported. When X is used, no correlation holds between the two interesting parameters.

P_{cc} P(r>)	F_{soft}	F_{hard}	$F_{rel-refl}$	$F_{tot-soft}$	$F_{tot-hard}$	Γ_{wc}	Γ_{hc}
F_{soft}	-	0.72 0.07	0.86 0.03	0.98 0.02	0.76 0.06	X	X
F_{hard}	0.72 0.07	-	0.78 0.05	0.83 0.04	0.91 0.02	-0.88 0.03	0.94 0.02
$F_{rel-refl}$	0.86 0.03	0.79 0.04	-	0.89 0.03	0.89 0.03	X	X
$F_{tot-soft}$	0.98 0.02	0.83 0.04	0.89 0.03	-	0.77 0.06	X	X
$F_{tot-hard}$	0.76 0.06	0.91 0.02	0.89 0.03	0.77 0.06	-	-0.83 0.04	0.74 0.06
Γ_{wc}	X	-0.88 0.03	X	X	-0.83 0.04	-	-0.82 0.04
Γ_{hc}	X	0.94 0.02	X	X	0.74 0.06	-0.82 0.04	-

arises from a warm and optically thick medium being the upper layer of a nearly passive accretion disc (Różańska et al. 2015). Again, following the procedure in Petrucci et al.

(2018), we also estimate the amplification factor corresponding to the hot component, $A_{\rm hc}$. In this case, the electron temperature is poorly constrained, and we estimate lower limits for this parameter. These lower limits translate to upper limits for the amplification factor of the hard corona $A_{\rm hc}$ found to be in the range 50-100. Following Eq. 18 and 23 in Petrucci et al. (2018), these translate to lower limits of the patchiness factor of the hard corona which is of the order of $2/A_{\rm hc}$ for an optically thin corona above a passive disc (i.e. with no intrinsic emission Petrucci et al. (2013b)). We obtain g >0.02 . These values are in agreement with a scenario in which an extended Thomson thick medium is responsible for the optical-UV/soft X-ray of NGC 4593, while a compact or patchy corona intercepting and Comptonising only a fraction (few %) of the disc seed photons explains the X-ray primary continuum.

Concerning the interplay between the warm and hot coronal emission, in Fig. 4.21 we show that the primary X-ray flux is tightly correlated with the flux of the soft-excess component. The Pearson correlation coefficient of $P_{\rm cc}$=0.95 (P(>r)=0.02) suggests that the soft-excess increases for an increasing primary flux. The tight correlation we find between the photon index of the hot and warm corona is quite unusual and difficult to explain. Concerning the evolution of the hot corona properties (Γ_{hc} and flux), it is interesting to note that the softer and more luminous spectra roughly correspond to the observations with the highest UV flux. This is not a strong effect given the small variability of the UV flux, but it suggests a simple interpretation. Qualitatively, the spectral and luminosity change can be explained assuming that the outer disc/warm corona structure pushes a bit closer to the black hole (the transition radius R_{tr} between the hot and the warm corona decreases), decreasing the portion of the hot corona which "sees" an increase of the UV-EUV soft radiation. This would cause a more effective cooling of the hot gas explaining the softening of the spectrum. If this interpretation is correct however, we would expect then a decrease in the hot corona temperature. This is in contradiction with the lowest value of the temperature, observed during observation 2, while the UV flux is also the lowest. Moreover, it is not easy to understand why, in these conditions, the warm corona photon index would evolve in an opposite way.

Actually the anticorrelation of $\Gamma_{\rm hc}$ and $\Gamma_{\rm wc}$ could be a by product of the radiative coupling between the two coronae. We have reported in Table 4.12 the correlation coefficient between the total corona flux, the seed soft photon flux and the photon index of both coronae. Interestingly, $F_{\rm tot-soft}$ strongly correlates with $F_{\rm hard}$ ($P_{\rm cc}$=0.83). This correlation agrees with the warm corona acting as the seed photon source for the hot corona. The larger $F_{\rm tot-soft}$ the larger $F_{\rm hard}$ but, at the same time, the steeper the hot corona spectrum due to the increase of the cooling ($\Gamma_{\rm hc}$ increases as indeed observed). On the other hand, $\Gamma_{\rm wc}$ anticorrelates quite strongly with $F_{\rm hard}$ (the correlation is even stronger than between $\Gamma_{\rm wc}$ and $\Gamma_{\rm hc}$). Possibly there is some feedback then in the sense that when $F_{\rm tot-soft}$ increases also $F_{\rm tot-hard}$ increases. Then, the heat deposit in the warm

corona by e.g. illumination increases (indeed, $F_{tot-hard}$ correlates with $F_{rel-refl}$), producing a hardening (Γ_{wc} decreases) of the warm corona spectrum.

The main problem with this interpretation is the evolution of the coronal temperature. We would expect the temperature to decrease/increase when the spectrum steepens/hardens. The present observations do not show clear evolution of these temperatures. This suggests that something else may have to change, e.g. the optical depth, to keep the temperature roughly constant.

Note that we have assumed a constancy of the warm corona geometry. Its variation is however plausible and should add another free parameter to explain the observations. Indeed, variability of the optical-UV-to-X-rays emission of NGC 4593 could result from geometrical variations of the 'two coronae' but also of the 'warm corona' and outer part of the disc, not covered by the warm corona, and, potentially, also contributing to the optical-UV emission. A detailed analysis of the parameter space, also adopting more sophisticated models (e.g. *agnsed,* Kubota & Done 2018) self-consistently accounting for the disc contribution in the frame-work of two Comptonising coronae is deferred to a future work.

4.7 Summary

We reported a spectrscopic analysis on the observational campaign targeting NGC 4593. In particular we tested the two-corona model (e.g. Petrucci et al. 2013b; Różańska et al. 2015) on this rich high S/N data-set. The obtained overall scenario is consistent with the two-corona model in which two Comptonisation processes dominate the soft and hard X-ray emission of the source. We report our findings and conclusions in the following:

- Strong flux variability is observed during the monitoring and variations are observed from daily down to hourly timescales. We adopted the normalised excess variance to quantify the source variability finding σ^2_{rms}=0.003±0.002 in the 2-10 keV band. Following Ponti et al. (2012), we convert this value into an estimate of the BH mass hosted by NGC 4593, obtaining M_{BH}=(5.8±2.1)×10^6 $M_\odot$. This values is marginally in agreement with the reverberation mapping measure by Denney et al. (2006).

- A hot Comptonisation component describes the high energy spectra of our campaign. This hot corona is phenomenologically described by a variable photon index ($1.71 \leq \Gamma_{hc} \leq 1.85$). The hot corona temperature remains unconstrained in five over six observations. On the other hand, hints of variability are found for this parameter and this is in agreement with the high-energy cut-off variability reported in P1.

In turn, we find upper limits for the optical depth of the hot corona. We notice that $kT_{\rm hc}$ and $\tau_{\rm hc}$ anticorrelate (P_{cc}=-0.85 P(r>)=4%).

- All spectra display a remarkable soft-excess, and a warm Comptonisation model best describes this component. The warm medium is characterized by a variable photon index $2.35 < \Gamma_{\rm wc} < 2.74$ and a constant $kT_{\rm wc} = 0.12 \pm 0.01$ keV. The optical depth of the warm corona is variable $35 \leq \tau_{\rm wc} \leq 47$. According to this analysis, most of the accretion power is released in the warm-corona than in the accretion disc.

- For the first time, we observe an anticorrelation between the photon indexes of the hot and the warm corona. The origin of this trend cannot be ascribed to a model degeneracy (see Fig. 4.19). The interpretation of such anticorrelation is not straightforward but can result from the radiative feedback between the two coronae.

- The present test on the two-corona model indicates that it reliably allows for reproducing the AGN broadband emission. Indeed, besides observational differences with other sources that can be explained in terms of different physical properties (e.g. Eddington ratio), notably the two-corona model provides good representations of the data suggesting that it accounts for a common Comptonising mechanism occurring in AGN. On the other hand, the existence of a warm corona at such temperature and optical depth above the accretion disk is expected to produce emission/absorption features from the ionized matter. The fact that we do not see any of them would imply specific physical properties (e.g. turbulence) that have to be tested with accurate radiative transfer codes.

Chapter 5

Estimating the coronal parameters with MoCA

As discussed in Chapter 3, both the photon index and high energy cut-off of the X-ray primary emission depend on the intrinsic properties of the Comptonising medium, namely its temperature, optical depth and geometry.

In this Chapter, we derive and discuss formulae through which it is possible to directly relate the phenomenological quantities Γ-E_c with the corresponding coronal properties kT_e-τ_e for the cases of a slab-like and a spherical corona.

The interplay between coronal parameters and the AGN X-ray spectral shape has been so far object of several investigations, especially when observatories capable of detecting hard X-rays have been launched. Perola et al. (2002) using BeppoSAX data collected and studied the photon index and E_c of a sample of AGN, while a similar work was performed on INTEGRAL data (e.g. Malizia et al. 2014). Then, NuSTAR (see Appendix A) greatly helped in studying the exponential cut-offs of the nuclear continuum in several AGN, (see e.g. Fabian et al. 2015, 2017; Tortosa et al. 2018).

These space missions allowed for a substantial corpus of high energy cut-off and photon index measurements, and many efforts have been made to find a way for converting such parameters into those describing the coronal properties.

In Petrucci et al. (2000) an approximate relation between the observed high-energy cut-off of NGC 5548 and the thermal energy of the corona is given ($E_c \sim$2-3kT_e), while in Petrucci et al. (2001) it was discussed for a larger sample of Seyfert 1s. However, this relation has been proved to be accurate for an extended slab geometry only, but it is often used for coronae of any geometry and size.

On the other hand, Beloborodov (1999) reports a relation between the spectral photon index and the Compton parameter y. This parameter introduced in Chapter 2 (Eq. 2.35) is the product of the average fractional energy change per scattering and the mean number of scatters that the photon undergoes (Rybicki & Lightman 1979). Then, y is

used to characterise the energy gain of a photon scattering within a finite medium. The Compton parameter encodes the physical conditions of the coronal plasma, and it can be defined as follows (see also Chapter 2 and Chapter 3):

$$y = 4(\theta_{\rm e} + 4\ \theta_{\rm e}^2)\tau_{\rm T}(\tau_{\rm T} + 1)\ , \tag{5.1}$$

where $\theta = kT_{\rm e}/m_e c^2$, and $\tau_{\rm T}$ is the Comptonising medium opacity. Beloborodov (1999) found that the photon index is related to y according to $\Gamma{=}\frac{4}{9}\ y^{-2/9}$. In his work, Beloborodov (1999) studied the dependence of Γ on y for only two values of electron temperatures (kT_e=50 keV and kT_e=100 keV) and letting free to vary the opacity of the corona. Moreover, in his work, the Comptonising corona is infinitely extended and spherical.

In the following, we use MoCA (MonteCarlo code for Comptonisation in Astrophysics) (Tamborra et al. 2018), to derive formulae for directly translating high energy cut-offs and photon indices into the corresponding physical parameters of the hot corona, namely the optical depth and electron temperature. We will derive formulae for a slab-like corona and for the case of a sphere.

5.1 *MoCA* & simulations setup

To our knowledge, MoCA (see detailed description in Tamborra et al. 2018) is the first MonteCarlo code devoted to study accretion of astrophysical sources based on a single photon approach and working in a fully special relativistic scenario and also accounting for polarisation signals. Moreover, compared to different codes in the literature, such as compTT, compPS, nthcomp (Titarchuk 1994; Poutanen & Svensson 1996; Zdziarski et al. 1996; Życki et al. 1999), the energy dependent Klein-Nishina cross section is taken into account (differently from Schnittman & Krolik 2010) and multiple geometries can be tested and investigated (see e.g. Beheshtipour et al. 2017).
MoCA is a flexible code, and it can account for various and different physical conditions of the AGN and of the corona.

Indeed, before running every simulation, MoCA allows for defining the source BH mass and its accretion rate. These two quantities mainly affect the seed photons spectrum produced by the multi-colour accretion disc. Accretion discs are taken with the typical properties for a Shakura-Sunyaev disc (see Chapter 2 for details and references), and it is possible to set different values for its inner and the outer radii.

The synthetic spectra produced through MoCA also account for the physical conditions of the hot corona that is modelled as a thermal distribution of electrons. Two geometries were considered for the corona: a sphere and a very oblate spheroid to which we will refer to as a slab. In this work, we have assumed the Comptonising corona to be as extended as the disc. Moreover, for the slab geometry case, MoCA allows for setting

up the corona height above the accretion disc (set to 10 r_g in our simulations). MoCA also allows for tuning the physical conditions of the corona, indeed it is possible to set up the coronal temperature and its opacity.

In the forthcoming analysis, we will use simulations computed assuming the source BH mass and accretion rate to be the same as *Ark 120* (e.g. Nardini et al. 2016; Reeves et al. 2016b; Porquet et al. 2018) i.e. $M_{BH} = 1.5 \times 10^8 M_\odot$ and $\dot{m} = L_{bol}/L_{Edd} = 0.1$. Then disc radii are always set to be $R_{out} = 500$ r_g and $R_{in} = 6$ r_g, respectively. For both the slab and spherical geometries, we have simulated the Comptonised spectra using a wide range of values for the electrons temperature and their optical depth: $0.5 < \tau_e < 4.5$ and $20 < kT_e < 120$ for the slab geometry, while $0.5 < \tau_e < 7$ and $20 < kT_e < 120$ were used for the spherical corona.

In Fig. 5.1 we show examples of spectra obtained produced by MoCA.

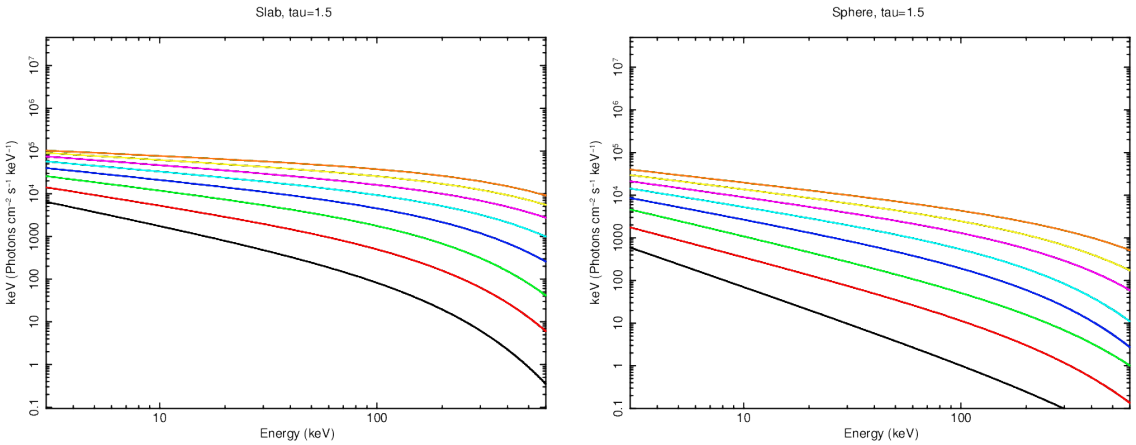

Figure 5.1. MoCA simulated spectra assuming τ=1.5 and different electron temperatures ranging from 50 keV (black) to 120 keV (orange) and adopting a step of 10 keV. Spectra assuming a slab-like corona are shown in the left panel, while, in the right panel, a spherical corona is adopted. Colour code is the same for the two panels. It is worth to notice that the same τ-kT couple gives rise to different spectra when the slab-like or the spherical geometries are considered.

5.2 Methods

For all the synthetic spectra, we performed a spectral fit using a phenomenological model. Indeed, by fitting simulations with a cut-off power law we are able to relate the obtained best-fit parameters (Γ-E_c) with the physical properties of the corona producing that specific spectrum. During the fitting procedure, the high energy cut-off, the normalisation and the photon index of the primary continuum emission are free to vary. Fits are performed in the 2-700 keV energy interval, or up to the last populated energy

bin, if lower than 700 keV. During the fitting procedure, we adopted the C statistics (Cash 1979).

This procedure yields for each fitted couple Γ-E_c a corresponding $kT_e - \tau_e$ couple particular of that spectrum and at priori known. At this stage of the analysis, we excluded all the spectra for which we obtained a photon index outside the interval 1.5-2.5. Indeed, we have no evidence of AGN with such a flat(steep) photon index (e.g. Bianchi et al. 2009; Sobolewska & Papadakis 2009; Serafinelli et al. 2017). Spectral indices outside this interval are unlikely for AGN, and, when observed, they cannot be directly ascribed to the primary X-ray emission.

5.3 Analysis

In the following, we will report on the various steps we pursed to obtain relations connecting Γ-E_c with kT_e-τ_e. For the slab geometry, spectra are simulated for optical depths ranging between 0.5-4.5 and electrons temperature within the interval of 20-120 keV, while assuming a spherical corona, we studied spectra simulated for $20<kT_e<120$ and with τ_e varying in the range 0.5-7.

First, we analysed the dependence of the photon index on the Compton parameter y. Then, for each Γ-E_c couple, we computed the corresponding y using the proper τ_e-kT_e. For all the kT_e (kept fixed), we plot the photon index as a function of y for different values of τ_e, see Fig. 5.2. Then, we perform linear fits between Γ and y. These two parameters are clearly correlated, although points are widely dispersed, see left(right) panel of Fig 5.2 for the case of a slab(sphere)-like geometry. On the other hand, we found that such a widespread dispersion is due to a further dependence of Γ on the coronal temperature, that we quantified studying how the slopes (a) and normalizations (b) of the just obtained fit behave as a function of kT_e. In particular, we performed additional fits between these parameters: a-kT_e and $b - kT_e$, respectively. This procedure leads to Eq. 5.2 for the case of a slab-like corona:

$$\begin{aligned} log\Gamma &= a(\theta_e) log\ y + b(\theta_e) \\ a(\theta_e) &= 0.51 \pm 0.05 \times \theta_e - 0.324 \pm 0.008 \\ b(\theta_e) &= -0.87 \pm 0.05 \times \theta_e + 0.468 \pm 0.008, \end{aligned} \tag{5.2}$$

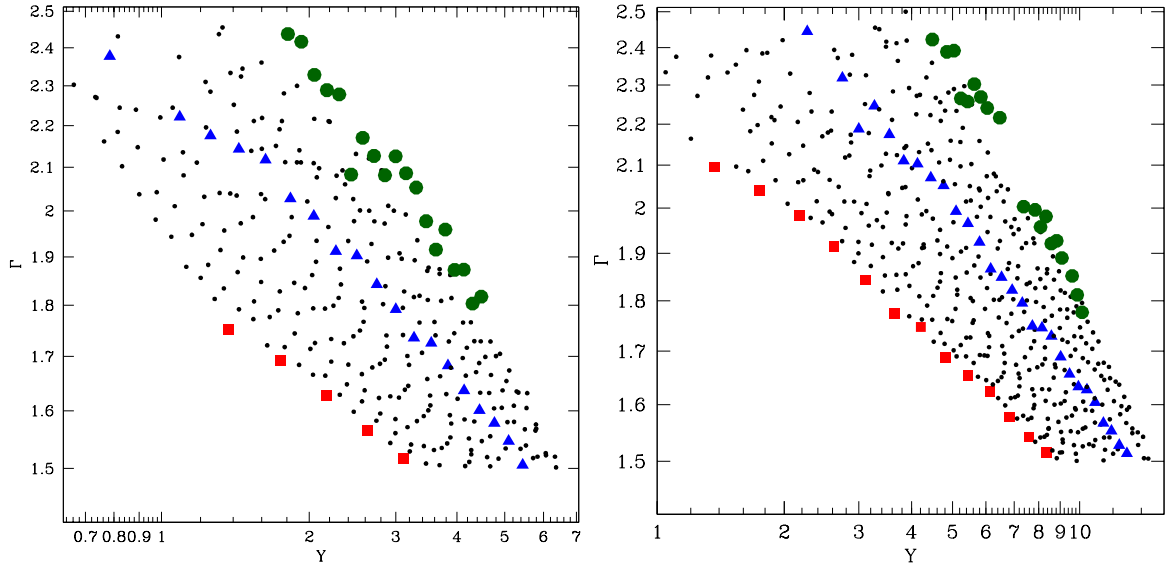

Figure 5.2. The photon index as a function of the Compton parameter. In particular, y is computed for all the temperature (kept fixed) for the various optical depths. To help the reader, are red square are used to show Γ as a function of y computed at fixed values of kT=120 keV for various values of τ. Blue triangles represent the same quantities but for kT=50 keV, while green circles identify points corresponding to kT_e=20 keV. Left panel reports correlations for the case of a slab-like corona, while results in right panel are obtained assuming the corona to be spherical.

where $\theta_e = \frac{kT_e}{m_e c^2}$.For the spherical case we obtain:

$$\begin{aligned} log\Gamma &= a(\theta_e) log\ y + b(\theta_e) \\ a(\theta_e) &= 0.86 \pm 0.10 \times \theta_e - 0.368 \pm 0.012 \\ b(\theta_e) &= -1.33 \pm 0.05 \times \theta_e + 0.633 \pm 0.015\ . \end{aligned} \tag{5.3}$$

According with these just reported formulae, the photon index does not depend only on y, rather it is a function of kT_e and y.

In a similar fashion, we derived relations connecting the high energy cut-off with the physical properties of the Comptonising plasma. The high energy roll-over is mainly dependent on the coronal temperature. Thus, we started studying the E_c as a function of kT_e keeping τ_e fixed, see Fig. 5.3. The dependence of E_c on the plasma temperature is estimated performing linear fits between this parameter and kT_e for different fixed values of τ_e. On the other hand, the obtained slopes (α) and normalizations (β) are found to depend on the coronal opacity. Therefore, we quantified this dependence on the optical depth performing linear fits for α and β as a function of τ_e. For the case of a slab-like

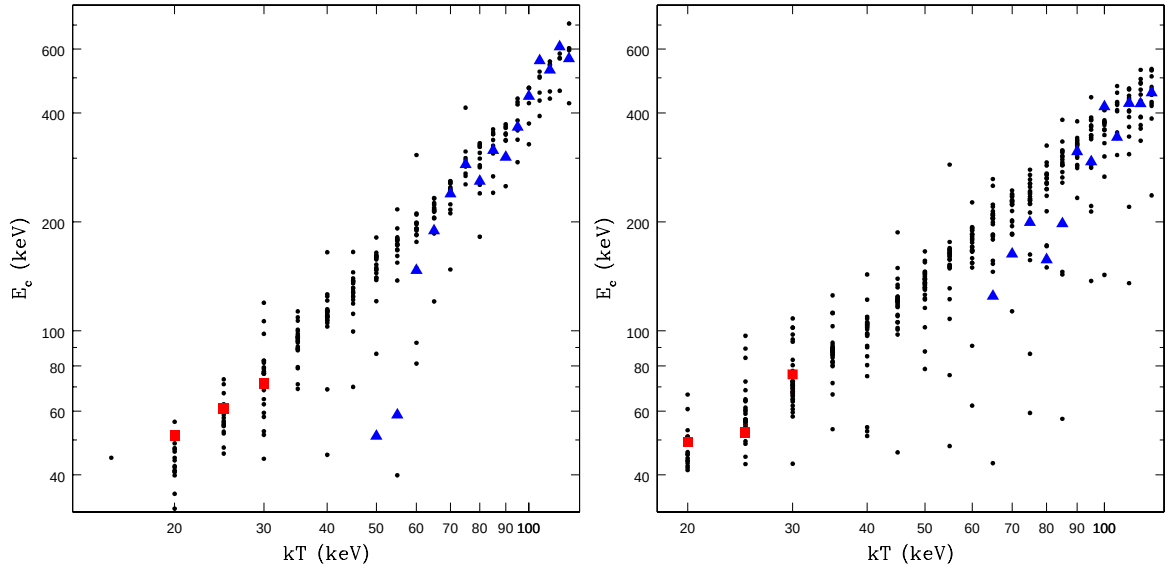

Figure 5.3. For a fixed optical depth, we plot the high energy cut-off as a function of the electron temperature. Red squares accounts for an optical depth of 4, while τ=0.8 is showed though blue triangles. The same quantities are reported in the left and right panels that account for a slab-like corona and a spherical one, respectively.

corona these steps yielded the following relations:

$$\begin{aligned} log\ \frac{E_c}{keV} &= \alpha(\tau) log\ \theta_e + \beta(\tau) \\ \alpha(\tau) &= -0.50 \pm 0.1 \times \tau + 6.1 \pm 0.3 \\ \beta(\tau) &= 0.398 \pm 0.08 \times \tau - 1.87 \pm 0.23\ . \end{aligned} \tag{5.4}$$

For a spherical Comptonised medium we obtained:

$$\begin{aligned} log\ \frac{E_c}{keV} &= \alpha(\tau) log\ \theta_e + \beta(\tau) \\ \alpha(\tau) &= -0.77 \pm 0.11 \times \tau + 7.1 \pm 0.5 \\ \beta(\tau) &= 0.558 \pm 0.08 \times \tau - 2.69 \pm 0.34\ . \end{aligned} \tag{5.5}$$

For both the geometries here considered, the high energy cut-off does not only depend on the electron temperature, but also on the coronal opacity. The above equations directly relate the high energy cut-off with the coronal temperature and encodes the dependence on opacity of the Comptonising electrons.

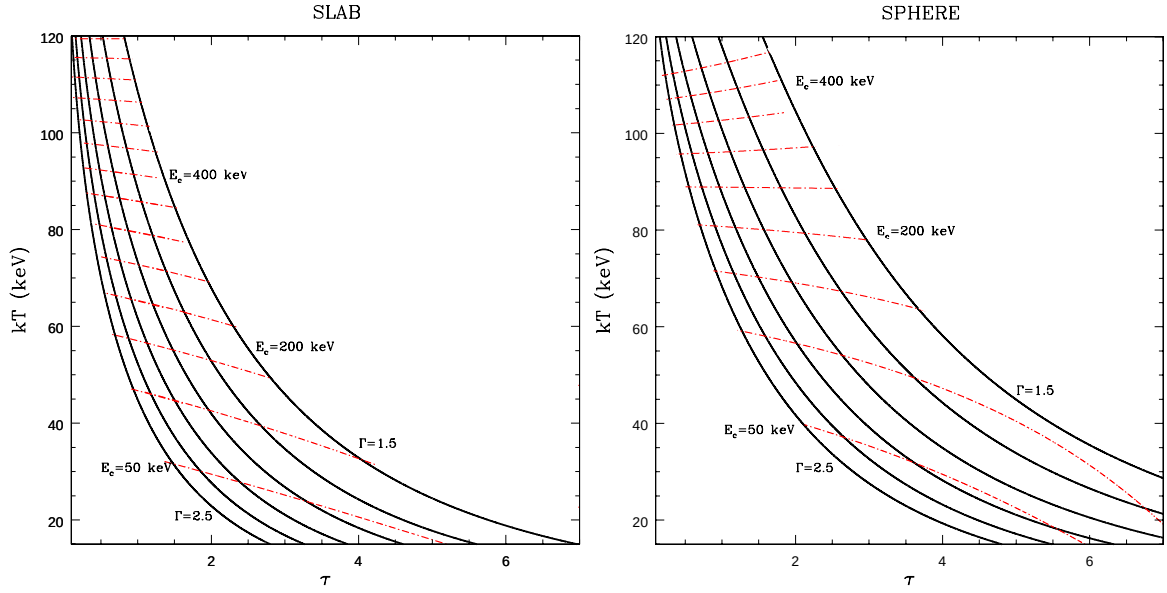

Figure 5.4. Black solid lines represent the iso-Γ curves, while iso-E_c are showed via the red solid-dashed lines. Iso-Γ curves have a 0.2 step and Γ steepens from right to left. A 50 keV step is used for representing the various high energy cut-off iso-curves. Right panel: The same quantities, but for a spherical corona.

Once the dependences between the phenomenological parameters and the physical kT_e and τ_e have been quantified, we use Eq. 5.2 and 5.4 for the slab case, and Eq. 5.3 and 5.5 for the sphere, to determine the interesting regions in the kT_e-τ_e parameters space. In particular, by plotting iso-Γ curves for $2.5 \leq \Gamma \leq 1.5$ and iso-E_c lines, we identify regions in the physical parameters plane corresponding to typically measured AGN photon indices and high energy cut-offs, see Fig.5.4.

On average, for a certain Γ, a slab corona returns lower values of optical depth and temperature, while, to reach the same spectral shape, higher kT_e and τ_e are required when a sphere-like corona is considered. Moreover, iso-E_c curves behaves differently for the two geometries. In particular, high energy cut-off for the sphere always correspond to higher temperature (∼10-20 keV more) if compared with the slab case. Noticeably, we observed that the commonly adopted relation E_c ∼2-3 kT_e is not valid for all the kT_e and τ_e regimes.

5.4 Studying the coronal parameters of HE 0436-4717, NGC 7469 and NGC 4593

All the above procedure can be used for studying the coronal properties of the AGN presented in this dissertation. Indeed, using Eq. 5.2, 5.4, 5.3 and 5.5 we can study the coronal properties of NGC 7469 and HE 0436-4717 using values presented in Chapter 4, and, for NGC 4593, adopting the phenomenological values reported by Ursini et al. (2016)

The HE 0436-4717 emission was well described by a constant photon index of 2.01±0.09 and a lower limit E_c >280 keV for its primary continuum emission was found. Both the photon index and high energy cut-off of NGC 7469 showed a constant behaviour during our observational campaign and corresponding values of Γ=1.78±0.01 and E_c=170^{+60}_{-40} keV were obtained. NGC 4593 displayed a strong spectral variability $1.59 < \Gamma < 1.85$ and its high energy cut-off was found to vary between 90 keV and >700 keV.

Then, using Eq. 5.2, 5.4, 5.3 and 5.5, we computed contours for the parameters of interest for NGC 7469 (green), HE 0436-4717 (blue) and NGC 4593 (gold), see Fig. 5.5. Left hand panel of Fig. 5.5 accounts for a slab corona, while right panel refers to a spherical geometry.

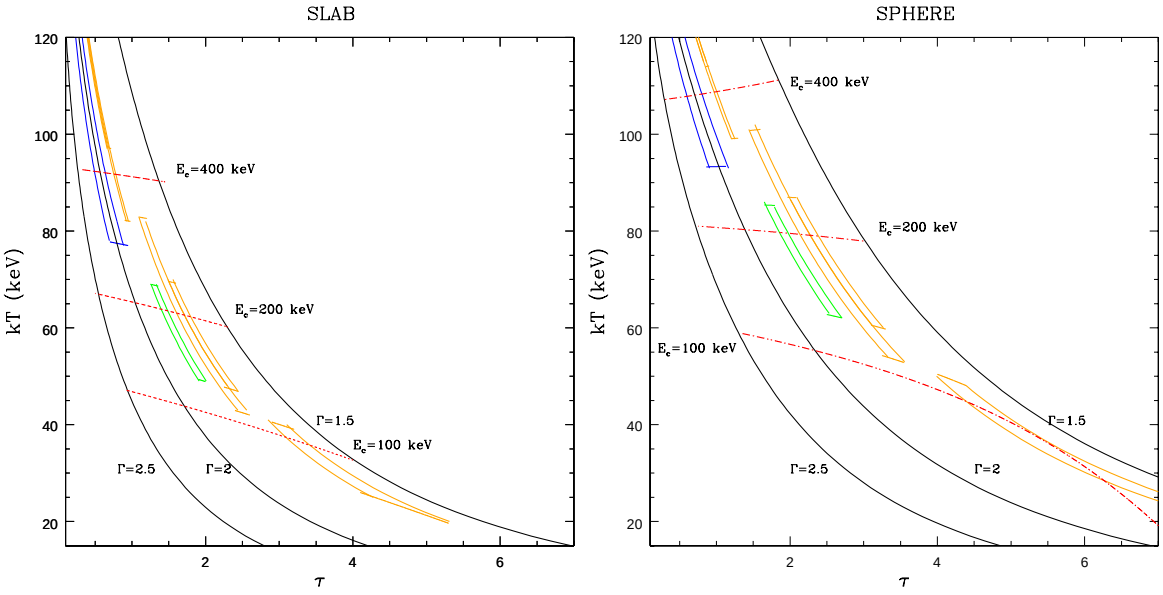

Figure 5.5. The contours in the τ_e-kT$_e$ for HE 0436-4717 (blue), NGC 7469 (green) and NGC 4593 (gold) are showed.

In Fig. 5.5 the objects studied in this thesis occupy the locus of the physical parameters considering in the simulations, and the obtained contours cover a large fraction of the region delimited by the iso-curves of the phenomenological parameters. Data of

HE 0436-4717 did not allow for measuring the source high energy cut-off, thus the corresponding contours, for both the geometries, are not limited at high kT_e. NGC 4593 contours corresponding the estimates above 120 keV are not displayed. Concerning this latter source, variability of the coronal properties is clearly observed.

Then, the obtained kT_e and τ_e measurements can be compared with those spectroscopically showed in Chapter 4 using *nthcomp*. The coronal temperature is a free parameter in *nthcomp*, while the electron opacity is computed using the internal routine accounting for the Thompson cross-section:

$$\tau_e = \sqrt{2.25 + 3/(\theta_e \times ((\Gamma + 9.5)^2 - 2.25))} - 1.5 \ . \tag{5.6}$$

This formula allows for computing the optical depth of an infinite spherical corona.

Therefore, in Table 5.1, we tabulate MoCA-based coronal values derived using Eq. (5.2), Eq. (5.4) Eq. (5.3), Eq. (5.5) and estimates provided by the spectral analyses reported in Chapter 4.

In Table 5.1, the optical depths and temperatures for the slab case are always smaller with respect to values derived assuming a spherical corona (see also Fig. 5.5). This behaviour results from the fact that in a Comptonising spherical corona the optical depth τ_e is the same in all the directions, while, for the slab-case, τ_e increases for all the directions that are different from the vertical one. On the other hand, the comparison between the MoCA-based estimates for the sphere with coronal properties obtained with *nthcomp* does not provide a clear trend for these sources.

As a further step, we can enlarge our study on the AGN coronal propertied by applying the formulae presented in previous Sect. 5.3 on a larger sample of AGN. This larger sample allows us to further compare MoCA-based results with those already published by other authors and obtained using different analytical models. To perform such a comparison we considered a sample of AGN reported by Tortosa et al. (2018). Using literature values for the high energy cut-off and the photon index we estimate the coronal parameters of the various objects, and subsequently, we compare these values with those from past studies. By computing the $kT_e - \tau_e$ contours with our formulae we obtain with Fig. 5.6.

The region of the kT_e-τ_e parameters simulated using MoCA is well covered by the data. In this Fig. 5.7, we estimated values for NGC 4593 by using best-fitting E_c and Γ for the summed spectra, (see Ursini et al. 2016). Higher temperatures have to be investigated NGC 5506 and assuming a spherical corona, indeed, although we have a measure for its high energy cut-off, its contour is not limited at high kT_e.

Then, we compare our estimates with those from other models, see Fig. 5.7. MoCA-based estimates of the slab-like coronal opacity seem, on average, larger than τ_e obtained with other models (see top left panel of Fig 5.7), while no trend is found between MoCA and literature values of the electron temperature. For the spherical case, MoCA estimates

Table 5.1. MoCA parameters for the sources analysed in Chapter 4 Moreover, for comparison the coronal parameters obtained using *nthcomp* are quoted.

NGC 7469	Slab	Sphere	*nthcomp*
kT_e(keV)	57^{+11}_{-6}	74^{+13}_{-11}	45^{+15}_{-12}
τ_e	$1.7^{+0.3}_{-0.5}$	$2.2^{+0.5}_{-0.6}$	$2.6^{+0.9}_{-0.9}$
HE 0436-4717			
kT_e(keV)	>77	>93	>65
τ_e	<0.8	<1.1	<1.3
NGC 4593 1a			
kT_e(keV)	>120	>134	>60
τ_e	<0.3	<0.4	<1.7
obs. 1b			
kT_e(keV)	56^{+26}_{-13}	74^{+28}_{-21}	>80
τ_e	$1.8^{+0.7}_{-0.8}$	2.5^{+1}_{-1}	<1.5
obs. 2			
kT_e(keV)	32^{+9}_{-12}	35^{+15}_{-15}	17^{+20}_{-4}
τ_e	$3.7^{+1.6}_{-0.8}$	$5^{+0.5}_{-0.5}$	$2.1^{0.4}_{-0.9}$
obs. 3			
kT_e(keV)	56^{+14}_{-9}	72^{+15}_{-12}	>30
τ_e	$2^{+0.5}_{-0.5}$	$2.7^{+0.6}_{-0.6}$	<3.2
obs. 4			
kT_e(keV)	99^{+35}_{-17}	115^{+30}_{-20}	>150
τ_e	$0.7^{+0.3}_{-0.4}$	$0.8^{+0.5}_{-0.4}$	<0.9
obs. 5			
kT_e(keV)	>97	>113	>140
τ_e	<0.7	<0.9	<0.9

of the coronal opacity and electron temperature, besides a few exceptions (e.g. NGC 5506), are compatible with measurements from *compTT* (slab and sphere), *nthcomp* (sphere), and *compPS* (sphere).

5.5 Discussion and Summary

In this Chapter, we have discussed the first systematic application of the code MoCA (Tamborra et al. 2018) to observe X-ray spectra of AGN. MoCA is flexible and allowed us to simulate X-ray spectra assuming a wide range of parameters describing the AGN as well as the Comptonising medium. Using a phenomenological model (cut-off power law), we fitted all the synthetic spectra and obtained relations through which convert

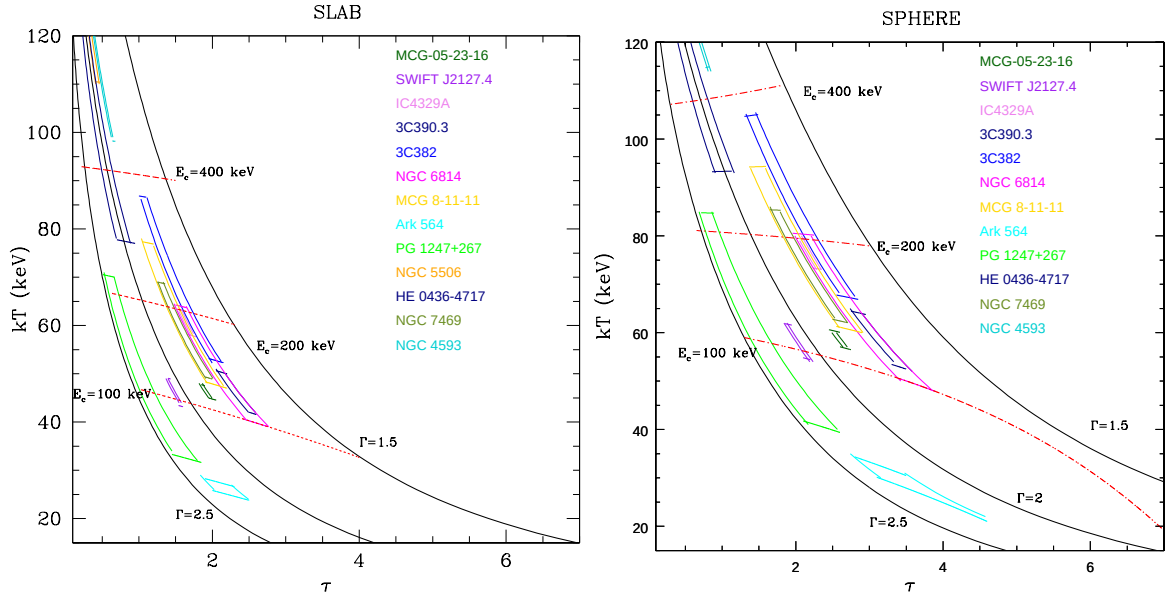

Figure 5.6. Black solid lines represent the iso-Γ curves, while iso-E_c are showed via the red solid-dashed lines. Iso-Γ curves have a 0.2 step and Γ steepens from right to left. A 50 keV step is used for representing the various high energy cut-off iso-curves. Right panel: For a sample of AGN in Tortosa et al. (2018) we computed the corresponding contours using Eq. 5.2 and 5.4.

phenomenological information (Γ and E_c) into the coronal electron temperature and optical depth.

Our analysis reveals that the observed Γ depends mainly on Compton parameter y but with a further dependence on kT_e. In a similar fashion, the measured E_c is not only a function of the coronal temperature, but also of the optical depth, see Eq. (5.2) Eq. (5.4), Eq. (5.3) and Eq. (5.5).

For the case of a spherical geometry, we can compare our Eq.(5.3) with the relation obtained by Beloborodov (1999): $\Gamma = \frac{4}{9} y^{-2/9}$. Beloborodov (1999) computed his equation by studying spectra simulated with the code by Coppi (1992) for only two values of kT_e (50 and 100 keV) and letting free to vary the electrons opacity. Moreover, in his computations, the Comptonising medium is infinite. In the work by Beloborodov (1999), the photon index is only a function of the Compton parameter and Γ-y points at fixed temperature are only weakly scattered around the best-fit relation. On the other hand, in our Eq.(5.3) (see also Fig. 5.3), Γ-y points are largely scattered, and the photon index has a further dependence on kT_e besides the one on y. The explanation of a such large spread is not trivial, but as a first order approximation, it can derive from differences between MoCA and the code by Coppi (1992). Besides the peculiar MonteCarlo approach

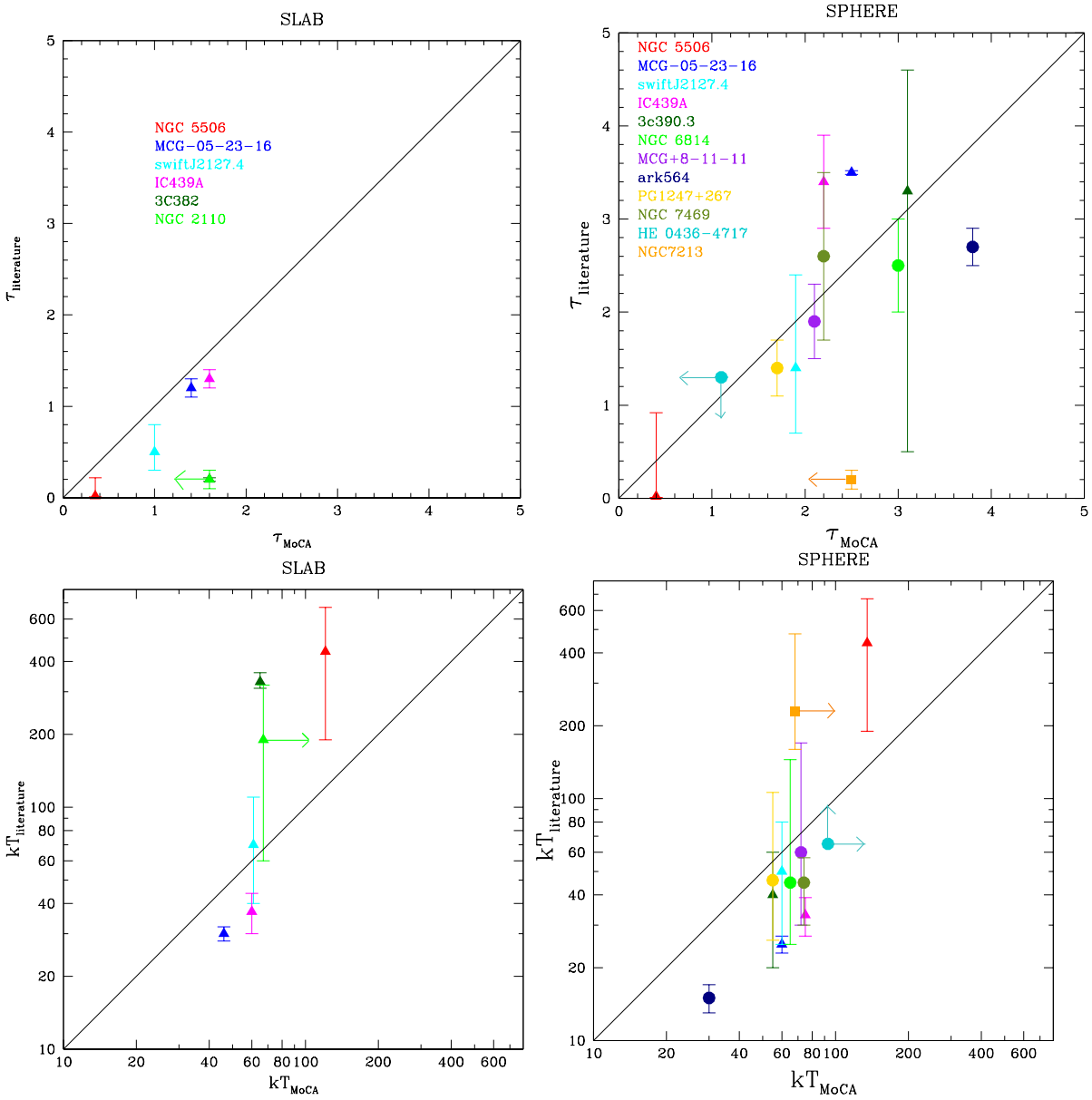

Figure 5.7. In the panels, we compare estimates of kT_e and τ_e obtained with MoCA and using different models *nthcomp* (triangles) *compTT* (circles) *compPS* (squares) (see Tortosa et al. 2018, and teferences therein). The secant to the graph is also showed. Top and bottom left panels are computed for a slab-like corona, while remaining panels account for the spherical case. Different coloured names correspond to the various sources that are the same between top and bottom left panels and top and bottom right panels.

of MoCA differences arises in the usage of the scattering cross-section and in the self-consistent way used by MoCA to account for special relativity. Moreover, discrepancies

can be due to geometrical issues.

Concerning the high energy cut-off, we found that the E_c=2-3 kT_e is valid only for a small range of parameters, in particular for low τ_e and kT_e, see Fig.5.4. Moreover, as showed by Eq. (5.4) and Eq. (5.5) this quantity also depends on the coronal optical depth.

The formulae presented in Sect. 5.3 have been used for investigating the coronal properties of the Seyfert galaxies studied in Chapter 4. In particular, we computed their coronal temperatures and optical depths using the corresponding high energy cut-offs and photon indices found in this thesis (for NGC 7469 and HE 0436-4717) and by Ursini et al. (2016) for NGC 4593 (see Table 5.1 and Fig 5.5). In a similar fashion and using literature values quoted by Tortosa et al. (2018), we computed MoCA-based estimates for the coronae of a sample of AGN studied by other authors in previous works. According with Fig. 5.7, values of τ_e derived for the case of a slab corona with MoCA are, on average, higher with respect to measurements of the same quantity obtained using *compTT*. However, the origin of this discrepancy is not trivial and it can be the result of differences between the codes and on the geometrical assumptions. On the other hand, MoCA-based estimates for the physical parameters are compatible within the errors with measurements obtained using other various models (*nthcomp,compTT,compPS*) for the case of a spherical geometry.

These findings are not conclusive and further work is required to refine our results. First of all, we have to quantify the dependence of our conversions on the physics of the AGN. In particular, we need to determine how much Eq. (5.2), Eq. (5.4), Eq. (5.3), Eq. (5.5) are a function of the BH mass and the AGN accretion rate, and, in turn, of the seed photon spectrum. From preliminary tests, the Comptonised spectra obtained varying the seed thermal photons spectral shape exhibit a similar behaviour with those presented in this thesis. Thus, it suggests that the resulting Comptonised spectrum is weakly affected by the spectral properties of the seed photons radiation field.

Then, we need to shed light on the origin of the highly scattered Γ-y relations and on the comparison with MoCA estimates for the slab corona with respect to *compTT*.

Moreover, all the simulations analysed in this Chapter have been produced for the case of an extended Comptonising corona characterised by an outer and inner radius of r_g=500 and r_g=6, respectively. On the other hand, different arguments provide evidence for the presence of a compact corona instead of an extended medium. First of all, variability arguments support the corona to be compact (Uttley et al. 2014, and references therein). Microlensing analyses also are in agreement with a scenario in which the X-ray emitting region has to be compact (e.g. Chartas et al. 2009; Morgan et al. 2012). For the specific case of the *Ark* 120, one of the proposed scenarios to explain its variable broad component of the Iron Kα envisages a change in the spatial extension of the hot/warm coronae, which leaves the innermost regions of the accretion disc uncovered (Nardini

et al. 2016). Then, it is of primary importance testing Comptonisation in such a scenario.

Finally, we find that from the spectroscopic point of view, we are not able to discriminate the coronal geometry. This is also showed by the case of *ARK* 120 (Marinucci et al. submitted), who demonstrate that only with polarised light we will spectroscopically distinguish between a slab or a spherical corona. AGN X-ray radiation is expected to be polarised and the polarisation degree depending mainly on the geometry and optical depth of the corona. Then, taking advantage of MoCA that is especially suited for studying polarised signals, we will perform simulations to investigate the AGN coronal emission in polarised light. Indeed, the analysis on these spectra will help us in understanding how X-rays emitted by coronae of different geometries behave. Then, the contribution of MoCA will be valuable in the context of the forthcoming observatories sensible on X-ray polarised photons such as IXPE (e.g. Weisskopf et al. 2016b,a) and eXTP (e.g. Zhang et al. 2016).

Chapter 6

Long-term variability analysis

A fundamental AGN feature is variability. Indeed, active galaxies have been observed to vary yearly and hourly. On the other hand, the key mechanism behind a such variable emission is debated.

Here we present the ensemble variability properties of a rich AGN sample extracted from MEXSAS (Vagnetti et al. 2016). In particular, we will discuss how flux variations behave on the longest temporal interval ever scrutinized in the X-ray, ∼20 years. The main objective of this work consists in identifying a typical timescale (corresponding to a flattening of the structure function, see Chapter 3) for flux variations occurring in the 0.2-2 keV, the X-ray band studied. Results will be discussed on light of the two-corona model, and assuming the soft-excess to be the component mainly contributing to the flux in this band. Concerning this latter point, we notice that although sources presented in the forthcoming analysis span a wide redshift interval, the majority of them lie at low z, thus we are likely observing their soft-excess emission in 0.2-2 kev band, being the contribution on the overall result of high redshift AGN (for which we are likely observing their primary emission rather than the soft-excess) negligible.

6.1 introduction

As already said, X-ray variability provides a formidable tool for investigating the X-ray emitting regions, and it provides a way to estimated the source black hole mass. If fast flux variations are directly related with the source black hole mass, long term fluctuations remains poorly studied.

Variability was selected as a defining characteristic of AGN (e.g. Matthews & Sandage 1963; Elliot & Shapiro 1974b). Flux variations occur on different timescales, from hours (Ponti et al. 2012), up to several years (e.g. de Vries et al. 2003; Vagnetti et al. 2011a, 2016; Gallo et al. 2018). The process originating Single-source analyses are often performed using the power spectral density analysis (PSD). However, this analysis needs

well sampled light curves that are only available for few objects. The PSD approach finds a break at high frequencies that is connected with the BH mass (e.g. Papadakis 2004b; McHardy et al. 2006), while, even if a low frequency break is expected, we have experimental evidences of it only for a couple of sources: for example, *Ark* 564 (Pounds et al. 2001b; Papadakis et al. 2002; McHardy et al. 2007b) and NGC 3783 (Markowitz et al. 2003b).

As reported by several authors (e.g. Zhang 2011; Young et al. 2012; Shemmer et al. 2014), AGN display flux variations also on larger temporal scales. It is possible to investigate variability on larger time intervals using the structure function (SF) analysis (e.g. Simonetti et al. 1985; Vagnetti et al. 2011a). SF works on the time domain and can be used in statistical studies even when objects have poorly sampled light curves, see details in Sect. 6.3 In this context, a statistical approach to characterise variability (Vagnetti et al. 2016) is useful to point out some averaged properties shared by AGN. Further to this, an ensemble study minimises the effect of anomalous sources if they are present. To date, we know that X-ray variability increases as a function of the time interval at which we investigate the sources. This means, in an average sense, that if we compare flux measures performed in two different epochs we can expect that, the larger is the delay τ between the two observations, the larger will be the difference between the two fluxes.

Variable X-ray absorption, which is commonly observed in Seyfert galaxies, can also contribute to the X-ray variations. In particular, changes of the X-ray absorbing column density are ubiquitous in type 2, with timescales ranging from hours to years (Risaliti et al. 2002). Moreover, X-ray absorption variability has also been found in a number of type 1 (see e.g. Markowitz et al. 2014; Puccetti et al. 2007; Turner et al. 2008).
The shorter-term variations in covering fraction of partially covering absorbers are generally ascribed to eclipses by clouds from the broad-line region (e.g. Risaliti et al. 2011). Longer-term variations both in type 1 and type 2, on timescales up to a few years, could be produced by a pc-scale torus with a clumpy structure, with type 2 having a much higher probability (e.g Markowitz et al. 2014). We do not investigate the absorption variability contribution in the present work, however a possible signature of this may be searched for by selecting a subsample of AGN inclined at large viewing angles, adopting angular indicators, as, for example, proposed by Shen & Ho (2014).

The source sample we analyse in this work is based on serendipitous observations performed by XMM-Newton and ROSAT data. ROSAT observations are needed in order to investigate variability on long timescales. In fact, other authors have already compared ROSAT and XMM-Newton data for different purposes (e.g. Saxton et al. 2011; Strotjohann et al. 2016); comparing data from these two satellites, we are now able to perform a long-term variability analysis for a sample of 2,856 AGN observed from early nineties up to 2015.

6.2 Data

In this work we have used X-ray data obtained by the XMM-Newton and ROSAT satellites. The 3XMMSSC-DR5[1] (Rosen et al. 2016) contains 565,962 X-ray detections belonging to 396,910 single sources. The observations were performed between February 2000 and December 2013, thus data cover a large time interval, see Fig. 6.1. Furthermore, this catalogue is very suitable for ensemble variability studies since it contains 70,453 sources observed at least twice (up to 48 times) for a total of 239,505 multi-epoch observations.

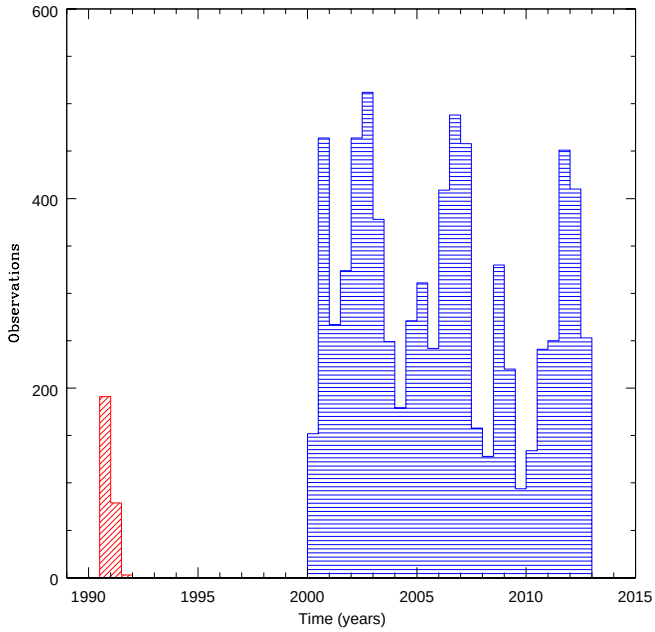

Figure 6.1. Time distribution of the observations coming from the XMM-Newton mission (blue, horizontal shading) and ROSAT (red, slanted shading).

As mentioned above, XMM-Newton observations were carried out over a period of 13 years, however because of the redshift, the maximum length for the rest-frame light curves of these sources is approximately eight years, as is shown in Fig. 6.2. To enlarge our investigating temporal window we have taken advantage of the RASS-BSC (Voges et al. 1999) and RASS-FSC (Voges et al. 2000), which store respectively 18,806 and 105,924 X-ray detections. ROSAT observations were obtained between July 1990 and August 1991, thus comparing this information with data performed by *XMM-Newton* we can study variability up to time lags of about 20 years.

[1] http://xmmssc.irap.omp.eu/

The 3XMMSSC-DR5 as well as the RASS catalogues contain X-ray detections with no information concerning their nature. Therefore to extract from the sample only AGN we cross-correlated these data with the quasar catalogues by the Sloan Digital Sky Survey (SDSS), the SDSS-DR7Q (Schneider et al. 2010) and the SDSS-DR12Q (Pâris et al. 2016). The SDSS quasar catalogues do not include classes of active galactic nuclei such as BL Lacertae and Type 2 objects, thus they allow us to build a homogeneous sample of type 1 AGN. To cross-match catalogues we took advantage of the software TOPCAT[2] (Taylor 2005, 2006).

We obtained our quasar sample extracting from the 3XMMSSC-DR5 only observations of AGN. To do this we cross-matched the serendipitous source catalogue by XMM-Newton with both SDSS-DR7Q and SDSS-DR12Q using a 5 arcsec cross-correlating radius. Moreover, we accounted for the quality of the observations selecting only the observations with a SUM_FLAG value smaller than three, as suggested by the 3XMMSSC team. This procedure led us to obtain 14,648 matches corresponding to 2700 multiply observed AGN (7,837 observations) and 6,801 pointed only once. The sample of sources with multiple observations corresponds to the Multi-Epoch XMM Serendipitous AGN Sample, MEXSAS[3], already presented in Vagnetti et al. (2016). In the following we will refer to the extended sample containing both multiple and single observations as eMEXSAS.

To test our matches we used a larger radius of 10 arcsec for which the cross-correlation algorithm produces 15,095 matches indicating a possible incompleteness of the order of 3%. Furthermore, we checked our cross-correlations, giving a set of spurious coordinates shifted by 1 arcmin in declination to the eMEXSAS entries and we obtain 44 matches indicating that our sample contains false occurrences of the order of 0.3%.

Then, we cross-correlated our extended sample eMEXSAS with the RASS-BSC and the RASS-FSC adopting a radius of 30 arcsec. This leads us to obtain 281 sources observed by the two satellites for a total of 490 available observations. This cross-match is a crucial point in our work, then we repeat the cross-correlations using a set of false coordinates, shifting by one degree in declination finding six matches. This suggests that our sample contains a $\sim$1% of possible contamination within the adopted matching radius. Then we checked our cross-correlations again using the column of quasar catalogues SDSS-DR12 and SDSS-DR7 in which a ROSAT count rate coming from the SDSS identification is available. We discarded a few sources from our sample for which there is no SDSS identification. This reduced our sample to 273 single sources observed both by XMM-Newton and ROSAT. For these sources the maximum length of the light curves Δt_{rest} is as long as 19 years, see Fig. 6.2.

[2]http://www.star.bris.ac.uk/$\sim$mbt/topcat/

[3]Available at:
http://vizier.cfa.harvard.edu/viz-bin/VizieR?-source=J/A+A/593/A55

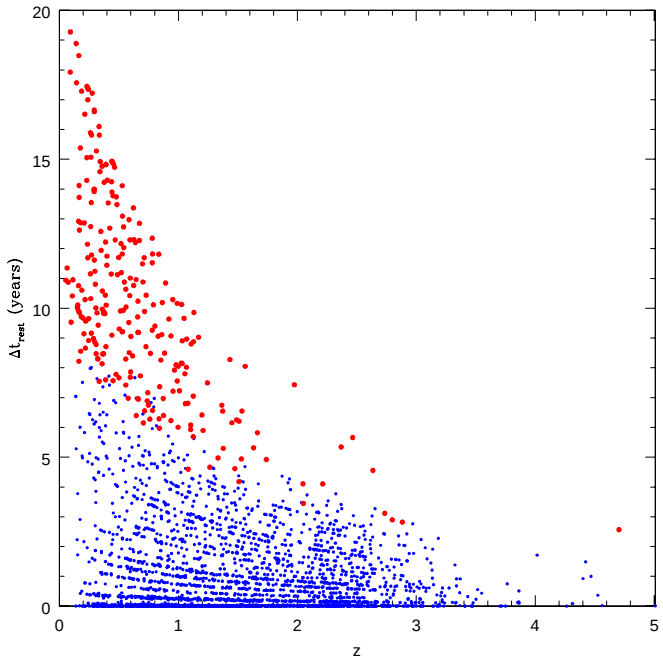

Figure 6.2. Length of the light curve in the rest frame, Δt_{rest}, for each source, as a function of the redshift. Small blue dots: XMM-Newton data alone, larger red points: combined XMM-Newton+ROSAT data.

Data used in this work are provided by two missions with different characteristics (e.g. Truemper 1982; Strüder et al. 2001b, respectively for ROSAT and XMM-Newton), therefore it is not possible to compare their measurements in a straightforward way. In the following we describe the steps we performed to produce a reliable comparison of our data. The first issue we face is due to the different energy bands used by ROSAT and XMM-Newton to scan the sky. The ROSAT X-ray telescope, in fact, operated in the 0.1-2.4 keV band while XMM-Newton performs observations in the energy band 0.2-12 keV. Due to the smaller energy range of ROSAT we can study variability at long time lags only in the soft X-ray band. In order to make the measure performed compatible in these different observational bands, we made use of the online tool WebPIMMS[4].

To convert ROSAT count rate to fluxes we set WebPIMMs as follows: Galactic absorption $N_H = 3 \times 10^{20}$ cm^{-2}, source model power law with a $\Gamma = 1.7$ (the same values are used in the 3XMMSSC-DR5 by Rosen et al. 2016), input energy range 0.1-2.4 keV and output energy range 0.2-2 keV. These flux measures have to be compared with those obtained from 3XMMSSC-DR5. The serendipitous catalogue reports flux measures in the small energy bands $EP1\_FLUX$ (0.2-0.5 keV), $EP2\_FLUX$ (0.5-1.0 keV), $EP3\_FLUX$ (1.0-2.0 keV). We combined the flux measures in the energy bands EP1, EP2, EP3 adopting the procedures described by Watson et al. (2009) in their Appendix 4, D.4, getting, for all the sources in our sample, a soft integrated flux in the energy band 0.2-2 keV.

6.3 Analysis

Structure function is a powerful method used in several electro-magnetic bands by many authors, in the Optical-UV (e.g. Trevese et al. 1994; Kawaguchi et al. 1998; de Vries et al. 2003; Bauer et al. 2009) as well as in the radio domain (e.g. Hughes et al. 1992). Since 2011 SF analysis has also been used in the X-ray band where authors produced variability studies for statistically rich AGN populations (Vagnetti et al. 2011a, 2016). Structure function works in the time domain and it is suitable for ensemble studies. This is a real advantage because, even if for single source variability characterization SF as well as PSD need richly sampled light curves, for an ensemble approach SF can be adopted also when only poorly sampled light curves are available. Structure function describes variability giving a measure of the mean change between two observations separated by a time lag τ. Different mathematical formulations for SF have been used in the past (e.g. Simonetti et al. 1985; di Clemente et al. 1996), however in this work we adopt the

[4]https://heasarc.gsfc.nasa.gov/cgi-bin/Tools/w3pimmw/w3pimms.pl

following definition for this variability estimator:

$$SF(\tau) = \sqrt{\langle [\log f_X(t+\tau) - \log f_X(t)]^2 \rangle - \sigma^2_{noise}} \ . \tag{6.1}$$

In Eq.1 τ is the lag elapsing between the two available flux measures and σ^2_{noise} is the quadratic contribution of the photometric noise to the observed variations:

$$\sigma^2_{noise} = \left\langle \sigma^2_n(t) + \sigma^2_n(t+\tau) \right\rangle \ , \tag{6.2}$$

where σ_n is the photometric error of the logarithmic flux at a given epoch. The average quantities in Eq. 6.1 and Eq. 6.2 are computed within an appropriate bin of time lag around τ.

Our sample of sources spreads on a large redshift interval, thus we compute the time lag in the source rest-frame,

$$\tau_{rest} = \frac{\tau_{obs}}{1+z} \ . \tag{6.3}$$

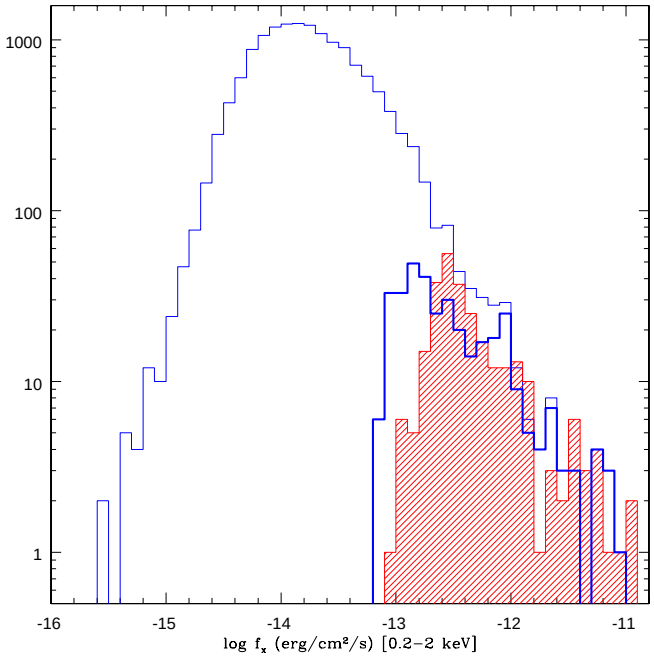

Figure 6.3. Flux distribution in the 0.2-2 keV band for the observations belonging to the different subsamples. Thin blue histogram: MEXSAS; thick blue histogram: XMM-Newton observations brighter than 7.5×10^{-14} erg/cm^2/s for the sources observed by ROSAT; red shaded histogram: ROSAT fluxes.

Our soft long-term SF analysis takes advantage of eMEXSAS and the AGN selection observed by ROSAT. SF is computed using all the light curves for the sources belonging to eMEXSAS and extending these light curves for the combined XMM-Newton and ROSAT relevant subsample.

Observations performed by a single mission allow us to compute structure function straightforwardly but in the case of combined light curves, data are obtained from two satellites with different instrumental properties. In particular for this study we take care of the different sensitivities of the two space observatories. For quasars observed by the two missions, ROSAT fluxes have values spanning between 6.6×10^{-14} erg/cm^2/s and 1.2×10^{-11} erg/cm^2/s. On the other hand, due to its more recent technology, fluxes detected by XMM-Newton are also fainter, down to 2.5×10^{-16} erg/cm^2/s. Structure function, as shown by Eq. 6.1, describes variability comparing flux measures performed in different epochs, thus the different sensitivities of the two satellites could introduce a bias, which would give an overestimate of the large flux variations (in this case the increase of the SF might be an artefact), being on average ROSAT detections much brighter than XMM-Newton measurements. Moreover, a possible bias for the cross calibrations between XMM-Newton and ROSAT observations has been discussed by Shemmer et al. (2014) who estimate that this does not exceed the 10% of the flux measures. Following the procedure outlined by Saez et al. (2012), we added in quadrature to the errors of each measured flux a 10% error. This increases slightly the estimate of the flux errors for the brightest sources, however its effect on our variability analysis is very small (see below).

Furthermore, ROSAT measures are systematically sampling earlier times. This means that when we evaluate SF, fluxes at earlier epochs are in average larger with respect to later epoch measures performed by XMM-Newton. Therefore light curves tend to have a decreasing behaviour, in average, for these sources. This leads us to define a common threshold for the XMM-Newton and ROSAT fluxes such that the corresponding flux distributions span a similar interval. The adopted threshold (7.5×10^{-14} erg/cm^2/s) optimises the overlap between the two distributions, see Fig. 6.3 where the flux distribution of the overall MEXSAS sample is also shown for comparison. This discards 53 ROSAT sources associated with XMM-Newton fluxes fainter than the threshold, so that our subsample of combined light curves is reduced to 220 sources. In Fig.6.4 we show on the $L_X - z$ plane the distribution of the sources we study in this work constituted by MEXSAS (2700 sources, small blue dots) plus the 220 from ROSAT (empty red squares). We note that the two samples span a similar range in luminosity, thus the luminosity dependence of X-ray variability (see e.g. Vagnetti et al. 2016) should not introduce a difference between the two samples.

We now discuss the effect of the different flux limits of the ROSAT and XMM-Newton catalogues displaying in Fig. 6.5 the distributions of the logarithmic flux variations expected for our combined lights curves in two cases: if we include XMM-Newton fluxes

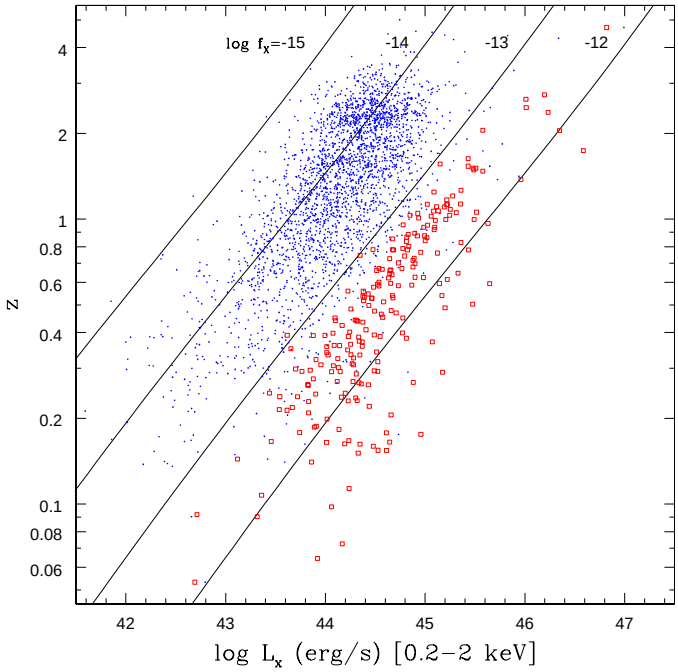

Figure 6.4. Distribution of the sources for which SF is computed in the L_X-z plane. The small blue dots represent the average values of the X-ray luminosity for sources with multiple XMM-Newton observations (MEXSAS), while empty squares represent the luminosity and redshift computed from ROSAT observations.

fainter than the adopted threshold we find an asymmetric distribution with an excess tail towards negative large variations (yellow shaded in Fig. 6.5); cutting instead the XMM-Newton measures to fluxes larger than the threshold, the asymmetry of the resulting distribution is strongly reduced (red histogram in Fig. 6.5). For comparison we display in the same figure also the corresponding distribution for the MEXSAS sample alone.

We show in Fig. 6.6 the distribution of the rest frame time lags for sources belonging to MEXSAS (blue histogram) and to the ROSAT and XMM-Newton combined sample (red shaded histogram). As Fig. 6.6 displays, the contribution of the ROSAT data is particularly important for the larger rest-frame timescale ($\tau \gtrsim 8$ years) while, for smaller time lags, this contribution is almost negligible compared to data of MEXSAS.

Finally, using Eq. 6.1 we are able to compute the longest structure function ever performed for ensemble X-ray variability studies. In Fig. 6.7 we present the binned structure function showing the contributions of the combined ROSAT-XMM-Newton data in red and only in the bin $\tau_{rest} \gtrsim 8$ years while, for the bins at smaller time lags, we plot only

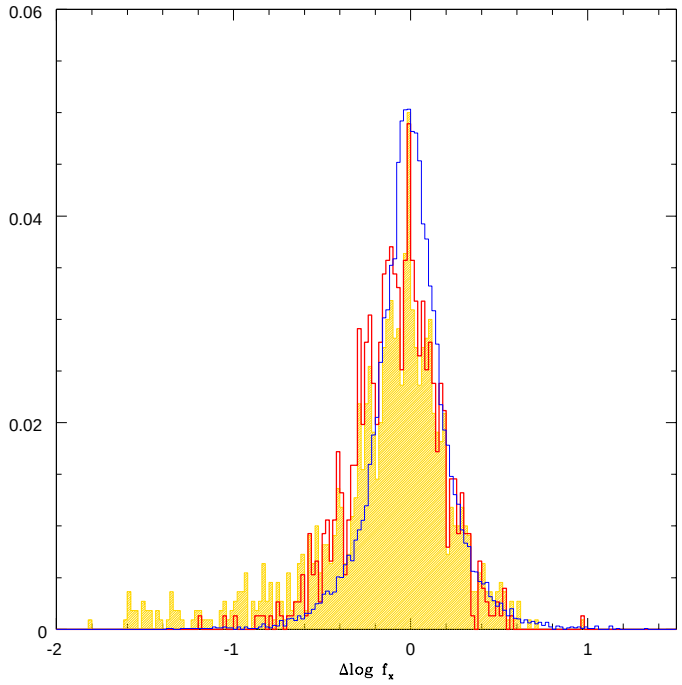

Figure 6.5. Distribution of the logarithmic flux variations, normalised to the total number. Yellow shaded histogram: combined ROSAT XMM-Newton light curves including all the data. Red histogram: the same as before but removing the XMM-Newton fluxes fainter than 7.5×10^{-14} erg/cm^2/s. Blue histogram: XMM-Newton-only light curves for the MEXSAS sample.

the dominant contribution coming from MEXSAS. For comparison, we also draw an estimate of the SF in the last bin using the full XMM-Newton light curves without removing the fluxes fainter than the previously discussed threshold. However, this corresponds to an overestimate ($\sim 75\%$) of the variability, while a more conservative estimate is also indicated on the figure, computed with only the ROSAT and XMM-Newton measurements brighter than the threshold. Figure 6.7 also shows the contribution of the measurements errors (dashed line); the previously discussed intercalibration errors are included in our analysis, slightly increasing the error contribution (by $\sim 5\%$) for the combined XMM-Newton/Rosat bin. However the effect on the SF (according to Eq. 6.1), is negligible, $\sim 1\%$.

The computed SF still increases for time lags as long as twenty years and we do not find evidence for a flattening. The increase of the structure function can be fitted by a power-law $SF \propto \tau^b$, with $b = 0.154 \pm 0.011$ for the eight bins spanned by XMM-Newton data, and $b = 0.153 \pm 0.010$ including the ROSAT bin in its conservative estimate discussed above. Our results are in agreement with those of Zhang (2011), who reported a lack of a low-frequency break in the PSD of local AGN, using RXTE light curves on

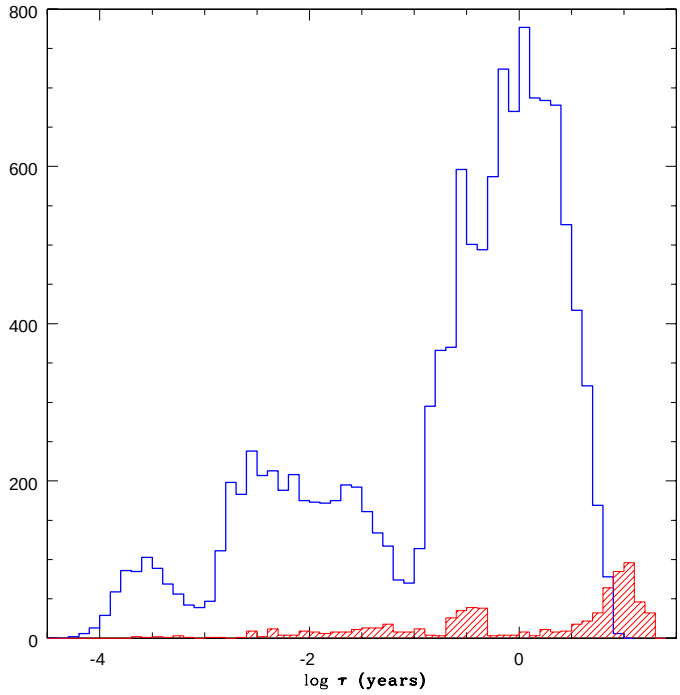

Figure 6.6. Distribution of the rest frame time lags for MEXSAS sources (in blue) and for the combined XMM-Newton (with fluxes brighter than 7.5×10^{-14} erg/cm^2/s.) and ROSAT data in red. Combined observations extend the distribution to larger time lags.

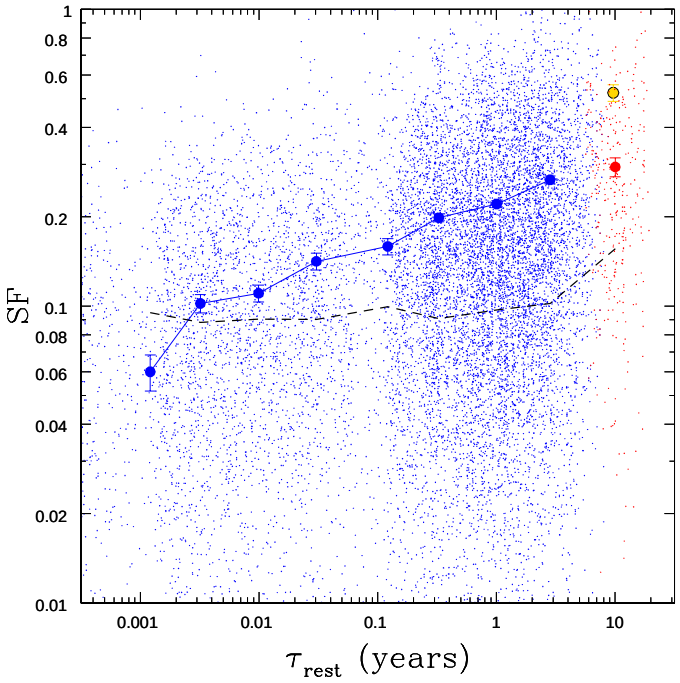

Figure 6.7. Ensemble structure function for the sources studied in this work. Blue points represent the averaged SF values and take advantage only of XMM-Newton observations, while the red point is obtained also using data from ROSAT. The red point refers to 220 AGN pointed by both the satellites and is computed cutting the XMM-Newton fluxes to the ROSAT flux threshold as discussed in the text. The yellow, black circled point is computed without removing the XMM-Newton fluxes fainter than the threshold, and it strongly overestimates the amount of variability. The black dashed line is the contribution of the noise (as defined in Eq. 6.2) for the whole investigated time-lag interval. Small dots represent the variations for the individual pairs of measurements contributing to the SF and the colours emphasise the different subsamples used during the SF calculation.

timescales of around ten years. This nicely complements our results on a large sample of high-z objects, suggesting a similar long-term variability trend in local AGN and quasars.

6.4 Discussion

The SF presented in the previous section does not show a flattening at long timescales which, in principle, could be expected considering the finite size of the emitting region. As discussed by, for example, Czerny (2006), X-ray variability on short timescales can be originated by intrinsic fluctuations of the X-ray source while, at longer timescales, the observed X-ray variations can be affected by optical-UV fluctuations. Indeed, also optical SF computed by de Vries et al. (2005) shows a similar behaviour with an increase at long time lags. However, MacLeod et al. (2012) report a SF flattening at about two years, although the authors do not rule out a continuing but slower rise.

It is possible to interpret our result considering previous works by Lyubarskii (1997) and Arevalo (2006). These authors discuss about the propagating fluctuations model in which optical long term variations originated in the external region of the disk propagate through it affecting variability in the X-ray band. Flux variations acting on short timescales produced in the disk regions closer to the central engine are therefore modulated by long term variations. We note that the influence of disk-born fluctuations on the X-ray variations is also supported by the variability of the X-ray-to-optical spectral index α_{ox}, which increases at year-long timescales (Vagnetti et al. 2010, 2013). In this scenario, the size of the disk could leave some track on our SF, therefore we want to estimate the characteristic timescales in the external part of the accretion disk.

Following Czerny (2006), we focus on the dynamical timescale, which is shorter than the viscous and thermal timescales, and can be expressed for a Keplerian optically thick and geometrically thin disk as follows:

$$\tau_{dyn} = 7 \times 10^{-5} (R/R_g)^{3/2} M/M_\odot \text{ yrs}, \tag{6.4}$$

where $R_g = GM/c^2$ is the gravitational radius and M is the black hole mass. The external size of the accretion disk is not well known, however it can be estimated following the work by Collin & Huré (2001), who argue that for large radii ($\gtrsim$ 1000 R_g) the disk becomes self gravitating. They estimate a critical radius R_{crit} at which the disk becomes gravitationally unstable, fragmenting and possibly giving rise to the broad line region. R_{crit} depends on the Eddington ratio and on BH mass. In the interval $0.01 < L/L_{bol} < 1$ the dependence on the mass can be approximated as

$$R_{crit}/R_g = 3 \times 10^7 (M/M_\odot)^{-0.46} , \tag{6.5}$$

which corresponds to a disk size $R = 1.5 \times 10^{-6} (M/M_\odot)^{0.54}$ pc. At this point we can combine the equations to get a self-consistent estimate for the dynamical time at the

outer border of the accretion disk R_{crit} as a function of the BH mass:

$$\tau_{dyn} = 0.35(M/M_{\odot})^{0.31} \text{ yrs.} \tag{6.6}$$

Equation 6 suggests timescales of several decades for black hole masses of $10^6 - 10^9$ $M_{\odot}$. Therefore an increase of SF at twenty years appears compatible with the estimated disk sizes.

The geometrical and physical properties of the X-ray-emitting region are not yet fully understood. On the one hand, the power law-like continuum emission in hard X-rays is generally believed to originate in a hot and compact corona, likely located in the inner part of the accretion flow (e.g. Reis & Miller 2013). However, on the other hand, an excess of emission below 1-2 keV above the extrapolated high-energy power law is commonly observed in the spectra of AGN (e.g Walter & Fink 1993; Bianchi et al. 2009). Albeit the nature of this so-called soft X-ray excess is uncertain (e.g. Done et al. 2012b), a possible explanation is thermal Comptonisation by a warm, optically thick medium (e.g. Magdziarz et al. 1998; Petrucci et al. 2013b). In particular, Petrucci et al. (2013b) studied the high-energy spectrum of Mrk 509 in detail, using the data from a long, multiwavelength campaign (Kaastra et al. 2011b). This source showed a correlation between the optical-UV and soft ($<$ 0.5 keV) X-ray flux, but no correlation between the optical-UV and hard ($>$ 3 keV) X-ray flux (Mehdipour et al. 2011b). Indeed, Petrucci et al. (2013b) found that the spectrum is well described by a two-corona model: a warm ($kT\sim$1 keV), optically thick ($\tau \sim 15$) corona responsible for both the optical-UV emission and the soft X-ray excess, and a hot ($kT\sim$ 100 keV), optically thin ($\tau \sim 0.5$) corona responsible for the hard X-ray emission. Moreover, the authors affirm that the warm corona agrees with a slab geometry, thus it may cover a large fraction of the disk (Petrucci et al. 2013b). Other authors (e.g. Janiuk et al. 2001b; Różańska et al. 2015) suggest that this warm corona could be the upper layer of the disks itself. According to this view, the presence of an extended warm corona could further increase the timescales for variability in the X-ray band.

6.5 Summary

In this work we have investigated the long-term AGN variability for the soft X-ray band using SF analysis. In order to do this we extracted AGN sources (observed at least twice) from data coming from XMM-Newton and ROSAT observations. Data from these two satellites cover a time interval of about $\sim$ 22 years (Fig. 6.1), corresponding to $\sim$ 20 years interval in the rest frame (see Fig. 6.2). Before performing our analysis we check our sample and we correct offsets due to the different satellite properties and sensibilities. After cleaning the data, we computed structure function in Fig. 6.7 that refers to a sample of 2864 sources in total and covers a time interval of $\sim$ 20 years rest

frame. Our analysis does not show any evidence of a plateau. Our SF shows an increase at long time lags which can be understood in a scenario in which relevant timescales are due to the variations occurring in the external region of the accretion disk or a large emitting region originates the soft photons.

Conclusions & future perspectives

The main objective of this thesis was the study and characterization of the high energy emission of AGN To achieve this aim, we exploited a number of techniques and various different approaches were pursued.

Concerning the questions raised in the Incipit of this dissertation:

- Detailed spectral studies allow for impressive scientific outcomes that largely increase our understanding of the physics of compact objects. We demonstrated that their results are enhanced when applied to multi-epoch broadband data sets on which it is possible to test physically motivated models at the same time and disentangle the different spectral components through the study of their variability. Analysing X-ray data obtained with limited bandwidth or via different facilities without simultaneous observations often provides inconclusive results and various alternative interpretations are equally likely. For instance, our study on the X-ray behaviour of HE 0436-4717 describes well the high energy emission spectrum of the AGN, but it does not rule out the rather extreme scenario proposed by Bonson et al. (2015) nor tests the origin of the soft-excess in this AGN. This further supports the importance of XMM-Newton-NuSTAR coordinate observations.

- Multi-epoch broadband NGC 7469 and NGC 4593 monitorings have been studied and discussed. In this context, we have been able (i) to provide an unprecedented detailed view of their innermost regions (ii) to disentangle the reflection component and the soft excess from the primary continuum, (iii) to test the two-corona model (iv) to study the correlations between the different spectral components, and (vi) to track the time-evolution of these components on different timescales.

- The Comptonisation origin of the soft-excess has been investigated using the high quality data-sets of the broadband observational campaigns of NGC 7469 and NGC 4593. By testing the two-corona model, the optical-UV to soft X-ray emission of NGC 7469 and NGC 4593 is consistent with a Comptonised spectrum from a warm, optically thick corona covering a nearly passive disc. The luminosity of the soft

phase (i.e. the disc) is thus consistent to result off reprocessing of the emission from a warm corona. For the prominent soft-excess of NGC 7469 we ruled out a possible origin due to relativistic lines blurring, thus demonstrating that a warm Comptonising medium model best-fits our high data. On the other hand, our test of the two-corona model on NGC 4593 allowed us to constrain better the warm corona geometry that is likely patchy and not fully covering the disc.

- We studied the origin of the reprocessed emission in both NGC 7469 and HE 0436-4717. By testing various possible origins for their reflection components we found their reprocessed emission was due to reprocessing arising from Compton-thick material located far away from the central BH. In both these sources, the neutral Fe Kα emission line was consistent in being narrow and its accompanying Compton reflection component was constant. In the high quality data of NGC 7469 there is no evidence of a relativistic broadening acting on the line. On the other hand, for HE 0436-4717 we only notice that to best-fit the data the presence of a relativistic component is not required.

- We have studied the properties of hot coronae in AGN using both spectroscopy and simulations. Indeed, for all the Seyferts discussed in this dissertation, we have tested self-consistent models accounting for a primary Comptonisation continuum. For NGC 7469, NGC 4593 and HE 0436-4717 we estimated the coronal parameters (obtaining both measurements and lower(upper) limits) using *nthcomp* that assumes the corona is spherical. On the other hand, using the formulae derived in Chapter 5 for converting E_c and Γ into kT_e τ_e, we measured the physical properties of the Comptonising media in these sources for both a spherical and slab-like corona. When using slab-like coronae, the electron temperature and the opacity were obtained always smaller with respect to the case of a spherical corona and this is due to geometrical issues. We further studied Comptonisation using the MoCA-base formulae by converting literature values of E_c and Γ into kT_e τ_e. For the slab corona, estimates of opacity seem systematically smaller with respect to values obtained using *compTT*, and this discrepancy could likely be due to various differences between the two codes. On the other hand, MoCA-based estimates are in agreement with those from other models when a spherical corona is considered.

- Our variability analyses revealed that X-ray flux variations are still observed on decades timescales. Within the framework of the two corona model, this result supports the presence of an extended medium allowing for long term fluctuations, although it does not rule out the propagating fluctuations scenario according to which X-rays are modulated by long amplitude variations generated within the accretion disc.

The present results bear out the two-corona scenario as being a promising model,

deserving further detailed analyses. More work will be devoted to understand better this model both from the observational and the theoretical point of view. In particular, we have to focus on the formation process, heating mechanism and structure of the warm and hot coronae since these are not yet fully understood, nor is their mutual interplay and the connection with the accretion disc. All of these points have to be discussed in light of the observed multi-scale variability. To understand better this model and to further characterize it, future multiple and broadband observations of nearby Seyfert galaxies are required. In particular, broadband observational campaigns on different classes of AGN (high and low-luminosity, high and low-black hole mass, broad-line and narrow-line Seyferts) are ongoing, and they will improve our understanding of the nature of their central engines.

The unprecedented capability of XMM-Newton of X-raying the sky is providing a series of catalogues including AGN detected by serendipity that are particularly suitable for performing ensemble studies. For a noticeable part of these objects, fundamental information such as their mass and accretion rate are available. Moreover, such kinds of analyses will benefit greatly on the forthcoming eROSITA facility that is especially suited for surveying the sky in X-rays and provide up to ~ 3 million new, distant active galactic nuclei. Then, in this context, by crossmatching the eROSITA results with optical spectroscopical large data-sets (e.g. SDSS) it will be possible to perform, on the largest sample ever investigated, an ensemble study on the variability of AGN focusing on their evolutionary behaviour and on their dependence on the host galaxy properties.

Finally, MoCA will be further exploited for studying polarised signals from AGN. Indeed, Compton scattering, as any scattering mechanism, produces a polarization signal which is strongly sensitive to the geometry of the scattering material. This means that studying X-ray polarised photons will give us an insight into the geometrical configuration of the corona and the BH surroundings. Thus, by performing simulations we will be able to predict the AGN emission behaviour as a function of the coronal geometry. Such an ulterior MoCA application will be valuable in the context of forthcoming facilities IXPE (Weisskopf et al. 2016b,a) and eXTP Zhang et al. (2016). Indeed, these observatories, a real new pair of eyes sensitive to polarized light, which will soon scrutinize the X-ray polarised Universe providing unprecedented information and allowing the determination of the geometry of AGN coronae, at least for more luminous objects.

Chapter 7

Bibliography

Abramowicz, M. A., Czerny, B., Lasota, J. P., & Szuszkiewicz, E. 1988, ApJ, 332, 646

Allevato, V., Paolillo, M., Papadakis, I., & Pinto, C. 2013, ApJ, 771, 9

Andrae, R., Kim, D.-W., & Bailer-Jones, C. A. L. 2013, A&A, 554, A137

Antonucci, R. 1993a, ARA&A, 31, 473

Antonucci, R. 1993b, ARA&A, 31, 473

Antonucci, R. R. J. & Miller, J. S. 1985, ApJ, 297, 621

Arevalo, P. 2006, in VI Microquasar Workshop: Microquasars and Beyond, 32.1

Arnaud, K. A. 1996, in Astronomical Society of the Pacific Conference Series, Vol. 101, Astronomical Data Analysis Software and Systems V, ed. G. H. Jacoby & J. Barnes, 17

Arnaud, K. A., Branduardi-Raymont, G., Culhane, J. L., et al. 1985, MNRAS, 217, 105

Aschenbach, B., Citterio, O., Ellwood, J. M., et al., eds. 1986, ESA Special Publication, Vol. 1084, The high-throughput X-ray Spectroscopy Mission. Report of the Telescope Working Group.

Baldwin, J. A., Phillips, M. M., & Terlevich, R. 1981, PASP, 93, 5

Bamford, S. P., Rojas, A. L., Nichol, R. C., et al. 2008, MNRAS, 391, 607

Barr, P. 1986, MNRAS, 223, 29P

Barstow, M. A. & Holberg, J. B. 2003, Extreme Ultraviolet Astronomy, 408

Barthelmy, S. D., Barbier, L. M., Cummings, J. R., et al. 2005, Space Sci. Rev., 120, 143

Barvainis, R. 1992, ApJ, 400, 502

Barvainis, R., Lehár, J., Birkinshaw, M., Falcke, H., & Blundell, K. M. 2005, ApJ, 618, 108

Bauer, A., Baltay, C., Coppi, P., et al. 2009, ApJ, 696, 1241

Beckmann, V. & Shrader, C. R. 2012, Active Galactic Nuclei (Wiley-VCH)

Behar, E., Peretz, U., Kriss, G. A., et al. 2017, A&A, 601, A17

Beheshtipour, B., Krawczynski, H., & Malzac, J. 2017, ApJ, 850, 14

Beloborodov, A. M. 1999, in Astronomical Society of the Pacific Conference Series, Vol. 161, High Energy Processes in Accreting Black Holes, ed. J. Poutanen & R. Svensson, 295

Bentz, M. C., Peterson, B. M., Netzer, H., Pogge, R. W., & Vestergaard, M. 2009, ApJ, 697, 160

Bentz, M. C., Peterson, B. M., & Pogge, R. W. 2006, in Bulletin of the American Astronomical Society, Vol. 38, American Astronomical Society Meeting Abstracts, 223.02

Bian, W. & Zhao, Y. 2003, MNRAS, 343, 164

Bianchi, S., Guainazzi, M., Matt, G., Fonseca Bonilla, N., & Ponti, G. 2009, A&A, 495, 421

Bianchi, S., La Franca, F., Matt, G., et al. 2008, MNRAS, 389, L52

Bianchi, S., Maiolino, R., & Risaliti, G. 2012, Advances in Astronomy, 2012, 782030

Bianchi, S. & Matt, G. 2002, A&A, 387, 76

Bianchi, S., Matt, G., Nicastro, F., Porquet, D., & Dubau, J. 2005, MNRAS, 357, 599

Blandford, R. D. 1985, in Numerical Astrophysics, ed. J. M. Centrella, J. M. Leblanc, & R. L. Bowers, 6

Blustin, A. J., Branduardi-Raymont, G., Behar, E., et al. 2003, A&A, 403, 481

Boissay, R., Paltani, S., Ponti, G., et al. 2014, A&A, 567, A44

Bon, E., Popović, L. Č., Ilić, D., & Mediavilla, E. 2006, New A Rev., 50, 716

Bondi, H. 1952, MNRAS, 112, 195

Bonson, K., Gallo, L. C., & Vasudevan, R. 2015, MNRAS, 450, 857

Brandt, W. N. & Alexander, D. M. 2015, A&A Rev., 23, 1

Brandt, W. N., Fabian, A. C., Nandra, K., & Tsuruta, S. 1993, MNRAS, 265, 996

Burrows, D. N., Hill, J. E., Nousek, J. A., et al. 2005, Space Sci. Rev., 120, 165

Cappi, M., De Marco, B., Ponti, G., et al. 2016, A&A, 592, A27

Cappi, M., Tombesi, F., Bianchi, S., et al. 2009, A&A, 504, 401

Cash, W. 1979, ApJ, 228, 939

Cerruti, M., Ponti, G., Boisson, C., et al. 2011, A&A, 535, A113

Chartas, G., Brandt, W. N., Gallagher, S. C., & Garmire, G. P. 2002, ApJ, 579, 169

Chartas, G., Kochanek, C. S., Dai, X., Poindexter, S., & Garmire, G. 2009, ApJ, 693, 174

Chen, X. & Taam, R. E. 1995, ApJ, 441, 354

Coffey, D., Longinotti, A. L., Rodríguez-Ardila, A., et al. 2014, MNRAS, 443, 1788

Collin, S. & Huré, J.-M. 2001, A&A, 372, 50

Coppi, P. S. 1992, MNRAS, 258, 657

Coppi, P. S. 1999, in Astronomical Society of the Pacific Conference Series, Vol. 161, High Energy Processes in Accreting Black Holes, ed. J. Poutanen & R. Svensson, 375

Costantini, E. 2010, Space Sci. Rev., 157, 265

Costantini, E., Kaastra, J. S., Korista, K., et al. 2010, A&A, 512, A25

Crenshaw, D. M., Kraemer, S. B., Gabel, J. R., et al. 2003, ApJ, 594, 116

Crummy, J., Fabian, A. C., Gallo, L., & Ross, R. R. 2006, MNRAS, 365, 1067

Czerny, B. 2006, in Astronomical Society of the Pacific Conference Series, Vol. 360, Astronomical Society of the Pacific Conference Series, ed. C. M. Gaskell, I. M. McHardy, B. M. Peterson, & S. G. Sergeev, 265

Czerny, B., Nikołajuk, M., Piasecki, M., & Kuraszkiewicz, J. 2001, MNRAS, 325, 865

Dauser, T., García, J., Walton, D. J., et al. 2016, A&A, 590, A76

De Marco, B., Iwasawa, K., Cappi, M., et al. 2009, A&A, 507, 159

De Marco, B., Ponti, G., Cappi, M., et al. 2013, MNRAS, 431, 2441

De Rosa, A., Fabian, A. C., & Piro, L. 2002, MNRAS, 334, L21

de Vries, W. H., Becker, R. H., & White, R. L. 2003, AJ, 126, 1217

de Vries, W. H., Becker, R. H., White, R. L., & Loomis, C. 2005, AJ, 129, 615

den Herder, J. W., Brinkman, A. C., Kahn, S. M., et al. 2001, A&A, 365, L7

Denney, K. D., Bentz, M. C., Peterson, B. M., et al. 2006, ApJ, 653, 152

di Clemente, A., Giallongo, E., Natali, G., Trevese, D., & Vagnetti, F. 1996, ApJ, 463, 466

Di Gesu, L., Costantini, E., Ebrero, J., et al. 2015, A&A, 579, A42

Done, C., Davis, S. W., Jin, C., Blaes, O., & Ward, M. 2012a, MNRAS, 420, 1848

Done, C., Davis, S. W., Jin, C., Blaes, O., & Ward, M. 2012b, MNRAS, 420, 1848

Done, C. & Fabian, A. C. 1989a, in IAU Symposium, Vol. 134, Active Galactic Nuclei, ed. D. E. Osterbrock & J. S. Miller, 194

Done, C. & Fabian, A. C. 1989b, MNRAS, 240, 81

Edelson, R. & Nandra, K. 1999, ApJ, 514, 682

Edelson, R. A., Krolik, J. H., & Pike, G. F. 1990, ApJ, 359, 86

Elitzur, M. & Shlosman, I. 2006, ApJ, 648, L101

Elliot, J. L. & Shapiro, S. L. 1974a, ApJ, 192, L3

Elliot, J. L. & Shapiro, S. L. 1974b, ApJ, 192, L3

Elvis, M., Risaliti, G., Nicastro, F., et al. 2004, ApJ, 615, L25

Fabian, A. C., Iwasawa, K., Reynolds, C. S., & Young, A. J. 2000, PASP, 112, 1145

Fabian, A. C., Lohfink, A., Belmont, R., Malzac, J., & Coppi, P. 2017, MNRAS, 467, 2566

Fabian, A. C., Lohfink, A., Kara, E., et al. 2015, MNRAS, 451, 4375

Fabian, A. C., Rees, M. J., Stella, L., & White, N. E. 1989, MNRAS, 238, 729

Fabian, A. C., Zoghbi, A., Ross, R. R., et al. 2009, Nature, 459, 540

Fanaroff, B. L. & Riley, J. M. 1974, MNRAS, 167, 31P

Fath, E. A. 1909, Lick Observatory Bulletin, 5, 71

Ferland, G. J., Porter, R. L., van Hoof, P. A. M., et al. 2013, Rev. Mexicana Astron. Astrofis., 49, 137

Forman, W., Jones, C., Cominsky, L., et al. 1978, ApJS, 38, 357

Frank, J., King, A., & Raine, D. J. 2002, Accretion Power in Astrophysics: Third Edition, 398

Gallo, L. C., Blue, D. M., Grupe, D., Komossa, S., & Wilkins, D. R. 2018, MNRAS

García, J., Dauser, T., Lohfink, A., et al. 2014a, ApJ, 782, 76

García, J., Dauser, T., Lohfink, A., et al. 2014b, ApJ, 782, 76

García, J., Dauser, T., Reynolds, C. S., et al. 2013, ApJ, 768, 146

García, J. & Kallman, T. R. 2010, ApJ, 718, 695

García, J. A., Steiner, J. F., McClintock, J. E., et al. 2015, ApJ, 813, 84

George, I. M. & Fabian, A. C. 1991, MNRAS, 249, 352

Ghisellini, G., ed. 2013, Lecture Notes in Physics, Berlin Springer Verlag, Vol. 873, Radiative Processes in High Energy Astrophysics

Ghisellini, G. & Haardt, F. 1994, ApJ, 429, L53

Ghisellini, G., Haardt, F., & Fabian, A. C. 1993, MNRAS, 263, L9

Ghisellini, G., Maraschi, L., & Treves, A. 1985, A&A, 146, 204

Giacconi, R., Gursky, H., Paolini, F. R., & Rossi, B. B. 1962, Physical Review Letters, 9, 439

Giallongo, E., Trevese, D., & Vagnetti, F. 1991, ApJ, 377, 345

Gierliński, M. & Done, C. 2004, MNRAS, 349, L7

Giustini, M., Cappi, M., Chartas, G., et al. 2011, A&A, 536, A49

Giveon, U., Maoz, D., Kaspi, S., Netzer, H., & Smith, P. S. 1999, MNRAS, 306, 637

Gofford, J., Reeves, J. N., Tombesi, F., et al. 2013, MNRAS, 430, 60

Green, A. R., McHardy, I. M., & Lehto, H. J. 1993, MNRAS, 265, 664

Grupe, D., Komossa, S., Leighly, K. M., & Page, K. L. 2010, ApJS, 187, 64

Guainazzi, M., Matsuoka, M., Piro, L., Mihara, T., & Yamauchi, M. 1994, ApJ, 436, L35

Guilbert, P. W., Fabian, A. C., & Rees, M. J. 1983, MNRAS, 205, 593

Guillot, S., Kaspi, V. M., Archibald, R. F., et al. 2016, MNRAS, 463, 2612

Gupta, A., Mathur, S., & Krongold, Y. 2015, ApJ, 798, 4

Haardt, F. & Maraschi, L. 1991a, ApJ, 380, L51

Haardt, F. & Maraschi, L. 1991b, ApJ, 380, L51

Haardt, F. & Maraschi, L. 1993, ApJ, 413, 507

Haardt, F., Maraschi, L., & Ghisellini, G. 1994, ApJ, 432, L95

Haardt, F., Maraschi, L., & Ghisellini, G. 1997, ApJ, 476, 620

Hailey, C. J., An, H., Blaedel, K. L., et al. 2010, in Proc. SPIE, Vol. 7732, Space Telescopes and Instrumentation 2010: Ultraviolet to Gamma Ray, 77320T

Hainline, K. N., Hickox, R., Greene, J. E., Myers, A. D., & Zakamska, N. L. 2013, ApJ, 774, 145

Halpern, J. P., Leighly, K. M., & Marshall, H. L. 2003, ApJ, 585, 665

Halpern, J. P. & Marshall, H. L. 1996, ApJ, 464, 760

Harrison, F. A., Craig, W. W., Christensen, F. E., et al. 2013, ApJ, 770, 103

Hughes, P. A., Aller, H. D., & Aller, M. F. 1992, ApJ, 396, 469

Ishibashi, W. & Courvoisier, T. J.-L. 2012, A&A, 540, L2

Janiuk, A., Czerny, B., & Madejski, G. M. 2001a, ApJ, 557, 408

Janiuk, A., Życki, P. T., & Czerny, B. 2001b, in Black Holes in Binaries and Galactic Nuclei, ed. L. Kaper, E. P. J. V. D. Heuvel, & P. A. Woudt, 232

Jansen, F., Lumb, D., Altieri, B., et al. 2001, A&A, 365, L1

Jin, C., Ward, M., Done, C., & Gelbord, J. 2012, MNRAS, 420, 1825

Kaastra, J. S., Kriss, G. A., Cappi, M., et al. 2014, Science, 345, 64

Kaastra, J. S., Mewe, R., Liedahl, D. A., Komossa, S., & Brinkman, A. C. 2000, A&A, 354, L83

Kaastra, J. S., Petrucci, P.-O., Cappi, M., et al. 2011a, A&A, 534, A36

Kaastra, J. S., Petrucci, P.-O., Cappi, M., et al. 2011b, A&A, 534, A36

Kalberla, P. M. W., Burton, W. B., Hartmann, D., et al. 2005, A&A, 440, 775

Kara, E., Alston, W. N., Fabian, A. C., et al. 2016, MNRAS, 462, 511

Kawaguchi, T., Mineshige, S., Umemura, M., & Turner, E. L. 1998, ApJ, 504, 671

Kelly, B. C., Bechtold, J., & Siemiginowska, A. 2009, ApJ, 698, 895

Khachikian, E. Y. & Weedman, D. W. 1974, ApJ, 192, 581

Komossa, S. 2008, in Revista Mexicana de Astronomia y Astrofisica, vol. 27, Vol. 32, Revista Mexicana de Astronomia y Astrofisica Conference Series, 86–92

Kozłowski, S. 2017, ApJ, 835, 250

Kubota, A. & Done, C. 2018, MNRAS

La Franca, F., Bianchi, S., Ponti, G., Branchini, E., & Matt, G. 2014, ApJ, 787, L12

Lansbury, G. B., Alexander, D. M., Aird, J., et al. 2017, ApJ, 846, 20

Laor, A. 1991, ApJ, 376, 90

Lawrence, A. & Papadakis, I. 1993, ApJ, 414, L85

Leighly, K. M. 2005, Ap&SS, 300, 137

Liedahl, D. A. 1999, in Lecture Notes in Physics, Berlin Springer Verlag, Vol. 520, X-Ray Spectroscopy in Astrophysics, ed. J. van Paradijs & J. A. M. Bleeker, 189

Lodders, K. 2003, ApJ, 591, 1220

Longinotti, A. L., Krongold, Y., Guainazzi, M., et al. 2015, ApJ, 813, L39

Lyubarskii, Y. E. 1997, MNRAS, 292, 679

MacLeod, C. L., Ivezić, Ž., Kochanek, C. S., et al. 2010, ApJ, 721, 1014

MacLeod, C. L., Ivezić, Ž., Sesar, B., et al. 2012, ApJ, 753, 106

Magdziarz, P., Blaes, O. M., Zdziarski, A. A., Johnson, W. N., & Smith, D. A. 1998, MNRAS, 301, 179

Magdziarz, P. & Zdziarski, A. A. 1995, MNRAS, 273, 837

Malizia, A., Molina, M., Bassani, L., et al. 2014, ApJ, 782, L25

Mantovani, G., Nandra, K., & Ponti, G. 2016, MNRAS, 458, 4198

Marconi, A., Axon, D. J., Maiolino, R., et al. 2009, ApJ, 698, L103

Marconi, A., Risaliti, G., Gilli, R., et al. 2004, MNRAS, 351, 169

Markowitz, A. & Edelson, R. 2004, ApJ, 617, 939

Markowitz, A., Edelson, R., Vaughan, S., et al. 2003a, ApJ, 593, 96

Markowitz, A., Edelson, R., Vaughan, S., et al. 2003b, ApJ, 593, 96

Markowitz, A. G., Krumpe, M., & Nikutta, R. 2014, MNRAS, 439, 1403

Mason, K. O., Breeveld, A., Much, R., et al. 2001a, A&A, 365, L36

Mason, K. O., Breeveld, A., Much, R., et al. 2001b, A&A, 365, L36

Matt, G., Fabian, A. C., & Reynolds, C. S. 1997, MNRAS, 289, 175

Matt, G., Fabian, A. C., & Ross, R. R. 1993, MNRAS, 262, 179

Matt, G., Fabian, A. C., & Ross, R. R. 1996, MNRAS, 278, 1111

Matt, G., Guainazzi, M., & Maiolino, R. 2003, MNRAS, 342, 422

Matt, G., Marinucci, A., Guainazzi, M., et al. 2014, MNRAS, 439, 3016

Matt, G., Perola, G. C., & Piro, L. 1991, A&A, 247, 25

Matthews, T. A. & Sandage, A. R. 1963, ApJ, 138, 30

McHardy, I. M. 2001, in Astronomical Society of the Pacific Conference Series, Vol. 224, Probing the Physics of Active Galactic Nuclei, ed. B. M. Peterson, R. W. Pogge, & R. S. Polidan, 205

McHardy, I. M., Arévalo, P., Uttley, P., et al. 2007a, MNRAS, 382, 985

McHardy, I. M., Arévalo, P., Uttley, P., et al. 2007b, MNRAS, 382, 985

McHardy, I. M., Koerding, E., Knigge, C., Uttley, P., & Fender, R. P. 2006, Nature, 444, 730

McHardy, I. M., Papadakis, I. E., & Uttley, P. 1999, Nuclear Physics B Proceedings Supplements, 69, 509

McHardy, I. M., Papadakis, I. E., Uttley, P., Page, M. J., & Mason, K. O. 2004, MNRAS, 348, 783

Mehdipour, M., Branduardi-Raymont, G., Kaastra, J. S., et al. 2011a, A&A, 534, A39

Mehdipour, M., Branduardi-Raymont, G., Kaastra, J. S., et al. 2011b, A&A, 534, A39

Mehdipour, M., Kaastra, J. S., Costantini, E., et al. 2018, A&A, 615, A72

Mehdipour, M., Kaastra, J. S., Kriss, G. A., et al. 2017, A&A, 607, A28

Mehdipour, M., Kaastra, J. S., Kriss, G. A., et al. 2015a, A&A, 575, A22

Mehdipour, M., Kaastra, J. S., Kriss, G. A., et al. 2015b, A&A, 575, A22

Middei, R., Bianchi, S., Cappi, M., et al. 2018, ArXiv e-prints

Middei, R., Vagnetti, F., Antonucci, M., & Serafinelli, R. 2016a, in Journal of Physics Conference Series, Vol. 689, Journal of Physics Conference Series, 012006

Middei, R., Vagnetti, F., Antonucci, M., & Serafinelli, R. 2016b, in Journal of Physics Conference Series, Vol. 689, Journal of Physics Conference Series, 012006

Miller, L., Turner, T. J., & Reeves, J. N. 2008, A&A, 483, 437

Mineshige, S., Kawaguchi, T., Takeuchi, M., & Hayashida, K. 2000, PASJ, 52, 499

Miniutti, G., Fabian, A. C., Anabuki, N., et al. 2007, PASJ, 59, 315

Miniutti, G., Sanfrutos, M., Beuchert, T., et al. 2014, MNRAS, 437, 1776

Molina, M., Bassani, L., Malizia, A., et al. 2013, MNRAS, 433, 1687

Molina, M., Bassani, L., Malizia, A., et al. 2009, MNRAS, 399, 1293

Momjian, E., Carilli, C. L., Walter, F., & Venemans, B. 2014, AJ, 147, 6

Morgan, C. W., Hainline, L. J., Chen, B., et al. 2012, ApJ, 756, 52

Murphy, K. D. & Yaqoob, T. 2009, MNRAS, 397, 1549

Mushotzky, R. F., Done, C., & Pounds, K. A. 1993, ARA&A, 31, 717

Nandra, K., Clavel, J., Edelson, R. A., et al. 1998, ApJ, 505, 594

Nandra, K., George, I. M., Mushotzky, R. F., Turner, T. J., & Yaqoob, T. 1997a, ApJ, 476, 70

Nandra, K., George, I. M., Mushotzky, R. F., Turner, T. J., & Yaqoob, T. 1997b, ApJ, 477, 602

Nandra, K., Le, T., George, I. M., et al. 2000, ApJ, 544, 734

Nandra, K., O'Neill, P. M., George, I. M., & Reeves, J. N. 2007, MNRAS, 382, 194

Narayan, R. & Yi, I. 1994, ApJ, 428, L13

Nardini, E., Porquet, D., Reeves, J. N., et al. 2016, ApJ, 832, 45

Nenkova, M., Sirocky, M. M., Ivezić, Ž., & Elitzur, M. 2008, ApJ, 685, 147

Nicastro, F., Piro, L., De Rosa, A., et al. 2000, ApJ, 536, 718

Nikolajuk, M., Papadakis, I. E., & Czerny, B. 2004, MNRAS, 350, L26

Novikov, I. D. & Thorne, K. S. 1973, in Black Holes (Les Astres Occlus), ed. C. Dewitt & B. S. Dewitt, 343–450

O'Neill, P. M., Nandra, K., Papadakis, I. E., & Turner, T. J. 2005, MNRAS, 358, 1405

Paczynski, B. 1980, Acta Astron., 30, 347

Paczyński, B. & Wiita, P. J. 1980, A&A, 88, 23

Page, K. L., Schartel, N., Turner, M. J. L., & O'Brien, P. T. 2004, MNRAS, 352, 523

Page, M. J., Simpson, C., Mortlock, D. J., et al. 2014, MNRAS, 440, L91

Pan, H.-W., Yuan, W., Zhou, X.-L., Dong, X.-B., & Liu, B. 2015, ApJ, 808, 163

Papadakis, I. E. 2004a, MNRAS, 348, 207

Papadakis, I. E. 2004b, MNRAS, 348, 207

Papadakis, I. E., Brinkmann, W., Negoro, H., & Gliozzi, M. 2002, A&A, 382, L1

Papadakis, I. E., Chatzopoulos, E., Athanasiadis, D., Markowitz, A., & Georgantopoulos, I. 2008, A&A, 487, 475

Papadakis, I. E., Nandra, K., & Kazanas, D. 2001, ApJ, 554, L133

Pâris, I., Petitjean, P., Ross, N. P., et al. 2016, ArXiv:1608.06483

Parker, M. L., Miller, J. M., & Fabian, A. C. 2017, ArXiv e-prints

Patrick, A. R., Reeves, J. N., Porquet, D., et al. 2011, MNRAS, 411, 2353

Peretz, U., Behar, E., Kriss, G. A., et al. 2017, ArXiv e-prints

Perola, G. C., Matt, G., Cappi, M., et al. 2002, A&A, 389, 802

Peterson, B. M. 1993, PASP, 105, 247

Peterson, B. M. 1997, An Introduction to Active Galactic Nuclei (New York Cambridge University Press)

Peterson, B. M., Grier, C. J., Horne, K., et al. 2014, ApJ, 795, 149

Petrucci, P. O., Haardt, F., Maraschi, L., et al. 2001, ApJ, 556, 716

Petrucci, P. O., Haardt, F., Maraschi, L., et al. 2000, ApJ, 540, 131

Petrucci, P. O., Maraschi, L., Haardt, F., & Nandra, K. 2004, A&A, 413, 477

Petrucci, P.-O., Paltani, S., Malzac, J., et al. 2013a, A&A, 549, A73

Petrucci, P.-O., Paltani, S., Malzac, J., et al. 2013b, A&A, 549, A73

Petrucci, P.-O., Ursini, F., De Rosa, A., et al. 2018, A&A, 611, A59

Piconcelli, E., Jimenez-Bailón, E., Guainazzi, M., et al. 2004, MNRAS, 351, 161

Piconcelli, E., Jimenez-Bailón, E., Guainazzi, M., et al. 2005, A&A, 432, 15

Ponti, G., Bianchi, S., Muñoz-Darias, T., et al. 2018, MNRAS, 473, 2304

Ponti, G., Miniutti, G., Cappi, M., et al. 2006a, MNRAS, 368, 903

Ponti, G., Miniutti, G., Fabian, A. C., Cappi, M., & Palumbo, G. G. C. 2006b, Astronomische Nachrichten, 327, 1055

Ponti, G., Papadakis, I., Bianchi, S., et al. 2012, A&A, 542, A83

Porquet, D., Reeves, J. N., Matt, G., et al. 2018, A&A, 609, A42

Pounds, K. 2014, Space Sci. Rev., 183, 339

Pounds, K., Edelson, R., Markowitz, A., & Vaughan, S. 2001a, ApJ, 550, L15

Pounds, K., Edelson, R., Markowitz, A., & Vaughan, S. 2001b, ApJ, 550, L15

Poutanen, J. & Svensson, R. 1996, ApJ, 470, 249

Protassov, R., van Dyk, D. A., Connors, A., Kashyap, V. L., & Siemiginowska, A. 2002, ApJ, 571, 545

Puccetti, S., Fiore, F., Risaliti, G., et al. 2007, MNRAS, 377, 607

Reeves, J. N., Braito, V., Nardini, E., et al. 2016a, ApJ, 824, 20

Reeves, J. N., Porquet, D., Braito, V., et al. 2016b, ApJ, 828, 98

Reeves, J. N. & Turner, M. J. L. 2000, MNRAS, 316, 234

Reis, R. C. & Miller, J. M. 2013, ApJ, 769, L7

Reynolds, C. S. & Nowak, M. A. 2003, Phys. Rep., 377, 389

Ricci, C., Trakhtenbrot, B., Koss, M. J., et al. 2017, ApJS, 233, 17

Risaliti, G., Elvis, M., & Nicastro, F. 2002, ApJ, 571, 234

Risaliti, G., Harrison, F. A., Madsen, K. K., et al. 2013, Nature, 494, 449

Risaliti, G., Miniutti, G., Elvis, M., et al. 2009, ApJ, 696, 160

Risaliti, G., Nardini, E., Salvati, M., et al. 2011, MNRAS, 410, 1027

Roming, P. W. A., Kennedy, T. E., Mason, K. O., et al. 2005, Space Sci. Rev., 120, 95

Rosen, S. R., Webb, N. A., Watson, M. G., et al. 2016, A&A, 590, A1

Ross, R. R. & Fabian, A. C. 1993, MNRAS, 261, 74

Ross, R. R. & Fabian, A. C. 2005, MNRAS, 358, 211

Różańska, A., Malzac, J., Belmont, R., Czerny, B., & Petrucci, P.-O. 2015, A&A, 580, A77

Rybicki, G. B. & Lightman, A. P. 1979, Radiative processes in astrophysics

Saez, C., Brandt, W. N., Gallagher, S. C., Bauer, F. E., & Garmire, G. P. 2012, ApJ, 759, 42

Saxton, R., Read, A., Esquej, P., Miniutti, G., & Alvarez, E. 2011, ArXiv:1106.3507

Schlafly, E. F. & Finkbeiner, D. P. 2011, ApJ, 737, 103

Schmidt, M. 1963, Nature, 197, 1040

Schmidt, M. & Green, R. F. 1983, ApJ, 269, 352

Schneider, D. P., Richards, G. T., Hall, P. B., et al. 2010, AJ, 139, 2360

Schnittman, J. D. & Krolik, J. H. 2010, ApJ, 712, 908

Scott, A. E., Stewart, G. C., & Mateos, S. 2012, MNRAS, 423, 2633

Scott, J. E., Kriss, G. A., Lee, J. C., et al. 2005, ApJ, 634, 193

Serafinelli, R., Vagnetti, F., & Middei, R. 2017, A&A, 600, A101

Seyfert, C. K. 1943, ApJ, 97, 28

Shakura, N. I. & Sunyaev, R. A. 1973, A&A, 24, 337

Shemmer, O., Brandt, W. N., Paolillo, M., et al. 2014, ApJ, 783, 116

Shen, Y. & Ho, L. C. 2014, Nature, 513, 210

Shih, D. C., Iwasawa, K., & Fabian, A. C. 2002, MNRAS, 333, 687

Shuder, J. M. & Osterbrock, D. E. 1981, ApJ, 250, 55

Simonetti, J. H., Cordes, J. M., & Heeschen, D. S. 1985, ApJ, 296, 46

Slipher, V. M. 1917, Lowell Observatory Bulletin, 3, 59

Sobolewska, M. A. & Papadakis, I. E. 2009, MNRAS, 399, 1597

Soldi, S., Beckmann, V., Baumgartner, W. H., et al. 2014, A&A, 563, A57

Stern, B. E., Poutanen, J., Svensson, R., Sikora, M., & Begelman, M. C. 1995, ApJ, 449, L13

Strotjohann, N. L., Saxton, R. D., Starling, R. L. C., et al. 2016, A&A, 592, A74

Strüder, L., Briel, U., Dennerl, K., et al. 2001a, A&A, 365, L18

Strüder, L., Briel, U., Dennerl, K., et al. 2001b, A&A, 365, L18

Sunyaev, R. A. & Titarchuk, L. G. 1980, A&A, 86, 121

Sunyaev, R. A. & Titarchuk, L. G. 1985, A&A, 143, 374

Tamborra, F., Matt, G., Bianchi, S., & Dovčiak, M. 2018, ArXiv e-prints

Tanaka, Y., Nandra, K., Fabian, A. C., et al. 1995, Nature, 375, 659

Taylor, M. B. 2005, in Astronomical Society of the Pacific Conference Series, Vol. 347, Astronomical Data Analysis Software and Systems XIV, ed. P. Shopbell, M. Britton, & R. Ebert, 29

Taylor, M. B. 2006, in Astronomical Society of the Pacific Conference Series, Vol. 351, Astronomical Data Analysis Software and Systems XV, ed. C. Gabriel, C. Arviset, D. Ponz, & S. Enrique, 666

Taylor, R. D., Uttley, P., & McHardy, I. M. 2003, MNRAS, 342, L31

Titarchuk, L. 1994, ApJ, 434, 570

Tombesi, F., Cappi, M., Reeves, J. N., et al. 2013, MNRAS, 430, 1102

Tombesi, F., Cappi, M., Reeves, J. N., et al. 2011, ApJ, 742, 44

Tombesi, F., Cappi, M., Reeves, J. N., et al. 2010a, A&A, 521, A57

Tombesi, F., Meléndez, M., Veilleux, S., et al. 2015, Nature, 519, 436

Tombesi, F., Sambruna, R. M., Reeves, J. N., et al. 2010b, ApJ, 719, 700

Torricelli-Ciamponi, G., Pietrini, P., Risaliti, G., & Salvati, M. 2014, MNRAS, 442, 2116

Tortosa, A., Bianchi, S., Marinucci, A., Matt, G., & Petrucci, P. O. 2018, A&A, 614, A37

Tortosa, A., Marinucci, A., Matt, G., et al. 2017, MNRAS, 466, 4193

Trevese, D., Kron, R. G., Majewski, S. R., Bershady, M. A., & Koo, D. C. 1994, ApJ, 433, 494

Trèvese, D. & Vagnetti, F. 2002, ApJ, 564, 624

Truemper, J. 1982, Advances in Space Research, 2, 241

Turner, M. J. L., Abbey, A., Arnaud, M., et al. 2001a, A&A, 365, L27

Turner, M. J. L., Abbey, A., Arnaud, M., et al. 2001b, A&A, 365, L27

Turner, T. J., George, I. M., Nandra, K., & Turcan, D. 1999, ApJ, 524, 667

Turner, T. J. & Miller, L. 2009, A&A Rev., 17, 47

Turner, T. J., Reeves, J. N., Kraemer, S. B., & Miller, L. 2008, A&A, 483, 161

Turner, T. J., Weaver, K. A., Mushotzky, R. F., Holt, S. S., & Madejski, G. M. 1991, ApJ, 381, 85

Ursini, F., Boissay, R., Petrucci, P.-O., et al. 2015, A&A, 577, A38

Ursini, F., Petrucci, P.-O., Matt, G., et al. 2018, MNRAS, 478, 2663

Ursini, F., Petrucci, P.-O., Matt, G., et al. 2016, MNRAS, 463, 382

Uttley, P., Cackett, E. M., Fabian, A. C., Kara, E., & Wilkins, D. R. 2014, A&A Rev., 22, 72

Vagnetti, F., Antonucci, M., & Trevese, D. 2013, A&A, 550, A71

Vagnetti, F., Middei, R., Antonucci, M., Paolillo, M., & Serafinelli, R. 2016, A&A, 593, A55

Vagnetti, F., Trevese, D., & Nesci, R. 2003, ApJ, 590, 123

Vagnetti, F., Turriziani, S., & Trevese, D. 2011a, A&A, 536, A84

Vagnetti, F., Turriziani, S., & Trevese, D. 2011b, A&A, 536, A84

Vagnetti, F., Turriziani, S., Trevese, D., & Antonucci, M. 2010, A&A, 519, A17

Vanden Berk, D. E., Richards, G. T., Bauer, A., et al. 2001, AJ, 122, 549

Vanden Berk, D. E., Wilhite, B. C., Kron, R. G., et al. 2004, ApJ, 601, 692

Vaughan, S., Edelson, R., Warwick, R. S., & Uttley, P. 2003a, MNRAS, 345, 1271

Vaughan, S., Edelson, R., Warwick, R. S., & Uttley, P. 2003b, MNRAS, 345, 1271

Véron-Cetty, M.-P. & Véron, P. 2006, A&A, 455, 773

Vignali, C., Iwasawa, K., Comastri, A., et al. 2015, A&A, 583, A141

Voges, W., Aschenbach, B., Boller, T., et al. 1999, A&A, 349, 389

Voges, W., Aschenbach, B., Boller, T., et al. 2000, IAU Circ., 7432

Walter, R. & Fink, H. H. 1993, A&A, 274, 105

Walton, D. J., Nardini, E., Fabian, A. C., Gallo, L. C., & Reis, R. C. 2013a, MNRAS, 428, 2901

Walton, D. J., Nardini, E., Fabian, A. C., Gallo, L. C., & Reis, R. C. 2013b, MNRAS, 428, 2901

Walton, D. J., Risaliti, G., Harrison, F. A., et al. 2014, ApJ, 788, 76

Wang, T., Otani, C., Matsuoka, M., et al. 1998, MNRAS, 293, 397

Watson, M. G., Schröder, A. C., Fyfe, D., et al. 2009, A&A, 493, 339

Weisskopf, M. C., Ramsey, B., O'Dell, S., et al. 2016a, in Proc. SPIE, Vol. 9905, Space Telescopes and Instrumentation 2016: Ultraviolet to Gamma Ray, 990517

Weisskopf, M. C., Ramsey, B., O'Dell, S. L., et al. 2016b, Results in Physics, 6, 1179

Wisotzki, L., Christlieb, N., Bade, N., et al. 2000, A&A, 358, 77

Woltjer, L. 1959, ApJ, 130, 38

Yaqoob, T. 2012, MNRAS, 423, 3360

Young, M., Brandt, W. N., Xue, Y. Q., et al. 2012, ApJ, 748, 124

Yuan, F. & Narayan, R. 2014, ARA&A, 52, 529

Zdziarski, A. A., Johnson, W. N., & Magdziarz, P. 1996, MNRAS, 283, 193

Zdziarski, A. A., Lubiński, P., Gilfanov, M., & Revnivtsev, M. 2003, MNRAS, 342, 355

Zhang, S. N., Feroci, M., Santangelo, A., et al. 2016, in Proc. SPIE, Vol. 9905, Space Telescopes and Instrumentation 2016: Ultraviolet to Gamma Ray, 99051Q

Zhang, Y.-H. 2011, ApJ, 726, 21

Zheng, X. C., Xue, Y. Q., Brandt, W. N., et al. 2017, ApJ, 849, 127

Zu, Y., Kochanek, C. S., Kozłowski, S., & Udalski, A. 2013, ApJ, 765, 106

Zycki, P. T. & Czerny, B. 1994, MNRAS, 266, 653

Życki, P. T., Done, C., & Smith, D. A. 1999, MNRAS, 309, 561

Zycki, P. T., Krolik, J. H., Zdziarski, A. A., & Kallman, T. R. 1994, ApJ, 437, 597

Acknowledgements

I would like to thank all the people who helped me during these three years to make this thesis possible.

First of all, I gratefully thank Stefano Bianchi for his advices and patience, for understanding my passion for music and, especially, for limiting and directing all my ideas. Moreover, I thank Stefano to introduce me to his collaborators allowing me to join a challenging international collaboration.

I thank Giorgio Matt and Fabio La Franca, great teachers that easily banish doubts and answer questions in just few simple words. Then, I thank Andrea Marinucci that, although in its peculiar way, always helped me in growing as an astrophysicist. I warmly thank Fausto Vagnetti who first showed me how AGN are fascinating sources. Finally, I am grateful to all the people I had the chance to collaborate with during the preparation of this thesis: Pierre Olivier Petrucci, Alessandra De Rosa, Massimo Cappi, Francesco Tombesi, Maurizio Paolillo, Francesco Ursini, Roberto Serafinelli and Alessia Tortosa.

This work would not have been possible without the support of my girlfriend Federica and the encouragement of all my relatives and friends. Then, I warmly thank all of them for helping me during a such bright three years long ph. D. experience.

References for this thesis

- **Chapter 4:**
  Middei, R., Vagnetti, F.; Tombesi, F.; Bianchi, S.; Marinucci, A.; Ursini, F.; Tortosa, A., NuSTAR view of the Seyfert Galaxy HE 0436-4717, 2018A&A...618A.167M
  Middei, R.; Bianchi, S.; Cappi, M.; Petrucci, P.-O.; Ursini, F.; Arav, N.; Behar, E.; Branduardi-Raymont, G.; Costantini, E.; De Marco, B.; Di Gesu, L.; Ebrero, J.; Kaastra, J.; Kaspi, S.; Kriss, G. A.; Mao, J.; Mehdipour, M.; Paltani, S.; Peretz, U.; Ponti, G., Multi-wavelength campaign on NCG 7469. IV. The broad-band X-ray spectrum, 2018A&A...615A.163M
  Middei, R., Bianchi, S., Petrucci, P.O., F. Ursini, M. Cappi, B. De Marco, A. De Rosa, J. Malzac, A. Marinucci, G. Matt, G. Ponti, and A. Tortosa, High-energy monitoring of NGC 4593 II. Broadband spectral analysis: testing the two-corona model, 2019MNRAS.483.4695M.

- **Chapter 5:**
  Middei, R., Bianchi, S., Matt, G., Marinucci, A., Tamborra, F. and Petrucci, P.-O., Estimating AGN coronal parameters with MoCA, in preparation.

- **Chapter 6:**
  Middei, R.; Vagnetti, F.; Bianchi, S.; La Franca, F.; Paolillo, M.; Ursini, F., A long-term study of AGN X-ray variability . Structure function analysis on a ROSAT-XMM quasar sample, 2017A&A...599A..82M

Appendices

Appendix A

X-raying the Universe

At present different X-rays observatories are orbiting around the Earth collecting X-ray photons. However, the X-ray window has been only recently open to the astronomers since focusing hard X-rays with mirror is a real technological challenge.

Indeed, high energy photons are only reflected at low angles, some degree between the a platinum or gold or iridium surface and its incidence direction (grazing incidence). This kind of focusing mode was idealized by Giacconi and Rossi and it was adopted for the *Einstein* telescope (1979). To focus X-rays, mirrors have to be really smoothed with the accuracy of the frequencies typical of the incident photons. Moreover, mirrors are made of two section: a paraboloid and hyperboloid section. However, since X-rays are hard to be focused, to increase the focal planes the technique of the nested mirrors is adopted. Therefore X-ray telescopes are characterized by large collectors and small detectors. A further problem concerning X-ray astrophysics is that Earth Atmosphere is an opaque barrier for high energy photons and only visible light and a few other infrared wavelengths can pass thought it (around 1 mm).

Therefore, to collect high energy photons we have to launch rockets and satellites. The very first X-ray observation was made, thanks to the Aerobee rocket, in 1948 and focused on the X-ray sun emission. These energetic sun photons were one of the major topic in the next ten years for Herbert Friedman and collaborators at the naval research laboratory. Indeed, various other rocket were launched by Friedman and collaborators and Geiger counter were used.

A crucial year for X-ray astronomy was 1962. Indeed, to this data correspond the first discovery of a Extrasolar X ray source and an large X ray background (Giacconi et al. 1962). In the original plot (see Fig. A.1), over a diffuse background, a very large line spanning 15 degrees can be observed. That line represent the detection of SCO X-1. One year later (1963) SCO X1 was confirmed and in the same year during an occultation by the moon it was discovered an extended X-ray emission from the Crab nebula. Then, in 1966 was discovered the optical counterpart of SCO-X1 and his X-ray

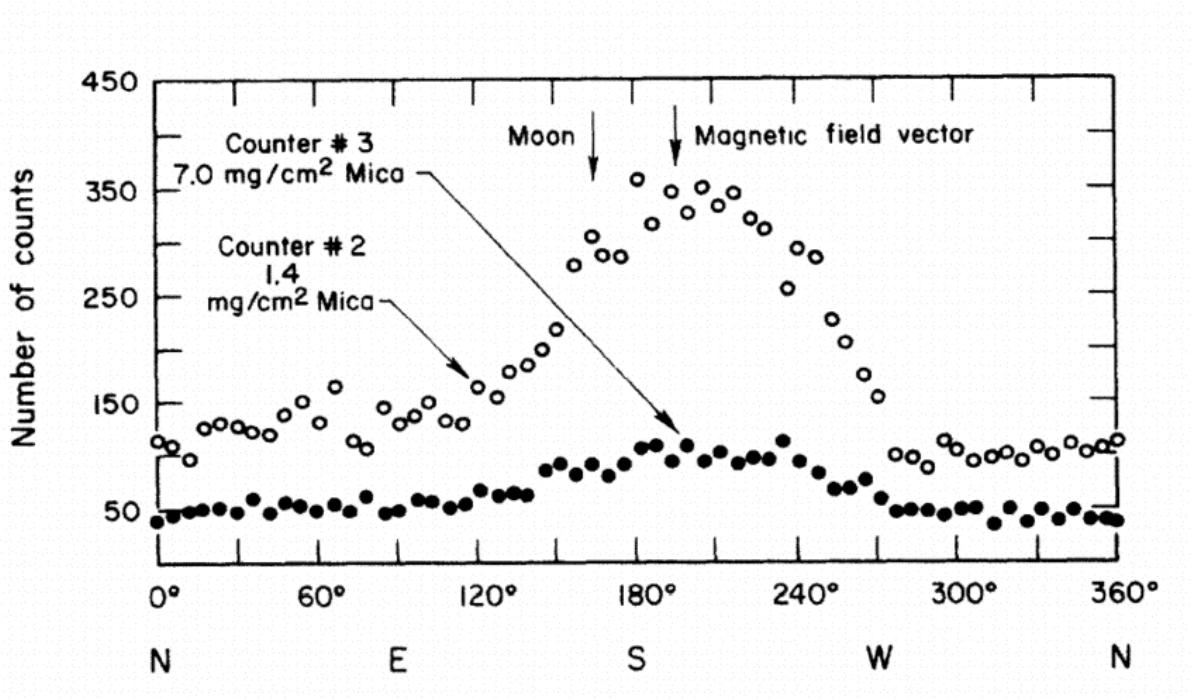

Figure A.1. The first extrasolar X-ray source as observed by the prof. R. Giacconi and his team (Giacconi et al. 1962). Here some number about this observations and the birth of the X-ray astronomy itself: 6 minutes the length of the observation, 230 km the altitude reached by the Aerobee rocket, 2 the geiger counters on board, 10 cm^2 the detector effective area in 1.5-6 Kev band, 1 the anti-coincidence scintillator on board.

localization arrive up to the $1'$ precision.
In the some year, it was recorded the first extragalactic emission from the coma cluster. The X-ray astronomy was growing and in the 1970 *Uhuru* the first mission with the goal of studying the X-ray sky was launched. It was equipped with two beryllium windows proportional counters, and *Uhuru* provided the first complete map of the X-ray sky with five degree of angular resolution. Fast the X-ray astronomy developed.
In the 1974 *Ariel V* was launched with the purpose of surveying all X-ray sky. Three years later the first high energy astrophysical observatory *HEAO1* was in orbit capable to detect the medium and the hard X-ray up to 100 kev with a modest angular resolution of some degrees. The Einstein telescope was the first X ray telescope launched for X ray observations. this telescope HEAO2 was the first having an focusing X-ray photons system with and angular resolution close to 2 sec. After *Einstein* we had a lot of missions looking at the X-ray sky:*EXOSAT* (the first *ESA* high energy astrophysics satellite), *GINGA* a large area detector from the Japanese space agency, the *ROSAT* mission, *ASCA*, and Italian observatory *BeppoSax*.

After this latter observatory, other facilities are still operating: *Chandra*, *XMM-Newton*, *INTEGRAL*, and, finally, about five years ago *NuSTAR*, the first X-ray telescope able to focus X-ray photons above 10 keV.

A.0.1 XMM-Newton

The X-ray space observatory XMM-Newton was launched on December 10, 1999, following a proposal originally made in 1982. The spacecraft weights 4 tons, it is 10 m long and it is composed by two payload modules, connected by a long carbon fibre tube. One of these modules is the Focal Plane Assembly, which contains the two high-resolution Reflection Grating Spectrometers (RGS den Herder et al. 2001), the EPIC (European Photon Imaging Camera) pn-CCD camera (Strüder et al. 2001b), with angular resolution of $15''$ 00 half-energy width (HEW) at 1.5 and 8 keV, and energy resolution of $\sim$ 100 eV at E = 2 keV, depending on window mode and distance from the focal point, and two EPIC MOS imaging detectors (Turner et al. 2001b), with same angular resolution as the pn camera, but slightly better energy resolution ($\sim$ 80 eV at E = 2 keV). The other one is the Service Module and it contains the majority of the spacecraft sub-systems, the Optical Monitor (OM) instrument (Mason et al. 2001b), astrometry equipment capable of absolute measurement accuracy of 4 arcsec, half-cone angle, and the three X-ray Mirror Modules. The most important improvement of XMM-Newton with respect of the previous X-ray detectors is the large collecting area (grazing angle ranging between 17 and 42 arcmin), which is made possible by the peculiar design of the three X-ray modules, consisting of 58 coaxial and confocal (Aschenbach et al. 1986) mirrors. In order to allow a simpler way to cool down the X-ray cameras, the satellite was placed in

a very eccentric orbit, with perigee at 7 000 km and apogee at 114 000 km (see Jansen et al. 2001, for a detailed discussion). The orbital period is approximately 48 hours. Given the fact that the orbit is so eccentric, some parts of it are contained within the radiation belt, giving rise to high background periods when the altitude is 60 000 km. Therefore, operations are limited above this altitude. However, all the elements of the observatory are designed to prevent a significant amount of damaging photons to reach the instruments, even during periods with the highest background.

A.0.2 NuSTAR

The Nuclear Spectroscopic Telescope Array (NuSTAR) is a NASA Small Explorer mission carrying the first telescope capable to focus hard X-rays up to $\sim$ 80 keV. This satellite was launched on June 13, 2012 from the Reagan Test Site on the Kwajalein Atoll in the South Pacific in a compact, stowed configuration on a Pegasus XL vehicle. This unprecedented eye scrutinizing the X-ray Universe is two orders of magnitudes more sensitive than any existing hard X-ray, and its angular resolution is one order of magnitude better than other satellites working in the same band. This NASA observatory is made up of two co-aligned Hard X-ray telescopes which are pointed at celestial targets by a three-axis-stabilized spacecraft. NuSTAR is composed by:

- an extendible mast, which holds the optics and detectors at a 10 meters distance: The low weight and compact mast is a sort of bridge between the optics and the detectors. Hard X-rays graze off the mirrors at nearly parallel angles, hard X-ray telescopes require long focal length. Moreover, it provides a stiff and stable structure connecting the precisely aligned benches.

- the two detectors:
  NuSTAR harbours two high-energy X-ray detectors capable of measuring the position and energy of the incoming X-rays. The two detectors are called focal-plane detectors because they reside where light from the telescope is focused. Each telescope has a corresponding Focal Plane Module (FPM) consisting of four 32×32 pixel Cadmium Zinc Telluride (CdZnTe) detectors surrounded by a Cesium Iodide (CsI) anti-coincidence shield. These detectors have energy resolution of $\sim$1% and high quantum efficiency over the entire NuSTAR energy range.

- the mirrors:
  NuSTAR has two optics units aligned to spot sky location. The two sets of images are then added together on the ground allowing detections of fainter emitters. NuSTAR employs low grazing angle focusing optics which are conical approximations to the Wolter Type 1 design (Hailey et al. 2010). Each of the two optics modules on board the spacecraft has 133 concentric, confocal shells with a focal length of 10.15

m. Then, the optics are characterized by an angular resolution of $\sim 12''$ (FWHM) and a field of view of $\sim 10'$. The reflectivity of optics shells starts decreasing with increasing angle of incidence of photons. This effect is more pronounced at higher energies and the field of view drops to $6'$ at 60 keV.

A.0.3 Swift Gamma Ray Burst Explorer

This observatory is a NASA Midex (medium-class explorer) mission. It was launched on November 20, 2004. This high energy facility is a composite observatory made up of three-telescopes. The Swift telescope was designed for studying the γ ray bursts (GRBs) and monitoring the afterglow in X-ray, and to identify the location of the event in the optical-UV domain. The satellite has a rapid-response capabilities and is equipped with three telescopes that cover a wide band of the electromagnetic spectrum, from the optical-UV domain up to γ-rays. In the following the main science instruments equipped by Swift are reported.

- **XRT**: 12 nested mirrors working according to the grazing incidence principle constitute the Wolter type 1 telescope XRT (Burrows et al. 2005). Photons are focused on single MOS charge-coupled device (CCD), similar to those equipped by XMM-Newton EPIC MOS cameras. It has an effective area of 110 cm^2 , $23.6' \times 23.6'$ field of view, $18''$ resolution and a 0.2-10 keV energy range. The X-ray telescope can acquire fluxes, perform spectral analysis and produce light curves of GRBs and their afterglow, covering a dynamic range that spans over seven order of magnitude.

- **UVOT**: UVOT (Roming et al. 2005) is a 30 cm modified Ritchey-Chrétien reflector with two micro-channel plate intensified CCD detectors that are modelled on the Optical Monitor on-board XMM-Newton. These photon counting devices are designed for working at very low signal levels, unaffected by CCD read-out noise and cosmic ray events. The UVOT facility contains three optical and three ultra-violet (UV) lenticular filters covering the wavelength range 1600 Å- 6000 Å, a white band filter that has a good response ranging from 1600 Å- 8000 Å, and a blocked filter.
  The instrument also has a visible grism and a UV grism, which provide low resolution spectra ($\lambda/d\lambda$ 75 eV) in the 2800 Å-5200 Åand 1600 Å-2900 Åenergy range, respectively, for sources that are brighter than 17 mag for the optical and 15 mag for the UV.

- **BAT**: The BAT instrument (Barthelmy et al. 2005) is designed to cover the prompt emission from GRBs over the whole sky. With a large field of view (1.4 sr) and a quick slew time, it can detect the position of GRBs in the sky with an accuracy of 1 - $4'$ in 15 seconds. The BAT uses a coded-aperture mask composed of $\sim$ 54000 lead

tiles, of dimensions 5 × 5 × 1 mm, which are mounted on a 5 cm thick composite honeycomb panel and placed 1 meter above the plane of the detector. The 12 ×0.6 m sensitive area of the BAT detector plane is formed by 32768 pieces of 4× 4 × 2 mm CdZnTe (CZT). Groups of 128 detector elements are collected into 8 × 16 arrays, each one of which is connected to 128-channel readout Application Specific Integrated Circuits (ASICs). The detector modules, which contain each two such arrays, are further grouped in blocks of eight. The hierarchical structure, together with the coded-aperture technique, allows the possibility of losing individual pixels, individual detector modules and even whole blocks without losing the ability to detect GRBs and determine positions.